Exploring the dynamics of strongly interacting media with dilepton tomography

Gojko Vujanovic

Department of Physics
McGill University
Montréal, Québec
Canada

A Thesis submitted to the
Faculty of Graduate Studies and Research
in partial fulfillment of the requirements for the degree of
Doctor of Philosophy

Contents

List of Figures

List of Tables

Abstract

The goal of current high-energy heavy-ion experiments is to study the properties of strongly interacting media. In particular, these experiments are trying to constrain the size of transport coefficients, such as shear viscosity, while at the same time probing the equation of state (EoS) of nuclear media. This equation of state admits the presence of a new state of matter the Quark-Gluon Plasma (QGP); a deconfined state of quarks and gluons — the building blocks of protons, neutrons, and nuclei.

Being emitted throughout the entire evolution of the medium, electromagnetic probes are sensitive to both the EoS of nuclear media and its transport coefficients. This thesis will show that the production of lepton pairs or dileptons (a particular class of electromagnetic radiation), can be used to study not only the overall size of the shear viscosity, which is modulated by a non-trivial temperature dependence, but also other transport coefficients. Furthermore, dileptons are also sensitive to the out-of-equilibrium properties of the initial state at the onset of evolution of the medium, currently best described via dissipative hydrodynamics. Particular attention will be given to the QGP, where the effects of various transport coefficients affecting its hydrodynamical evolution will be assessed. As soon as more precise experimental dilepton data become available, the framework presented in this thesis can be used in order to put (tight) constraints on various transport coefficients of strongly interacting media. This thesis focuses on describing the physics occuring at energies accessible to the Relativistic Heavy Ion Collider (RHIC) at Brookhaven National Laboratory (NY).

Résumé

L'objectif principal des expériences de collisions d'ions lourds aux énergies relativistes est d'étudier les propriétés de milieux régis par l'interaction nucléaire forte. En effet, ces expériences visent, entre autres, à cerner la valeur des coefficients de transport comme la viscosité de cisaillement et à déterminer l'équation d'état de l'environnement nucléaire. Celle-ci admet l'existence d'un nouvel état de la matière, le plasma quark-gluon, où les quarks et les gluons n'existent plus dans un état lié comme à l'intérieur des nucléons et des autres particules hadroniques.

Étant émise durant toute l'évolution du milieu, la radiation électromagnétique est influencée autant par les coefficients de transport que par l'équation d'état. Cette thèse va démontrer que la production de paires de leptons (ou dileptons), une forme d'émission électromagnétique, peut être utilisée afin d'étudier la viscosité de cisaillement ainsi que plusieurs autres coefficients de transport. De plus, les dileptons sont également sensibles aux propriétés hors d'équilibre de l'état initial. Présentement, le meilleur modèle de l'évolution du milieu régi par l'interaction forte repose sur l'hydrodynamique dissipative. Une attention particulière est donnée aux effets des coefficients de transport dans la phase plasma quark-gluon, ainsi qu'à leur influence sur l'évolution hydrodynamique. Les calculs élaborés dans cette thèse serviront de balises théoriques aux résultats de mesures expérimentales sur les paires de lepton qui seront prises très bientôt. Ces estimations théoriques sont faites pour les expériences réalisées au "Relativistic Heavy-Ion Collider" (RHIC), situé au Brookhaven National Laboratory (NY).

Acknowledgments

I would first like to express my deepest gratitude to my supervisor Professor Charles Gale for his great insight in choosing a very active research subject and for his relentless guidance and support throughout the past years, without which none of this would have been possible. Additionally, I would like to thank Professor Sangyong Jeon for numerous enlightening discussions and his advice regarding best manners to present physics results. I would also like to thank all the post doctoral associates that I've collaborated and/or interacted with over the years: Dr. Björn Schenke, Dr. Clint Young, Dr. Aleksi Kurkela, Dr. Gabriel S. Denicol, Dr. Matthew Luzum, Dr. Jacopo Ghiglieri, Dr. Chun Shen and Dr. Thomas Epelbaum for taking the time to answer my numerous questions. Furthermore, I would like to thank Prof. Ralf F. Rapp for his interesting comments and suggestions, especially during the first half of my PhD. I am also indebted to my friends and colleagues in the Theoretical Nuclear Physics Group and in the Department. Especially, Jean-François Paquet, Igor Kozlov, Michael Richard, and Sangwook Ryu for their continuous help and enlightening discussions. I would also like to thank the entire staff of the Guillimin supercomputer at McGill University, under the auspices of Calcul Québec and Compute Canada, for allocating time on the Guillimin supercomputer to perform the computationally intensive calculations. Lastly, I would like to thank my parents for believing in me and supporting me for all these years.

My research was funded in part by the Natural Science and Engineering Research Council (NSERC), the Seymor Schulich Graduate Fellowship and the Graduate Fellowship from the Canadian Institute of Nuclear Physics.

Statement of originality

The results presented in this thesis are original work, with the following precisions.

In Chapter 3, I computed the thermal dilepton production rates from the ϕ mesons and all viscous corrections to thermal dilepton production from the hadronic medium. I have also computed the baryon diffusion correction in the quark gluon plasma and the hadronic dilepton rate, with the modification to the thermal distribution function entering in the rate calculation provided by Gabriel S. Denicol.

Chapter 4 includes my original work except for the calculation of heavy quark diffusion in section 4.2.3 which was done by Clint Young. The results in section 4.4 were obtained after I have folded the dilepton rates in Refs. [6, 7, 8], which were provided to me by the authors of those references, with my hydrodynamical evolution obtained using the hydrodynamical code MUSIC developed at McGill. Based Ref. [9], I've also calculated the cocktail dilepton rates provided in section 4.5.

All the results in chapter 5 are my original work except for the calculation of the modification to the thermal distribution function present in section 5.2 (with details in appendix B) which was done by Gabriel S. Denicol, and the fit to hadronic observables (sections 5.1 and 5.2) which was done by Jean-François Paquet. Also, the evolution of the hydrodynamical medium in section 5.3, including the fit of the hydrodynamical free parameters, was done by Chun Shen.

1

Introduction

1.1 Quantum Chromodynamics: Basic concepts and experimental implications

More than 99.9% of the mass of the matter that surrounds us in everyday lives is coming from atomic nuclei. Physicists are naturally driven to try to understand what kind of forces are responsible for generating all this mass. The best current description of the forces governing nuclear interactions comes from a Quantum Field Theory (QFT) known as Quantum Chromodynamics (QCD). The building blocks of a nucleus, the proton and the neutron, are not elementary particles in QCD and are themselves bound states of fundamental nuclear particles. These fundamental nuclear particles, the quarks and gluons, carry nuclear charges — i.e. color charges: red, green, and blue – which are sourced by quarks, bound together under a potential mediated by gluons.

The color charges of quarks can be used to construct QCD analogously to Quantum Electrodynamics (QED). Following the QED analogy, quarks in QCD act as charged leptons (electron, muon, and tau) in QED while gluons (bosons mediating color forces) are similar to photons which mediate electromagnetic forces. However that is as far as that analogy can be used in constructing QCD. Indeed, QCD possesses a different gauge group than QED: QCD is SU(3) while QED is U(1). So, the gauge group of QCD implies that, unlike the photon of QED, gluons carry their own color (i.e. strong) charges. In fact QCD has 8 gluons, each possessing a color charge and anti-charge pair. Their representation in color space can be written as :

$$\begin{array}{llll} (r\bar{g}+g\bar{r})/2 & -i(r\bar{g}-g\bar{r})/2 & (r\bar{b}+b\bar{r})/2 & -i(r\bar{b}-b\bar{r})/2 \\ (b\bar{g}+g\bar{b})/2 & -i(b\bar{g}-g\bar{b})/2 & (r\bar{r}-b\bar{b})/2 & (r\bar{r}+g\bar{g}-2b\bar{b})/2\sqrt{3}, \end{array} \tag{1.1}$$

where r=red, g=green, and b=blue, while the bar denotes the anti-color. The representation above is equivalent to the Gell-Mann matrices [10], which will be labeled as t_a, where $a = 1 \ldots 8$ are the 8 generators of SU(3). For example $(r\bar{g}+g\bar{r})/2$ can be written as :

$$2t_1 = \begin{pmatrix} 0 & 1 & 0 \\ 1 & 0 & 0 \\ 0 & 0 & 0 \end{pmatrix}. \tag{1.2}$$

The fact that gluons possess both a color and an anti-color implies that upon interaction with another colored object (be it a quark or another gluon), they can change the color charge of that object. So unlike photons which cannot change electric charges, gluons can change the color charges of quarks and furthermore can self-interact. This self-interaction is possible because of QCD's non-Abelian SU(3) gauge group and is the key distinction between QCD and QED. The QCD Lagrangian illustrates this:

$$\begin{gathered} \mathcal{L}_{QCD} = \bar{\psi}_{(ej)} \left(i\gamma^{\mu} D_{\mu}^{jj'} - m\delta^{jj'} \right) \psi_{(j')}^{(e)} - \frac{1}{4} G_a^{\mu\nu} G_{\mu\nu}^a, \\ D_{\mu}^{jj'} = \delta^{jj'} \partial_{\mu} - i g_s A_{\mu}^a t_a^{jj'}, \quad G_{\mu\nu}^a = \partial_{\mu} A_{\nu}^a - \partial_{\nu} A_{\mu}^a + g_s f^{abc} A_{\mu}^b A_{\nu}^c, \end{gathered} \tag{1.3}$$

where color indices in the fundamental representation (j, j') are explicitly written down, $\psi^{(e)}$ is the quark field of flavor e =up, down, strange, charm, bottom, and top, whose strength of interaction with gluon fields A_{μ}^a is encoded in the coupling g_s. These gluon fields have generators t_a, whose commutator $[t_a, t_b] = i f_{abc} t_c$ gives rise to the SU(3) structure constants f_{abc}. This commutator is another way of distinguishing between gluons and photons: the generator for photons is a scalar. To make the commutator more explicit in the QCD Lagrangian, gluon kinetic term $-\frac{1}{4} G_a^{\mu\nu} G_{\mu\nu}^a$

can be rewritten, using $\mathrm{Tr}\left(t^a t^b\right) = \delta^{ab}/2$:

$$
\begin{aligned}
-\frac{1}{4}G_a^{\mu\nu}G_{\mu\nu}^a &= -\frac{1}{2}\ \mathrm{Tr}\left(G_a^{\mu\nu}t_a G_{\mu\nu}^a t^a\right) \\
&= -\frac{1}{2}\mathrm{Tr}\left(\left(\partial^\mu A_a^\nu - \partial^\nu A_a^\mu + g_s f_{abc} A_b^\mu A_c^\nu\right) t_a \left(\partial_\mu A_\nu^a - \partial_\nu A_\mu^a + g_s f^{abc} A_\mu^b A_\nu^c\right) t^a\right) \\
&= -\frac{1}{2}\mathrm{Tr}\left(\left(\left(\partial^\mu A_a^\nu - \partial^\nu A_a^\mu\right) t_a - i g_s \left[t_b, t_c\right] A_b^\mu A_c^\nu\right)\right. \\
&\quad \times \left.\left(\left(\partial_\mu A_\nu^a - \partial_\nu A_\mu^a\right) t^a - i g_s [t^b, t^c] A_\mu^b A_\nu^c\right)\right) \\
&= -\frac{1}{4}\left(\partial^\mu A_a^\nu - \partial^\nu A_a^\mu\right)\left(\partial_\mu A_\nu^a - \partial_\nu A_\mu^a\right) \\
&\quad + \frac{i g_s}{2}\mathrm{Tr}\left(\left(\partial^\mu A_a^\nu - \partial^\nu A_a^\mu\right) t_a \left[t^b, t^c\right] A_\mu^b A_\nu^c\right) \\
&\quad + \frac{i g_s}{2}\mathrm{Tr}\left(\left(\partial_\mu A_\nu^a - \partial_\nu A_\mu^a\right) t^a \left[t_b, t_c\right] A_b^\mu A_c^\nu\right) \\
&\quad + \frac{g_s^2}{2}\mathrm{Tr}\left(\left[t^b, t^c\right] A_\mu^b A_\nu^c \left[t_b, t_c\right] A_b^\mu A_c^\nu\right),
\end{aligned} \tag{1.4}
$$

where the photon-like kinetic term is the first term in the equation above while the other terms are possible self-interactions of the gluon and only appear because of gluon's color charge-carrying nature. Lastly, the fact that gluons can change the color charge of quarks is encoded in quark's gauge covariant derivative D_μ. These two properties of gluons play a central role in modern ultra-relativistic heavy-ion experiments.

Like many interacting quantum field theories, QCD cannot yet be solved analytically. So, more attention is given towards approximate solutions, e.g. perturbative solutions. The use of perturbation theory was very successful to approximately solve quantum field theories such as QED owing to the fact that the strength of the electromagnetic charge (or electromagnetic coupling) was measured to be small. Indeed, free electric charges are observed in everyday life. The same cannot be said about color charges. This lead to the belief (as conclusive proof is lacking) that QCD, at energy scales typical of hadronic physics must be strongly coupled (i.e. its color charge, or equivalently its coupling constant, is large) and yield color-neutral objects, such as protons and neutrons, and hence perturbation theory cannot be applied. In the middle of the 1970's, an important breakthrough was accomplished in applying perturbation theory to QCD. This breakthrough is the emergence of renormalization theory formulated through the renormalization group (RG) equations (see e.g. [11]). RG provides a robust mathematical framework within which one can study changes in the behavior of physical system as perceived from different energy scales. In particular it is possible to study the variation of the strength of an interaction, i.e. the size of the coupling constant, as the energy scale is being varied. This change in the coupling constant with the energy scale is a non-perturbative process. A formulation of the RG equations that is commonly used in QFT are the Callan-Symanzik equations [10]. The Callan-Symanzik equations can be perturbatively solved allowing to gain access to the running of the coupling and thereby to non-perturbative physics. When applying RG equations to the coupling constant of the strong interactions, a groundbreaking discovery was made: strong (nuclear) interactions become smaller with increasing energy scale, in other words QCD was "asymptotically free" [12] (see Fig. 1.1).

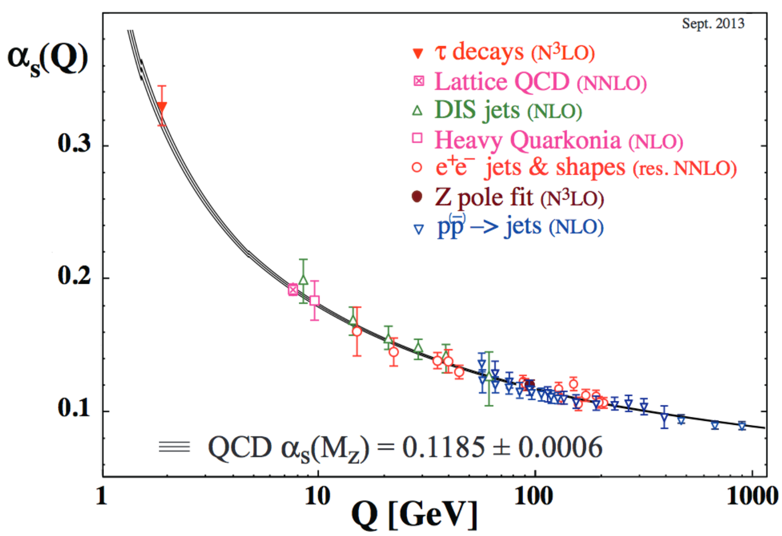

Figure 1.1: Comparison of experimental measurements of the strong coupling constant $\alpha_s = \frac{g_s^2}{4\pi}$ at various energy scales Q with the theoretical prediction [1].

This is a direct result of the SU(3) nature of the gluon coupling, and is in stark contrast with QED whose charge diverges as the energy scale is increased. This discovery earned Frank Wilczek, David Gross, and independently David Politzer the physics Nobel Prize in 2004.[1] Asymptotic freedom implies that in the high energy regime, the strong coupling constant becomes small and hence perturbative QCD can be used to study, in a laboratory, the fundamental particles of QCD and their strong interactions. The interaction can be studied on a more individual-particle level in very high energy proton-(anti)proton or electron-proton collisions or as a collective phenomenon, in a thermal medium produced in relativistic heavy-ion collisions. Indeed, in sufficiently energetic collisions this thermalized medium contains a new phase of matter known as the Quark-Gluon Plasma (QGP). The QGP is a system where bound states of quarks and gluons are not expected to be present, i.e. a state composed of "quasi-free" quarks and gluons. Though early calculations have suggested that a state of "quasi-free" quarks and gluons is formed, modern lattice calculations and phenomenological analysis revealed a slightly more complicated picture: one where even at high temperatures the Stefan-Boltzmann limit is not reached [13]. Understanding the properties of the QGP is at the center of the modern relativistic heavy-ion program.

1.2 Quantum Chromodynamics: Equation of state

One of the goals of current ultra-relativistic heavy-ion colliders, the Relativistic Heavy Ion Collider (RHIC) at Brookhaven National Laboratory (BNL) and the Large Hadron Collider (LHC) at CERN, is to experimentally map out the equation of state (EoS) of the thermal QCD medium, paying particular interest to the QGP. The QCD EoS can be studied at lower and higher collisions energies. At the high-energy front, the increase of the beam energy from RHIC to LHC has created media with increasing average temperature, along with an increasing space-time volume of the QGP phase, allowing for more detailed studies of the QGP to be performed. Of equal interest and importance is to study possible phase transitions accessible to experiments at lower beam energies. To that end, RHIC has put in place a Beam Energy Scan (BES) program. RHIC is however not the only laboratory to study the phase diagram of QCD

[1] http://www.nobelprize.org/nobel_prizes/physics/laureates/2004/

at low beam energies. The Facility for Antiproton and Ion Research (FAIR) at GSI Helmholtz Centre for Heavy Ion Research, which is currently being constructed, is partly designed to complement and improve the studies started during the BES program at RHIC. While the BES program covers energies $\sqrt{s_{NN}}$ = 7.7–200 GeV [14], the Compressed Baryonic Matter (CBM) program at FAIR will produce even more collisions at lower beam energies, namely from 2–45 GeV/nucleon in a fixed target setup [15], which roughly translates into $\sqrt{s_{NN}} \lesssim 10$ GeV [16]. With its improved setup, giving high statistics[1], the FAIR facility will be exploring more in-depth the phase diagram of QCD, and possibly providing a precise region where the critical point of QCD may lie. Though FAIR is not a subject of this thesis, a discussion of the BES will be presented. Schematically, the explored phase space of the QCD EoS can be summarized via the sketch in Fig. 1.2.

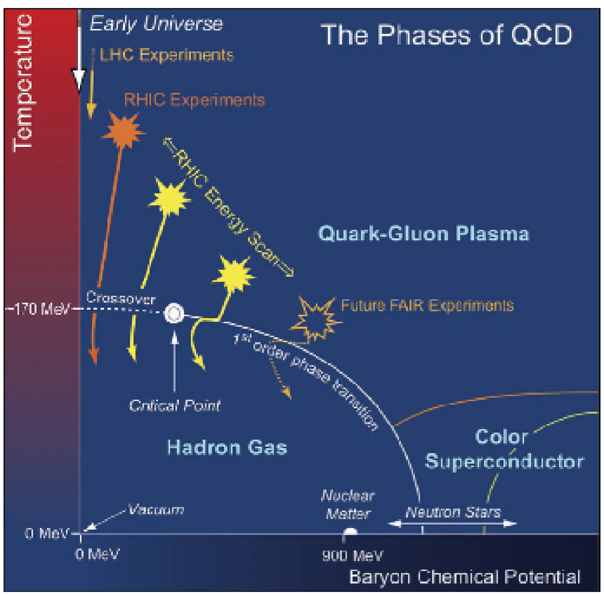

Figure 1.2: Phases of QCD [2]. The sensitivity to the QCD EoS of various of the relativistic heavy-ion experiments is illustrated.

On the theory front, in recent years there has been an immense progress in calculat-

[1]Being a fixed target experiment, the FAIR facility will have a much higher luminosity than RHIC, translating into a collision rate that is expected to be 5–6 orders of magnitude greater than RHIC in the region where the two experiments overlap in collision energies [16].

ing the QCD EoS from first principles using lattice QCD (ℓQCD). These calculations were performed using the canonical and grand canonical formalisms. ℓQCD calculations within the canonical formalism have shown that, for the energies available at RHIC and the LHC, the transitions from the QGP to the hadronic medium, composed of mesons (quark-antiquark bound states) and baryons (3-quark bound states) is not a first nor a second order phase transition but rather a smooth crossover [17, 18]. The state-of-the-art lattice calculations can describe the QCD EoS from the high temperatures QGP phase to just after the crossover takes place. Going lower in temperatures becomes more and more difficult, requiring smaller lattice spacings and larger simulated volumes, to keep both finite size and discretization errors reasonably small [13]. Such calculations are currently in development. Hence, to describe the QCD medium at low temperatures, that is in the hadronic phase, a hadron resonance gas (HRG) model is being used where the masses of all hadrons are set to their experimental values. The HRG model describes the low temperature QCD EoS as gas of non-interacting low lying hadronic states and their higher mass resonances (i.e. excited 2- and 3-quark bound states). In the limit where an elastic scattering between particles introduces a sharp transition in the phase shift in the outgoing particles' wavefuction, thus producing long-lived particles, Ref. [19] has shown that an interacting gas of low mass resonances is equivalent to a non-interacting gas of hadronic resonances, i.e. a HRG. There are two main arguments behind using a non-interacting hadron resonance gas model instead of a more complicated interacting model. First, the number densities of heavy particles are small $n_i \sim \exp(-m_i/T)$, while their mutual interaction given by the product $n_i n_j \sim \exp(-(m_i + m_j)/T)$, is even smaller. Hence only the interaction of low mass particles becomes relevant. The second reason for using a HRG comes from a study by Prakash and Venugopalan [20], which showed that a gas of interacting particles containing only pions and kaons[1] as constituents of the heat bath behaves closely to a non-interacting gas of hadrons (including hadronic

[1] In Ref. [20], experimentally measured phase shifts were used for pions an kaons, while all hadronic resonances were excluded from the composition of the thermal bath.

resonances). Thus the result of Ref. [19] is reinforced. These two arguments are further supported by the actual comparison, at low temperatures, between the pressure of the HRG model and the pressure from ℓQCD. Indeed, a non-interacting hadron resonance gas matches quite well with ℓQCD in the low temperature region, if the masses of the low lying resonances are the same as those in the ℓQCD calculation (see e.g. [21]). This is not the end of the story, however, as the Review of Particle Physics [1] contains a lot more *short-lived* resonances than the few included by Prakash and Venugopalan. To fully confirm that a non-interacting hadron resonance gas model is compatible with an interacting hadron gas model, a lot more *short-lived* resonances need to be included. Such a calculation has not been done yet, however recent studies by Weinhold, Friman, and Nörenberg [22, 23, 24, 25] seem to indicate that the inclusion of short lived resonances in an interacting hadron gas model yield results different from those of non-interacting hadron resonance gas model. Thus more studies are needed.

When comparing the lowest temperature lattice results with the high temperature HRG results [21], there is an "overlap" region over which the two calculations yield similar results. Hence, modern parametrizations of QCD EoS interpolate between ℓQCD results and HRG results (see e.g. [21] for a particular prescription).

Within the last decade or so there has been increasing activity in the ℓQCD community in computing the QCD EoS using the grand canonical formalism. Previously there were no successful attempts to compute the ℓQCD EoS in this formalism, since introducing a chemical potential associated with a conserved charge (e.g. net baryon number and the associated net baryon chemical potential μ_B) within the Helmholtz free-energy for QCD incurs mathematical challenges in its computation. Indeed, the integration measure becomes a complex-valued function. Standard Monte Carlo Integrations Techniques (MCITs), used to integrate over the huge field-configuration space, require that the integration measure be positive semi-definite. However the determinant has to be allowed to take complex values in order to produce the correct physics [26]. Hence MCITs fail and cause what is known as the "sign problem".

To circumvent these mathematical difficulties, techniques such as Taylor expansion around $\mu_i = 0$ (where i is the conserved charge in question), analytic continuation from an imaginary μ_i were developed, among others. These two methods are however limited to small chemical potentials over temperature ratios, i.e. $\mu_i/T \lesssim 1$. Compared to the more mature EoS obtained at $\mu_i = 0$, where agreement between various ℓQCD groups was achieved, results at finite μ_i need to be more thoroughly scrutinized. However, in all ℓQCD calculations using the grand canonical formalism, no signature of a first (or second) order phase transition was found to date [17, 18].

There are recent developments, using complex Langevin dynamics, that bear promise in not only circumventing the "sign problem" of traditional ℓQCD techniques [27], but also offer the possibility of efficiently extract the QCD EoS at large values of μ_i/T. At lower values μ_i/T, where both the Taylor expansion techniques and the complex Langevin dynamics are applicable, more detailed analysis are currently underway [27]. A summary of the complex Langevin method along with some of its promising new results can be found in Ref. [28].

1.3 Hydrodynamics

Having established a macroscopic description of a thermalized QCD medium, through its EoS, the next natural question that arises is: "After the medium is created in a heavy-ion collision, how does it evolve in time?" The full answer to this question would come from non-perturbative, off-thermal-equilibrium QCD. Since such a theory is still in development, theoretical models are used to explain experimental data from RHIC and LHC, thus putting some constraints on the possible physical processes at play. Currently, the most successful model describing the available data coming from relativistic heavy-ion collisions relies on relativistic dissipative hydrodynamics. In order for the medium to be described by dissipative hydrodynamics, the medium needs to quickly transition from a non-perturbative off-equilibrium state to one that is close to being in thermal equilibrium. The typical "thermalization time", that is the starting time of the hydrodynamical evolution needed by modeling, ranges from

0.1–1fm/c (see, e.g. [29, 30, 31, 32, 33, 34]). Such a short "thermalization time" is obtained by fitting hydrodynamical calculations to the experimental particle spectra. Within the quantum field theory framework, it is not easy to obtain such a short value for the "thermalization time" and in fact, the physical mechanisms responsible for driving this fast thermalization are still under investigation. There are two fronts of recent development: i) in the limit where the coupling constant is small so that perturbation theory is applicable, ii) and in the limit of large coupling where a holographic approach is used. On the non-perturbative front, progress was made using the gauge-gravity duality present in String Theory (also known as AdS/CFT correspondence [35]), where a strongly coupled conformal field theory (i.e. not QCD) in 3+1D space-time is dual to a weakly coupled gravity theory in a 4+1D. These theories have shown that a fast thermalization of the order 0.1-1 fm/c is possible (see [36] and [37]). On the perturbative side, specifically using non-Abelian gauge theory, developments happened on two complementary fronts: in the limit of low gluon occupation number where Kinetic Theory is applicable, and in the high gluon occupation where a solution of the classical Yang-Mills equations equation is necessary. For recent developments via the Kinetic Theory approach within the SU(3) gauge group, see [38, 39], and references therein. As far as solving classical Yang-Mills equations goes, recent developments, using SU(2) gauge theory, can be found in [40, 41]. Both approaches also indicate that thermalization can happen within 0.1–1 fm/c. The overall result found in all of these investigations is consistent with a fast thermalization of the medium.

Fortunately, the system is not required to be in perfect thermal equilibrium for the hydrodynamical equations of motion to be valid. Indeed, the key assumption that needs to be satisfied in order for hydrodynamics to be a valid description of the medium's space-time evolution is that the typical distance ℓ between particle collisions, i.e. the mean free path, is sufficiently shorter than the typical size L of the medium (i.e. the Knudsen number is much smaller than unity $K_n = \ell/L \ll 1$). As soon as this assumption is satisfied, i.e. at "thermalization time", the hydrodynamical equations of motion can be used to describe the evolution of the medium [42] (see also the beginning of section 2.3 for more details). Part of hydrodynamical equations of motion (see section 2.1 for more details) are independent conservation equations of energy–momentum, baryon (B) number, strangeness (S), and electric charge (Q) densities. These conservation equations read:

$$\partial_\mu T^{\mu\nu} = 0 \tag{1.5}$$

$$\partial_\mu J^\mu_B = 0,\, \partial_\mu J^\mu_S = 0, \text{and}\, \partial_\mu J^\mu_Q = 0 \tag{1.6}$$

where $T^{\mu\nu}$ is the energy-momentum tensor, J^μ_B is the baryon density current, J^μ_S is the strangeness current, and J^μ_Q is the electric charge current. To get non-dissipative (ideal) hydrodynamics further assumptions need to be made. These assumptions are for an observer traveling at the same (local) velocity as the fluid. That observer perceives i) the medium as being isotropic and homogeneous while ii) there is no flux in the local (conserved) number densities, i.e. there is no diffusion of conserved charges. These assumptions can be viewed as a consequence of the basic assumption of hydrodynamics in the limit $\ell \to 0$ or $K_n \to 0$, which implies that local thermal equilibrium is maintained at all times. In that limit, only Eq. (1.5) and Eq. (1.6) need to be solved and all the complicated non-perturbative QCD dynamics on the microscopic scale is stored in the ℓQCD EoS. In that limit, $T^{\mu\nu}$ is completely described by the following properties of a fluid cell: its energy density ε, its fluid four-velocity $u^\mu = (\gamma, \gamma\boldsymbol{\beta})$[1], and its pressure P which is related to ε and net baryon, strangeness, and electric charge densities $n_{B,S,Q}$ via the ℓQCD EoS[2]. Hence the energy–momentum tensor and baryon current density of an ideal fluid can be written as (see section 2.1 for more details):

$$T^{\mu\nu}_{(0)} = \varepsilon u^\mu u^\nu - P(g^{\mu\nu} - u^\mu u^\nu) \tag{1.7}$$

$$= \varepsilon u^\mu u^\nu - P\Delta^{\mu\nu} \tag{1.8}$$

$$J^\mu_{B,S,Q} = n_{B,S,Q} u^\mu \tag{1.9}$$

[1] $\gamma = (1-\boldsymbol{\beta}^2)^{-1/2}$, $\boldsymbol{\beta} = \mathbf{v}/c$, $\mathbf{v}$ is the fluid three-velocity and c is the speed of light.

[2] The net baryon, strangeness, and electric charge density is the difference between the density of baryons and anti-baryons, strange hadrons and anti-strange hadrons, and the sum of positive and negative charges. These are conserved quantities in QCD.

In the above equations, notice that the tensor $\Delta^{\mu\nu} = g^{\mu\nu} - u^\mu u^\nu$ is orthogonal to velocity, i.e. $u_\mu \Delta^{\mu\nu} = 0$. This means that in a relativistic fluid, the pressure accelerating the fluid elements is acting orthogonal to the fluid 4-velocity. Also note that the fluid velocity tracks the flow of energy density and net baryon density in an ideal medium. The EoS used in this thesis will only contain the net baryon density in the canonical $n_B = \mu_B = 0$ and grand canonical type $n_B > 0$, $\mu_B \geq 0$. The effects of strangeness and electric charge are left for future studies.

When going beyond ideal hydrodynamics, the deviations from local thermal equilibrium are assumed to be small such that the ℓQCD EoS can still be used to relate pressure to other thermodynamical variables. However, collisions between particles of the medium are now allowed to modify the ideal hydrodynamical expansion rate of the fluid velocities (i.e. modify the velocity gradients). Both the radial and angular directions will be affected through non-vanishing mean free paths between particle collisions. This mean free path is stored in two transport coefficients known as the bulk and shear viscosities of the fluid affecting the radial and angular velocities, respectively.[1] For a non-zero net baryon density, collisions can cause net baryon number diffusion. In this case, J_B^μ ceases to be collinear with u^μ. The equations for dissipative hydrodynamics will be presented in the next chapter.

1.4 Electromagnetic probes and study of strongly interacting media

The transport properties of fluids that exist in a typical laboratory can be indirectly studied with pre-engineered calibrated probes. As these probes interact with the medium, their properties get changed, and thus the observer can infer the properties of the medium via the modifications the probes acquire after traveling through the medium. Another possibility is to use a device that would directly study the properties of the medium: for example if the device generates any normal modes of oscillation of the medium (e.g sound waves), and then detects the propagation of those

[1]Note that the effects of bulk viscosity will not be studied in this thesis.

modes within medium. Using such a device will give direct information about the properties of the medium. However, these sound waves don't have to be man-made; they can be naturally occurring. Geophysicists study the composition of inner layers of the Earth by using naturally-occurring sound waves: earthquakes. Similarly, in astrophysics, prolonged observation of the light coming off Sun's surface has allowed detection of sound waves within its plasma, providing valuable information about the Sun's inner structure/composition via helioseismology [43].

However, there are several situations where this approach is not feasible and one must resort to other indirect methods. Indeed, the medium created in relativistic heavy-ion collisions cannot be studied via laboratory-made "calibrated probes", since the system does not live long enough for that to be feasible. Thus radiation coming from the medium itself must be used in order to learn about its properties.

Among the main goals of high-energy heavy-ion physics is to learn about as many transport properties of strongly interacting media as possible, while pinning down the initial conditions of the medium created right after a relativistic heavy-ion collision has occurred. For that purpose, the ideal probe would be one which is emitted throughout the entire evolution of the medium and is able to escape it, without being significantly modified; in essence, a fully penetrating probe. Since the medium is described by QCD whose coupling constant g_s is larger than the electromagnetic coupling e,[1] a QED probe would be ideally suited. Thus, electromagnetic radiation is arguably the "cleanest" probe, as it can leave the strongly interacting medium with negligible re-scatterings. Hence, electromagnetic radiation is the main topic of this thesis. There are two main classes of electromagnetic emission: real photons and lepton pairs (dileptons) created from the decay of virtual photons $\gamma^* \to \ell^+\ell^-$.

The penetrating nature of electromagnetic probes allows them to gain access to the entire evolution of the medium and its initial conditions. Thus electromagnetic probes in principle are more sensitive to the medium's microscopic properties (such as viscosity and equation of state) than hadrons, which mostly give information about

[1] At collision energies accessible by current heavy-ion colliders.

the last, kinetic freeze-out, stage of the medium.[1] This high sensitivity of electromagnetic probes was realized early on in the history of high-energy heavy ion collisions, i.e. in the first half of the 1980's and even slightly before that (see [44, 45] and references therein). This thesis will concentrate on dileptons. Compared to photons, dileptons have an additional degree of freedom: the center of mass energy of the lepton pair or the invariant mass M. This extra feature allows to differentiate dileptons from the QGP and those originating in the hadronic medium. There are, however, other sources of dileptons than those from the QGP and the hadronic medium, hence a review of the important ones is instructive.

There are two main categories of dilepton sources: those that originate from the thermal medium and those that do not. These non-thermal sources of dileptons are masking, to a certain degree, the thermal signal being pursued here. The non-thermal dilepton sources come from QCD+QED processes as well as weak interactions, and from decays of light mesons — composed of up, down, and strange quarks. The dilepton contribution coming from the decay of light mesons is known as the "dilepton cocktail", which is discussed in section 4.5. A summary of all the important non-thermal dilepton sources is given in Fig. 1.3, where the data are taken from the deuteron-gold (d-Au) collisions carried out at RHIC by the PHENIX experiment. At RHIC energies, d-Au collisions were assumed to have no medium effects hence there is no thermal contribution in Fig. 1.3. However, all the non-thermal sources of dileptons present in these collisions also exist in Au-Au collisions at RHIC, except for the ρ-meson contribution. Since the treatment of the ρ is rather intricate, it will be discussed later.

The important sources of non-thermal dileptons are: cocktail dileptons, Drell-Yan (DY) processes, decays of open charm and beauty hadrons (see curves labeled $c\bar{c}$ and $b\bar{b}$ in the main plot of Fig. 1.3), i.e. hadrons with a charm or bottom quark combined with a light up and/or down quark(s), as well as decays of high-mass vector mesons

[1] Kinetic freeze-out is a process during which the medium ceases to exist as all collisions between its constituent particles stop occurring, thus particles follow a free-streaming trajectory established at their last scattering.

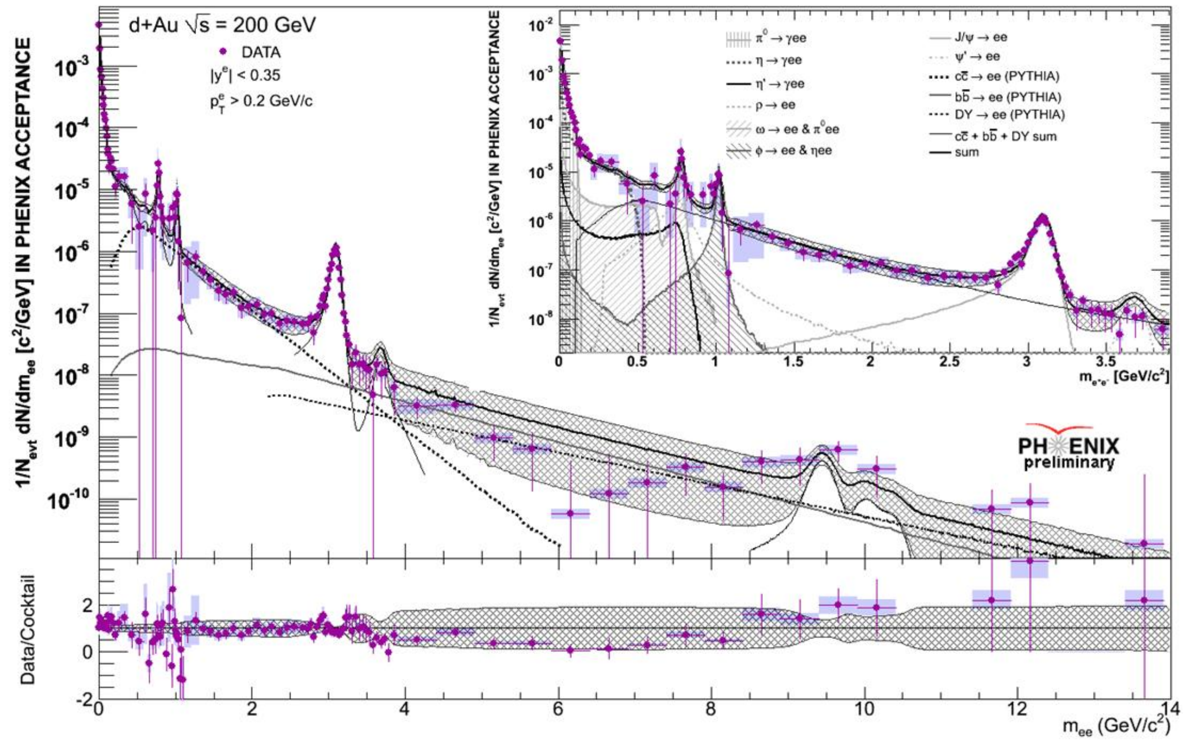

Figure 1.3: The yield as a function of dielectron invariant mass m_{ee} for all important non-thermal sources of dileptons is plotted. This plot is taken from the preliminary dielectron measurements done by the PHENIX Collaboration at RHIC [3].

— quark-antiquark ($q\bar{q}$) spin-1 states. Vector mesons involving charm quarks (also known as charmonium states) are $J/\psi(1S)$, $\psi(2S)$ (labeled ψ' in the plot), while those involving beauty quarks (also known as bottomonium) are $\Upsilon(1S)$ and $\Upsilon(2S)$ [1]. Those are illustrated in the main panel of Fig. 1.3.

The leading order Drell-Yan processes are shown in Fig. 1.4 (e) and can be described via a combination of perturbative QED and QCD. In all other cases, the leading order non-thermal perturbative QCD (pQCD) mechanisms involved in dilepton production proceed through the production of a high energy gluon. This hard gluon can be obtained through either direct $q\bar{q}$ annihilation or gluon-gluon fusion as shown in Fig. 1.4 (a) and (b). Once this gluon is produced, it decays into a pair of charm or bottom quarks, i.e. heavy flavor quarks. Up to this point, the process can be correctly described through pQCD. Then, these charm and bottom quarks "hadronize", while interacting with the QCD medium. A discussion about how this

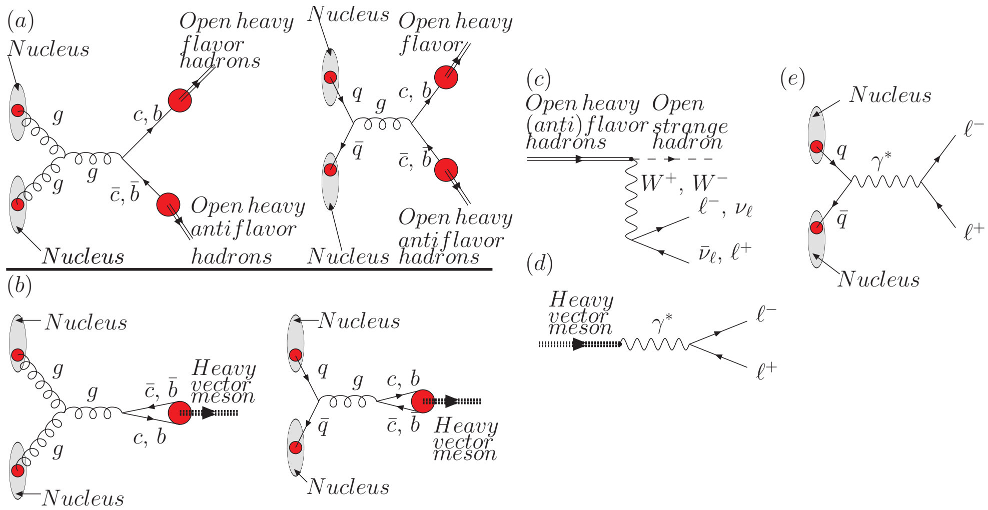

Figure 1.4: In all diagrams, the red circle implies a non-perturbative process is at play. Jet beams from the nuclei are not shown. (a) The main production mechanisms of open heavy flavor hadrons. (b) The main leading order (LO) pQCD production mechanisms of heavy vector mesons. (c) The decay of open heavy flavor into leptons goes through a weak interaction. Each charged lepton $\ell^{\pm}$ from the decay of the open heavy flavor-antiflavor pair is used to form the dilepton spectrum. (d) The decay of heavy vector mesons may produce dileptons directly. (e) Drell-Yan dilepton production to LO pQCD.

interaction with the medium happens will be done in section 4.2.1. Once the medium is gone and only hadrons remain, the decay of either open charm and bottom hadrons, and heavy flavor vector mesons, then proceeds as illustrated in Fig. 1.4 (c) and (d), respectively. Looking specifically at 1.4 (d), the dilepton production from heavy flavor vector mesons is obvious. In the case of open charm/beauty hadrons, i.e. open heavy flavor hadrons illustrated in Fig. 1.4 (c), the lepton pair production comes from combining the leptons and antileptons coming from the weak decay of open heavy flavor and antiflavor hadrons.

The upper right corner of Fig. 1.3 depicts dilepton production coming from the dilepton cocktail, i.e. the decay of low mass vector and pseudoscalar mesons.[1] These decays proceed as in proton-proton collisions (i.e. in the vacuum) as they occur after the medium has frozen-out. The distributions of these mesons are measured when possible, otherwise scaling relations are used. In terms of Feynman diagrams, Fig.

[1]Pseudoscalar mesons are spin-0 mesons. However, under a parity transformation, their wave-function acquires an overall minus sign, hence the word "pseudo" in their name.

1.5 depicts the important processes involved in the decay of vector and pseudoscalar mesons into dileptons [9].

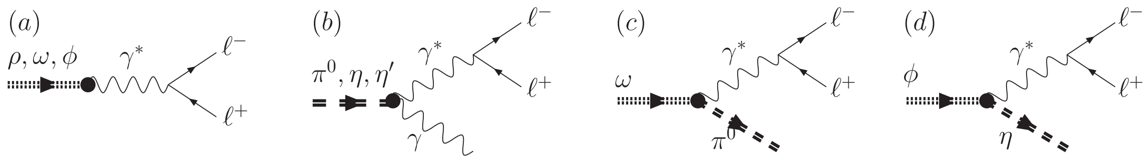

Figure 1.5: (a)Vector mesons decay into dileptons. (b) Pseudoscalar mesons decay into dileptons. Special ω (c) and ϕ (d) decay channels contributing to dileptons.

The only source of dileptons that hasn't been covered yet is the thermal radiation. As was already mentioned, in the high temperature limit, the main source of dileptons comes from the QGP. At leading order in the electromagnetic coupling $\alpha_{EM} = \frac{e^2}{4\pi}$ (where e is the electric charge), and to zeroth order in the strong coupling, or simply at leading order, dileptons come from $q\bar{q} \to \gamma^*$: the Born approximation of dilepton production. This is the main source of dileptons at intermediate and high invariant masses, above ~1 GeV. In the low mass sector, reactions of the form gluon absorption/emission and Compton scattering of a quark off a gluon need be included [46, 47, 48]. These are depicted in Fig. 1.6. There are, however, important coherence

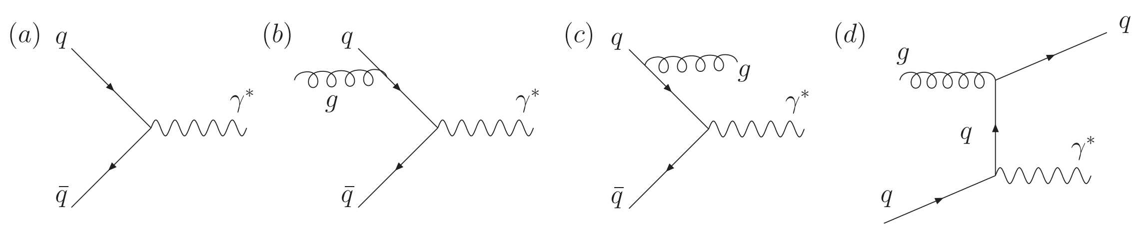

Figure 1.6: (a) Born term (b) Gluon absorption (c) Gluon emission (d) Compton scattering.

effects that need to be added to the diagrams in Fig. 1.6, and, given their complexity, will be discussed in section 4.4.

In the low invariant mass sector, there is an equally important (if not more important) source of thermal dileptons that needs to be considered, namely dileptons coming from the *in-medium* decay of vector mesons; the operative words being *in-medium*. Indeed, the properties of all hadrons are modified once they are surrounded by a strongly interacting medium, same as any other bound states in physics. The question that needs answering is whether these modifications have an impact on dilepton production. In cases of short-lived mesons — with lifetimes comparable to the total lifetime of the medium – which decay into dileptons, it becomes difficult to say whether the decay occurs inside or outside the medium. The prime example of this is the ρ meson whose lifetime is $\tau_\rho \sim 0.44 \times 10^{-23}$ seconds in the vacuum [1]. The typical hydrodynamical calculations of heavy-ion collisions at RHIC and LHC last ~ 10 fm/c or $\sim 3 \times 10^{-23}$ seconds [29, 30, 31, 32, 33]. For this reason, most ρ mesons are expected to decay inside the medium and any contribution of ρ mesons outside the medium comes from the decays of heavy resonances $R \to \rho + X$ [49]. As for the ω and ϕ mesons, though these particles live $\tau_\omega \sim 8.3 \times 10^{-23}$ and $\tau_\phi \sim 16.5 \times 10^{-23}$ seconds in vacuum, they have significant in-medium effects shrinking their in-medium lifetime to $\sim 1 - 2 \times 10^{-23}$ seconds allowing for them to decay in the medium created at RHIC and LHC [49]. On the other hand, pseudoscalar mesons live substantially longer ($> 10^{-21}$ seconds) and hence any in-medium decay is not expected. Some of the important interactions in the hadronic gas responsible for shortening the lifetime of vector mesons are illustrated in Fig. 1.7. These types

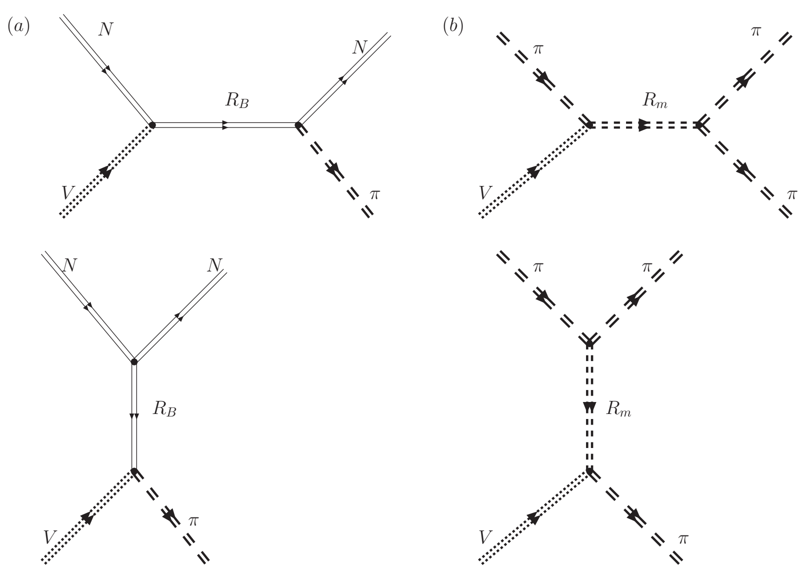

Figure 1.7: Important interactions affecting the lifetime of vector mesons. (a) Nucleon interactions going through baryon resonances R_B. (b) Meson interactions going through mesonic resonances R_m.

of interactions are responsible for the (collisional) broadening of vector meson width $\Gamma_{V=\rho,\omega,\phi}$ — related to the lifetime via $\Gamma_V = \hbar/\tau_V$. To complete the picture of thermal dilepton sources, another (though less significant) source of dileptons that needs to be mentioned comes from resonances of vector mesons; also known as the 4π contribution [49]. The name 4π comes from the fact that these higher mass vector mesons are created from the "fusion" of 4π. The lowest such resonance is that of the ρ mesons via $4\pi \to \rho(1450) \to \ell^+\ell^-$. Of course since the ρ meson is created almost exclusively via $\pi + \pi \to \rho$, the reaction $\rho + \rho \to \rho(1450)$ is also counted as a 4π contribution. This covers all the important sources of dileptons, and except for the 4π contribution, all major sources of dilepton production from low to intermediate invariant masses ($M < 2.5$ GeV), will be considered in this work.

The rest of this thesis is organized as follows. Chapter 2 will discuss the hydrodynamical modeling of the (dissipative) evolution of the medium, chapter 3 will describe the production rates of dileptons in more detail, chapter 4 will combine all the main sources of dileptons for $M < 2.5$ GeV and discuss dilepton yield and anisotropic flow, chapter 5 analyzes the sensitivity of thermal dileptons to various transport coefficients of dissipative hydrodynamics, and lastly chapter 6 presents concluding remarks.

2

Dissipative hydrodynamics

The dissipative hydrodynamics are at the heart of modern modeling of the medium created in high energy heavy-ion collisions [50]. However, hydrodynamics can only model the medium in a particular region of space-time. Thus, hydrodynamical equations of motion must be supplemented by the initial conditions of the medium and freeze-out conditions describing how to stop the hydrodynamical simulation. Of course, part of the freeze-out prescription also includes the manner in which to convert the fluid elements into particles that are ultimately detected in experiment. Hence, this chapter is separated into three sections. The first section explores the hydrodynamical equations of motion themselves. The second section deals with the initial conditions for the fluid equations that will be used throughout this thesis, and the last section is reserved for the freeze-out conditions: the conversion of fluid elements to particles. This section will also explore the manner in which initial geometry influences the distribution of particles detected in experiment.

2.1 Fluid dynamics equations

The theory of fluid dynamics is entirely composed of two ingredients: thermodynamics/statistical mechanics and conservation equations. The main conservation equations include conservation of energy and momentum and conservation of charge(s). If thermodynamical fluctuations are neglected[1], as will be done throughout this the-

[1] Thermodynamical fluctuations would enter via the fluctuation dissipation theorem, which would introduce a non-trivial two point correlation function between hydrodynamical degrees of freedom [51, 52].

sis, then all the microscopic degrees of freedom are contained within the equation of state and the transport coefficients. In fact, the equation of state and the transport coefficients encode the *average values* of microscopic degrees of freedom of the fluid. The macroscopic degrees of freedom of the fluid are:

- the velocity of the fluid element u^α,
- its energy density ε,
- its net baryon number density n_B,
- the equation of state $P(\varepsilon, n_B)$ relating the energy density and the net baryon number density to the pressure P,
- second order dissipative corrections to entropy: Π, $\pi^{\alpha\beta}$, and V^α, which will be defined later.

Derivatives $\partial^\beta u^\alpha$, $\partial^\alpha u_\alpha$, $\partial^\alpha(\mu_B/T)$, $\nabla^\alpha P$ and so on can only be present in the stress-energy tensor $T^{\alpha\beta}$ and the baryon current J_B^α for dissipative fluids. Navier-Stokes [53] hydrodynamics describes dissipative fluids using solely derivatives of thermodynamic quantities (including the fluid velocity u^α) and transport coefficients. A description using these degrees of freedom is only appropriate at late times, i.e. after a few fm/c of evolution for ultra-relativistic media such as those created in heavy-ion collisions. At early times, new degrees of freedom are needed in addition to thermodynamic degrees of freedom, such as bulk (Π) and shear ($\pi^{\alpha\beta}$) viscous pressures and the net baryon number diffusion vector (V^α). These new degrees of freedom are required by causality; imposing that derivatives of thermodynamic quantities cannot build-up instantaneously. Therefore, a set of relaxation equations is present, known as Müller-Israel-Stewart fluid dynamics [54, 55, 56, 57], which govern the entire dynamics of the system including the new degrees of freedom. Müller-Israel-Stewart equations converge towards the Navier-Stokes hydrodynamics at later times. Thus, the new degrees of freedom, though physical as they describe the dynamics of dissipation, become superfluous at late times, since the dissipative dynamics, at that point, can be entirely captured by derivatives of macroscopic degrees of freedom.

2.1.1 Non-dissipative (ideal) hydrodynamics

In addition to conservation laws, the assumption that the medium is in local thermal equilibrium is a necessary and sufficient condition to entirely determine the form of the energy-momentum tensor $T^{\alpha\beta}_{(0)}$ and the net baryon current $J^{\alpha}_{B,(0)}$ of non-dissipative (ideal) hydrodynamics. Using the degrees of freedom mentioned, non-dissipative fluid dynamics is constructed using the Lorentz scalars, ε, P, and n_B, the vector u^α, and the metric tensor $g^{\alpha\beta}$, which is taken to be the Minkowski metric $g^{\alpha\beta} = \mathrm{diag}(1, -1, -1, -1)$. Since the net baryon number is conserved, the baryon current $J^{\alpha}_{B,(0)}$ must satisfy $\partial_\alpha J^{\alpha}_{B,(0)} = 0$. In non-dissipative hydrodynamics, $J^{\alpha}_{B,(0)}$ can only be constructed out of n_B and u^α, thus $J^{\alpha}_{B,(0)} = n_B u^\alpha$ [58, 59, 60]. Furthermore, using the degrees of freedom available to non-dissipative hydrodynamics, the most general energy-momentum tensor that can be written is [53]:

$$T^{\alpha\beta}_{(0)} = \varepsilon(c_0 g^{\alpha\beta} + c_1 u^\alpha u^\beta) + P(c_2 g^{\alpha\beta} + c_3 u^\alpha u^\beta). \tag{2.1}$$

Determining $c_0, \ldots, c_3$ is easiest in the local rest frame (LRF). In the LRF of a medium, local thermodynamical equilibrium requires that $T^{00}_{(0)} = \varepsilon$ and $T^{0i}_{(0)} = 0$, which represent the local energy density and momentum of the fluid. The latter should naturally vanish in the LRF. The diagonal spatial components of $T^{\alpha\beta}_{(0)}$ should be proportional to the pressure, i.e. $T^{ij}_{(0)} = \delta^{ij} P$, while off-diagonal components are zero owing to the assumption that the medium is homogeneous and isotropic in the LRF. Using these three conditions to solve for $c_0, \ldots, c_3$, yields:

$$c_0 = 0, \quad c_1 = 1 \quad c_2 = -1 \quad c_3 = 1, \tag{2.2}$$

or

$$\begin{aligned} T^{\alpha\beta}_{(0)} &= \varepsilon u^\alpha u^\beta - P(g^{\alpha\beta} - u^\alpha u^\beta) \\ &= \varepsilon u^\alpha u^\beta - P\Delta^{\alpha\beta} \end{aligned} \tag{2.3}$$

where $\Delta^{\alpha\beta}$ is a projection operator orthogonal to the fluid flow. Since there are no other sources contributing to $T^{\alpha\beta}_{(0)}$:

$$\partial_\alpha T^{\alpha\beta}_{(0)} = 0. \tag{2.4}$$

Projecting Eq. (2.4) along the fluid flow and orthogonal to it, allows to recover the more commonly used non-relativistic non-dissipative fluid equations [58, 59, 60]. Projecting along flow gives:

$$\begin{aligned} u_\beta \partial_\alpha T^{\alpha\beta}_{(0)} &= u^\alpha \partial_\alpha \varepsilon + \varepsilon \left[\partial_\alpha u^\alpha\right] - P u_\beta \partial_\alpha \Delta^{\alpha\beta} \\ &= u^\alpha \partial_\alpha \varepsilon + (\varepsilon + P) \left[\partial_\alpha u^\alpha\right] = 0, \end{aligned} \tag{2.5}$$

where the following relation were used $u_\beta \partial_\alpha u^\beta = \frac{1}{2}\partial_\alpha(u_\beta u^\beta) = 0$ as $u_\beta u^\beta = 1$, and $\partial_\alpha g^{\alpha\beta} = 0$ for the Minkowski metric. Projecting orthogonal to flow yields:

$$\begin{aligned} \Delta^\nu_\beta \partial_\alpha T^{\alpha\beta}_{(0)} &= \varepsilon u^\alpha \Delta^\nu_\beta \partial_\alpha u^\beta - \Delta^{\alpha\nu} \left[\partial_\alpha P\right] + P u^\alpha \Delta^\nu_\beta \partial_\alpha u^\beta \\ &= (\varepsilon + P) u^\alpha \partial_\alpha u^\nu - \Delta^{\alpha\nu} \partial_\alpha P = 0. \end{aligned} \tag{2.6}$$

It is useful to decompose the derivative 4-vector ∂^α into direction along and orthogonal to the flow, namely:

$$\begin{aligned} \partial^\alpha = u^\alpha u_\beta \partial^\beta + \Delta^\alpha_\beta \partial^\beta &= u^\alpha \frac{d}{d\tau} + \nabla^\alpha, \text{ where} \\ \frac{d}{d\tau} &= u^\alpha \partial_\alpha, \text{ and } \nabla^\alpha = \Delta^{\alpha\beta} \partial_\beta, \end{aligned} \tag{2.7}$$

while τ is the proper time.[1] So, $u^\alpha \partial_\alpha$ acts like a time derivative operator while ∇^α acts as a gradient operator. Using Eq. (2.7), Eq. (2.5) and Eq. (2.6) can we rewritten as

$$\frac{d\varepsilon}{d\tau} + (\varepsilon + P)\partial_\alpha u^\alpha = 0 \tag{2.8}$$

$$(\varepsilon + P)\frac{du^\nu}{d\tau} - \nabla^\nu P = 0. \tag{2.9}$$

At non-relativistic velocities, $u^\alpha \to (1, \boldsymbol{\beta})$ and $P \ll \varepsilon$ therefore $\frac{d}{d\tau} \to \partial_t + \boldsymbol{\beta} \cdot \boldsymbol{\partial}$, and $\nabla^\nu \to (0, \boldsymbol{\partial}) + (\boldsymbol{\beta} \cdot \boldsymbol{\partial}, -\boldsymbol{\beta}\left[\partial_t - \boldsymbol{\beta} \cdot \boldsymbol{\partial}\right])$. These non-relativistic relations can be used to rewrite Eq. (2.8) and Eq. (2.9) as

$$\partial_t \rho + \boldsymbol{\partial} \cdot (\rho \boldsymbol{\beta}) = 0 \tag{2.10}$$

$$\partial_t \boldsymbol{\beta} - \frac{1}{\rho} \boldsymbol{\partial} P = 0 \tag{2.11}$$

[1] The proper time is the time as measured by an observer flowing with the fluid, i.e. in the LRF.

where in the non-relativistic limit $\varepsilon \to \rho$, with ρ being the mass density[1]. Eq. (2.10) is the continuity equation and Eq. (2.11) is the Euler equation of non-relativistic ideal hydrodynamics.[2] Furthermore, since there are no sources of dissipation, the total entropy of the system must be conserved. Labeling the entropy density as s, the entropy current is [55, 56, 57, 58, 59]:

$$\begin{aligned} S^\alpha_{(0)} &= s u^\alpha \\ S^\alpha_{(0)} &= P\frac{u^\alpha}{T} - \frac{\mu_B}{T} J^\alpha_{B,(0)} + \frac{u_\beta}{T} T^{\alpha\beta}_{(0)}, \end{aligned} \tag{2.12}$$

where the the Euler relation $\varepsilon = Ts - P + \mu_B n_B$ was used to go from first to second line. The formulation in the second line of Eq. (2.12) will become useful for dissipative fluids. The first law of thermodynamics $d\varepsilon = Tds + \mu_B dn_B$ and the Euler relation, can be used to rewrite Eq. (2.5) as:

$$\begin{aligned} T\left[\frac{ds}{d\tau} + s\partial_\alpha u^\alpha\right] + \mu_B\left[\frac{dn_B}{d\tau} + n_B\partial_\alpha u^\alpha\right] &= 0 \\ T\partial_\alpha\left[s u^\alpha\right] + \mu_B \partial_\alpha\left[n_B u^\alpha\right] &= 0 \\ \partial_\alpha S^\alpha_{(0)} + \partial_\alpha J^\alpha_{B,(0)} &= 0 \\ \partial_\alpha S^\alpha_{(0)} &= 0 \end{aligned} \tag{2.13}$$

where the conservation of the net baryon number current was used to prove conservation of the entropy density current.

2.1.2 Dissipative hydrodynamics: effects of viscosity and diffusion

Going beyond ideal hydrodynamics implies that total entropy is no longer required to be conserved. Indeed, dissipative effects are augmenting the space of independent variables present in ideal hydrodynamics by introducing new dissipative variables in the conservation equations. The goal of this section is to find the equation of motion

[1] Also note that in order to obtain non-relativistic fluid dynamics, the equation of state needs to be changed by removing all relativistic effects present in its computation.

[2] Moreover, note that in a relativistic system it is awkward to use the mass density ρ as this is not a well defined quantity. For example, a gas of photons has no well defined mass density but has a well defined energy density.

of these novel variables. It is important to note that while the equations of motion for non-dissipative variables are given by conservation equations, there are in general no criteria specifying the specific evolution for each dissipative variable. However, as will be seen, the equation of motion for dissipative variables are restricted by the second law of thermodynamics, where the definition of entropy is generalized to include dissipative degrees of freedom.

Assuming that the deviations from exact thermal equilibrium are small, the energy-momentum tensor, the baryon current, and the entropy current can be written as [58, 59]:

$$\begin{aligned} T^{\alpha\beta} &= T^{\alpha\beta}_{(0)} + \delta T^{\alpha\beta} \\ J^{\alpha}_{B} &= J^{\alpha}_{B,(0)} + \delta J^{\alpha}_{B} \\ S^{\alpha} &= S^{\alpha}_{(0)} + \delta S^{\alpha}. \end{aligned} \tag{2.14}$$

As $\delta T^{\alpha\beta}$ and δJ^{α}_{B} change the original definitions of $T^{\alpha\beta}_{(0)}$ and $J^{\alpha}_{B,(0)}$, the meaning of energy density and net baryon number is no longer clear. To clarify the meaning of these two quantities, the following matching conditions are used:

$$u_\alpha u_\beta T^{\alpha\beta} = \varepsilon \tag{2.15}$$

$$u_\alpha J^{\alpha}_{B} = n_B \tag{2.16}$$

These equations imply that $u_\alpha u_\beta \delta T^{\alpha\beta} = 0$ and $u_\alpha \delta J^{\alpha}_{B} = 0$. A further decomposition of $\delta T^{\alpha\beta}$ can be made by separating the piece which modify the trace of $T^{\alpha\beta}$, which will be labeled as Π, from the components which do not. The components that leave the trace invariant are shear stresses (labeled $\pi^{\alpha\beta}$) and energy density diffusion W^{α}. The energy density diffusion W^{α} has in general two components $W^{\alpha} = \frac{\varepsilon+P}{n_B} V^{\alpha} + q^{\alpha}$, where q^{α} is heat diffusion, and $V^{\alpha} = \delta J^{\alpha}_{B}$ is the net baryon number diffusion. Thus,

$$\delta T^{\alpha\beta} = -\Pi \Delta^{\alpha\beta} + (u^{\alpha} W^{\beta} + W^{\alpha} u^{\beta}) + \pi^{\alpha\beta}, \tag{2.17}$$

where the negative sign in front of Π is chosen for later convenience. Lastly δS^{α} is the entropy diffusion current.

A slight digression: Note that $\pi^{\alpha\beta}$ has two important properties: the trace $g_{\alpha\beta}\pi^{\alpha\beta} = 0$, which is to be expected as it doesn't change the trace of $T^{\mu\nu}$, and $u_\beta\pi^{\alpha\beta} = 0$, hence $\pi^{\alpha\beta}$ is orthogonal to u^α. Putting these two properties together: $\Delta_{\alpha\beta}\pi^{\alpha\beta} = 0$.

At this point the flow 4-velocity u^α is an ill-defined quantity as it is not clear which physical quantity is flowing. In non-relativistic fluid dynamics, particle number (density) can be used to define the 3-velocity $\boldsymbol{\beta}$, i.e. $\boldsymbol{\beta} \cdot \mathbf{J_B} = n_B$. Choosing this convention, also known as the Eckart [61] definition, in the relativistic setting implies $u_\alpha J_B^\alpha = n_B$, which means that $V^\alpha = 0$ and energy diffusion is really just heat conduction ($W^\alpha = q^\alpha$).

The problem with this definition arises at ultra-relativistic energies such as those at the LHC or at the top beam energy at RHIC. In that case, net baryon number density plays essentially no role in the evolution of the medium. The physical reason for this comes from the fact that nucleus-nucleus collisions, at the highest energies accessible, create a medium mostly from gluon interactions, while valence quarks play a negligible role.

Indeed, very few (if any) nuclei are significantly deflected while the medium is being created in a nucleus-nucleus collision; they pass through each other at ultra-relativistic velocities[1] and their gluon interactions are responsible for creating most of the medium. Valence quarks only play a role at lower beam energies. Indeed, the parton distribution functions of nucleons, giving the probability density of finding a quark or a gluon in a nucleon in high energy collisions — measured by the HERA (Hadron-Elektron-Ring-Anlage; German for Hadron Electron Ring Facility) collider [63] at DESY (Deutsches Elektronen-Synchrotron; German for Electron Synchrotron), reveals that most of the composition of the proton (or neutron) at high energy comes from the gluons. The modifications owing to the fact that nucleons in a nucleus are different then nucleons outside of the nucleus do not change the fact that gluons dominate the modified parton distribution function of nucleons in a nucleus. Thus

[1] This interpretation was first proposed by Björken [62].

the particles being detected mostly comes from a gluon-induced medium.

So, since the net baryon number density plays a negligible role at high energies, a different definition of 4-velocity should be used. A convenient definition of u^α is one where it is parallel to energy density flow, i.e. the Landau-Lifshitz definition [53].[1] More specifically, the following eigenvalue equation should be solved

$$T^{\alpha\beta}u_\beta = \varepsilon u^\alpha. \tag{2.18}$$

This equation implies that $W^\alpha = 0$, and thus $V^\alpha = -\frac{n_B}{\varepsilon+P}q^\alpha$. Since this definition of energy density is the same in non-dissipative and dissipative hydrodynamics, it becomes clear (by going to the LRF) that Π and π^{ij} are corrections to the pressure tensor $T^{ij}_{(0)} = \delta^{ij}P$. Π changes the value of the equilibrium thermodynamic pressure P, while π^{ij} introduces off-diagonal elements to the pressure tensor. Hence the diagonal and the off diagonal terms of the pressure tensor, are modified via [58, 59]:

$$\Pi = -\frac{1}{3}\Delta_{\alpha\beta}T^{\alpha\beta} - P \tag{2.19}$$

$$\begin{aligned}
\pi^{\alpha\beta} &= \Delta^{\alpha\beta}_{\rho\sigma}T^{\rho\sigma} \\
\pi^{\alpha\beta} &= \left[\frac{1}{2}\left(\Delta^\alpha_\rho\Delta^\beta_\sigma + \Delta^\beta_\rho\Delta^\alpha_\sigma\right) - \frac{1}{3}\Delta^{\alpha\beta}\Delta_{\rho\sigma}\right]T^{\rho\sigma}
\end{aligned} \tag{2.20}$$

where $\Delta^{\alpha\beta}_{\rho\sigma}$ is a double symmetric traceless projection operator [64]. Furthermore, it should be noted that V^α is always orthogonal to velocity, i.e. $V^\alpha = \Delta^\alpha_\beta V^\beta$. Putting all the above results together, the energy-momentum tensor, baryon current, and entropy currents read:

$$\begin{aligned}
T^{\alpha\beta} &= \varepsilon u^\alpha u^\beta - (P+\Pi)\Delta^{\alpha\beta} + \pi^{\alpha\beta} \\
J^\alpha_B &= n_B u^\alpha + V^\alpha \\
S^\alpha &= P\frac{u^\alpha}{T} - \frac{\mu_B}{T}J^\alpha_B + \frac{u_\beta}{T}T^{\alpha\beta} + Q^\alpha\left(\delta J^\alpha_B, \delta T^{\alpha\beta}\right)
\end{aligned} \tag{2.21}$$

The entropy current in Eq. (2.21) includes a new term Q^α which will now be discussed. Obtained by generalizing Eq. (2.12), the entropy current not only includes first order (i.e. linear in Knudsen number) dissipation corrections [see second and third terms of

[1] Note that the Landau-Lifshitz definition of flow is also well suited to treat fluid mixtures.

Eq. (2.21)] but also second and higher order corrections absorbed in the variable Q^α. Any third or higher order dissipative correction will not be considered in this thesis.

The second law of thermodynamics applied on the entropy current can be used to relate Π and $\pi^{\alpha\beta}$ to derivatives of the fluid velocity $\partial_\alpha u^\alpha$ and $\partial^\alpha u^\beta$, respectively, while also relating V^α to $\partial^\alpha\left[\frac{\mu_B}{T}\right]$. Thus, Navier-Stokes hydrodynamics can be obtained through the second law if Q^α is neglected, while Müller-Israel-Stewart hydrodynamics is obtained if it isn't. The the Gibbs-Duhem relation $dP = sdT + Nd\mu$ can be rewritten as:

$$\partial_\alpha\left[P\frac{u^\alpha}{T}\right] = J^\alpha_{B,(0)}\partial_\alpha\left[\frac{\mu_B}{T}\right] - T^{\alpha\beta}_{(0)}\partial_\alpha\left[\frac{u_\beta}{T}\right]. \tag{2.22}$$

In this form, the Gibbs-Duhem relation can be used to simplify the conservation of entropy equation to

$$\begin{aligned}
\partial_\alpha S^\alpha &= -\delta J^\alpha_B\partial_\alpha\left[\frac{\mu_B}{T}\right] + \delta T^{\alpha\beta}\partial_\alpha\left[\frac{u_\beta}{T}\right] + \partial_\alpha Q^\alpha \\
&= -V^\alpha\partial_\alpha\left[\frac{\mu_B}{T}\right] + \left[-\Pi\Delta^{\alpha\beta} + \pi^{\alpha\beta}\right]\frac{\partial_\alpha u_\beta}{T} + \partial_\alpha Q^\alpha \\
&= -V^\alpha\nabla_\alpha\left[\frac{\mu_B}{T}\right] + -\Pi\frac{\partial_\alpha u^\alpha}{T} + \pi^{\alpha\beta}\frac{\Delta^{\rho\sigma}_{\alpha\beta}\partial_\rho u_\sigma}{T} + \partial_\alpha Q^\alpha
\end{aligned} \tag{2.23}$$

where the orthogonality conditions $\Delta^{\alpha\beta}u_\beta = \pi^{\alpha\beta}u_\beta = V^\alpha u_\alpha = 0$ were used. The simplest way to satisfy the second law of thermodynamics is to impose a linear relationship between dissipative flows and thermodynamic forces [58, 59],

$$\begin{aligned}
\Pi &= -\zeta\partial_\alpha u^\alpha = -\zeta\theta \\
V^\alpha &= \kappa\nabla^\alpha\left[\frac{\mu_B}{T}\right] = \kappa\nabla^\alpha\alpha_0 \\
\pi^{\alpha\beta} &= 2\eta\Delta^{\alpha\beta}_{\rho\sigma}\partial^\rho u^\sigma = 2\eta\sigma^{\alpha\beta}
\end{aligned} \tag{2.24}$$

where $\zeta \geq 0$ is the bulk viscosity, $\kappa \geq 0$ is the net baryon number conductivity (which is related to heat conductivity as $q^\alpha \propto V^\alpha$), and $\eta \geq 0$ is the shear viscosity. With these definitions at hand, the second law of thermodynamics for the Navier-Stokes fluid can be rewritten as

$$\partial_\alpha S^\alpha = \frac{\Pi^2}{\zeta T} - \frac{V^\alpha V_\alpha}{\kappa} + \frac{\pi^{\alpha\beta}\pi_{\alpha\beta}}{2\eta T} \geq 0, \tag{2.25}$$

where the Q^α term was neglected. Since all terms on the right hand side of Eq. (2.25) are quadratic[1], the second law of thermodynamics is manifestly satisfied. The Navier-Stokes stress-energy tensor, baryon, and entropy current read:

$$T^{\alpha\beta} = \varepsilon u^\alpha u^\beta - (P - \zeta\theta)\Delta^{\alpha\beta} + 2\eta\sigma^{\alpha\beta} \tag{2.26}$$

$$J_B^\alpha = n_B u^\alpha + \kappa\nabla^\alpha\alpha_0 = n_B u^\alpha + \frac{\kappa}{T}\nabla^\alpha\mu_B - \frac{\kappa\mu_B}{T^2}\nabla^\alpha T \tag{2.27}$$

$$S^\alpha = s u^\alpha - \alpha_0 V^\alpha = s u^\alpha - \alpha_0\kappa\nabla^\alpha\alpha_0 \tag{2.28}$$

The physical meaning of the coefficients η, ζ and κ is as follows. The shear viscosity η measures the amount of friction between adjacent fluid layers, while bulk viscosity ζ measures the system's isotropic compressibility. Indeed for an incompressible fluid, bulk viscosity vanishes exactly. Lastly, κ measures the ease with which baryons can flow from one fluid element to another, similar to heat conductivity. In fact, the Fourier law of heat conduction can be seen in Eq. (2.27). In the limit where $\partial^\alpha\mu_B = 0$, $q^\alpha = -\frac{\varepsilon+P}{n_B}V^\alpha \propto \nabla^\alpha T$ just as in the Fourier law of heat conduction.[2]

However, Navier-Stokes equations of motion cannot be used for relativistic fluids as they are acausal (see [65] as well as [50], and references therein). Indeed, if a small patch of a fluid acquires a non-zero $\delta T^{\alpha\beta}$, it will instantaneously also acquire gradients of flow velocities, thus clearly violating causality. Hence a relaxation equation is required to relate $\delta T^{\alpha\beta}$ to derivatives of velocity, chemical potential, pressure and so on.[3] These relaxation equations can still be obtained by using the second law of thermodynamics, but one has to take into account contributions to Q^α that are of second order in the dissipative currents. For this reason, these hydrodynamical equations are commonly referred to as second order fluid dynamics.

To derive Müller-Israel-Stewart equations, the original work of these three authors

---

[1]Note that $V^\alpha V_\alpha$ <0. This can easily be seen by using the property $V^\alpha u_\alpha = 0$ and going to the LRF of the medium.

[2]Note that in the non-relativistic limit $\nabla^\alpha T \to -\nabla T$.

[3]Nevertheless, for non-relativistic fluids Navier-Stokes equation is a good description, since $\delta T^{\alpha\beta}$ relaxes very quickly towards $\zeta\theta\Delta^{\alpha\beta} + 2\eta\sigma^{\alpha\beta}$, while δJ_B^α relaxes to $\kappa\nabla^\alpha\alpha_0$.

will be used. To start, first define Q^α as [55, 56, 57]:

$$Q^\alpha = -\left[b_0\Pi^2 - b_1 V_\beta V^\beta + b_2\pi^{\rho\sigma}\pi_{\rho\sigma}\right]\frac{u^\alpha}{2T} - a_0\Pi V^\alpha - a_1\pi^{\alpha\beta}V_\beta, \tag{2.29}$$

where a_i and b_i are undetermined coefficients at this point. Notice that Eq. (2.29) is second order in dissipative variables. Using Q^α in Eq. (2.21), the effective entropy density measured by a co-moving observer is:

$$u_\alpha S^\alpha = s - \left[b_0\Pi^2 - b_1 V_\beta V^\beta + b_2\pi^{\rho\sigma}\pi_{\rho\sigma}\right]\frac{1}{2T} \tag{2.30}$$

which is independent of a_i (as $V^\alpha u_\alpha = 0$). A state in complete thermodynamical equilibrium must maximize entropy, hence $u_\alpha Q^\alpha \leq 0$, which imposes that the coefficients b_i are positive semi-definite. Additionally, note that the second order correction to the entropy current, not only corrects the piece that is parallel to u^α but also introduces a component orthogonal flow. The orthogonal piece:

$$\Delta^\alpha_\beta \delta S^\beta = -\alpha_0 V^\alpha - a_0\Pi V^\alpha - a_1\pi^{\alpha\beta}V_\beta \tag{2.31}$$

is independent of b_i. The 4-divergence of the entropy current, including the second order term $\partial_\alpha Q^\alpha$, can be expressed as

$$\begin{aligned}\partial_\alpha S^\alpha = &\frac{\Pi}{T}\left\{-\theta - b_0 T\frac{d\Pi}{d\tau} - \frac{T}{2}\Pi\frac{db_0}{d\tau} - \frac{T}{2}b_0\Pi\theta - a_0 T\partial_\alpha V^\alpha - \frac{T}{2}V^\alpha\nabla_\alpha a_0\right\}\\ &+ V_\alpha\left\{-\nabla^\alpha\alpha_0 + b_1\Delta^\alpha_\beta\frac{dV^\beta}{d\tau} + \frac{V^\alpha}{2}\frac{db_1}{d\tau} + \frac{b_1}{2}V^\alpha\theta - a_0\nabla^\alpha\Pi - \frac{\Pi}{2}\nabla^\alpha a_0 - a_1\Delta^\alpha_\rho\partial_\beta\pi^{\rho\beta} - \frac{\pi^{\alpha\beta}}{2}\nabla_\beta a_1\right\}\\ &+ \frac{\pi_{\alpha\beta}}{T}\left\{\sigma^{\alpha\beta} - b_2 T\Delta^{\alpha\beta}_{\rho\sigma}\frac{d\pi^{\rho\sigma}}{d\tau} - \frac{T}{2}\pi^{\alpha\beta}\frac{db_2}{d\tau} - \frac{T}{2}b_2\pi^{\alpha\beta}\theta - a_1 T\Delta^{\alpha\beta}_{\rho\sigma}\nabla^\rho V^\sigma - \frac{T}{2}\Delta^{\alpha\beta}_{\rho\sigma}V^\rho\nabla^\sigma a_1\right\}\end{aligned} \tag{2.32}$$

where

$$\begin{aligned}\partial_\alpha Q^\alpha = &- b_0\Pi\frac{d\Pi}{d\tau} + b_1 V^\beta\frac{dV_\beta}{d\tau} - b_2\pi^{\rho\sigma}\frac{d\pi_{\rho\sigma}}{d\tau}\\ &- \frac{1}{2}\left[\Pi^2\frac{db_0}{d\tau} - V_\beta V^\beta\frac{db_1}{d\tau} + \pi^{\rho\sigma}\pi_{\rho\sigma}\frac{db_2}{d\tau}\right] - \frac{1}{2}\left[b_o\Pi^2 - b_1 V^\beta V_\beta + b_2\pi^{\rho\sigma}\pi_{\rho\sigma}\right]\theta\\ &- a_0\Pi\partial_\beta V^\beta - a_0 V^\beta\nabla_\beta\Pi - \Pi V^\beta\nabla_\beta a_0\\ &- a_1\pi_{\rho\sigma}\Delta^{\rho\sigma}_{\mu\nu}\partial^\mu V^\nu - \pi_{\rho\sigma}\Delta^{\rho\sigma}_{\mu\nu}V^\mu\nabla^\nu a_1 - a_1 V_\sigma\Delta^\sigma_\beta\partial_\rho\pi^{\rho\beta}\end{aligned} \tag{2.33}$$

and $\partial_\alpha T^{\alpha\beta} = 0$ and $\partial_\alpha J_B^\alpha = 0$ were used. The only way to explicitly satisfy $\partial_\alpha S^\alpha \geq 0$ is to ensure that the right hand side is a positive definite quadratic function of dissipative flows, that is by requiring (or defining)

$$\partial_\alpha S^\alpha \equiv \frac{\Pi^2}{\zeta T} - \frac{V^\alpha V_\alpha}{\kappa} + \frac{\pi^{\alpha\beta}\pi_{\alpha\beta}}{2\eta T}, \tag{2.34}$$

which imposes that the dissipative currents must satisfy the following equations:

$$\frac{\tau_\Pi}{\zeta}\frac{d\Pi}{d\tau} + \frac{1}{\zeta}\Pi = -\theta - \frac{T}{2}\Pi\frac{db_0}{d\tau} - \frac{T}{2}b_0\Pi\theta - a_0 T\partial_\alpha V^\alpha - \frac{T}{2}V^\alpha\nabla_\alpha a_0 \tag{2.35}$$

$$\begin{aligned}\frac{\tau_V}{\kappa}\Delta^\alpha_\beta\frac{dV^\beta}{d\tau} + \frac{1}{\kappa}V^\alpha = {} & \nabla^\alpha\alpha_0 - \frac{V^\alpha}{2}\frac{db_1}{d\tau} - \frac{b_1}{2}V^\alpha\theta + a_0\nabla^\alpha\Pi + \frac{\Pi}{2}\nabla^\alpha a_0 \\ & + a_1\Delta^\alpha_\rho\partial_\beta\pi^{\rho\beta} + \frac{\pi^{\alpha\beta}}{2}\nabla_\beta a_1\end{aligned} \tag{2.36}$$

$$\begin{aligned}\frac{\tau_\pi}{2\eta}\Delta^{\alpha\beta}_{\rho\sigma}\frac{d\pi^{\rho\sigma}}{d\tau} + \frac{1}{2\eta}\pi^{\alpha\beta} = {} & \sigma^{\alpha\beta} - \frac{T}{2}\pi^{\alpha\beta}\frac{db_2}{d\tau} - \frac{T}{2}b_2\pi^{\alpha\beta}\theta - a_1 T\Delta^{\alpha\beta}_{\rho\sigma}\nabla^\rho V^\sigma \\ & - \frac{T}{2}\Delta^{\alpha\beta}_{\rho\sigma}V^\rho\nabla^\sigma a_1.\end{aligned} \tag{2.37}$$

Eqs. (2.35), (2.36), (2.37) is a set of relaxation equations where the relaxation times for bulk viscous pressure, baryon diffusion current, and shear viscous pressure are $\tau_\Pi = \zeta T b_0$, $\tau_V = \kappa b_1$, and $\tau_\pi = 2\eta T b_2$, respectively. All coefficients in Eqs. (2.35), (2.36), (2.37) are to be determined from a microscopic theory. In the case of hydrodynamical simulations of relativistic heavy-ion collisions, that microscopic theory is QCD. In literature, however, the coefficients in Eqs. (2.35), (2.36), (2.37) are defined in terms of more commonly used transport coefficients. So to be consistent with other work [58, 59, 60], $\frac{db_i}{d\tau}$ and $\nabla_\alpha a_i$ must be expressed differently. Using the chain rule, $\frac{db_i}{d\tau}$ and $\nabla_\alpha a_i$ read

$$\frac{db_i}{d\tau} = \frac{\partial b_i}{\partial\alpha_0}\frac{d\alpha_0}{d\tau} + \frac{\partial b_i}{\partial\beta_0}\frac{d\beta_0}{d\tau} \tag{2.38}$$

$$\nabla_\alpha a_i = \frac{\partial a_i}{\partial\alpha_0}\nabla_\alpha\alpha_0 + \frac{\partial a_i}{\partial\beta_0}\nabla_\alpha\beta_0, \tag{2.39}$$

where $\alpha_0 = \frac{\mu_B}{T}$ while $\beta_0 = \frac{1}{T}$. Furthermore, $\nabla^\alpha\beta_0$ in Eq. (2.39) can be converted via the Gibbs-Duhem relation Eq. (2.22) into

$$\nabla^\alpha\beta_0 = \frac{1}{\varepsilon + P}\left[n_B\nabla^\alpha\alpha_0 - \frac{\nabla^\alpha P}{T}\right]. \tag{2.40}$$

Converting $\frac{d\beta_0}{d\tau}$ and $\frac{d\alpha_0}{d\tau}$ in Eq. (2.38), into an expression containing $\theta, \Pi, \sigma^{\alpha\beta}$ and so on, requires the use of conservation equations, namely conservation of particle number, energy, respectively. Also, the conservation of momentum will be needed. So, the conservation of particle number, energy, and momentum imply [66, 67]:

$$\frac{d\alpha_0}{d\tau} = \frac{1}{A}\left\{\frac{\partial\varepsilon}{\partial\beta_0}\left[n_B\theta + \partial_\alpha V^\alpha\right] - \frac{\partial n_B}{\partial\beta_0}\left[\left(\varepsilon + P + \Pi\right)\theta - \pi^{\alpha\beta}\sigma_{\alpha\beta}\right]\right\} \tag{2.41}$$

$$\frac{d\beta_0}{d\tau} = \frac{1}{A}\left\{-\frac{\partial\varepsilon}{\partial\alpha_0}\left[n_B\theta + \partial_\alpha V^\alpha\right] + \frac{\partial n_B}{\partial\alpha_0}\left[\left(\varepsilon + P + \Pi\right)\theta - \pi^{\alpha\beta}\sigma_{\alpha\beta}\right]\right\} \tag{2.42}$$

$$\frac{du^\alpha}{d\tau} = \frac{1}{\varepsilon + P}\left[\nabla^\alpha P - \Pi\frac{du^\alpha}{d\tau} + \nabla^\alpha\Pi - \Delta^\alpha_\beta\partial_\rho\pi^{\beta\rho}\right] \tag{2.43}$$

where

$$A = \frac{\partial\varepsilon}{\partial\alpha_0}\frac{\partial n_B}{\partial\beta_0} - \frac{\partial\varepsilon}{\partial\beta_0}\frac{\partial n_B}{\partial\alpha_0} \tag{2.44}$$

Combining Eq. (2.38) through Eq. (2.44), and using the fact that

$$\partial_\alpha V^\alpha = u_\alpha\frac{dV^\alpha}{d\tau} + \nabla_\alpha V^\alpha = -V^\alpha\frac{du_\alpha}{d\tau} + \nabla_\alpha V^\alpha, \tag{2.45}$$

which follows from $u_\alpha V^\alpha = 0$, allows to rewrite the relaxation equations for bulk viscous pressure, baryon diffusion current, and shear viscous pressure as:

$$\tau_\Pi\frac{d\Pi}{d\tau} + \Pi = -\zeta\theta - \delta_{\Pi\Pi}\Pi\theta - \lambda_{\Pi V}V_\alpha\nabla^\alpha\alpha_0 - \tau_{\Pi V}V_\alpha\nabla^\alpha P \tag{2.46}$$

$$\begin{aligned}\tau_V\Delta^\alpha_\beta\frac{dV^\beta}{d\tau} + V^\alpha &= \kappa\nabla^\alpha\alpha_0 - \delta_{VV}V^\alpha\theta \\ &+ \ell_{V\Pi}\nabla^\alpha\Pi \qquad + \lambda_{V\Pi}\Pi\nabla^\alpha\alpha_0 \ + \tau_{V\Pi}\Pi\nabla^\alpha P \\ &+ \ell_{V\pi}\Delta^\alpha_\rho\nabla_\beta\pi^{\rho\beta} - \lambda_{V\pi}\pi^{\alpha\beta}\nabla_\beta\alpha_0 - \tau_{V\pi}\pi^{\alpha\beta}\nabla_\beta P\end{aligned} \tag{2.47}$$

$$\begin{aligned}\tau_\pi\Delta^{\alpha\beta}_{\rho\sigma}\frac{d\pi^{\rho\sigma}}{d\tau} + \pi^{\alpha\beta} &= 2\eta\sigma^{\alpha\beta} - \delta_{\pi\pi}\pi^{\alpha\beta}\theta \\ &+ \ell_{\pi V}\Delta^{\alpha\beta}_{\rho\sigma}\nabla^\rho V^\sigma + \lambda_{\pi V}\Delta^{\alpha\beta}_{\rho\sigma}V^\rho\nabla^\sigma\alpha_0 - \tau_{\pi V}\Delta^{\alpha\beta}_{\rho\sigma}V^\rho\nabla^\sigma P\end{aligned} \tag{2.48}$$

where the transport coefficients for bulk viscous pressure are:

$$\delta_{\Pi\Pi} = \frac{\zeta}{2\beta_0}\left[\frac{n_B}{A}\left(\frac{\partial b_0}{\partial\alpha_0}\frac{\partial\varepsilon}{\partial\beta_0} + \frac{\partial b_0}{\partial\beta_0}\frac{\partial n_B}{\partial\beta_0}\right) + b_0\right] \tag{2.49}$$

$$\lambda_{\Pi V} = \frac{\zeta}{\beta_0}\left[\frac{\partial a_0}{\partial\alpha_0} + \frac{\partial a_0}{\partial\beta_0}\frac{n_B}{\varepsilon + P} + a_0\right] \tag{2.50}$$

$$\tau_{\Pi V} = \frac{\zeta a_0}{\beta_0\left(\varepsilon + P\right)} \tag{2.51}$$

while the transport coefficients for net baryon number diffusion and shear viscous pressure are determined similarly.[1] The terms in Eqs. (2.46), (2.47), and (2.48) are only kept up to second order in dissipative corrections, with all higher orders — present in Eqs. (2.35), (2.36), (2.37) — being neglected.

The mere fact that Eqs. (2.46), (2.47), and (2.48) are relaxation equations does not directly imply that the equations are causal. A stability analysis of a fluid under the sole influence of shear viscous pressure [68] has shown that in order Eq. (2.48) to be causal, the following inequality must hold:

$$\frac{\tau_\pi(\varepsilon + P)}{\eta} \geq \frac{4}{3(1-c_s^2)}, \tag{2.52}$$

where $c_s^2 = \frac{\partial P}{\partial \varepsilon}$ is the speed of sound square in the medium. So for an ultra-relativistic ideal gas, e.g. a fluid composed solely of photons, $c_s^2 = \frac{1}{3}$ and hence $\frac{\tau_\pi(\varepsilon+P)}{\eta} \geq 2$.

The relaxation equations Eqs. (2.46), (2.47), (2.48) can be made dimensionless if one divides by the pressure on the left and right hand sides of Eqs. (2.46) and (2.48); while the Eq. (2.47) can be made dimensionless if one divides by the net baryon density on both sides of the equation. As these equations are second order in dissipative degrees of freedom, they implicitly contain terms that are proportional to Knudsen numbers and inverse Reynolds numbers. Each derivative of a macroscopic field is proportional to L^{-1}, the inverse of the macroscopic length, while the transport coefficient that accompany it is proportional to ℓ, the microscopic length. So terms that are proportional to derivatives in macroscopic degrees of freedom, accompanied by the respective transport coefficient, are proportional to powers of the Knudsen number. Terms that only contain powers of the dissipative degrees of freedom, namely Π, V^α, and $\pi^{\alpha\beta}$, are proportional to inverse Reynolds number. More specifically, the three inverse Reynolds numbers encountered in Eqs. (2.46), (2.47), (2.48) are: $R_\Pi^{-1} \propto \frac{|\Pi|}{P}$, $R_V^{-1} \propto \frac{|V^\alpha|}{n_B}$, and $R_\pi^{-1} \propto \frac{|\pi^{\alpha\beta}|}{P}$. Since Π, V^α, and $\pi^{\mu\nu}$ are assumed to me small relative to their thermodynamic counterparts, P and $n_B u^\alpha$, just counting the number of times Π, V^α, and $\pi^{\alpha\beta}$ appear in the relaxation equations for is sufficient. So, the term $\delta_{VV} V^\alpha \theta$ in Eq. (2.47) contains one power of Knudsen number (from $\delta_{VV}\theta$) and

[1] For specific values of transport coefficients explored within this thesis, see sections 4.1, 5.1 and 5.2.

one power of inverse Reynolds number (from V^α), and similarly for all other terms. Hence equations (2.46), (2.47), (2.48) are mixed second order dissipative hydrodynamic equations. These equations however do not contain all the possible terms (up to second order) as they were not derived from microscopic theory. A derivation from microscopic theory [69] shows that there are other terms, e.g. $\Delta^{\alpha\beta}_{\mu\nu}\sigma^{\mu}_{\rho}\omega^{\nu}_{\rho}$ proportional to vorticity $\omega^{\alpha\beta} \equiv \nabla^\alpha u^\beta - \nabla^\beta u^\alpha$, which are not present in this derivation.

The last important remark to be made before moving to the next section regards the manner in which the transport coefficients are determined. Ultimately, the field of heavy-ion collisions would like to use transport coefficients from first principle calculations such as ℓQCD. However, ℓQCD calculations cannot reliably provide most of the hydrodynamical transport coefficients, at the moment. The only transport coefficient which has recently been extracted from ℓQCD calculations, under some assumptions, is the electrical conductivity [70]. Indeed, that transport coefficient, which would appear in the equations of motion for the electric charge current J^α_Q (not included in the above discussion), is related to dilepton production rate, assuming a particular analytic form of the rate.

In order to perform hydrodynamical simulations, transport coefficients must be determined by other means than ℓQCD. One possible way of doing this is via the relativistic Boltzmann equation. Assuming a classical Boltzmann gas of hard spheres with a constant interaction cross section, a wealth of transport coefficients were determined in Refs. [66, 67].

From effective theory considerations it is possible to extract a scaling relation between transport coefficients or between a transport coefficient and thermodynamic variables. For example one such scaling relation was already mentioned $\frac{\tau_\pi(\varepsilon+P)}{\eta} \propto C$. Another is $\frac{\eta}{s} \propto C$.

In both cases C is constructed to be dimensionless and is determined from a particular microscopic theory or can be treated as a constant fitted to the available experimental data on charged hadrons (such as the transverse momentum spectra of protons, pions etc.). This type of scaling relations will be used throughout this thesis and C will often be treated as an effective constant adjusted to reproduce experimental data. However, we will also study a situation where a temperature dependent $\frac{\eta}{s}$ is used (see section 5.2).

2.2 Initial conditions

Having established the equations of motion for hydrodynamics in Eqs. (1.5), (1.6), (2.35), (2.36), and (2.37), the next step is to solve them.[1] To do so, initial conditions must be specified. The initial conditions used in this thesis are those of the Glauber model (see [71] and references therein).

> *A slight digression.* There are more sophisticated initial condition models in the literature, such as Monte-Carlo KLN model [72, 73, 74, 75], the EKRT model [76], EPOS [77], to cite a few. One model which has received a lot of attention recently is the IP-Glasma model [78, 79]: a combination of the Impact Parameter dependent Saturation (also known as IP-Sat) model [80, 81] an the Glasma phase [82, 83, 84, 85, 86, 87, 88]. The IP-Sat model describes the initial gluonic wave-function of hadrons/nuclei before the collision has occurred[2], while the Glasma phase subsequently evolves the Classical Yang-Mills equations of motion to describe the evolution of the gluon fields, which are the dominant contribution of the energy density[3], leading up to the onset of hydrodynamics at $\tau = \tau_0$. The IP-Glasma model has several advantages over the Glauber model. It naturally gives rise to a non-zero initial flow profile in the transverse (x, y)-plane and can describe very well the probability distributions of event-by-event fluc-

[1] For details about transport coefficients appearing in the fluid equations being solved along with their values, see Chapter 4 and 5.

[2] This is shown by a good agreement between the IP-Sat model and HERA data [89], obtained from deep-inelastic scattering electron-proton collisions, as well as electron-nucleus data from the EMC and E665 experiments [90].

[3] Recall the discussion on page 27.

> tuations of anisotropic flow of charged hadrons [91], which is defined in section 2.3.3. However, the IP-Glasma model doesn't produce a thermalized medium by the time it is matched to a hydrodynamical evolution. In that regard, the models based on Kinetic Theory [38, 39], or models solving Yang-Mills equation including quantum corrections of the initial conditions [40, 41], are more promising avenues to be further investigated in the future. Without ever addressing thermalization and solely providing an initial energy density distribution, the Glauber model is nevertheless remarkably successful phenomenologically [71, 92], despite its simplicity relative to the models just discussed, and therefore will be used from now on. In future studies, these more sophisticated models will be utilized.

In order for the Glauber model to specify the the initial energy density distribution, one must determine whether or not a collision between nucleons of the target and projectile nuclei has occurred.

2.2.1 Inelastic cross section

For the sake of simplicity, consider the case of $2 \to 2$ nucleon scattering. In quantum field theory, the $2 \to 2$ scattering cross-section is defined as :

$$\frac{d\sigma_{1,2\to 3,4}}{d\Omega} \equiv \frac{\sqrt{\lambda\left(s, m_3^2, m_4^2\right)}}{64\pi^2 s\sqrt{\lambda\left(s, m_1^2, m_2^2\right)}}\left|f(s,t)\right|^2 \tag{2.53}$$

where $\lambda\left(x,y,z\right) = x^2+y^2+z^2-2xy-2xz-2yz$, m_i are the masses of the incoming $(1,2)$ and outgoing $(3,4)$ particles, and the Mandelstam variables s and t are defined as $s=(p_1^\mu+p_2^\mu)^2=(p_3^\mu+p_4^\mu)^2$ and $t=(p_1^\mu-p_3^\mu)^2=(p_2^\mu-p_4^\mu)^2$, while p_i^μ is the 4-momentum of the particle $i=1,2,3,4$, and $f(s,t)$ is the scattering amplitude. The square of the scattering amplitude physically represents the probability of the incoming state $|p_1^\mu, p_2^\mu\rangle$ to transition to the outgoing state $|p_3^\mu, p_4^\mu\rangle$. In a model-independent way, one can write the scattering amplitude for $2 \to 2$ collisions in terms of a partial wave series. Assuming that all 4 particles are identical with mass m and spin-0, this series reads

$$f(s,t(s,z_s)) = 16\pi \sum_{l=0}^{\infty} f_l(s)(2l+1)P_l(z_s), \tag{2.54}$$

where $z_s = \cos(\theta_s) = 1 + \frac{2t}{s-4m^2}$, and t is fixed. $P_l(z_s)$ is the Legendre polynomial satisfying the orthogonality condition:

$$\int_{-1}^{1} dz_s P_l(z_s) P_{l'}(z_s) = \frac{2}{2l+1}\delta_{ll'}. \tag{2.55}$$

Hence,

$$f_l(s) = \int_{-1}^{1} dz_s P_l(z_s) f(s,t(s,z_s)) \tag{2.56}$$

which is also commonly written as

$$f_l(s) = \frac{e^{2i\chi_l(s)} - 1}{2i\rho(s)} \tag{2.57}$$

where $\rho(s) = 2q_{\text{c.m.}}/\sqrt{s}$, $q_{\text{c.m.}} = \sqrt{\frac{\lambda\left(s,m_1^2,m_2^2\right)}{4s}}$, $\text{Re}\left[\chi_l(s)\right]$ corresponds to the phase shift acquired due to elastic scattering while inelastic portion of the scattering is stored in $\text{Im}\left[\chi_l(s)\right]$.

Using the optical theorem, one can show that the total $2 \to 2$ scattering cross-section can be written as:

$$\sigma^{\text{total}}_{1,2\to 3,4} = \frac{1}{2|q_{\text{c.m.}}|\sqrt{s}} \,\text{Im}\left[f(s,t=0)\right]. \tag{2.58}$$

Assuming that one has a large l and a small scattering angle θ_s, one can rewrite the optical theorem as [93, 94]:

$$\sigma^{\text{total}}_{1,2\to 3,4} = 2\int d^2\mathbf{b}\left\{1 - \text{Re}\left[e^{2i\chi(\mathbf{b},s)}\right]\right\} \tag{2.59}$$

where $\mathbf{b}$ is the impact parameter vector lying in the plane orthogonal to the beam axis, labeling the transverse separation between the colliding partons. Knowing that χ stores both the inelastic and elastic portions of the total cross section, it can be shown [94] that the inelastic cross section is

$$\sigma^{\text{inelastic}}_{1,2\to 3,4} = \int d^2\mathbf{b}\left\{1 - \left|e^{2i\chi(\mathbf{b},s)}\right|\right\} \tag{2.60}$$

from which the probability of having a $2 \to 2$ nucleon-nucleon scattering reads [94]:

$$\mathcal{P}(\mathbf{b}) = \left\{1 - \left|e^{2i\chi(\mathbf{b},s)}\right|\right\} \equiv t(\mathbf{b})\sigma^{\text{inelastic}}_{1,2\to 3,4} = t(\mathbf{b})\sigma^{\text{inel.}} \tag{2.61}$$

where $t(\mathbf{b})$ is called the *nucleon-nucleon thickness function* and is normalized such that $\int d^2\mathbf{b}\, t(\mathbf{b}) = 1$. Using the *nucleon-nucleon thickness function* one can determine whether or not an inelastic collision has occurred. To determine the number of collisions in a nucleus-nucleus collision, the distribution function of nucleons in a nucleus is required.

2.2.2 Woods-Saxon distribution of the nucleus and binary collisions

To this end, the distribution by Woods and Saxon [95] was quite successful in phenomenologically describing the nucleon distribution a variety of nuclei. According to Woods and Saxon, the probability of finding a nucleon in a nucleus A is:

$$\rho_A(r) = \frac{\rho_0}{A}\frac{1}{1+\exp\left[\frac{r-R}{a}\right]} \tag{2.62}$$

where $r = |\mathbf{r}| = \sqrt{x^2+y^2+z^2}$ is the radial coordinate, A is the number of nucleons in a nucleus, R is the size of the nucleus and a is the nuclear skin depth while ρ_0 is determined by requiring that $4\pi\rho_0 R^3/3 = A$. For the Au nucleus A=197, $\rho_0 = 0.17\,\text{fm}^{-3}$, a=0.535 fm, and R=6.38 fm.

It is now possible to define the *nucleus-nucleus thickness function*, to reflect the averaged probability that two nucleons collide in a nucleus-nucleus collision. This quantity counts the number of binary nucleon-nucleon collisions in a nucleus-nucleus collision. In order to do that, one must change the definition of the impact parameter $\mathbf{b}$. In the nucleus-nucleus case, the impact parameter is the distance between the centers of the two nuclei as shown in Fig. 2.1. Labeling the colliding nuclei as A and B, the *nucleus-nucleus thickness function* is defined as

$$T_{AB}(\mathbf{b}) \equiv \int dz_A \int dx_A dy_A \rho_A(x_A,y_A,z_A) \int dz_B \int dx_B dy_B \rho_B(x_B,y_B,z_B) t(\mathbf{b}+\mathbf{r}_B-\mathbf{r}_A). \tag{2.63}$$

Incidentally, it can be shown that $\int d^2b T_{AB} = 1$, justifying the interpretation of $T_{AB}\sigma^{\text{inel.}}$ as a probability. Since the *nucleon-nucleon thickness function* varies on a

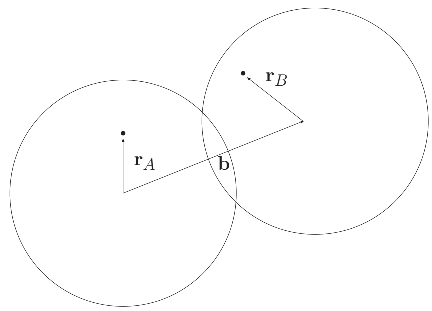

Figure 2.1: The impact parameter $\mathbf{b}$ represents the distance between the centers of nuclei A and B in (x, y)-plane. The vectors $\mathbf{r}_A$ and $\mathbf{r}_B$ label the positions of the nucleons in the nuclei that are about to collide.

sub-nucleon size, which is much smaller than the size probed by the variables $\mathbf{r}_A$ and $\mathbf{r}_B$, one can assume that $t(\mathbf{b}) \to \delta^{(2)}(\mathbf{b})$.[1] This approximation allows to perform the integral over x_B and y_B yielding

$$T_{AB}(\mathbf{b}) = \int dz_A \int dx_A dy_A \rho_A(x_A, y_A, z_A) \int dz_B \rho_B(b_x - x_A, b_y - y_A, z_B) \quad (2.64)$$

$$= \int dx_A dy_A T_A(x_A, y_A) T_B(b_x - x_A, b_y - y_A) \quad (2.65)$$

changing variables,

$$T_{AB}(\mathbf{b}) = \int dx dy T_A \left(x + \frac{b_x}{2}, y + \frac{b_y}{2} \right) T_B \left(x - \frac{b_x}{2}, y - \frac{b_y}{2} \right). \quad (2.66)$$

Analogously to T_{AB}, T_A and T_B can be interpreted as *nucleon-nucleus thickness functions*. Therefore, the probability of n inelastic collisions occurring inside a collision between nucleus A and B is:

$$\mathscr{P}(n; AB; \mathbf{b}) = \begin{pmatrix} AB \\ n \end{pmatrix} \left[1 - T_{AB}\sigma^{\text{inel.}}\right]^{AB-n} \left[T_{AB}\sigma^{\text{inel.}}\right]^{n}. \quad (2.67)$$

The average number $\bar{n}$ of binary collisions in a nucleus-nucleus collision, commonly

[1] Note that $t(\mathbf{b})$ was not replaced by $\delta^{(3)}(\mathbf{b})$. The reason for this is simple. In relativistic heavy ion collisions, the z-direction is typically chosen to be along the beam axis. Hence the z-direction is Lorentz contracted by very large values hence only the (x, y)-plane is of importance and the z-axis almost always integrated over.

labeled as N_{bin}, is

$$N_{\text{bin}} = \bar{n} = \sum_{n=1}^{AB} n\mathscr{P}(n; AB; \mathbf{b}) = ABT_{AB}\sigma^{\text{inel.}}. \tag{2.68}$$

2.2.3 Wounded nucleons

T_{AB} does not give the complete picture however, since a nucleon in nucleus A can interact with more than one nucleon in B, and this possibility should also be taken into account. To this end, care must be taken when defining probabilities. Since, in the Glauber model, the collisions between individual nucleons are independent, the total probability is obtained by combining, under multiplication, the individual probabilities. Assuming for the sake of simplicity, that nucleus A is just a nucleon and that nucleus B is the deuteron. In that case $\mathbf{r}_A = \mathbf{0}$. Furthermore assume that the nucleon-nucleon cross section doesn't change whether a nucleon is inside or outside of the nucleus. This is most likely not true in actual experiment, however it is an important computational simplification. Taking a snapshot of the nucleus, one can fix the nucleon positions in nucleus B to compute the probability; an averaging over the nucleon positions in B will be done later. Then the probability that either there is no collision or that the collision is elastic; that is, the probability that there *may have been* an *elastic* collision between the nucleon A and any of the nucleons in B is $\left[1 - t\left(\mathbf{b} + \mathbf{r}_B^{(1)} - \mathbf{0}\right)\sigma^{\text{inel.}}\right]\left[1 - t\left(\mathbf{b} + \mathbf{r}_B^{(2)} - \mathbf{0}\right)\sigma^{\text{inel.}}\right]$. Thus the probability that there was at least one *inelastic* collision between the nucleon A and any of the nucleons in B is

$$\begin{aligned} &\mathcal{P}\left(\mathbf{r} = \mathbf{0}, A = 1; \mathbf{r}_B^{(1)}, \mathbf{r}_B^{(2)}, B; \mathbf{b}\right) = \\ &= 1 - \left[1 - t\left(\mathbf{b} + \mathbf{r}_B^{(1)} - \mathbf{0}\right)\sigma^{\text{inel.}}\right]\left[1 - t\left(\mathbf{b} + \mathbf{r}_B^{(2)} - \mathbf{0}\right)\sigma^{\text{inel.}}\right] \end{aligned} \tag{2.69}$$

Generalizing this probability to large nuclei is straightforward. Let a label the nucleons from nucleus A and b label the nucleons from nucleus B. The probability for *an inelastic* collision between a nucleon a and any of the nucleons in B is [94]:

$$\mathcal{P}\left(\mathbf{r}_A^{(a)}, A; \mathbf{r}_B^{(1)}, \dots, \mathbf{r}_B^{(B)}, B; \mathbf{b}\right) = 1 - \prod_{b=1}^{B}\left[1 - t\left(\mathbf{b} + \mathbf{r}_B^{(b)} - \mathbf{r}_A^{(a)}\right)\sigma^{\text{inel.}}\right]. \tag{2.70}$$

The nucleons distributed according to this probability are called *wounded* nucleons or *participants*. Averaging over the possible positions of the nucleons a in A gives:

$$\begin{aligned}\bar{\mathcal{P}}\left(A;\mathbf{r}_B^{(1)},\ldots,\mathbf{r}_B^{(B)},B;\mathbf{b}\right) &= \int dx_A dy_A T_A(x_A,y_A)\mathcal{P}\left(\mathbf{r}_A^{(a)};\mathbf{r}_B^{(1)}\ldots\mathbf{r}_B^{(B)};\mathbf{b}\right)\\ &= \int dx_A dy_A T_A(b_x-x_A,b_y-y_A)\times\\ &\times\left\{1-\prod_{b=1}^{B}\left[1-t\left(\mathbf{r}_B^{(b)}-\mathbf{r}_A^{(a)}\right)\sigma^{\text{inel.}}\right]\right\}. \end{aligned}\tag{2.71}$$

Hence the probability of having w_A wounded nucleons is

$$\begin{aligned}\mathscr{P}\left(w_A,A;\mathbf{r}_B^{(1)},\ldots,\mathbf{r}_B^{(B)},B;\mathbf{b}\right) &= \begin{pmatrix} A\\ w_A\end{pmatrix}\left[1-\bar{\mathcal{P}}\left(A;\mathbf{r}_B^{(1)},\ldots,\mathbf{r}_B^{(B)},B;\mathbf{b}\right)\right]^{A-w_A}\times\\ &\times\left[\bar{\mathcal{P}}\left(A;\mathbf{r}_B^{(1)},\ldots,\mathbf{r}_B^{(B)},B;\mathbf{b}\right)\right]^{w_A}\end{aligned}\tag{2.72}$$

while the average number of wounded nucleons $\left[\text{at a fixed set of locations }\left(\mathbf{r}_B^{(1)},\ldots,\mathbf{r}_B^{(B)}\right)\right]$ is

$$\begin{aligned}\bar{w}_A\left(A;\mathbf{r}_B^{(1)}\ldots\mathbf{r}_B^{(B)},B;\mathbf{b}\right) &= \sum_{w_A=1}^{A} w_A\mathscr{P}\left(w_A,A;\mathbf{r}_B^{(1)}\ldots\mathbf{r}_B^{(B)},B;\mathbf{b}\right)\\ &= A\bar{\mathcal{P}}\left(A;\mathbf{r}_B^{(1)},\ldots,\mathbf{r}_B^{(B)},B;\mathbf{b}\right).\end{aligned}\tag{2.73}$$

Lastly, averaging over the possible set of configurations of nucleons b in B gives [94]

$$\begin{aligned}\bar{w}_A\left(A;B;\mathbf{b}\right) = A\prod_{b=1}^{B}\left\{\int dx_B^{(b)}T_B(x_B^{(b)},y_B^{(b)})\right\}\int dx_A dy_A T_A(b_x-x_A,b_y-y_A)\times\\ \times\left\{1-\prod_{b=1}^{B}\left[1-t\left(\mathbf{b}+\mathbf{r}_B^{(b)}-\mathbf{r}_A^{(a)}\right)\sigma^{\text{inel.}}\right]\right\}\end{aligned}\tag{2.74}$$

and using the usual approximation $t\left(\mathbf{b}+\mathbf{r}_B^{(b)}-\mathbf{r}_A^{(a)}\right)\to\delta^{(2)}\left(\mathbf{b}+\mathbf{r}_B^{(b)}-\mathbf{r}_A^{(a)}\right)$ yields [94]

$$\begin{aligned}\bar{w}_A\left(A;B;\mathbf{b}\right) = A\int dx_A dy_A T_A(b_x-x_A,b_y-y_A)\times\\ \times\left\{1-\left[1-T_B(x_B,y_B)\sigma^{\text{inel.}}\right]^{B}\right\},\end{aligned}\tag{2.75}$$

which is the average number of wounded nucleons in nucleus A. The total number of wounded nucleons is simply the sum of those present in nucleus A and B

$$\bar{w}(A;B;\bar{b}) = A\int dx_A dy_A T_A(b_x - x_A, b_y - y_A)\left\{1 - \left[1 - T_B(x_A, y_A)\sigma^{\text{inel.}}\right]^B\right\} + \\ + B\int dx_B dy_B T_B(b_x - x_B, b_y - y_B)\left\{1 - \left[1 - T_A(x_B, y_B)\sigma^{\text{inel.}}\right]^A\right\}, \tag{2.76}$$

changing variables again leads to

$$\bar{w}(A;B;\bar{b}) = A\int dxdyT_A\left(x + \frac{b_x}{2}, y + \frac{b_y}{2}\right)\left\{1 - \left[1 - T_B\left(x - \frac{b_x}{2}, y - \frac{b_y}{2}\right)\sigma^{\text{inel.}}\right]^B\right\} + \\ + B\int dxdyT_B\left(x - \frac{b_x}{2}, y - \frac{b_y}{2}\right)\left\{1 - \left[1 - T_A\left(x + \frac{b_x}{2}, y + \frac{b_y}{2}\right)\sigma^{\text{inel.}}\right]^A\right\}. \tag{2.77}$$

2.2.4 *Optical Glauber initial conditions*

Using the average number of wounded nucleons and binary collisions, the initial energy density profile of a nucleus-nucleus collision in the (x, y)-plane can be written as

$$\varepsilon_T(x, y, b) = \varepsilon_0 W(x, y, b)/W(0, 0, 0) \tag{2.78}$$

where ε_0 is an overall energy normalization, chosen to fit experimental data, while

$$W(x, y, b) = (1 - \alpha)n_{WN}(x, y, b) + \alpha n_{BC}(x, y, b), \tag{2.79}$$

where α is again chosen to fit experimental data,

$$n_{WN}(x, y, b) = AT_A\left(x + \frac{b_x}{2}, y + \frac{b_y}{2}\right)\left\{1 - \left[1 - T_B\left(x - \frac{b_x}{2}, y - \frac{b_y}{2}\right)\sigma^{\text{inel.}}\right]^B\right\} + \\ + BT_B\left(x - \frac{b_x}{2}, y - \frac{b_y}{2}\right)\left\{1 - \left[1 - T_A\left(x + \frac{b_x}{2}, y + \frac{b_y}{2}\right)\sigma^{\text{inel.}}\right]^A\right\}, \tag{2.80}$$

and

$$n_{BC} = \sigma^{\text{inel.}} ABT_A\left(x + \frac{b_x}{2}, y + \frac{b_y}{2}\right)T_B\left(x - \frac{b_x}{2}, y - \frac{b_y}{2}\right). \tag{2.81}$$

Now, since the hydrodynamical equations are being solved in three spatial dimensions, there needs to be a rapidity profile. This profile is assumed to be

$$H(\eta_s) = \exp\left[-\frac{(|\eta_s| - \eta_{\text{flat}}/2)^2}{2\sigma_\eta^2}\theta\left(|\eta_s| - \eta_{\text{flat}}/2\right)\right] \tag{2.82}$$

where θ is the Heaviside function, $\eta_s = (1/2)\ln\left[(t+z)/(t-z)\right]$, whith t the time and z the spatial dimension directed along the beam. So the distribution in $|\eta_s|$ is flat until $|\eta_s| = \eta_{\text{flat}}$ and decays like a Gaussian after. The size of η_{flat} is chosen to fit the experimental data. Hence the initial energy density distribution in (x, y, η_s) that will be used to investigate the hydrodynamical equations of motion is:

$$\varepsilon(x, y, \eta_s, b) = \varepsilon_0 H(\eta_s) W(x, y, b)/W(0, 0, 0). \tag{2.83}$$

2.2.5 Monte-Carlo Glauber initial conditions

The optical Glauber model provides a smooth initial density profile. A more realistic scenario takes into account that the amount of energy density being deposited in each nucleus-nucleus collision varies event by event. To take these fluctuations into account, a Monte-Carlo Glauber model was devised.

The Monte-Carlo Glauber model is a little simpler to understand relative to the Optical Glauber model. One starts by sampling the impact parameter space according to the chosen experimental centrality, a measure of how central (or peripheral) a nucleus-nucleus collision is. There are several ways to relate centrality to the impact parameter. The method used throughout this thesis was proposed in Ref. [96] which computes the fraction of the inelastic cross section as a function of impact parameter

$$c(b) = \frac{\int_0^b |\mathbf{b}'| d|\mathbf{b}'| \int_0^{2\pi} d\phi_b \left(1 - \exp\left[-\sigma^{\text{inel.}} AB T_{AB}(\mathbf{b})\right]\right)}{\int_0^\infty |\mathbf{b}'| d|\mathbf{b}'| \int_0^{2\pi} d\phi_b \left(1 - \exp\left[-\sigma^{\text{inel.}} AB T_{AB}(\mathbf{b})\right]\right)} \tag{2.84}$$

with T_{AB} given in Eq. (2.66). So, once the range in centrality is specified, $c_{\text{min}} < c < c_{\text{max}}$, the minimum and maximum impact parameters can be determined by requiring that $c_{\text{min/max}} = c(b_{\text{min/max}})$. At this point, a random sampling of the impact parameters between b_{min} and b_{max} is done according to the probability:

$$P(|\mathbf{b}|) d|\mathbf{b}| = \frac{2|\mathbf{b}| d|\mathbf{b}|}{b_{\text{max}}^2 - b_{\text{min}}^2}. \tag{2.85}$$

For a given value of $|\mathbf{b}|$, this method then proceeds to randomly sample positions of nucleons inside a nucleus, with the probability of finding a nucleon given by the Wood-Saxon profile in Eq. (2.62). Once the positions of the nucleons are known, a collision happens whenever their transverse separation $D \leq \sqrt{\sigma^{\text{inel.}}/\pi}$. The energy deposition then proceeds by enveloping each wounded nucleon with a Gaussian profile, while for binary collisions is deposited in the center between each pair of nucleons and the same Gaussian shape is preserved.

$$n_{\text{BC/WN}}\left(x,y\right) = \frac{1}{2\pi\sigma^2}\sum_{i=1}^{N_{\text{bin/part}}} \exp\left[-\frac{\left(x-x_i\right)^2+\left(y-y_i\right)^2}{2\sigma^2}\right]. \tag{2.86}$$

In Eq. (2.86), N_{part} and N_{bin} are the number of participants and binary collision of a given event, respectively, (x_i,y_i) are the coordinates of the corresponding participant or binary collision on the transverse plane, while the longitudinal direction is summed over. Of course, N_{part} and N_{bin} are determined by counting the number of nucleons and nucleon pairs within $D \leq \sqrt{\sigma^{\text{inel.}}/\pi}$. Once n_{BC} and n_{WN} are known the 3-dimensional profile of the energy density is obtained via Eq. (2.79) and Eq. (2.83).

2.3 Freeze-out, particle production and flow

To describe experimental observables, hydrodynamical equations of motion cannot be run until zero temperature as the assumptions behind fluid-dynamical behavior break down before low temperatures are reached. So prior to that point, hydrodynamical simulations must be halted. This is typically done at a fixed temperature for high energy heavy ion collisions (and fixed energy density at lower beam energies), at which point the hydrodynamical degrees of freedom are converted to hadronic particles. Further, if those particles are assumed not to interact among themselves below that chosen temperature (or energy density), known as the freeze-out temperature (or energy density), then a thermal emission of particles can be employed to compute the particle spectra which is then compared with experimental data. Other possibilities are to freeze-out based on a dynamical criterion [97, 98] or at a given Knudsen number [42], below which the assumptions behind hydrodynamical equations are no longer met, computing the hadron production by again using a thermal distribution.

> *A slight digression.* Recall that the Knudsen number is $K_n = \ell/L$. In a dilute gas, the mean free-path between particles can be used as a microscopic scale ℓ which, in such a system, can be related to relaxation time of the shear viscous pressure $\ell \propto \tau_\pi$, if the only dissipative term in the fluid equations is the shear viscous pressure.[1] For the sake of this argument, set $\ell = \tau_\pi$. However, there are many macroscopic quantities that can act as the scale L: $1/\theta$, $P/\sqrt{\nabla_\alpha P \nabla^\alpha P}$, $1/\sqrt{\sigma^{\alpha\beta}\sigma_{\alpha\beta}}$, and so on. Again, for the sake of simplicity, set $L = 1/\theta$.[2] Recent studies [42] simulating strongly interacting media, at top beam energy at RHIC and at the available energy for the LHC, have shown that for freeze-out temperatures greater than $\sim$140 MeV, the Knudsen number is small enough so that freeze-out happens in a region where hydrodynamical equations are still valid.

Throughout this thesis the constant temperature freeze-out condition will be used for top beam energy collisions at RHIC, with the typical freeze-out temperatures $T \sim$ 140 MeV giving a good description of the hadronic particle spectra. Also, recall that all effects arising from the bulk viscous pressure are neglected.

2.3.1 Cooper-Frye formula

Once the freeze-out temperature is determined, hadron production follows the Cooper-Frye prescription [99]. Assuming that the number of particles of a particular species

[1] However, the medium produced in high energy heavy-ion collisions is not dilute and is strongly interacting. For strongly interacting systems, it is not know what the microscopic scale, acting like τ_π, is. As already mentioned ℓQCD calculations currently cannot reliably be used in order to extract transport coefficient and hence for now lattice has little information to offer regarding what this microscopic scale is.

[2] The fluid dynamical equations cease to be valid whence the largest Knudsen number is obtained, i.e. for the smallest L. So in principle, one should choose the minimum value of L among the different possibilities.

a is conserved, the particle multiplicity is :

$$N_a = \int d^4x \partial_\mu N_a^\mu \tag{2.87}$$

where N_a^μ is the current density of particle a. Using the generalized Stokes' theorem,

$$N_a = \int d^3\Sigma_\mu N_a^\mu \tag{2.88}$$

where $d^3\Sigma_\mu$ is the four-vector normal to the hyper-surface $d^3\Sigma$, while $d^3\Sigma$ itself corresponds to the volume of the fluid element that has reached the freeze-out temperature. In a fluid that has no dissipation, the number current must be parallel with the flow of the system hence $N^\mu = Nu^\mu$. Furthermore, since the system has $T \sim 140$ MeV when the evolution is being stopped, it must be distributed according to the thermal distribution of either bosons or fermions depending on the nature of a. Hence,

$$N_a^\mu = N_a u^\mu = \int \frac{d^3p}{(2\pi)^3 p^0} p^\mu n_{a,0} \left[\frac{p^\mu}{T} u_\mu\right] \tag{2.89}$$

where $n_{a,0}$ is a Fermi-Dirac or Bose-Einstein distribution whose argument is shown in the square brackets. Therefore,

$$N_a = \int \frac{d^3p}{(2\pi)^3 p^0} \int d^3\Sigma_\mu p^\mu n_{a,0} \left[\frac{p^\mu}{T} u_\mu\right]. \tag{2.90}$$

The particle number computed this way only accounts for thermally emitted hadrons. So, only the highest mass hadrons can be accounted for using solely the Cooper-Frye prescription. To describe low-mass hadrons, both the Cooper-Frye formula and decays of high-mass hadronic resonances are employed.

Notice that in the fluid rest frame, $u^\mu = (1, 0, 0, 0)$, the distribution function is spherically symmetric, which should be the case for a perfectly thermal system. However, if dissipation is present, such as through shear viscous pressure, spherical symmetry must be broken and hence a correction δn_a should be present in order to take into account angular dependence in n_a induced by shear stresses [i.e. $n_a \to n_{a,0} + \delta n_a$]. A similar argument can be made by using the stress-energy tensor. Indeed, assuming that only shear viscous pressure is present in a single-component fluid,

$$\begin{aligned} T^{\mu\nu} &= \int \frac{d^3p}{(2\pi)p^0} p^\mu p^\nu n_a \\ &= \int \frac{d^3p}{(2\pi)p^0} p^\mu p^\nu n_{a,0} + \int \frac{d^3p}{(2\pi)p^0} p^\mu p^\nu \delta n_a \\ &= \varepsilon u^\mu u^\nu - P\Delta^{\mu\nu} + \pi^{\mu\nu} \end{aligned} \tag{2.91}$$

where, $\varepsilon = \int \frac{d^3p}{(2\pi)p^0}(p\cdot u)^2 n_{a,0}$ and $P = \int \frac{d^3p}{(2\pi)p^0}\left(-\frac{1}{3}\Delta_{\mu\nu}p^\mu p^\nu\right) n_{a,0}$, assuming that the contribution coming from bulk viscosity is neglected. So the presence of δn_a is required in order for $T^{\mu\nu}$ to be continuous across the freeze-out surface, i.e. it is needed for energy-momentum conservation. Furthermore, since $\pi^{\mu\nu}$ is non-vanishing in all frames, the fact that $T^{\mu\nu}$ has off-diagonal elements automatically implies that $T^{\mu\nu}$ has a non-trivial angular dependence.

2.3.2 Shear δn correction to the thermal distribution function

To take into account deformations in the distribution coming from shear stresses, particle momenta are coupled to $\pi^{\mu\nu}$:

$$\frac{p^\mu}{T}u_\mu \rightarrow \frac{p^\mu}{T}u_\mu + \mathcal{G}\left[\frac{p^\mu}{T}u_\mu\right]\frac{p^\mu}{T}\frac{p^\nu}{T}\frac{\pi_{\mu\nu}}{2(\varepsilon+P)}. \tag{2.92}$$

To determine $\mathcal{G}\left[\frac{p^\mu}{T}u_\mu\right]$ requires the use of a microscopic theory [64]. In a multi-hadron species environment, a popular practice has been to set $\mathcal{G}\left[\frac{p^\mu}{T}u_\mu\right] = 1$. In that case, the full distribution function n_a is:

$$\begin{aligned} n_a &= n_{a,0}\left[\frac{p^\mu}{T}u_\mu\right] + \delta n_a + \mathcal{O}(\delta n_a^2) \\ n_a &= n_{a,0}\left[\frac{p^\mu}{T}u_\mu\right] + \frac{1}{2}n_{a,0}\left[\frac{p^\mu}{T}u_\mu\right]\left(1 \pm n_{a,0}\left[\frac{p^\mu}{T}u_\mu\right]\right)\frac{p^\mu}{T}\frac{p^\nu}{T}\frac{\pi_{\mu\nu}}{\varepsilon+P} + \mathcal{O}(\delta n_a^2) \end{aligned} \tag{2.93}$$

where the upper (lower) sign refers to bosons (fermions) and only the leading order term in $\frac{p^\mu}{T}\frac{p^\nu}{T}\frac{\pi_{\mu\nu}}{\varepsilon+P}$ is kept. An important property of the shear viscous δn is that it doesn't change the total particle multiplicity. That is:

$$\begin{aligned} \int \frac{d^3p}{(2\pi)^3p^0}\delta n_a &= \int \frac{d^3p}{(2\pi)^3p^0}\frac{1}{2}n_{a,0}\left[\frac{p^\mu}{T}u_\mu\right]\left(1 \pm n_{a,0}\left[\frac{p^\mu}{T}u_\mu\right]\right)\frac{p^\mu}{T}\frac{p^\nu}{T}\frac{\pi_{\mu\nu}}{\varepsilon+P} \\ &= 0 \end{aligned} \tag{2.94}$$

The simplest way to see this is to rewrite

$$\begin{aligned}\int \frac{d^3p}{(2\pi)^3p^0}\delta n_a &= \frac{\pi_{\mu\nu}}{2T^2(\varepsilon+P)}\int \frac{d^3p}{(2\pi)^3p^0}p^\mu p^\nu n_{a,0}\left[\frac{p^\mu}{T}u_\mu\right]\left(1\pm n_{a,0}\left[\frac{p^\mu}{T}u_\mu\right]\right)\\ &= \frac{\pi_{\mu\nu}}{2T^2(\varepsilon+P)}I^{\mu\nu}\\ &= \frac{\pi_{\mu\nu}}{2T^2(\varepsilon+P)}\left[I_0u^\mu u^\nu + I_1 g^{\mu\nu}\right]\\ &= 0. \end{aligned} \tag{2.95}$$

Going from the first to second line the integration over p^μ is performed. To determine the $I^{\mu\nu}$ tensor, a tensor decomposition is being employed. The only tensors available to construct $I^{\mu\nu}$ is the metric $g^{\mu\nu}$ and the fluid velocities $u^\mu u^\nu$. However, $g^{\mu\nu}\pi_{\mu\nu}=0$ and $u^\mu\pi_{\mu\nu}=0$, thus the δn_a coming from the shear viscous pressure cannot change the particle multiplicity N_a.

2.3.3 Particle flow and geometry of the initial state

Using the Cooper-Frye formula, one can compute the hadron spectrum

$$p^0\frac{d^3N_a}{d^3p} = \frac{d^3N_a}{dyp_Tdp_Td\phi} = \int d^3\Sigma_\mu p^\mu n_{a,0}\left[\frac{p^\mu}{T}u_\mu\right] \tag{2.96}$$

where the momentum rapidity y and the transverse momentum are defined as

$$y \equiv \frac{1}{2}\ln\left[\frac{p^0+p^z}{p^0-p^z}\right],\quad p_T\equiv\sqrt{p_x^2+p_y^2}. \tag{2.97}$$

Particle yield is not the only experimentally observed quantity that can be obtained through Eq. (2.96). Particle flow, a measure of the collective expansion observed in relativistic heavy-ion collisions, can also be obtained. It is common to expand the azimuthal distribution of particles in a Fourier series:

$$\begin{aligned}\frac{d^3N_a}{dyp_Tdp_Td\phi} &= \frac{1}{2\pi}\frac{dN_a}{dyp_Tdp_T}\left[1+2\sum_{n=1}^{\infty}V_{n,a}^c\cos(n\phi)+2\sum_{n=1}^{\infty}V_{n,a}^s\sin(n\phi)\right]\\ &= \frac{1}{2\pi}\frac{dN_a}{dyp_Tdp_T}\left[1+2\sum_{n=1}^{\infty}v_{n,a}\cos\left(n\phi-n\Psi_{n,a}\right)\right]\end{aligned} \tag{2.98}$$

where $v_{n,a}=\sqrt{\left(V_{n,a}^c\right)^2+\left(V_{n,a}^s\right)^2}$ while

$$\Psi_{n,a} = -\frac{1}{n}\arctan\left[\frac{\int_0^{2\pi}d\phi\sin(n\phi)\frac{d^3N_a}{dyp_Tdp_Td\phi}}{\int_0^{2\pi}d\phi\cos(n\phi)\frac{d^3N_a}{dyp_Tdp_Td\phi}}\right]. \tag{2.99}$$

These Fourier coefficients are useful as they are a measure of the collective motion of the hadrons. In addition, v_n have a geometrical interpretation. Indeed, there is correlation between the p_T-integrated Fourier coefficients v_n (where $v_n = \left[\sum_a N_a v_{n,a}\right] / \left[\sum_a N_a\right]$), evaluated at $y = 0$, and the geometrical distribution of the energy density in the initial conditions. To simplify the discussion, optical Glauber initial conditions are used. Set the impact parameter vector $\mathbf{b}$ be aligned with the x-axis (this can always be done without loss of generality). Using these two assumptions, the position-space and momentum-space distribution are depicted in Fig. 2.2. The gray region in Fig. 2.2 (a) is where the strongly interacting medium will be created, i.e. where part of the energy stored in the colliding nuclei will be converted into the initial energy density profile to be evolved via hydrodynamics. For optical

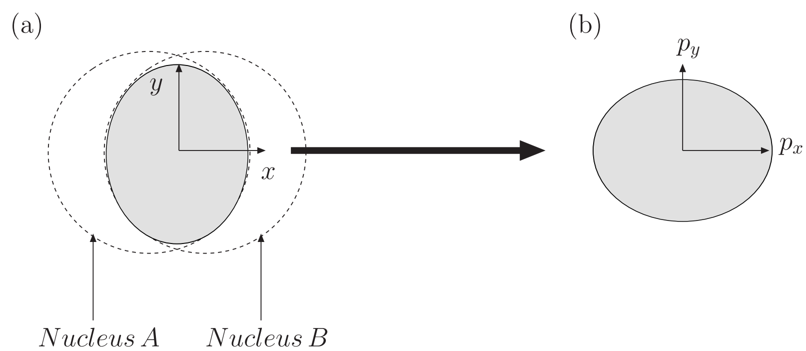

Figure 2.2: The panel (a) illustrates position-space anisotropy, while the panel (b) illustrates the shape of the momentum-space anisotropy after a hydrodynamical evolution (denoted by the arrow).

Glauber initial conditions, all odd Fourier coefficients in the momentum-space greater than $n = 1$ are zero by symmetry of the initial energy density profile. Hence odd harmonics only arise from fluctuations in the initial profile. Furthermore, v_1 can be set to zero if the origin of the (x, y)-plane is aligned with the maximum in the energy density. Thus, only even Fourier coefficients are non-vanishing. Hydrodynamical simulations have shown that there is a tight correlation between the momentum anisotropy and the original spatial anisotropy. This correlation comes from the evolution of the medium. The latter is governed by the pressure gradients which are larger along the x-axis than along the y-axis. These pressure gradients will be converted into flow gradients pushing matter more in the x-direction than in the y-direction, thus generating more particles flowing along the x-axis than the y-axis. So a prolate initial elliptical profile in Fig. 2.2 (a) is converted into an oblate elliptical distribution after a hydrodynamical evolution in Fig. 2.2 (b), which gives rise to a non-zero p_T-integrated v_2 contribution in Eq. (2.98).

It is also possible to relate other p_T-integrated Fourier coefficients v_n to the geometrical shape of the initial distribution profile. For a general non-symmetrical initial condition, the relationship between the Fourier coefficients of the particle distribution and the Fourier coefficients of the initial geometry is not straightforward. However, there is a key observation that will lead to a relationship between the angular modulations in the original energy density profile and the v_n of the particle flow. If one takes the Fourier transform of the energy density profile if Fig. 2.2 (a), one obtains an object similar in shape to Fig. 2.2 (b). This fact can be used to relate the Fourier coefficients of the geometrical distribution to v_n. As the discussion below is rather general, the assumption of optical Glauber modeling of the initial conditions is not required.

The discussion presented in the rest of this chapter follows [100]. For later convenience, the Fourier transform of the energy density profile is defined as a normalized quantity:

$$\frac{\varepsilon(\mathbf{k})}{\varepsilon(0)} = \frac{\int d^2x e^{i\mathbf{k}\cdot\mathbf{x}}\varepsilon(\mathbf{x})}{\int d^2x \varepsilon(\mathbf{x})}. \tag{2.100}$$

Recalling that both the optical Glauber model and the Monte-Carlo Glauber model generates an energy density profile that decays (roughly) as a Gaussian at large distances, $\frac{\varepsilon(\mathbf{k})}{\varepsilon(0)}$ should be rewritten as $\frac{\varepsilon(\mathbf{k})}{\varepsilon(0)} = \exp[W(\mathbf{k})]$. Performing a Fourier series expansion of $W(\mathbf{k})$ and of $\varepsilon(\mathbf{k})$ yields:

$$\begin{aligned} W(\mathbf{k}) &= W_0(k) + \sum_{n=1}^{\infty} W_n^c(k)\cos(n\phi_k) + \sum_{n=1}^{\infty} W_n^s(k)\sin(n\phi_k) \\ \varepsilon(\mathbf{k}) &= \varepsilon_0(k) + \sum_{n=1}^{\infty} \varepsilon_n^c(k)\cos(n\phi_k) + \sum_{n=1}^{\infty} \varepsilon_n^s(k)\sin(n\phi_k) \end{aligned} \tag{2.101}$$

where the vector $\mathbf{k}$ is expressed in polar coordinates $\mathbf{k} = (k, \phi_k)$, while

$$
\begin{aligned}
W_n^c &= \frac{1}{2\pi} \int d\phi_k \cos(n\phi_k) W(\mathbf{k}) \\
W_n^s &= \frac{1}{2\pi} \int d\phi_k \sin(n\phi_k) W(\mathbf{k})
\end{aligned}
\tag{2.102}
$$

and similarly for $\varepsilon_n^{c,s}$. Only the first few terms in the Fourier series of W are required to have a fast convergence to $\frac{\varepsilon(\mathbf{k})}{\varepsilon(0)}$. Inverting the equation for W, one gets

$$
W(\mathbf{k}) = \ln\left[\frac{\varepsilon(\mathbf{k})}{\varepsilon(0)}\right] = \sum_{i=1}^{\infty} \frac{(-1)^{j-1}}{j} \left[\frac{\varepsilon(\mathbf{k})}{\varepsilon(0)} - 1\right]^j \tag{2.103}
$$

Using the relation:

$$
e^{i\mathbf{k}\cdot\mathbf{x}} = e^{ikr\cos(\phi-\phi_k)} = J_0(kr) + 2\sum_{n=1}^{\infty} i^n J_n(kr)\cos(n\phi - n\phi_k) \tag{2.104}
$$

where the position vector $\mathbf{x}$, which spans the (x, y)-plane, is expressed in polar coordinates $\mathbf{x} = (r, \phi)$ and J_n are the Bessel functions of the first kind, one can write the the Fourier coefficients $\varepsilon_n^{c,s}$ as

$$
\begin{aligned}
\frac{\varepsilon_0(k)}{\varepsilon(0)} &= \frac{1}{\varepsilon(0)} \int r dr d\phi J_0(kr) \varepsilon(\mathbf{x}) \\
\frac{\varepsilon_n^c(k)}{\varepsilon(0)} &= \frac{1}{\varepsilon(0)} \int r dr d\phi i^n J_n(kr) \cos(n\phi) \varepsilon(\mathbf{x}) \\
\frac{\varepsilon_n^s(k)}{\varepsilon(0)} &= \frac{1}{\varepsilon(0)} \int r dr d\phi i^n J_n(kr) \sin(n\phi) \varepsilon(\mathbf{x}).
\end{aligned}
\tag{2.105}
$$

The Bessel function has a series expansion:

$$
J_n(kr) = \left(\frac{kr}{2}\right)^n \sum_{m=0}^{\infty} (-1)^m \frac{\left(\frac{kr}{2}\right)^{2m}}{m!(n+m)!}. \tag{2.106}
$$

Hence,

$$
\begin{aligned}
\frac{\varepsilon_0(k)}{\varepsilon(0)} &= \frac{1}{\varepsilon(0)} \int r dr d\phi \sum_{m=0}^{\infty} (-1)^m \frac{\left(\frac{kr}{2}\right)^{2m}}{(m!)^2} \varepsilon(\mathbf{x}) \\
&= 1 + (-1)\frac{k^2}{4\varepsilon(0)} \epsilon_2 + \mathcal{O}\left((kr)^4\right) \\
\frac{\varepsilon_n^c(k)}{\varepsilon(0)} &= \frac{1}{\varepsilon(0)} \sum_{m=0}^{\infty} (-1)^m \left(\frac{k}{2}\right)^{n+2m} \frac{1}{m!(n+m)!} \epsilon_{n,n+m}^c \\
\frac{\varepsilon_n^s(k)}{\varepsilon(0)} &= \frac{1}{\varepsilon(0)} \sum_{m=0}^{\infty} (-1)^m \left(\frac{k}{2}\right)^{n+2m} \frac{1}{m!(n+m)!} \epsilon_{n,n+m}^s
\end{aligned}
\tag{2.107}
$$

so that the only term in the Fourier series of $\frac{\varepsilon(\mathbf{k})}{\varepsilon(0)}$ that has a piece which doesn't depend on a power of (kr) is $\frac{\varepsilon_0(k)}{\varepsilon(0)}$. In Eq. (2.107), the cumulants of the distribution $\varepsilon(\mathbf{x})$ are implicitly defined via

$$\begin{aligned}
\epsilon_2 &= \int r dr d\phi r^2 \epsilon(\mathbf{x}) \\
\epsilon^c_{n,n+2m} &= \int r dr d\phi r^{n+2m} \cos(n\phi)\varepsilon(\mathbf{x}) \\
\epsilon^s_{n,n+2m} &= \int r dr d\phi r^{n+2m} \sin(n\phi)\varepsilon(\mathbf{x}).
\end{aligned} \tag{2.108}$$

Hence the Taylor expansion of $\ln\left[\frac{\varepsilon(\mathbf{k})}{\varepsilon(0)}\right]$ has only terms that are non-zero powers of (kr). This is the reason why a Fourier transform was being done on $\frac{\varepsilon(\mathbf{k})}{\varepsilon(0)}$ instead of $\varepsilon(\mathbf{k})$. Also note that the smallest power allowed in series for $\ln\left[\frac{\varepsilon(\mathbf{k})}{\varepsilon(0)}\right]$ is k^2. At this point, a power series expansion of $W_n^{c,s}(k)$ can be performed yielding:

$$W(\mathbf{k}) = \sum_{m=2}^{\infty} W_{0,m}k^m + \sum_{n=1}^{\infty}\sum_{m=2}^{\infty} W^c_{n,m}k^m \cos(n\phi_k) + \sum_{n=1}^{\infty}\sum_{m=2}^{\infty} W^s_{n,m}k^m \sin(n\phi_k) \tag{2.109}$$

Using Eq. (2.109) and matching powers of k^m, $k^m\cos(n\phi_k)$, and $k^m\sin(n\phi_k)$ on both sides of Eq. (2.103) allows to determine $W_{n,m}$ and $W^{c,s}_{n,m}$. The first terms of the various harmonics are [100]

$$\begin{aligned}
&W_{0,2} = \frac{1}{2}\epsilon_2 \qquad W^c_{1,3} = \frac{3}{8}\epsilon^c_{1,3} \quad W^s_{1,3} = \frac{3}{8}\epsilon^s_{1,3} \quad W^c_{2,2} = \frac{1}{4}\epsilon^c_{2,2} \quad W^s_{2,2} = \frac{1}{4}\epsilon^s_{2,2} \\
&W^c_{3,3} = \frac{3}{8}\epsilon^c_{3,3} \quad W^s_{3,3} = \frac{3}{8}\epsilon^s_{2,2} \quad W^c_{4,4} = \frac{1}{16}\left[\epsilon^c_{4,4} - 3\left(\epsilon^c_{2,2}\right)^2\right] \quad W^s_{4,4} = \frac{1}{16}\epsilon^s_{4,4} \\
&W^c_{5,5} = \frac{1}{32}\left[\epsilon^s_{5,5} - 10\epsilon^c_{2,2}\epsilon^c_{3,3}\right] \qquad W^s_{5,5} = \frac{1}{32}\left[\epsilon^s_{5,5} - 10\epsilon^s_{2,2}\epsilon^s_{3,3}\right].
\end{aligned} \tag{2.110}$$

Given that hydrodynamic equations of motion are not valid to describe the evolution of the energy density at very short length scales, only the first few terms in Eq. (2.109) are actually evolved via hydrodynamics. Furthermore, since there is an exponential relationship between $\frac{\varepsilon(\mathbf{k})}{\varepsilon(0)}$ and $W(\mathbf{k})$ [recall Eq. (2.103)], the first few terms in Eq. (2.110) should give a reasonable description of the most important modulations of the initial distribution profile. Indeed, it was shown in Ref. [101] that the p_T-integrated v_2 can be obtained from geometrical considerations, i.e. $v_2 = C\frac{\sqrt{\left(W^c_{2,2}\right)^2+\left(W^s_{2,2}\right)^2}}{W_{0,2}}$ where

C is a proportionality constant that captures the entire hydrodynamical response of the system. Including higher order terms $W_{2,4}^{c,s}$ yields a small correction. A similar result was also found to hold v_3. So it would seem that v_n is proportional to $W_{n,m}^{c,s}$; an observation confirmed by v_4 and v_5. Indeed, Ref. [101] has also shown that v_4 cannot be obtained by using solely $\epsilon_{4,4}^{c,s}$: both $\epsilon_{4,4}^{c,s}$ and $\left(\epsilon_{2,2}^{c,s}\right)^2$ must be present to adequately reproduce v_4, as $W_{n,m}^{c,s}$ would suggest. Lastly, to obtain v_5 both $\epsilon_{5,5}^{c,s}$ and the product $\epsilon_{2,2}^{c,s}\epsilon_{3,3}^{c,s}$ are required further confirming that $v_n \propto W_{5,5}^{c,s}$. Physically, the hydrodynamical response is linear, i.e. $v_n \propto \epsilon_{n,n}^{c,s}$, only for v_2 and v_3 and in sufficiently central collisions, see [76]. Therein lies the geometrical interpretation of v_2 and v_3. Schematically, at $y = 0$, the p_T-integrated v_2 and v_3 arise from geometry as illustrated in Fig. 2.3, while v_1 simply points towards a hot spot in the initial conditions that is not centered at the origin of the (x, y)-plane.

To summarize, v_2 and v_3 have a simple geometrical interpretation: they are tightly related to the second and third coefficients of the Fourier expansion of the initial geometrical profile. For higher flow harmonics, the hydrodynamical response is non-

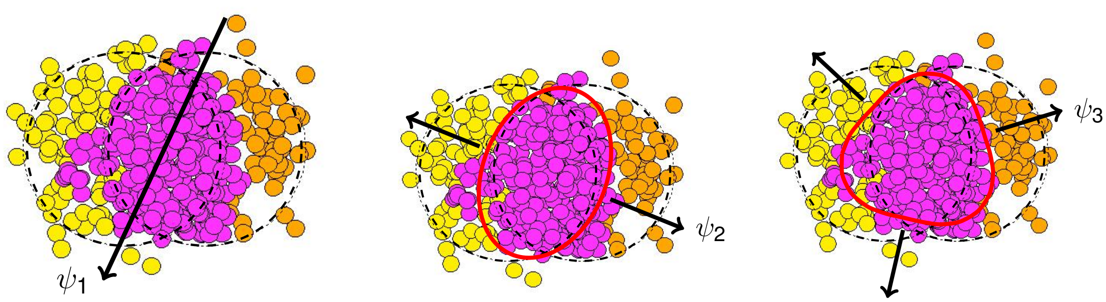

(a) (b) (c)

Figure 2.3: Geometrical configurations giving rise to the p_T-integrated v_1, v_2, and v_3. v_1 is non-zero whenever there is a hot spot on the initial conditions of the hydro and Ψ_1 is pointing along the axis where the hot spot is located (see (a)). Elliptic flow is given by the geometrical shape in panel (b) with Ψ_2 pointing towards the directions of along which the hydrodynamical expansion will take place. Lastly, v_3 is originating from the geometrical shape depicted in panel (c), while Ψ_3 points in the directions where flow will develop [4].

linear (in $\epsilon_{n,n}^{c,s}$) and a simple geometrical interpretation is not possible. However, in the limiting case where the impact parameter is small [101], i.e. for very central collisions, the geometrical interpretation does hold as v_4 and v_5.

2.4 Summary

The relativistic hydrodynamical equations of motion and their initial conditions have been derived in section 2.1 and 2.2. A prescription for converting the fluid dynamical degrees of freedom to particles was also described in sections 2.3.1 and 2.3.2. Lastly, the correlation between the initial geometrical anisotropy and the final momentum anisotropy measured via the Fourier coefficients of final state particle distributions was just discussed. Putting all of these together allows to describe the hadronic spectra and anisotropic flow (i.e. Fourier) coefficients v_n. The goal of the next chapter is to describe the dilepton production mechanisms. Then, these two aspects will be integrated in chapter 4.

3

Dilepton production rates

In the Introduction, it was already argued that dileptons are ideally suited to study the properties of strongly interacting media. The reasons were twofold. First, the strength of the QED coupling constant is much smaller than that of QCD and hence electromagnetic probes can leave the medium with negligible re-scatterings. Second, the virtuality (i.e. the center of mass energy of the pair) of the photon sourcing the lepton pair can be used to separate emission sources. Highly virtual photons are emitted from the QGP[1] while low virtuality photons are emitted from a mixture of QGP and hadronic contributions, with the relative proportion of each specified in the next section. The goal of this chapter is to present and compute the production rates of these two sources.

3.1 Dilepton radiation at finite temperature

The dilepton production in a thermalized medium can be computed exactly at leading order in the electromagnetic coupling strength $\alpha_{EM} = \frac{e^2}{4\pi}$. The probability in quantum field theory of an initial state $|i\rangle$ to make a transition to a final state $|f\rangle$ and a lepton pair $\ell^+\ell^-$ is given by:

$$|\mathcal{M}|^2 = \left| \left\langle f, \ell^+\ell^- \middle| T \left\{ \exp\left[-i \int dt H_I \right] \right\} \middle| i \right\rangle \right|^2 \tag{3.1}$$

where $\mathcal{M}$ is the transition amplitude, T is a time ordering operator, and H_I is the interaction Hamiltonian [10]. Strictly speaking, the transition amplitude is an element

[1]For the center of mass energy of the lepton pair $M \gtrsim 1$ GeV, QGP dominates the dilepton emission.

of the S-matrix, given by

$$S = T\left\{\exp\left[-i\int dt H_I\right]\right\}. \tag{3.2}$$

The key quantity entering the S-matrix is the interaction Hamiltonian. For dilepton production, the latter is given by:

$$H_I = \int d^3x J_\mu^{QCD} A^\mu + \int d^3x J_\mu^\ell A^\mu. \tag{3.3}$$

In Eq. (3.3), A^μ is the 4-vector potential of the electromagnetic field, while J_μ^ℓ represents the leptonic current. In fact, the lepton current can be read from the quantum electrodynamics (QED) Lagrangian:

$$\mathcal{L}_{QED} = \sum_{L=e,\mu;\ell=e,\mu}\left[\bar{L}(i\gamma^\mu D_\mu - m_\ell)L\right] - \frac{1}{4}F^{\mu\nu}F_{\mu\nu}, \tag{3.4}$$

where, L is lepton (i.e. electron/muon) spinor, γ_μ is the Dirac γ-matrix, $\bar{L} = L^\dagger\gamma^0$, $D_\mu = \partial_\mu - ieA_\mu$, and $F_{\mu\nu} = \partial_\mu A_\nu - \partial_\nu A_\mu$ is the electromagnetic field strength tensor. The lepton current is $J_\mu^\ell = e\bar{L}\gamma_\mu L$ [10]. In principle the τ lepton should also be present in the QED Lagrangian. However, its large mass compared to the typical temperatures present in relativistic heavy-ion collision [$T \sim \mathcal{O}(100\text{ MeV})$] prevents it from participating in thermal mechanism of dilepton production, and hence it is omitted.

The current J_μ^{QCD} is a little more complicated. The complication comes through the fact that, as a function of temperature T, QCD's effective degrees of freedom change, and so does J_μ^{QCD}. At high temperatures, the asymptotic freedom of QCD dictates that the degrees of freedom contributing to J_μ^{QCD} should be the quarks and gluons. Hence, the current $J_\mu^{QCD} = \delta^{ee'}\bar{\psi}_e\gamma_\mu\psi'_e$, where ψ was defined in Eq. (1.3). At low temperatures however, the degrees of freedom are hadronic. In sum,

$$J_\mu^{QCD} = \begin{cases} \delta^{ee'}\bar{\psi}_e\gamma_\mu\psi_{e'} = J_\mu^{QGP} & \text{if } T \gtrsim 0.22\text{ GeV}, \\ J_\mu^{\text{hadron}} & \text{if } T \lesssim 0.18\text{ GeV}, \\ r_{QGP}J_\mu^{QGP} + (1-r_{QGP})J_\mu^{\text{hadron}}, & \text{otherwise} \end{cases}, \tag{3.5}$$

where, r_{QGP} is a fraction measuring how much of a particular fluid element is in the QGP phase. If the transition from a QCD to a hadronic fluid was of the first order,

r_{QGP} would actually have some thermodynamical meaning. However, as mentioned in the Introduction, the transition between QGP and hadronic fluid is a cross-over as shown by recent ℓQCD calculations [17, 18]. Hence, r_{QGP} is nothing but a computational tool that interpolates between the production rates of the QGP and those from the hadronic fluid. The temperatures cited above will be used to interpolate between the hadronic and partonic contributions to dilepton production for media produced at top beam energy at RHIC.[1] The fact that there is cross-over phase transition is indirectly hinted upon via T^{μ}_{μ}, the trace of $T^{\mu\nu}$.[2] Indeed, the deviation from an ideal relativistic gas $\varepsilon = 3P$ is contained within T^{μ}_{μ}, also known as the trace anomaly, which can be used as guidance regarding temperatures over which an interpolation between the QGP and hadronic dilepton rates should be applied. As dilepton rates from ℓQCD are currently not available in a regime that is of phenomenological interest [70], an interpolation between the rates in the QGP rates from perturbative QCD and the dilepton rates from the hadronic phase must be used. From the discussion in the Introduction regarding the QCD equation of state, it is already known that hadronic degrees of freedom accurately describe lattice data for temperatures $T \lesssim 180$ MeV. A recent calculation [102] shows that using resummed perturbation, where soft quark/gluon momenta are resummed using the hard thermal loop formalism [103], one can obtain a good agreement between ℓQCD calculations and (resummed) perturbative calculation down to temperatures as low as a 200-300 MeV [102]. Hence it is reasonable to interpolate between the QGP rates and the hadronic rates in the region $0.18 \lesssim T \lesssim 0.22$ GeV, as the relevant degrees of freedom change in that region.

[1] This prescription would also hold true for LHC energies.

[2] The actual proof from ℓQCD that there is no first or second order phase transition comes from the derivatives of the free Helmholtz energy. Indeed, if there was a first order (or a second) order phase transition, a discontinuity in the first (or second) order derivatives of the Helmholtz free energy with respect to thermodynamical variables should have been found. This is not the case, even when the grand canonical free energy was used [17, 18] instead of the Helmholtz free energy. However, recall that the ℓQCD calculation using the grand canonical formalism was performed using a Taylor expansion, valid for small μ_B. Therefore a first (and second) order phase transition can still exist at large μ_B values.

Assuming a general J^{QCD}_μ, the dilepton production probability is:

$$\begin{aligned}
|\mathcal{M}|^2 &= \left|\left\langle f,\ell^+\ell^- \left| \int d^4x d^4y J^\ell_\mu(x) T\left[A^\mu(x)A^\nu(y)\right] J^{QCD}_\nu(y) \right| i \right\rangle\right|^2 \\
&= \left| \int d^4x d^4y \left\langle \ell^+\ell^- \left| J^\ell_\mu(x) \right| 0 \right\rangle \left\langle 0 \left| T\left[A^\mu(x)A^\nu(y)\right] \right| 0 \right\rangle \left\langle f \left| J^{QCD}_\nu(y) \right| i \right\rangle \right|^2 \quad (3.6)
\end{aligned}$$

The expectation value of the leptonic current in can be expressed as [10],

$$\left\langle \ell^+\ell^- \left| J^\ell_\mu(x) \right| 0 \right\rangle = e\bar{u}_s(p_-)\gamma_\mu v_{s'}(p_+) e^{ix\cdot(p_+ + p_-)}, \tag{3.7}$$

where $p_\pm$ refers to the momentum of the lepton and antilepton respectively, while the indices s and s' refer to their spin degrees of freedom. The expectation value of the electromagnetic vector potential correlator, the photon propagator, is given by [10],

$$T\left[A^\mu(x)A^\nu(y)\right] = -i \int \frac{d^4q}{(2\pi)^4} e^{-iq\cdot(x-y)} \frac{g^{\mu\nu}}{q^2}. \tag{3.8}$$

Combining these two results,

$$\begin{aligned}
|\mathcal{M}|^2 &= \left| -ie \int d^4x d^4y \frac{d^4q}{(2\pi)^4} \bar{u}_s(p_-)\gamma_\mu v_{s'}(p_+) e^{ix\cdot(p_+ + p_- - q)} e^{-iq\cdot(x-y)} \frac{g^{\mu\nu}}{q^2} \left\langle f \left| J^{QCD}_\nu(y) \right| i \right\rangle \right|^2 \\
&= \left| -ie \int d^4y d^4q \bar{u}_s(p_-)\gamma_\mu v_{s'}(p_+) \delta^4(p_+ + p_- - q) e^{iq\cdot y} \frac{g^{\mu\nu}}{q^2} \left\langle f \left| J^{QCD}_\nu(y) \right| i \right\rangle \right|^2 \\
&= \left| -ie \int d^4y \bar{u}_s(p_-)\gamma_\nu v_{s'}(p_+) e^{iy\cdot(p_+ + p_-)} \frac{g^{\mu\nu}}{(p_+ + p_-)^2} \left\langle f \left| J^{QCD}_\nu(y) \right| i \right\rangle \right|^2 \quad (3.9) \\
&= e^2 \int d^4y d^4y' \bar{u}_s(p_-)\gamma_\mu v_{s'}(p_+) \bar{v}_{s'}(p_+)\gamma_\alpha u_s(p_-) e^{i(y-y')\cdot(p_+ + p_-)} \times \\
&\times \frac{g^{\mu\nu}}{(p_+ + p_-)^2} \frac{g^{\alpha\beta}}{(p_+ + p_-)^2} \left\langle f \left| J^{QCD}_\nu(y) \right| i \right\rangle \left\langle i \left| J^{QCD}_\beta(y') \right| f \right\rangle. \quad (3.10)
\end{aligned}$$

The variables y and y' in Eq. (3.10) are really referring to the same point in space-time such that $\int d^4y' \to \int d^4y' V t \delta^4(y - y')$, where Vt is the space-time volume associated with $\int d^4y'$. Therefore,

$$\begin{aligned}
|\mathcal{M}|^2 &= e^2 \int d^4y d^4y' V t \delta^4(y-y') \bar{u}_s(p_-)\gamma_\mu v_{s'}(p_+) \bar{v}_{s'}(p_+)\gamma_\alpha u_s(p_-) e^{i(y-y')\cdot(p_+ + p_-)} \times \\
&\times \frac{g^{\mu\nu}}{(p_+ + p_-)^2} \frac{g^{\alpha\beta}}{(p_+ + p_-)^2} \left\langle f \left| J^{QCD}_\nu(y) \right| i \right\rangle \left\langle i \left| J^{QCD}_\beta(y') \right| f \right\rangle. \quad (3.11)
\end{aligned}$$

One can simplify $\left\langle f \left| J^{QCD}_\mu(y) \right| i \right\rangle$ somewhat by using translational invariance. Indeed,

$$\langle f | J^{QCD}_\beta(y') | i \rangle = e^{ip_i\cdot y'} \left\langle f \left| J^{QCD}_\beta(0) \right| i \right\rangle e^{-ip_f\cdot y'} = e^{iy'\cdot(p_+ + p_-)} \left\langle f \left| J^{QCD}_\beta(0) \right| i \right\rangle, \tag{3.12}$$

where the momentum of the initial state p_i and that of the final state p_f are related via $p_i - p_f = p_+ + p_-$ by momentum conservation. Inserting Eq. (3.12) in Eq. (3.11), yields

$$
\begin{aligned}
|\mathcal{M}|^2 &= e^2 \int d^4y d^4y' V t \delta^4(y-y') \bar{u}_s(p_-)\gamma_\mu v_{s'}(p_+)\bar{v}_{s'}(p_+)\gamma_\alpha u_s(p_-) e^{iy\cdot(p_+ + p_-)} \times \\
&\times \frac{g^{\mu\nu}}{(p_+ + p_-)^2}\frac{g^{\alpha\beta}}{(p_+ + p_-)^2}\left\langle f \left| J_\nu^{QCD}(y) \right| i \right\rangle \left\langle i \left| J_\beta^{QCD}(0) \right| f \right\rangle \\
&= e^2 V t \int d^4y \bar{u}_s(p_-)\gamma_\mu v_{s'}(p_+)\bar{v}_{s'}(p_+)\gamma_\alpha u_s(p_-) e^{iy\cdot(p_+ + p_-)} \times \\
&\times \frac{g^{\mu\nu}}{(p_+ + p_-)^2}\frac{g^{\alpha\beta}}{(p_+ + p_-)^2}\left\langle f \left| J_\nu^{QCD}(y) \right| i \right\rangle \left\langle i \left| J_\beta^{QCD}(0) \right| f \right\rangle . \qquad (3.13)
\end{aligned}
$$

In order to be able to compare this calculation with experimental measurements, a sum over the spin-states of the lepton pairs must be performed. The spin summed transition probability will be labeled as $\left|\hat{\mathcal{M}}\right|^2$. Performing this spin sum, yields

$$
\begin{aligned}
\sum_{s,s'} \bar{u}_s(p_-)\gamma_\mu v_{s'}(p_+)\bar{v}_{s'}(p_+)\gamma_\alpha u_s(p_-) &= \mathrm{Tr}\left[(\not{p}_- + m_\ell)\gamma_\mu(\not{p}_+ - m_\ell)\gamma_\alpha\right] \qquad (3.14) \\
&= 4\left[p_{+,\mu}p_{-,\alpha} + p_{+,\alpha}p_{-,\mu} - g_{\mu\alpha}(p_+\cdot p_- + m_\ell^2)\right] .
\end{aligned}
$$

Inserting Eq. (3.14) in Eq. (3.13) yields:

$$
\begin{aligned}
\left|\hat{\mathcal{M}}\right|^2 &= e^2 V t \int d^4y \frac{4}{(p_+ + p_-)^4}\left[p_+^\nu p_-^\beta + p_+^\beta p_-^\nu - g^{\nu\beta}(p_+\cdot p_- + m_\ell^2)\right] e^{iy\cdot(p_+ + p_-)} \times \\
&\times \left\langle f \left| J_\nu^{QCD}(y) \right| i \right\rangle \left\langle i \left| J_\beta^{QCD}(0) \right| f \right\rangle . \qquad (3.15)
\end{aligned}
$$

To obtain the dilepton production rate of experimental significance, an average over the initial state must also be performed. Since the production is happening inside a thermalized system, one must apply a thermal weight for each term in the series. The weight is $\frac{e^{-\beta_0 p_i^0}}{Z}$, where $Z = \sum_n e^{-\beta_0 p_n}$, and $\beta_0 = T^{-1}$ as before. The dilepton rate per unit volume finally reads:

$$
\begin{aligned}
R^{\ell^+\ell^-} &= \sum_{i,f} \int \frac{d^3p_+}{(2\pi)^3 2p_+^0} \frac{d^3p_-}{(2\pi)^3 2p_-^0} \frac{\left|\hat{\mathcal{M}}\right|^2}{Vt} \frac{e^{-\beta_0\left(p_+^0+p_-^0+p_f^0\right)}}{Z} \\
&= e^2 \sum_{i,f} \int \frac{d^3p_+}{(2\pi)^3 2p_+^0} \frac{d^3p_-}{(2\pi)^3 2p_-^0} e^{-\beta_0\left(p_+^0+p_-^0\right)} \frac{4\left[p_+^\nu p_-^\beta + p_+^\beta p_-^\nu - g^{\nu\beta}(p_+\cdot p_- + m_\ell^2)\right]}{(p_+ + p_-)^4} \times \\
&\times \int d^4y e^{iy\cdot(p_+ + p_-)} \left\langle f\left| J_\nu^{QCD}(y)\right| i\right\rangle \left\langle i\left| J_\beta^{QCD}(0)\right| f\right\rangle \frac{e^{-\beta_0 p_f^0}}{Z} \\
&= e^2 \int \frac{d^3p_+}{(2\pi)^3 p_+^0} \frac{d^3p_-}{(2\pi)^3 p_-^0} e^{-\beta_0\left(p_+^0+p_-^0\right)} \frac{\left[p_+^\nu p_-^\beta + p_+^\beta p_-^\nu - g^{\nu\beta}(p_+\cdot p_- + m_\ell^2)\right]}{(p_+ + p_-)^4} \times \\
&\times \int d^4y e^{iy\cdot(p_+ + p_-)} \sum_f \left\langle f\left| J_\nu^{QCD}(y) J_\beta^{QCD}(0)\right| f\right\rangle \frac{e^{-\beta_0 p_f^0}}{Z},
\end{aligned} \tag{3.16}
$$

where, in going from the second to the third line, the completeness relation $\mathbf{1} = \sum_i |i\rangle\langle i|$ was used. At this point it is important to define the correlation function

$$
\begin{aligned}
\Pi_{\nu\beta}^{>}(q) &= \int d^4y e^{iy\cdot(p_+ + p_-)} \sum_f \left\langle f\left| J_\nu^{QCD}(y) J_\beta^{QCD}(0)\right| f\right\rangle \frac{e^{-\beta_0 p_f^0}}{Z} \\
&= \int d^4y e^{iy\cdot(p_+ + p_-)} \mathrm{Tr}\left[e^{-\beta_0 H} J_\nu^{QCD}(y) J_\beta^{QCD}(0)\right],
\end{aligned} \tag{3.17}
$$

which is one of the Wightman functions [104].[1] The other Wightman function is obtained by reversing the order of the J operators appearing in Eq. (3.17), that is

$$
\Pi_{\nu\beta}^{<}(q) = \int d^4y e^{iy\cdot(p_+ + p_-)} \mathrm{Tr}\left[e^{-\beta_0 H} J_\nu^{QCD}(0) J_\beta^{QCD}(y)\right]. \tag{3.18}
$$

The two Wightman functions are not independent and can be related to each other, known as the Kubo-Martin-Schwinger relation [104]. Since time translations are unitary transformations, it is possible to rewrite $J_\nu^{QCD}(y)$ as

$$
J_\nu^{QCD}(y) = J_\nu^{QCD}(t,\vec{y}) = e^{iHt} J_\nu^{QCD}(0,\vec{y}) e^{-iHt}, \tag{3.19}
$$

where H is the QCD Hamiltonian. Inserting Eq. (3.19) in Eq. (3.17) and performing

[1] Recall that $q^\mu = p_+^\mu + p_-^\mu$, hence $\Pi_{\nu\beta}^{>}$ only depends on q.

an inverse Fourier transform on both sides of Eq. (3.17) gives

$$\begin{aligned}
\Pi^{>}_{\nu\beta}(t,\vec{y}) &= \mathrm{Tr}\left[e^{-\beta_0 H} J^{QCD}_{\nu}(t,\vec{y}) J^{QCD}_{\beta}(0,\vec{0})\right] \\
&= \mathrm{Tr}\left[e^{-\beta_0 H} e^{iHt} J^{QCD}_{\nu}(0,\vec{y}) e^{-iHt} e^{\beta_0 H} e^{-\beta_0 H} J^{QCD}_{\beta}(0,\vec{0})\right] \\
&= \mathrm{Tr}\left[e^{i(t+i\beta_0)H} J^{QCD}_{\nu}(0,\vec{y}) e^{-i(t+i\beta_0)H} e^{-\beta_0 H} J^{QCD}_{\beta}(0,\vec{0})\right] \\
&= \mathrm{Tr}\left[J^{QCD}_{\nu}\left(t+i\beta_0,\vec{y}\right) e^{-\beta_0 H} J^{QCD}_{\beta}(0,\vec{0})\right] \\
&= \mathrm{Tr}\left[e^{-\beta_0 H} J^{QCD}_{\beta}(0,\vec{0}) J^{QCD}_{\nu}\left(t+i\beta_0,\vec{y}\right)\right] \\
&= \Pi^{<}_{\beta\nu}(t+i\beta_0,\vec{y}). \qquad (3.20)
\end{aligned}$$

Since J^{QCD}_{ν} and J^{QCD}_{β} are vectors, their tensor product $J^{QCD}_{\nu} J^{QCD}_{\beta}$ must give a symmetric tenor. Therefore

$$\Pi^{<}_{\beta\nu}(t,\vec{y}) = \Pi^{<}_{\nu\beta}(t,\vec{y}). \qquad (3.21)$$

Taking the Fourier transform on both sides of the equation gives

$$\begin{aligned}
\int d^4y e^{iq\cdot y} \Pi^{>}_{\nu\beta}(t,\vec{y}) &= \int d^4y e^{iq\cdot y} \Pi^{<}_{\nu\beta}\left(t+i\beta_0,\vec{y}\right) \\
&= \int d^3y e^{-i\vec{q}\cdot\vec{y}} \int dt e^{iq^0 t} \Pi^{<}_{\nu\beta}\left(t+i\beta_0,\vec{y}\right) \\
&= \int d^3y e^{-i\vec{q}\cdot\vec{y}} \int d\tau e^{iq^0(\tau-i\beta_0)} \Pi^{<}_{\nu\beta}\left(\tau,\vec{y}\right) \\
&= e^{\beta_0 q^0} \int d^3y e^{-i\vec{q}\cdot\vec{y}} \int d\tau e^{iq^0\tau} \Pi^{<}_{\nu\beta}\left(\tau,\vec{y}\right) \\
\Longrightarrow \Pi^{>}_{\nu\beta}(q) &= e^{\beta_0 q^0} \Pi^{<}_{\nu\beta}(q). \qquad (3.22)
\end{aligned}$$

Eq. (3.22) is the Kubo-Martin-Schwinger (KMS) relation [105]. Now, defining the photon spectral function as $\Pi^{\rho}_{\nu\beta}(q) \equiv \Pi^{<}_{\nu\beta}(q) - \Pi^{>}_{\nu\beta}(q)$ it is easy to show using Eq. (3.22) that $\Pi^{\rho}_{\nu\beta}(q) = \left(e^{-\beta_0 q^0} - 1\right) \Pi^{>}_{\nu\beta}(q)$. At leading order in the electromagnetic coupling e, the spectral function reduces to the photon self-energy $\Pi^{\rho}_{\nu\beta}(q) = -2\mathrm{Im}\Pi^{R}_{\nu\beta}(q)$, where $\mathrm{Im}\Pi^{R}_{\nu\beta}$ is the imaginary part of the proper retarded photon self-energy.[1] Therefore, the dilepton rate density is

$$\begin{aligned}
R^{\ell^+\ell^-} &= e^2 \int \frac{d^3p_+}{(2\pi)^3 p_+^0} \frac{d^3p_-}{(2\pi)^3 p_-^0} e^{-\beta_0\left(p_+^0+p_-^0\right)} \frac{\left[p_+^\nu p_-^\beta + p_+^\beta p_-^\nu - g^{\nu\beta}(p_+\cdot p_- + m_\ell^2)\right]}{(p_+ + p_-)^4} \times \\
&\times \frac{-2\mathrm{Im}\Pi^R_{\nu\beta}(q)}{\left(e^{-\beta_0\left(p_+^0+p_-^0\right)} - 1\right)} \\
&= e^2 \int \frac{d^3p_+}{(2\pi)^3 p_+^0} \frac{d^3p_-}{(2\pi)^3 p_-^0} \frac{\left[p_+^\nu p_-^\beta + p_+^\beta p_-^\nu - g^{\nu\beta}(p_+\cdot p_- + m_\ell^2)\right]}{(p_+ + p_-)^4} \times \\
&\times \frac{2\mathrm{Im}\Pi^R_{\nu\beta}(q)}{\left(e^{\beta_0\left(p_+^0+p_-^0\right)} - 1\right)}. \qquad (3.23)
\end{aligned}$$

Thus the differential rate reads:

$$\begin{aligned}
p_+^0 p_-^0 \frac{d^6 R^{\ell^+\ell^-}}{d^3p_+ d^3p_-} &= \frac{2e^2}{(2\pi)^6} \frac{\left[p_+^\nu p_-^\beta + p_+^\beta p_-^\nu - g^{\nu\beta}(p_+\cdot p_- + m_\ell^2)\right]}{(p_+ + p_-)^4} \frac{\mathrm{Im}\Pi^R_{\nu\beta}(q)}{\left(e^{\beta_0\left(p_+^0+p_-^0\right)} - 1\right)} \\
&= \left[p_+^\nu p_-^\beta + p_+^\beta p_-^\nu - g^{\nu\beta}(p_+\cdot p_- + m_\ell^2)\right] \frac{2e^2}{(2\pi)^6} \frac{1}{q^4} \frac{\mathrm{Im}\Pi^R_{\nu\beta}(q)}{(e^{\beta_0 q^0} - 1)}, \qquad (3.24)
\end{aligned}$$

where in the second line the leptonic contribution is separated from the electromagnetic contribution. Lastly, the dilepton production rate density will often be quoted as a function of the 4-momentum q of the virtual photon. Rewriting the rate as a function of q yields:

$$\begin{aligned}
\frac{d^4 R^{\ell^+\ell^-}}{d^4 q} &= \int \frac{d^3p_+}{p_+^0} \frac{d^3p_-}{p_-^0} (2\pi)^4 \delta^4\left(q - p_+ - p_-\right) p_+^0 p_-^0 \frac{d^6 R^{\ell^+\ell^-}}{d^3p_+ d^3p_-} \\
&= \left\{ \int \frac{d^3p_+}{p_+^0} \frac{d^3p_-}{p_-^0} \delta^4\left(q - p_+ - p_-\right) \left[p_+^\nu p_-^\beta + p_+^\beta p_-^\nu - g^{\nu\beta}(p_+\cdot p_- + m_\ell^2)\right] \right\} \times \\
&\times \frac{2e^2}{(2\pi)^2 q^4} \frac{\mathrm{Im}\Pi^R_{\nu\beta}(q)}{(e^{\beta_0 q^0} - 1)} \\
&= \left[1 + \frac{2m_\ell^2}{q^2}\right] \left[1 - \frac{4m_\ell^2}{q^2}\right]^{1/2} \left[q^\nu q^\beta - q^2 g^{\nu\beta}\right] \frac{\alpha_{EM}}{12\pi^4 q^4} \frac{\mathrm{Im}\Pi^R_{\nu\beta}(q)}{(e^{\beta_0 q^0} - 1)}, \qquad (3.25)
\end{aligned}$$

where $4\pi\alpha_{EM} = e^2$. Since J_ν^{QCD} is a conserved current, i.e. $\partial^\nu J_\nu^{QCD} = 0$ or in Fourier space $q^\nu J_\nu^{QCD} = 0$, it is possible to show that $q^\nu \Pi^R_{\nu\beta} = 0$ [10]. Therefore, Eq. (3.25)

[1] At higher orders, the spectral function is related to the imaginary part of the improper photon self-energy $\mathrm{Im}P^R_{\mu\nu}$, which is not equal to $\mathrm{Im}\Pi^R_{\nu\beta}$ in general. For more information, see [106].

reduces to:

$$\frac{d^4R^{\ell^+\ell^-}}{d^4q} = -\left[1+\frac{2m_\ell^2}{q^2}\right]\left[1-\frac{4m_\ell^2}{q^2}\right]^{1/2}\frac{\alpha_{EM}}{12\pi^4q^2}\frac{g^{\nu\beta}\mathrm{Im}\Pi^R_{\nu\beta}(q)}{(e^{\beta_0 q^0}-1)} \tag{3.26}$$

This is the fundamental formula for dilepton production [104, 105].

3.2 Dilepton production from the Hadronic Medium

The most important source of dileptons in the hadronic phase comes from the direct decay of low mass vector mesons ρ, ω, ϕ into a lepton pair. To describe the interaction between vector mesons and the electromagnetic fields, the very successful vector dominance model (VDM), first proposed by Sakurai [107], is used. The VDM interaction Lagrangian is:

$$\mathcal{L}_{VDM} = -eA^\mu\left[\sum_{V=\rho,\omega,\phi}\frac{m_V^2}{g_V}V_\mu\right], \tag{3.27}$$

where the vector potential V_μ is that of vector mesons, m_V is the mass of a vector meson, and g_V measures the strength of the coupling between photons and vector mesons. g_V will be tuned such at the theoretical production rate of dileptons matches the experimentally observed rate. The difference between photons and vector mesons lies in the fact that vector mesons have a different Lagrangian, namely:

$$\mathcal{L}_V = \sum_{V=\rho,\omega,\phi}\left[-\frac{1}{4}F_V^{\mu\nu}F^V_{\mu\nu}+m_V^2V^\mu V_\mu\right], \tag{3.28}$$

where $F^V_{\mu\nu} = \partial_\mu V_\nu - \partial_\nu V_\mu$. The VDM model changes the coupling in the interaction Hamiltonian in Eq. (3.3) that relates A^μ to J^{QCD}_μ. Specifically,

$$\int d^3x J^{QCD}_\mu A^\mu \to \int d^3x\left[\mathcal{L}_V+\mathcal{L}_{VDM}+V^\mu I^{\mathrm{hadron}}_\mu\right]. \tag{3.29}$$

Eq. (3.29) implies that the square matrix element is as depicted in Fig. 3.1. Since the QCD current is being replaced by the vector meson vector potential coupled to a hadronic current, the imaginary part of the retarded photon self-energy becomes the imaginary part of the vector meson propagator. The black disk in Fig. 3.1 illustrates

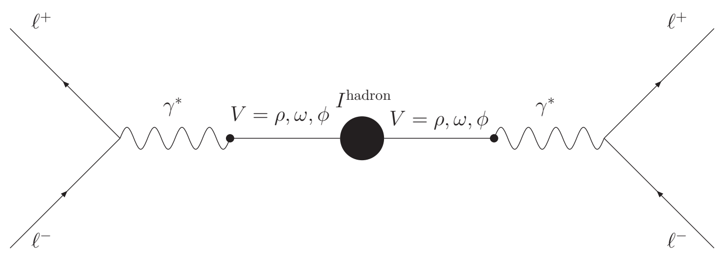

Figure 3.1: The squared matrix element describing dilepton production from the hadronic medium.

the interaction between hadrons and vector mesons. Putting everything together, the thermal dilepton rate from the hadronic medium reads:

$$\begin{aligned}\frac{d^4R^{\ell^+\ell^-}}{d^4q} &= -\sum_{V=\rho,\omega,\phi}\left[1+\frac{2m_\ell^2}{q^2}\right]\left[1-\frac{4m_\ell^2}{q^2}\right]^{1/2}\frac{\alpha^2}{3\pi^3}\frac{m_V^4}{g_V^2}\frac{1}{q^2}\frac{g^{\mu\nu}\mathrm{Im}D^{R,V}_{\mu\nu}(q)}{(e^{\beta_0 q^0}-1)} \\ &= -\sum_{V=\rho,\omega,\phi}\left[1+\frac{2m_\ell^2}{q^2}\right]\left[1-\frac{4m_\ell^2}{q^2}\right]^{1/2}\frac{\alpha^2}{\pi^3}\frac{m_V^4}{g_V^2}\frac{1}{q^2}\frac{\mathrm{Im}D^R_V(q)}{(e^{\beta_0 q^0}-1)},\end{aligned} \tag{3.30}$$

where $\mathrm{Im}D^R_V = \frac{1}{3}g^{\mu\nu}\mathrm{Im}D^{R,V}_{\mu\nu}$, $\frac{1}{q^2}$ comes from the photon propagator, and $\frac{m_V^4}{g_V^2}$ originates from the photon to vector meson conversion vertex. Expanding out $\mathrm{Im}D^R_V$ gives

$$\mathrm{Im}D^R_V = \mathrm{Im}\left[\frac{1}{q^2-m_V^2-\Pi^R_V}\right] \tag{3.31}$$

where Π^R_V is the vector meson self-energy whose Lorentz structure was collapsed via $\Pi \equiv \frac{1}{3}\Pi^\mu_\mu$. To go further, a specific interactions between vector mesons and the medium must be supplied, so that the vector meson self-energy can be computed. To do that, the model first devised in [108] will be used. In that model, the self-energy has two components:

$$\Pi^R_V = \Pi^R_{V,\text{vac}}(M) + \Pi^R_{V,\text{th}}(M = m_V, |\mathbf{q}|, T) \tag{3.32}$$

where $q^2 = M^2$, while $\Pi^{R,V}_{\text{vac}}$ and $\Pi^{R,V}_{\text{th}}$ correspond to the vacuum and thermal contributions, respectively. This decomposition of the self-energy is true in general [104]. Note that unlike other models, which rely on effective hadronic Lagrangians in finite temperature field theory to compute the self-energy of vector mesons (see e.g. [106, 109] and the review [49]) and whose thermal piece of the self-energy Π^R_V has an M-dependence, the thermal contribution of the self-energy in the model [108] is limited to the mass pole $M = m_V$. The advantage of the model [108], as will soon be evident, lies in the fact that the typical values of $|\mathbf{q}|$ can be higher than those accessible to models based on effective hadronic Lagrangians. Though models relying on effective hadronic Lagrangians, such as that in Ref. [49], are not restricted to $M = m_V$, those models are currently not amenable to a dissipative description of the medium. This limitation is not present in the model in Ref. [108], and that model will be used throughout this thesis. Another model of dilepton production that should be mentioned is the Parton Hadron String Dynamics (PHSD) [see [110] for a recent review]. Since the evolution of the medium within PHSD is quite different than dissipative hydrodynamics, this model will not be discussed further.

All elements are now in place to compute the couplings g_V of vector mesons to the photon. Using the Lagrangian [104] describing the electromagnetic decay of vector mesons:

$$\mathcal{L} = \mathcal{L}_{QED} + \mathcal{L}_{VDM} + \mathcal{L}_V \tag{3.33}$$

where $\mathcal{L}_{QED}$, $\mathcal{L}_{VDM}$, and $\mathcal{L}_V$ are defined in Eq. (3.4), Eq. (3.27), and Eq. (3.28), respectively. The coupling constants g_V in $\mathcal{L}_{VDM}$ are easily determined by calculating the diagram in Fig. 3.2.

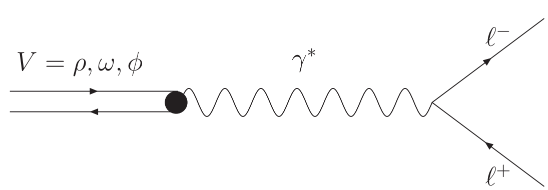

Figure 3.2: Feynman Diagram used in the calculation of the width of a vector meson going into dileptons.

The decay width of a vector meson into dileptons is:

$$\begin{aligned} m_V \Gamma_{V\to l^+l^-} &= -\mathrm{Im}\Pi^R_V(M = m_V) \\ &= \frac{\alpha^2}{3} \frac{m_V^4}{g_V^2/(4\pi)} \frac{1}{m_V^2} \left(1 + \frac{2m_\ell^2}{m_V^2}\right) \left(1 - \frac{4m_\ell^2}{m_V^2}\right)^{1/2}, \end{aligned} \tag{3.34}$$

where $\frac{\alpha^2}{3}\frac{m_V^4}{g_V^2/(4\pi)}$ is the vertex and the rest of the expression gives the invariant mass dependence of $\Gamma_{V\to l^+l^-}$ if the substitution $m_V \to M$ is made. Taking the experimental values of the widths Γ_V, yields: $\frac{g_\rho^2}{4\pi} = 2.54$, $\frac{g_\omega^2}{4\pi} = 20.5$, and $\frac{g_\phi^2}{4\pi} = 11.7$ [111].

3.2.1 Vacuum contribution to vector meson self-energies

To compute the vacuum contribution of the vector meson self-energies, the form of the interaction Lagrangian between vector mesons and their scattering partners is now provided. As their interaction Lagrangian is similar, the ρ and ϕ mesons will be considered first. The most important contribution to the ρ meson[1] self-energy, at zero temperature, comes from its interaction with pions. Indeed, the ρ meson almost exclusively decays into two pions [1]. The ϕ meson on the other hand interacts the most with charged kaons and decays into them about 90% of the time [1]. Furthermore, the interaction of the ρ with pions and the ϕ with kaons proceeds via the same Lagrangian. For the ϕ meson this Lagrangian is:

$$\mathcal{L}_{\phi\to K\bar{K}} = \frac{1}{2}\left|D_\mu K\right|^2 - \frac{1}{2}m_K^2\left|K\right|^2 - \frac{1}{4}F_\phi^{\mu\nu}F_{\mu\nu}^\phi + \frac{1}{2}m_\phi^2\phi^\mu\phi_\mu \tag{3.35}$$

where K in the complex charged kaon field containing both K^+ and K^- or more generically between K and $\bar{K}$, $F_{\mu\nu}^\phi$ is the ϕ field strength and $D_\mu = \partial_\mu - ig_{\phi\to K\bar{K}}\phi_\mu$ is the covariant derivative. It is sufficient to make the following replacements $\phi \to \rho$ and $K \to \pi$ to obtain the interaction Lagrangian between ρ and $\pi^\pm$. To get dilepton production, $\mathcal{L}_{QED}$ and $\mathcal{L}_{VDM}$ must be added to $\mathcal{L}_{\phi\to K\bar{K}}$. A similar statement holds true for the $\mathcal{L}_{\rho\to\pi\bar{\pi}}$.

Furthermore, the ϕ meson also decays into a ρ and π final state with a probability of about 10%.[2] This 3-pion decay channel however has some mixing with the ω meson

[1] Experimentally, there are three ρ mesons: ρ^+, ρ^-, and ρ^0. Throughout this thesis, whenever the ρ meson is mentioned, an implicit reference to ρ^0 should be made. Given its charge, only ρ^0 can couple directly to photons, which is required by VDM.

[2] About 10% if the decays of the ϕ mesons end up in a 3π final state. Clearly separating the 3π final state as a ρ-π final state (recall that the ρ which naturally decays into 2π), and direct 3π final state cannot experimentally be done yet [1]. Indeed, the ρ is such a short lived resonance that reconstructing its peak in a 3-body pion decay is difficult.

as the ω also decays into 3π. This mixing is included via the Wess-Zumino Lagrangian [109]:

$$\mathcal{L}_{(\omega,\phi)\rho\pi} = g_{\phi\to\rho\pi}\varepsilon^{\alpha\beta\mu\nu}\partial_\alpha\rho_\beta\cdot\pi\left(\frac{\partial_\mu\omega_\nu^8+\sqrt{2}\partial_\mu\omega_\nu^s}{\sqrt{3}}\right) \tag{3.36}$$

where

$$\omega^8 = \phi\cos(\theta_V)+\omega\sin(\theta_V) \tag{3.37}$$

$$\omega^s = -\phi\sin(\theta_V)+\omega\cos(\theta_V)\,. \tag{3.38}$$

The Wess-Zumino interaction between the ϕ meson and the ρ and π mesons is illustrated in Fig. 3.3 (a), while interactions involving the ϕ meson and the kaons is in Fig. 3.3 (b). Note that Fig. 3.3 (b) also holds for the ρ and π mesons.

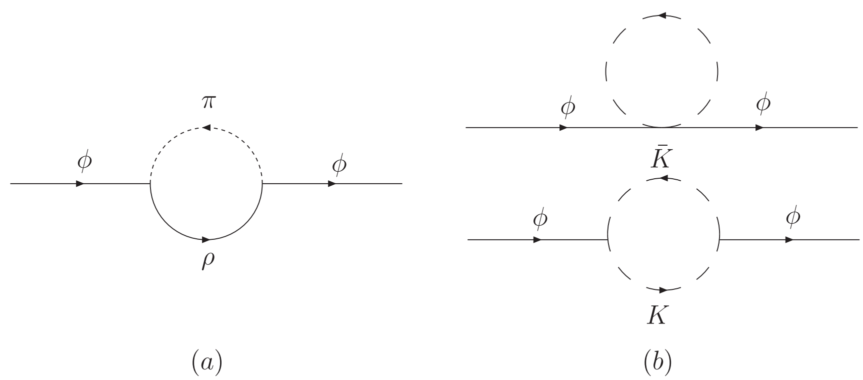

Figure 3.3: The one-loop vacuum self-energy of the ϕ meson.

The self-energy corresponding to $\phi\to K\bar{K}$ is [112]:

$$\begin{aligned}\mathrm{Re}\left[\Pi^{\mathrm{vac}}_{\phi\to K\bar{K}}(M)\right] &= \frac{g^2_{\phi\to K\bar{K}}M^2}{48\pi^2}\left[\left(1-4m_K^2/M^2\right)^{3/2}\ln\left|\frac{1+\sqrt{1-4m_K^2/M^2}}{1-\sqrt{1-4m_K^2/M^2}}\right| + \right.\\ &\left. + 8m_K^2\left(\frac{1}{M^2}-\frac{1}{m_\phi^2}\right)-2\left(\frac{p_0}{\omega_0}\right)^3\ln\left(\frac{p_0+\omega_0}{m_K}\right)\right]\end{aligned} \tag{3.39}$$

$$\mathrm{Im}\left[\Pi^{\mathrm{vac}}_{\phi\to K\bar{K}}(M)\right] = -\frac{g^2_{\phi\to K\bar{K}}M^2}{48\pi}\left(1-4m_K^2/M^2\right)^{3/2}\Theta(M^2-4m_K^2), \tag{3.40}$$

where $2\omega_0 = m_\phi = 2\sqrt{m_K^2+p_0^2}$, $\Theta(M^2-4m_K^2)$ is the Heaviside function, and $g^2_{\phi\to K\bar{K}}/(4\pi) = 1.602$ and 1.682 for charged kaons and neutral kaons, respectively

[112]. For the ρ meson, $g^2_{\rho\to\pi\bar{\pi}}/(4\pi) = 2.86$ for both charged and neutral pions [106]. The Wess-Zumino contribution to the ϕ meson self-energy is:

$$\Pi^{\text{vac}}_{\phi\to\rho\pi}(M) = M^2 \frac{g^2_{\phi\to\rho\pi}}{(4\pi)^2}\left(\sqrt{\frac{1}{3}}\cos(\theta_V) - \sqrt{\frac{2}{3}}\sin(\theta_V)\right)^2 \times$$
$$\times \int_0^1 dx\Delta\left[-\ln(\Delta) + \ln(4\pi) + 1 - \gamma_{\text{E}}\right] + C, \qquad (3.41)$$

where $\Delta = m_\rho^2 - x\left(m_\rho^2 - m_\pi^2\right) - x(1-x)M^2$, and γ_{E} is the Euler-Mascheroni constant. The renormalization constant C is chosen such that $\text{Re}\left[\Pi\left(M^2 = m_\phi^2\right)\right] = 0$. The coupling $g_{\phi\to\rho\pi}$ is determined such that the decay rate $\phi\to\rho\pi$ is reproduced. Indeed, the partial width is [113],

$$\Gamma_{\phi\to\rho\pi} = \frac{1}{16} m_\phi^2 \frac{g^2_{\phi\to\rho\pi}}{4\pi}\left(\sqrt{\frac{1}{3}}\cos(\theta_V) - \sqrt{\frac{2}{3}}\sin(\theta_V)\right)^2 \frac{1}{m_\phi^5}\left[\left(m_\phi^2 - m_\rho^2 - m_\pi^2\right)^2 - 4m_\pi^2 m_\phi^2\right]^{3/2} \qquad (3.42)$$

so that

$$m_\phi^2 \frac{g^2_{\phi\to\rho\pi}}{4\pi}\left(\sqrt{\frac{1}{3}}\cos(\theta_V) - \sqrt{\frac{2}{3}}\sin(\theta_V)\right)^2 = 0.31128 \qquad (3.43)$$

and $\theta_V = 40.1^\circ$, obtained from [114]. Lastly, the ω meson has a 2-loop structure illustrated in Fig. 3.4. Given that the width of the ω is small ($\Gamma_\omega^{vac} = 8.49$ MeV) and

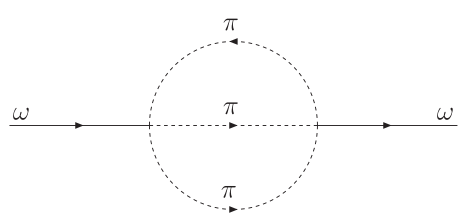

Figure 3.4: The 2-loop vacuum self-energy of the ω meson.

that its evaluation through the loop calculation in is rather involved, a model for the self-energy of the ω is used [108]:

$$\text{Re}\left[\Pi^{\text{vac}}_{\omega\to 3\pi}(M)\right] = 0 \qquad (3.44)$$
$$\text{Im}\left[\Pi^{\text{vac}}_{\omega\to 3\pi}(M)\right] = \begin{cases} \Theta\left(M^2 - 9m_\pi^2\right)\left[\frac{(M^2-9m_\pi^2)}{(m_\omega^2-9m_\pi^2)}\right]^2 \Gamma_\omega^{vac} & M \le m_\omega \\ \Gamma_\omega^{vac} & M \ge m_\omega \end{cases}. \qquad (3.45)$$

3.2.2 Thermal contribution to vector meson self-energies

The finite temperature contribution to vector meson self-energy can either be computed via effective Lagrangians, such as those introduced in the previous section, or through effective models of particle scattering that have proven to be effective in describing experimental observables. The approach used throughout this thesis falls in the latter category [108].

Assuming low-density medium, such that the de Broglie wavelength is less that the inter-particle spacing, it is possible to relate the self-energy of a particle to its forward scattering amplitude. It is precisely this relation that will be used to compute the in-medium self-energy of vector mesons. To do so, start from the dispersion relation for a vector meson V:

$$E_V^2 = m_V^2 + p_V^2 + \Pi_V^R \tag{3.46}$$

The analytic structure of the dispersion relation is determined via the poles[1] of the propagator $\frac{1}{E_V^2 - p_V^2 - m_V^2 - \Pi_V}$. To obtain the pole locations, a sum over all the particle species a interacting with with vector mesons V must be taken into account, that is

$$\Pi_V^R = \sum_a \Pi_{Va}^R. \tag{3.47}$$

In the non-relativistic limit, the dispersion relation in Eq. 3.46 simplifies to [104]:

$$E_V = m_V + \frac{p_V^2}{2m_V} + \sum_a U_{Va}^R, \tag{3.48}$$

where U_{Va} is the optical potential. In general, U_{Va} is a complex potential. Therefore the energy E_V of the vector meson is complex, i.e. $E_V = E_R - i\Gamma_V/2$. Furthermore, in a low density environment, the vector meson width Γ_V is related to the mean free path λ_{Va} between scattering partners V and a via $\Gamma_V = \frac{u_{Va}}{\lambda_{Va}}$, where the relative velocity between V and a is u_{Va}. In addition, the low density approximation allows to relate λ_{Va} to the scattering cross section σ_{Va}: $\lambda_{Va} = \frac{1}{\rho_a \sigma_{Va}}$, where ρ_a is the density of

[1]In general, the analytic structure of the dispersion relation is determined by identifying the location of all its poles and branch cuts. As branch cuts are not relevant for the particular construction of the forward scattering amplitude [108], they will not be considered here.

the scattering partners a. Using the forward scattering amplitude f_{Va} and the optical theorem, $|\mathbf{k}|\sigma_{Va} = 4\pi \ \mathrm{Im}\left[f_{Va}\right]$, yields [104]

$$\mathrm{Im}\left[\Pi^R_{Va}\right] = 2m_V \ \mathrm{Im}\left[U^R_{Va}\right] = -4\pi\rho_a \ \mathrm{Im}\left[f_{Va}\right], \tag{3.49}$$

where $|\mathbf{k}|$ is norm the center of mass 3-momentum of the Va system. The same relation actually holds for the real part of the self-energy as well, as is now shown. The average potential energy of a vector meson V in a thermal bath of particles a,

$$\mathrm{Re}\left[U^R_{Va}\right] = \rho_a \int d^3x V_{Va}(\mathbf{x}) \tag{3.50}$$

where V_{Va} is a two body potential between the vector meson V and its scattering partner a. Using the Born approximation in the low energy limit yields [104]

$$\mathrm{Re}\left[f_{Va}\right] = -\frac{m_V}{2\pi} \int d^3x V_{Va}(\mathbf{x}). \tag{3.51}$$

Thus the relation

$$\Pi^R_{Va} = -4\pi\rho_a f_{Va} \tag{3.52}$$

holds for both the real and the imaginary part of the self-energy. A more careful calculation shows that Eq. (3.52) is in fact the leading term in a multiple-scattering expansion [115], and is therefore a more general result than this derivation suggests. In a relativistic setting Eq. (3.52) reads

$$\begin{aligned}\Pi^R_{Va} &= -4\pi\rho_a f_{Va} \\ &= -4\pi \int \frac{d^3k}{(2\pi)^3\omega} n_a\left(\beta_0\omega\right)\sqrt{s} f^{c.m.}_{Va}(s) \\ &= -4\pi \int \frac{d^3k}{(2\pi)^3\omega} n_a\left(\beta_0\omega\right) m_a f^{\text{a's rest frame}}_{Va}\left(\frac{m_V}{m_a}\omega\right)\end{aligned} \tag{3.53}$$

where $s = (p^\mu + k^\mu)^2$, p^μ is the 4-momentum of V and k^μ is the 4-momentum of a, while $k^0 = \omega$ its energy, and $\beta_0 = T^{-1}$ where T is the temperature of the medium. Note that the relation $\sqrt{s} f^{c.m.}_{Va}(s) = m_a f^{\text{a's rest}}_{Va}\left(\frac{m_V}{m_a}\omega\right)$ [108] was used to go from the second to the third line. To simplify the calculation, and without loss of generality, choose the z-axis such that $p^\mu = (E, 0, 0, |\mathbf{p}|)$. Further, define the angle θ between the z-axis and the momentum $k^\mu = (\omega, \mathbf{k})$. Note that θ is *not* the angle between p^μ and k^μ.

In the rest frame of particle a, it is possible to evaluate the angular part of the self-energy integral. From now on, prime ($'$) is used to denote energy and momentum in V's rest frame and double prime ($''$) is used to label a's rest frame. One can relate the energy in the two frames via:

$$s = m_V^2 + m_a^2 + 2E''m_a = m_V^2 + m_a^2 + 2m_V\omega' \tag{3.54}$$

Hence, $E'' = \frac{m_V}{m_a}\omega'$. Furthermore, in V's rest frame, $\omega = \frac{E\omega' + |\mathbf{p}||\mathbf{k}'|z'}{m_V}$, where $z' = \cos\theta'$. Putting everything together,

$$\begin{aligned} \Pi^R_{Va}(|\mathbf{p}|, T) &= -4\pi \int \frac{|\mathbf{k}'|^2 d|\mathbf{k}'|dz'}{(2\pi)^2\omega'} n_a \left(\frac{E\omega' + |\mathbf{p}||\mathbf{k}'|z'}{Tm_V}\right) m_a f^{\text{a's rest}}_{Va}\left(\frac{m_V}{m_a}\omega'\right) \\ &= -\frac{m_V m_a}{\pi} \int_{m_a}^{\infty} |\mathbf{k}'|d\omega' f^{\text{a's rest}}_{Va}\left(\frac{m_V}{m_a}\omega'\right) \int_{-1}^{1} dz' n_a \left(\frac{E\omega' + |\mathbf{p}||\mathbf{k}'|z'}{m_V T}\right) \\ &= -\frac{m_V m_a T}{\pi|\mathbf{p}|} \int_{m_a}^{\infty} d\omega' \ln\left[\frac{1 \pm \exp\left(-\omega_+/T\right)}{1 \pm \exp\left(-\omega_-/T\right)}\right] f^{\text{a's rest}}_{Va}\left(\frac{m_V}{m_a}\omega'\right) \end{aligned} \tag{3.55}$$

where

$$\omega_\pm = \frac{E\omega' \pm |\mathbf{p}||\mathbf{k}'|}{m_V}. \tag{3.56}$$

To generalize the formula in Eq. (3.55) for a medium with finite baryon chemical potential μ_B, the simple replacement $\omega_\pm \to \omega_\pm - \mu_B$ for nucleons and $\omega_\pm \to \omega_\pm + \mu_B$ for antinucleons is all that is required. This expression for the self-energy is evaluated on the mass shell of the vector meson V. The last piece of the puzzle required to compute the self-energy is a model of the forward scattering amplitude (FSA).

We consider interactions with pions (π), nucleons (N), and antinucleons ($\bar{N}$) as scatterings partners a contributing to vector meson's self-energy. A two-component duality approach due to Harari [116] is used (see also Collins [117]) within which the FSA is composed of two contributions, namely a resonance (R) contribution and a background term. In the center of mass (c.m.) frame, the low energy FSA at fixed Mandelstam variable t reads [108]:

$$f^{c.m.}_{Va}(s) = \frac{1}{2q_{c.m.}} \sum_R W^R_{Va} \frac{\Gamma_{R\to Va}}{M_R - \sqrt{s} - \frac{1}{2}i\Gamma_R} - \frac{q_{c.m.}}{4\pi s} \frac{1 + \exp(-i\pi\alpha_P)}{\sin(\pi\alpha_P)} r^P_{Va} s^{\alpha_P}. \tag{3.57}$$

while the high energy contribution to the FSA at fixed t is given by:

$$f_{Va}^{c.m.}(s) = -\frac{q_{c.m.}}{4\pi s} \sum_{i=P,P'} \left[\frac{1+\exp(-i\pi\alpha_i)}{\sin(\pi\alpha_i)}\right] r_{Va}^{i} s^{\alpha_i}. \tag{3.58}$$

The derivation of the high energy piece $\propto \frac{1+\exp(-i\pi\alpha_P)}{\sin(\pi\alpha_P)} r_{Va}^{P} s^{\alpha_P}$ is given in Appendix A.

Starting the discussion with the simpler high energy form of the FSA, one can see that only two terms are considered to be present [see Eq. (3.58)]. Such a construction of the high energy FSA is motivated previous work done by Donnachie and Landshoff [118] where the authors have used a four parameter parametrization to characterize the total cross section $\sigma(s) = \sum_i r_i s^{\alpha_i - 1}$. Indeed, that study showed that such a parametrization seems to describe cross section data very well. Using the optical theorem, $\sigma_{Va}(s) = \frac{4\pi}{q_{c.m.}} \, \mathrm{Im}\,[f_{Va}^{c.m.}(s)]$, the parametrization given in Eq. (3.58) reduces to the form used by Donnachie and Landshoff.

At high energies, scattering is dominated by contributions from individual quarks, hence the additive quark model is applicable [108]. Using this model, the residues r_i and the intercepts (or pole positions) α_i are $\alpha_P = 1.093$ and $\alpha_{P'} = 0.642$ with $r_P^{VN} = 11.88$ and $r_{P'}^{VN} = 28.59$ [108]. Furthermore, for the $V\pi$ decays, the residues are $r_P^{V\pi} = 7.508$ and $r_{P'}^{V\pi} = 12.74$ [108]. The intercepts α_i are universal quantities. The parameters obtained here are also used in Eq. (3.57).

In order to have a complete description of the FSA, one matches its low and high energy parts. This matching is done via a single half-sided Gaussian function $g(E_V)$, for both the real and imaginary parts:

$$g(E_V) = \begin{cases} \exp\left[\frac{(E_V - b)}{\sigma}\right] & E_V \geq b \\ 1 & E_V \leq b \end{cases} \tag{3.59}$$

where b and σ are free parameters. The matched function takes the form:

$$f_{Va}^{total}(E_V) = g(E_V)\, f_{Va}^{low}(E_V) + (1 - g(E_V))\, f_{Va}^{high}(E_V). \tag{3.60}$$

where $f_{Va}^{low}(E_V)$ and $f_{Va}^{high}(E_V)$ are the FSAs of Eq.(3.57) and Eq.(3.58), respectively, written in the rest frame of the heat bath.

To verify that the matching introduces minimal violations to the Kramers-Kronig relations, a dispersion integral relating the real part of the total FSA to a principal value integral over its imaginary part [108] is used:

$$\mathrm{Re}\left[f_{Va}^{total}\left(E_V\right)\right] = \mathrm{Re}\left[f_{Va}^{total}\left(0\right)\right] + \frac{2E_V^2}{\pi}\mathrm{P.V.}\int_{m_V}^{\infty}\frac{\mathrm{Im}\left[f_{Va}^{total}\left(E'\right)\right]dE'}{E'\left(E'+E_V\right)\left(E'-E_V\right)}. \quad (3.61)$$

The free parameters b and σ of the Gaussian are chosen such that the subtraction of the real part of f^{total} obtained via Gaussian matching and the real part obtained via the dispersion relation is as close as possible to $\mathrm{Re}\left[f_{Va}(0)\right]$. The low-energy and the high-energy pieces are best matched onto one another at $E_V - m_V \sim 4$ GeV for pions and $E_V - m_V \sim 1$ GeV for nucleons, where E_V is in the rest frame of pions and nucleons, respectively.

Now that the high energy tail of the FSA is explained, the understanding of the low energy piece needs to be completed. The sum in Eq. (3.57) ranges over all Breit-Wigner resonances that decay into a vector meson V and the particle a, nucleon or a pion. The Breit-Wigner term is derived in several undergraduate textbooks on quantum mechanics (see e.g. [93]), and it will not be derived here. The mass of the resonance R in the Breit-Wigner distribution is $\mathrm{M_R}$ and its total width is Γ_R. s is the usual Mandelstam variable and the magnitude of the c.m. momentum is given by:

$$q_{c.m.} = \frac{1}{2}\frac{\sqrt{\left[s-\left(m_V+m_a\right)^2\right]\left[s-\left(m_V-m_a\right)^2\right]}}{\sqrt{s}} \quad (3.62)$$

where $m_a = m_N, m_\pi$ with $m_N = \frac{(m_p+m_n)}{2}$ and $m_\pi = \frac{m_{\pi^0}+2m_{\pi^\pm}}{3}$. The statistical spin/isospin averaging factor is:

$$W_{Va}^{R} = \frac{(2s_R+1)}{(2s_V+1)(2s_a+1)}\frac{(2t_R+1)}{(2t_V+1)(2t_a+1)} \quad (3.63)$$

where s_i (with i generic) is the spin of particle i and t_i is the isospin of that particle. Averaging over spin and isospin has two implications: i) there is no distinction between longitudinal and transverse spin directions, and ii) all charged states of particle a are equally populated.

The computation of the partial widths $\Gamma_{R\to Va}$ in Eq. (3.57) is not particularly enlightening, so the details will not be presented here as they were already discussed in depth in Refs. [108, 119, 112]. These references also include the list of particles contributing to the FSA of vector mesons in a thermal bath of pions, nucleons, and antinucleons.

In summary, to compute the dilepton production from the hadronic medium, one first reconstructs the FSA. Once the FSA is at hand, the thermal self-energy is obtained via Eq. (3.55), which can then be combined with the vacuum self-energy presented in Section 3.2.1. Lastly, the total self-energy can be inserted into the dilepton rate Eq. (3.30). Note that this approach, combined with a simple fireball model, was used to successfully interpret NA60 dimuon data from the Super Proton Synchrotron at CERN [120].

3.3 Dilepton production from the Quark Gluon Plasma

An important source of dileptons comes from the quark antiquark annihilation process $q\bar{q} \to \gamma^* \to \ell^+\ell^-$. In fact, at high q^2 this is the most important source. Since this is a $2 \to 2$ scattering that is leading order in electromagnetic coupling α_{EM} and zeroth order in strong coupling α_s, it is truly a perturbative process.[1] Such a process can be computed within finite temperature quantum field theory or within kinetic theory, and both approaches give the same result (at leading order in α_{EM} and zeroth order in α_s). It is simplest to compute the rate within kinetic theory approximation. The dilepton rate is given by

$$\frac{d^4R^{\ell^+\ell^-}}{d^4q} = \int \frac{d^3p_1}{(2\pi)^3}\frac{d^3p_2}{(2\pi)^3} n_{FD}\left(p_1^0\right) n_{FD}\left(p_2^0\right) v_{12}\sigma\delta^4(q-p_1-p_2) \tag{3.64}$$

where $v_{12} = \frac{q^2/2}{E_1E_2}$, $n_{FD}(p^0) = \frac{1}{e^{\beta_0 p^0}+1}$, while

$$\sigma = \int d\phi d\left(\cos\theta\right)\frac{1}{2q^2}\frac{|\mathbf{p_3}|}{(2\pi)^2 4q^0}\left|\bar{\mathcal{M}}\right|^2. \tag{3.65}$$

[1] In the context of heavy-ion collisions higher order corrections are proportional to α_s. However, typical temperatures reached at RHIC/LHC are $T \sim \mathcal{O}(0.1\text{ GeV})$, imply that $\alpha_s \sim 0.3 \Rightarrow g_s \sim 2$, and therefore perturbation theory breaks down. However, the shape of the α_s corrected dilepton rate is in good qualitative agreement with ℓQCD calculations of dilepton radiation, even for $\alpha_s \sim 0.3$ [6, 7].

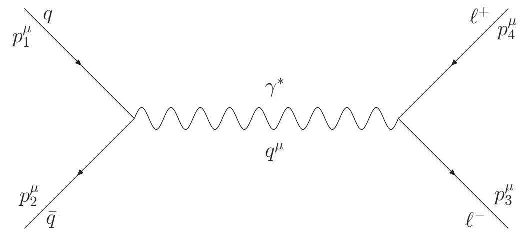

Figure 3.5: Feynman diagram used in the calculation of dilepton rate from the QGP. Note that $q^\mu = p_1^\mu + p_2^\mu = p_3^\mu + p_4^\mu$.

The transition probability $\left|\bar{\mathcal{M}}\right|^2$ for $q\bar{q} \to \ell^+\ell^-$ can be calculated in within quantum field theory [10] and is averaged over the initial states spins and colors and summed over the final states spins. In the approximation of massless quarks, it is given by

$$\begin{aligned}\left|\bar{\mathcal{M}}\right|^2 &= \sum_{c=r,g,b} \sum_{q=u,d,s} \frac{1}{4} \sum_{s,s',r,r'} \frac{e_q^2 e^4}{q^4} \left\{\left[\bar{v}_s^{c,q}(p_2)\gamma^\mu u_{s'}^{c,q}(p_1)\right]\left[\bar{u}_r^q(p_3)\gamma_\mu v_{r'}^q(p_4)\right]\right\} \times \{\text{h.c.}\} \\ &= N_c \left[\sum_{q=u,d,s} e_q^2\right] \frac{8e^4}{q^4} \left[(p_1 \cdot p_4)(p_2 \cdot p_3) + (p_1 \cdot p_3)(p_2 \cdot p_4) + m_\ell^2 (p_1 \cdot p_2)\right]\end{aligned} \tag{3.66}$$

where {h.c.} stands for the hermitian conjugate, $N_c = 3$ is the total number of colors, and e_q is the charge of a quark and p_1^μ through p_4^μ are defined in Fig. 3.6. Using energy and momentum conservation, one can label $p_1^\mu = (E, 0, 0, E)$, $p_2^\mu = (E, 0, 0, -E)$, $p_3^\mu = (E, 0, \mathbf{k})$, $p_4^\mu = (E, 0, -\mathbf{k})$, and $|\mathbf{k}| = \sqrt{E^2 - m_\ell^2}$, such that:

$$|\mathcal{M}|^2 = N_c \left[\sum_{q=u,d,s} e_q^2\right] \frac{8e^4}{q^4} E^2 \left[2E^2 + 2\left(E^2 - m_\ell^2\right)\cos\theta + 2m_\ell^2\right], \tag{3.67}$$

and θ is defined in Fig. 3.6.

Hence, inserting Eq. (3.67) in Eq. (3.65) yields

$$\sigma = N_c \left[\sum_{q=u,d,s} e_q^2\right] \frac{4\pi}{3} \frac{\alpha_{EM}^2}{q^2} \left[1 + \frac{2m_\ell^2}{q^2}\right] \left[1 - \frac{4m_\ell^2}{q^2}\right]^{1/2}. \tag{3.68}$$

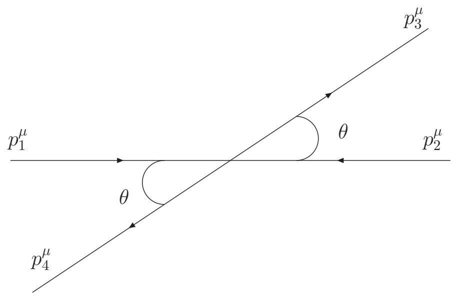

Figure 3.6: The angle θ in $2 \to 2$ scattering. The center of mass frame of the colliding quarks is depicted.

Finally, inserting Eq. (3.68) in Eq. (3.64) yields

$$\begin{aligned}\frac{d^4R^{\ell^+\ell^-}}{d^4q} &= N_c\left[\sum_{q=u,d,s} e_q^2\right]\frac{\alpha_{EM}^2}{12\pi^4}\left[1+\frac{2m_\ell^2}{q^2}\right]\left[1-\frac{4m_\ell^2}{q^2}\right]^{1/2}\frac{1}{e^{\beta_0 q^0}-1}\left\{1-\frac{2}{\beta_0|\mathbf{q}|}\ln\left[\frac{n_-}{n_+}\right]\right\}\\ &= \frac{\alpha_{EM}^2}{6\pi^4}\left[1+\frac{2m_\ell^2}{q^2}\right]\left[1-\frac{4m_\ell^2}{q^2}\right]^{1/2}\frac{1}{e^{\beta_0 q^0}-1}\left\{1-\frac{2}{\beta_0|\mathbf{q}|}\ln\left[\frac{1+e^{-\frac{\beta_0\left(q^0-|\mathbf{q}|\right)}{2}}}{1+e^{-\frac{\beta_0\left(q^0+|\mathbf{q}|\right)}{2}}}\right]\right\}.\end{aligned} \tag{3.69}$$

For a medium at finite chemical potential μ_B, the Born QGP rates read:

$$\begin{aligned}\frac{d^4R^{\ell^+\ell^-}}{d^4q} &= \int\frac{d^3p_1}{(2\pi)^3}\frac{d^3p_2}{(2\pi)^3}n_{FD}\left(p_1^0-\mu_B/3\right)n_{FD}\left(p_2^0+\mu_B/3\right)v_{12}\sigma\delta^4(q-p_1-p_2)\\ &= \frac{\alpha_{EM}^2}{6\pi^4}\left[1+\frac{2m_\ell^2}{q^2}\right]\left[1-\frac{4m_\ell^2}{q^2}\right]^{1/2}\frac{1}{e^{\beta_0 q^0}-1}\times\\ &\times\left\{1-\frac{1}{\beta_0|\mathbf{q}|}\ln\left[\frac{1+e^{-\frac{\beta_0\left(q^0-|\mathbf{q}|+\mu_B/3\right)}{2}}}{1+e^{-\frac{\beta_0\left(q^0+|\mathbf{q}|+\mu_B/3\right)}{2}}}\right]-\frac{1}{\beta_0|\mathbf{q}|}\ln\left[\frac{1+e^{-\frac{\beta_0\left(q^0-|\mathbf{q}|-\mu_B/3\right)}{2}}}{1+e^{-\frac{\beta_0\left(q^0+|\mathbf{q}|-\mu_B/3\right)}{2}}}\right]\right\}.\end{aligned} \tag{3.70}$$

The effects of including higher order $\mathcal{O}(\alpha_s)$ corrections to the Born rates, which will modify the dilepton rate/yield in the low invariant mass sector while leaving the high invariant mass sector more or less unaffected[1], will be considered in section 4.4.

[1] Indeed, there will be small corrections of $\mathcal{O}(\alpha_s)$ as the result of Ref. [6] needs to converge to the Operator Product Expansion result of Ref. [121], which depends of α_s (see section 4.4 for a more details).

3.4 Dissipative corrections to dilepton production

Since dilepton production is occurring in a dissipative medium, it is important to include dissipative corrections to the Bose-Einstein/Fermi-Dirac distribution functions present in the thermal dilepton rates. The following sections will discuss in some detail the various corrections involved. Before exploring these effects, it is important to note that in perturbative calculations, the Kubo-Martin-Schwinger relation was recently found not to be modified by the presence of dissipative effects [122].

3.4.1 Viscous correction to QGP rate

The ansatz for the form of the viscous correction that is utilized here for the QGP was previously explored in Ref. [123] and also in Ref. [5]. This ansatz originates from the continuity requirement between the macroscopic degrees of freedom being used in describing the fluid, i.e. through its the stress-energy tensor (assuming no conserved currents are present), and its microscopic degrees of freedom relying on the distribution function of the constituent particles of the fluid. In the particular case discussed here, the stress-energy tensor from the hydrodynamical simulation is matched to its kinetic theory description. That is,

$$T_0^{\mu\nu} + \pi^{\mu\nu} = \int \frac{d^3p}{(2\pi)^3 p^0} p^\mu p^\nu \left[n(p\cdot u) + \delta n(p\cdot u) \right]. \tag{3.71}$$

Requiring that the stress-energy tensor is equally well described using microscopic or macroscopic degrees of freedom during the entire hydrodynamical simulation implies that the viscous correction δn to the equilibrium distribution function must be present in dilepton production rates. The following extension, known as the 14-moment (or Israel-Stewart) approximation within kinetic theory [69], to the thermal distribution is used:

$$\begin{aligned} n_{\text{total}}(p\cdot u) &= n(p\cdot u) + \delta n(p\cdot u) \\ &= n(p\cdot u) + \frac{C}{2T^2(\varepsilon+P)} n(p\cdot u)\left[1 \pm n(p\cdot u)\right] p^\alpha p^\beta \pi_{\alpha\beta} \\ &= n(p\cdot u) + \frac{C}{2} n(p\cdot u)\left[1 \pm n(p\cdot u)\right] \frac{p^\alpha}{T}\frac{p^\beta}{T}\frac{\pi_{\alpha\beta}}{\varepsilon+P} \end{aligned} \tag{3.72}$$

where p^α is the 4-momentum of one of the incoming partons. Recall that the same off-equilibrium extension to the distribution function was used in Section 2.3.2. Substituting Eq. (3.72) into Eq. (3.71) yields

$$\pi^{\mu\nu} = \left[\frac{C}{2}\int \frac{d^3p}{(2\pi)^3 p^0} n(p\cdot u)\left[1 \pm n(p\cdot u)\right] p^\mu p^\nu \frac{p^\alpha}{T}\frac{p^\beta}{T}\right] \frac{\pi_{\alpha\beta}}{\varepsilon + P}, \tag{3.73}$$

where C is a proportionality constant that relates the hydrodynamical shear-stress tensor to its kinetic theory counterpart. In the context of a single component thermal ensemble, C can be determined via [124]:

$$\eta = \frac{C}{15T^3}\int \frac{d^3p}{(2\pi)^3 p^0} n(p\cdot u)\left[1 \pm n(p\cdot u)\right]\left[p^2 - (u\cdot p)^2\right]^2. \tag{3.74}$$

One can solve for C in Eq. (3.74) by expressing T^3 in terms of entropy density:

$$s = \frac{4}{3}\frac{\varepsilon}{T} \text{ where} \tag{3.75}$$

$$\varepsilon = \frac{T^4 g}{2\pi^2}\int_y^\infty \frac{x^3\sqrt{1-(y/x)^2}dx}{e^x \mp 1}, \tag{3.76}$$

with ε is the average energy density of a Fermi or Bose gas with distribution n, $x = (p\cdot u)/T$, $y = \sqrt{p^2}/T$, g is the spin degeneracy factor, and p^2 is the 4-momentum squared. Finally solving for C is simplest in the rest frame of the fluid.

$$\begin{aligned} C &= \frac{4\tilde{a}}{3\tilde{b}} \\ \tilde{a} &= \frac{1}{2\pi^2}\int_y^\infty dx \frac{x^3\sqrt{1-(y/x)^2}}{e^x \mp 1} \\ \tilde{b} &= \frac{1}{30\pi^2}\int_y^\infty dx \frac{x^5\left[1-(y/x)^2\right]^{5/2}}{e^x \mp 1}\left\{1 \pm \frac{1}{e^x \mp 1}\right\} \end{aligned} \tag{3.77}$$

For the specific case of the QGP, in the approximation of a single component fluid of massless quarks, C can be evaluated analytically and is $C_q = \frac{7\pi^4}{675\zeta(5)} \approx 0.97$.

The modification of the distribution functions owing to viscosity have a non-trivial effect on the viscous rates of QGP dileptons. Since the same viscous corrections to the thermal distribution function will be included on the hadronic dilepton rates, it is instructive to carefully explore the manner in which the simpler Born QGP rates get modified. The same procedure will be used for the dileptons from the hadronic medium (HM).

In the massless quark limit,

$$\frac{d^4R}{d^4q} = \int \frac{d^3p_1 d^3p_2}{(2\pi)^6 p_1^0 p_2^0} n(p_1\cdot u)n(p_2\cdot u)\frac{q^2}{2}\sigma\delta^4(q-p_1-p_2) \tag{3.78}$$
$$+ \int \frac{d^3p_1 d^3p_2}{(2\pi)^6 p_1^0 p_2^0} n(p_1\cdot u)n(p_2\cdot u)\left[1-n(p_1\cdot u)\right]\frac{q^2}{2}\sigma\delta^4(q-p_1-p_2)C_q\frac{p_1^\alpha}{T}\frac{p_1^\beta}{T}\frac{\pi_{\alpha\beta}}{\varepsilon+P}$$
$$\frac{d^4R}{d^4q} = \frac{d^4R_0}{d^4q} + \frac{d^4\delta R}{d^4q}$$
$$\frac{d^4R}{d^4q} = \frac{d^4R_0}{d^4q} + C_q\frac{J^{\alpha\beta}}{T^2}\frac{\pi_{\alpha\beta}}{\varepsilon+P} \tag{3.79}$$

where the rate was decomposed into its ideal and viscous contribution ignoring all viscous corrections of order $(\delta n)^2$. Performing this integral is non-trivial. However, the tensor $J^{\alpha\beta}$ of viscous correction to the rate must solely depend on the momentum of the virtual photon q^α, the flow u^α, and the metric $g^{\alpha\beta}$. Hence,

$$J^{\alpha\beta} = b_0 g^{\alpha\beta} + b_1 u^\alpha u^\beta + b_2 q^\alpha q^\beta + b_3(u^\alpha q^\beta + u^\beta q^\alpha) + b_4(u^\alpha q^\beta - u^\beta q^\alpha) \tag{3.80}$$

This is the most general form of $J^{\alpha\beta}$. However, since $J^{\alpha\beta}$ is contracted with $\pi^{\alpha\beta}$ — which must be a symmetric tensor (as it is part of $T^{\alpha\beta}$); any anti-symmetric piece of $J^{\alpha\beta}$ must not contribute to this calculation. This is shown below. The coefficients b_0 through b_4 are obtained as

$$\begin{bmatrix} g^{\alpha\beta}J_{\alpha\beta} \\ u^\alpha u^\beta J_{\alpha\beta} \\ q^\alpha q^\beta J_{\alpha\beta} \\ (u^\alpha q^\beta + u^\beta q^\alpha)J_{\alpha\beta} \\ (u^\alpha q^\beta - u^\beta q^\alpha)J_{\alpha\beta} \end{bmatrix} = \begin{bmatrix} 4 & 1 & q^2 & 2(u\cdot q) & 0 \\ 1 & 1 & (u\cdot q)^2 & 2(u\cdot q) & 0 \\ q^2 & (u\cdot q)^2 & q^4 & 2q^2(u\cdot q) & 0 \\ 2(u\cdot q) & 2(u\cdot q) & 2q^2(u\cdot q) & 2(q^2+(u\cdot q)^2) & 0 \\ 0 & 0 & 0 & 0 & 2q^2 \end{bmatrix} \begin{bmatrix} b_0 \\ b_1 \\ b_2 \\ b_3 \\ b_4 \end{bmatrix} \tag{3.81}$$

whose solution is

$$\begin{bmatrix} b_0 \\ b_1 \\ b_2 \\ b_3 \\ b_4 \end{bmatrix} = \begin{bmatrix} \frac{1}{2} & -\frac{1}{2}\frac{q^2}{q^2-(u\cdot q)^2} & -\frac{1}{2}\frac{1}{q^2-(u\cdot q)^2} & \frac{1}{2}\frac{u\cdot q}{q^2-(u\cdot q)^2} & 0 \\ -\frac{1}{2}\frac{q^2}{q^2-(u\cdot q)^2} & \frac{3}{2}\left[\frac{q^2}{q^2-(u\cdot q)^2}\right]^2 & \frac{1}{2}\frac{q^2+2(u\cdot q)^2}{[q^2-(u\cdot q)^2]^2} & -\frac{3}{2}\frac{q^2(u\cdot q)}{[q^2-(u\cdot q)^2]^2} & 0 \\ -\frac{1}{2}\frac{1}{q^2-(u\cdot q)^2} & \frac{1}{2}\frac{q^2+2(u\cdot q)^2}{[q^2-(u\cdot q)^2]^2} & \frac{3}{2}\frac{1}{[q^2-(u\cdot q)^2]^2} & -\frac{3}{2}\frac{u\cdot q}{[q^2-(u\cdot q)^2]^2} & 0 \\ \frac{1}{2}\frac{u\cdot q}{q^2-(u\cdot q)^2} & -\frac{3}{2}\frac{q^2(u\cdot q)}{[q^2-(u\cdot q)^2]^2} & -\frac{3}{2}\frac{(u\cdot q)}{[q^2-(u\cdot q)^2]^2} & \frac{1}{2}\frac{q^2+2(u\cdot q)^2}{[q^2-(u\cdot q)^2]^2} & 0 \\ 0 & 0 & 0 & 0 & \frac{1}{2q^2} \end{bmatrix} \begin{bmatrix} g^{\alpha\beta}J_{\alpha\beta} \\ u^\alpha u^\beta J_{\alpha\beta} \\ q^\alpha q^\beta J_{\alpha\beta} \\ (u^\alpha q^\beta + u^\beta q^\alpha)J_{\alpha\beta} \\ (u^\alpha q^\beta - u^\beta q^\alpha)J_{\alpha\beta} \end{bmatrix}$$

A simplification of the second rank tensor $J^{\alpha\beta}$ is made possible by using the identities $u^\alpha \pi_{\alpha\beta} = g^{\alpha\beta}\pi_{\alpha\beta} = 0$. Indeed, $J^{\alpha\beta}$ is only proportional to $q^\alpha q^\beta$ and the proportionality constant b_2 is obtained via the projection operator

$$\begin{aligned} P_{\alpha\beta} = & \frac{1}{2}\frac{g_{\alpha\beta}}{(u\cdot q)^2 - q^2} + \frac{1}{2}\left[\frac{q^2 + 2(u\cdot q)^2}{[q^2 - (u\cdot q)^2]^2}\right] u_\alpha u_\beta + \frac{3}{2}\frac{q_\alpha q_\beta}{[q^2 - (u\cdot q)^2]^2} \\ & - \frac{3}{2}\left[\frac{u\cdot q}{[q^2 - (u\cdot q)^2]^2}\right](u_\alpha q_\beta + u_\beta q_\alpha) \end{aligned} \tag{3.82}$$

Since $P_{\alpha\beta}J^{\alpha\beta}$ is a Lorentz invariant quantity, it can be computed in any frame. The most efficient way to compute it is in the rest frame of the fluid cell. Performing that computation yields:

$$\begin{aligned} b_2 = P_{\alpha\beta}J^{\alpha\beta} &= \frac{1}{2|\mathbf{q}|^5}\int_{E_-}^{E_+}\frac{dE_1}{(2\pi)^5}\frac{q^2}{2}\sigma n(E_1)n(q^0 - E_1)(1 - n(E_1))D \\ D &= \left[(3q_0^2 - |\mathbf{q}|^2)E_1^2 - 3q^0 E_1 q^2 + \frac{3}{4}q^4\right] \end{aligned} \tag{3.83}$$

where $E_\pm = \frac{q^0 \pm |\mathbf{q}|}{2}$. Finally, the Born Rate with viscous corrections reads:

$$\begin{aligned} \frac{d^4R}{d^4q} &= \frac{d^4R_0}{d^4q} + \frac{d^4\delta R}{d^4q} \\ \frac{d^4R}{d^4q} &= \frac{q^2}{2}\frac{\sigma}{(2\pi)^5}\left[\frac{1}{e^{q^0/T} - 1}\left\{1 - \frac{2T}{|\mathbf{q}|}\ln\left[\frac{1 + e^{-\frac{\left(q^0 - |\mathbf{q}|\right)}{2T}}}{1 + e^{-\frac{\left(q^0 + |\mathbf{q}|\right)}{2T}}}\right]\right\}\right. \\ &\left. + C_q \frac{q^\alpha}{T}\frac{q^\beta}{T}\frac{\pi_{\alpha\beta}}{\varepsilon + P}\frac{1}{2|\mathbf{q}|^5}\int_{E_-}^{E_+} dE_1 n(E_1)n(q^0 - E_1)(1 - n(E_1))D\right] \end{aligned} \tag{3.84}$$

3.4.2 *The vector meson self-energy and its viscous correction*

Using the tools of the previous section (see also Ref. [5]) the goal of this section is to derive the viscous correction to the self-energy by including the δn correction to the thermal distribution function. Unlike the Bose-Einstein distribution function present in the rates [see Eq. (3.26)] — which originates from the KMS relation given in Eq. (3.22) and therefore is not related to the thermal distribution function of vector mesons – the distribution function present in the self-energy Eq. (3.53) is indeed a distribution function of thermal particles. So the viscous correction to the thermal distribution [see Eq. (3.72)] can be applied to Eq. (3.55). Thus,

$$\delta\Pi^{\mathrm{T}}_{Va}(|\mathbf{p}|, T) = -4\pi\int\frac{d^3k}{(2\pi)^3\omega}\delta n_a(k\cdot u)\sqrt{s}f^{\mathrm{c.m.}}_{Va}(s) = C_a\frac{K^{\alpha\beta}}{T^2}\frac{\pi_{\alpha\beta}}{\varepsilon + P}. \tag{3.85}$$

Note that C_a cannot be computed via Eq. (3.77), since $\delta\Pi^T_{Va}$ is describing a multi-component mixture. Hence, a simplifying assumption is made: $\forall a: C_a = 1$. Expanding the tensor $K^{\mu\nu}$ in the same manner as the QGP $J^{\mu\nu}$ tensor encountered earlier yields:

$$K^{\mu\nu} = B_0 g^{\alpha\beta} + B_1 u^\alpha u^\beta + B_2 p^\alpha p^\beta + B_3(u^\alpha p^\beta + u^\beta p^\alpha) + B_4(u^\alpha p^\beta - u^\beta p^\alpha). \tag{3.86}$$

Since the relation $u^\alpha \pi_{\alpha\beta} = g^{\alpha\beta}\pi_{\alpha\beta} = 0$ still holds, the same projection operator as in Eq. (3.82) can be used to determine B_2. Thus,

$$\begin{aligned}
B_{2,Va} &= P_{\alpha\beta}K^{\alpha\beta} \\
&= -4\pi \int \frac{d^3k}{(2\pi)^3} n_a(u\cdot k)(1 \pm n_a(u\cdot k))\frac{\sqrt{s}}{\omega} f_{Va}(s) \times \\
\times &\left[\frac{1}{2}\frac{m_a^2}{(u\cdot p)^2 - p^2} + \frac{1}{2}\left[\frac{p^2 + 2(u\cdot p)^2}{[p^2 - (u\cdot p)^2]^2}\right](u\cdot k)^2 + \frac{3}{2}\frac{(p\cdot k)^2}{[p^2 - (u\cdot p)^2]^2} - 3\frac{(u\cdot p)(u\cdot k)(p\cdot k)}{[p^2 - (u\cdot p)^2]^2}\right].
\end{aligned} \tag{3.87}$$

Using the convention that the upper (lower) sign refers to Bosons (Fermions), in the rest frame of the medium (and using $z = \cos\theta$) yields:

$$\begin{aligned}
B_{2,Va} &= -4\pi \int \frac{d^3k}{(2\pi)^3\omega} n_a(1 \pm n_a)\sqrt{s} f_{Va}\left[\frac{m_a^2}{2|\mathbf{p}|^2} + \left(\frac{3E^2}{2|\mathbf{p}|^4} - \frac{1}{2|\mathbf{p}|^2}\right)\omega^2 \right. \\
&\quad \left. + \frac{3}{2}\frac{(E\omega - |\mathbf{p}||\mathbf{k}|z)^2}{|\mathbf{p}|^4} - \frac{3E\omega(E\omega - |\mathbf{p}||\mathbf{k}|z)}{|\mathbf{p}|^4}\right] \\
&= -4\pi \int \frac{d^3k}{(2\pi)^3\omega} n_a(1 \pm n_a)\sqrt{s} f_{Va}\left[\frac{m_a^2}{2|\mathbf{p}|^2} + \frac{3|\mathbf{k}|^2 z^2 - \omega^2}{2|\mathbf{p}|^2}\right].
\end{aligned} \tag{3.88}$$

Evaluating the integral in the rest frame of a results in:

$$
\begin{aligned}
B_{2,Va} &= -4\pi m_a \int \frac{d^3k'}{(2\pi)^3\omega'} n_a\left(\frac{E\omega' + |\mathbf{p}||\mathbf{k}'|z'}{m_V}\right)\left[1 \pm n_a\left(\frac{E\omega' + |\mathbf{p}||\mathbf{k}'|z'}{m_V}\right)\right] \times \\
&\times f_{Va}^{\mathrm{a's\ rest}}\left(\frac{m_V}{m_a}\omega'\right)\left[\frac{m_a^2}{2|\mathbf{p}|^2} + \frac{3\left(\frac{E|\mathbf{k}'|z' + |\mathbf{p}|\omega'}{m_V}\right)^2 - \left(\frac{E\omega' + |\mathbf{p}||\mathbf{k}'|z'}{m_V}\right)}{2|\mathbf{p}|^2}\right] \\
&= -\frac{m_a}{2\pi|\mathbf{p}|^2}\int_{m_a}^{\infty} d\omega'|\mathbf{k}'| f_{Va}^{\mathrm{a's\ rest}}\left(\frac{m_V}{m_a}\omega'\right) \times \\
&\times \int_{-1}^{1} dz' n_b\left(\frac{E\omega' + |\mathbf{p}||\mathbf{k}'|z'}{m_V}\right)\left[1 \pm n_a\left(\frac{E\omega' + |\mathbf{p}||\mathbf{k}'|z'}{m_V}\right)\right] \times \\
&\times \left[m_a^2 + (3|\mathbf{p}|^2 - E^2)\frac{\omega'^2}{m_V^2} + 4E|\mathbf{p}|\frac{\omega'|\mathbf{k}'|}{m_V^2}z' + (3E^2 - |\mathbf{p}|^2)\frac{|\mathbf{k}'|^2}{m_V^2}z'^2\right], \qquad (3.89)
\end{aligned}
$$

where $|\mathbf{k}|z = \frac{E}{m_V}|\mathbf{k}'|z' + \frac{|\mathbf{p}|}{m_V}\omega'$. Performing the angular integral yields:

$$
B_{2,Va} = -\frac{m_a}{2\pi|\mathbf{p}|^2}\int_{m_a}^{\infty} d\omega'|\mathbf{k}'| f_{Va}^{\mathrm{a's\ rest}}\left(\frac{m_V}{m_a}\omega'\right) \times (\mathcal{A} + \mathcal{B} + \mathcal{C} + \mathcal{D} + \mathcal{E}), \qquad (3.90)
$$

where

$$
\begin{aligned}
\mathcal{A} &= \left(\frac{m_V T}{|\mathbf{p}||\mathbf{k}'|}\right)\left[m_a^2 + \frac{(E|\mathbf{k}'| - |\mathbf{p}|\omega)^2 - (E\omega' - |\mathbf{p}||\mathbf{k}'|)^2}{m_V^2}\right][\exp(\omega_-/T) \mp 1]^{-1} \\
\mathcal{B} &= -\left(\frac{m_V T}{|\mathbf{p}||\mathbf{k}'|}\right)\left[m_a^2 + \frac{(E|\mathbf{k}'| + |\mathbf{p}|\omega)^2 - (E\omega' + |\mathbf{p}||\mathbf{k}'|)^2}{m_V^2}\right][\exp(\omega_+/T) \mp 1]^{-1} \\
\mathcal{C} &= \pm 2\left(\frac{m_V T}{|\mathbf{p}||\mathbf{k}'|}\right)^2\left[(3E^2 - |\mathbf{p}|^2)\frac{|\mathbf{k}'|^2}{m_V^2} + 2\frac{E\omega'|\mathbf{p}||\mathbf{k}'|}{m_V^2}\right]\ln\left[1 \mp \exp(-\omega_+/T)\right] \\
\mathcal{D} &= \pm 2\left(\frac{m_V T}{|\mathbf{p}||\mathbf{k}'|}\right)^2\left[(3E^2 - |\mathbf{p}|^2)\frac{|\mathbf{k}'|^2}{m_V^2} - 2\frac{E\omega'|\mathbf{p}||\mathbf{k}'|}{m_V^2}\right]\ln\left[1 \mp \exp(-\omega_-/T)\right] \\
\mathcal{E} &= \mp 2\left(\frac{m_V T}{|\mathbf{p}||\mathbf{k}'|}\right)^3\left[(3E^2 - |\mathbf{p}|^2)\frac{|\mathbf{k}'|^2}{m_V^2}\right]\left\{\mathrm{Li}_2\left[\pm\exp(-\omega_+/T)\right] - \mathrm{Li}_2\left[\pm\exp(-\omega_-/T)\right]\right\},
\end{aligned}
\qquad (3.91)
$$

and Li_2 is the dilogarithm function, while $\omega_\pm$ is defined in Eq. (3.56). Thus, the total self-energy is

$$
\begin{aligned}
\Pi_V^{\mathrm{tot}}(M, |\mathbf{p}|, T) &= \Pi_V^{\mathrm{vac}}(M) + \qquad (3.92) \\
&+ \sum_{a=N,\bar{N},\pi}\left\{-\frac{m_V m_a T}{\pi|\mathbf{p}|}\int_{m_a}^{\infty} d\omega' \ln\left[\frac{1 \pm \exp(-\omega_+/T)}{1 \pm \exp(-\omega_-/T)}\right] f_{Va}^{\mathrm{a's\ rest}}\left(\frac{m_V}{m_a}\omega'\right)\right. \\
&\left.+ C_a B_{2,Va}\frac{p_V^\alpha p_V^\beta}{2T^2}\frac{\pi_{\alpha\beta}}{\varepsilon + P}\right\}.
\end{aligned}
$$

For a medium with bulk viscous pressure, a bulk viscous contribution to the dilepton rates should also be present. Any effects arising from the bulk viscous pressure will not be studied in this thesis, and is left for future work.

3.4.3 Baryon diffusion correction δn to the thermal distribution function

For media at a non-zero net baryon number, another correction to the thermal Bose-Einstein/Fermi-Dirac distributions must be included in order to account for diffusion of net baryon number. In that case, the following equation must be satisfied:

$$J^\mu_B = n_B u^\mu + V^\mu = \int \frac{d^3p}{(2\pi)^3 p^0} p^\mu \left[n(p\cdot u) + \delta n(p\cdot u)\right]. \tag{3.93}$$

The Boltzmann equation in kinetic theory will again be used to determine δn.

$$p^\mu \partial_\mu n = \mathcal{C}\left[n\right] \tag{3.94}$$

To simplify Eq. (3.94), first linearize the collision kernel

$$p^\mu \partial_\mu n^{(0)} = \mathcal{C}\left[n^{(1)}\right], \tag{3.95}$$

where the approximation $n = n^{(0)} + n^{(1)}$ was used. In the relaxation time approximation, where $\mathcal{C}\left[n^{(1)}\right] = -p^0 \delta n/\tau_R$, the Boltzmann equation reads

$$p^\mu \partial_\mu n^{(0)} = -p^0 \frac{\delta n}{\tau_R}. \tag{3.96}$$

Assuming that

$$\begin{aligned}
\delta n &= d\left\{n\right\} \\
&= d\left\{\frac{1}{\exp\left[\beta_0 u_\mu p^\mu - b_i \beta_0 \mu_B\right] \pm 1}\right\} \\
&= -\left\{\frac{1}{\exp\left[\beta_0 u_\mu p^\mu - b_i \beta_0 \mu_B\right] \pm 1}\right\}^2 \exp\left[\beta_0 u_\mu p^\mu - b_i \beta_0 \mu_B\right] \times \\
&\times \left\{d\left[\beta_0\right] u_\mu p^\mu + \beta_0 d\left[u_\mu\right] p^\mu - b_i d\left[\beta_0 \mu_B\right]\right\} \\
&= -\frac{\exp\left[\beta_0 u_\mu p^\mu - b_i \beta_0 \mu_B\right]}{\left\{\exp\left[\beta_0 u_\mu p^\mu - b_i \beta_0 \mu_B\right] \pm 1\right\}^2} \left\{d\left[\beta_0\right] u_\mu p^\mu + \beta_0 d\left[u_\mu\right] p^\mu - b_i d\left[\beta_0 \mu_B\right]\right\} \\
&= -\frac{\exp\left[\beta_0 u_\mu p^\mu - b_i \beta_0 \mu_B\right] \pm 1 \mp 1}{\left\{\exp\left[\beta_0 u_\mu p^\mu - b_i \beta_0 \mu_B\right] \pm 1\right\}^2} \left\{d\left[\beta_0\right] u_\mu p^\mu + \beta_0 d\left[u_\mu\right] p^\mu - b_i d\left[\beta_0 \mu_B\right]\right\} \\
&= -n\left[1 \pm n\right] \left\{d\left[\beta_0\right] u_\mu p^\mu + \beta_0 d\left[u_\mu\right] p^\mu - b_i d\left[\beta_0 \mu_B\right]\right\},
\end{aligned} \tag{3.97}$$

where d stands for the differential operator. Using the Euler equation, the Gibbs-Duhem relation, and the first law of thermodynamics, it is possible to solve for δn. The result reads:

$$\begin{aligned} n_{\text{total}}(p\cdot u) &= n(p\cdot u - b_i\mu_B) + \delta n(p\cdot u - b_i\mu_B) \\ &= n(p\cdot u - b_i\mu_B) + Cn(p\cdot u - b_i\mu_B)(1 \pm n(p\cdot u - b_i\mu_B))\left[\frac{n_B T}{\varepsilon + P} - \frac{b_i T}{p\cdot u}\right]\frac{p^\mu V_\mu}{T\hat{\kappa}} \end{aligned} \tag{3.98}$$

where μ_B is the net baryon chemical potential present in the equation of state, $\hat{\kappa} = \frac{\kappa}{\tau_V}$ with κ and τ_V being the net baryon number conductivity and the relaxation time for net baryon diffusion, respectively [see Eq. (2.36)], $C = 1$ for simplicity, while

$$b_i = \begin{cases} -1 & \text{if } i \text{ is a antibaryon} \\ 1 & \text{if } i \text{ is a baryon,} \\ 0 & \text{otherwise} \end{cases} \qquad b_i = \begin{cases} -\frac{1}{3} & \text{if } i \text{ is a antiquark} \\ \frac{1}{3} & \text{if } i \text{ is a quark,} \\ 0 & \text{otherwise,} \end{cases} \tag{3.99}$$

for the hadronic and partonic sectors, respectively.

3.4.4 *Baryon diffusion correction to the QGP rate*

Inserting equation Eq. (3.98) in the dilepton rate from the QGP yields:

$$\begin{aligned} \frac{d^4R}{d^4q} &= \int \frac{d^3p_1 d^3p_2}{(2\pi)^6 p_1^0 p_2^0} n(p_1\cdot u - \mu_B/3) n(p_2\cdot u + \mu_B/3)\frac{q^2}{2}\sigma\delta^4(q - p_1 - p_2) \qquad (3.100) \\ &+ \int \frac{d^3p_1 d^3p_2}{(2\pi)^6 p_1^0 p_2^0} n(p_1\cdot u - \mu_B/3) n(p_2\cdot u + \mu_B/3)\left[1 - n(p_1\cdot u - \mu_B/3)\right] \times \\ &\times \left[\frac{n_B T}{\varepsilon + P} - \frac{T}{3(p_1\cdot u)}\right]\frac{p_1^\alpha V_\alpha}{T\hat{\kappa}}\frac{q^2}{2}\sigma\delta^4(q - p_1 - p_2) \\ &+ \int \frac{d^3p_1 d^3p_2}{(2\pi)^6 p_1^0 p_2^0} n(p_1\cdot u - \mu_B/3) n(p_2\cdot u + \mu_B/3)\left[1 - n(p_2\cdot u + \mu_B/3)\right] \times \\ &\times \left[\frac{n_B T}{\varepsilon + P} + \frac{T}{3(p_2\cdot u)}\right]\frac{p_2^\alpha V_\alpha}{T\hat{\kappa}}\frac{q^2}{2}\sigma\delta^4(q - p_1 - p_2) \\ \frac{d^4R}{d^4q} &= \frac{d^4R_0}{d^4q} + \frac{d^4\delta R_\kappa}{d^4q} \\ \frac{d^4R}{d^4q} &= \frac{d^4R_0}{d^4q} + \frac{a^\alpha V_\alpha}{T\hat{\kappa}}. \qquad (3.101) \end{aligned}$$

At this point, we perform a tensor decomposition of a^α as:

$$a^\alpha = a_0 u^\alpha + a_1\frac{q^\alpha}{T}. \tag{3.102}$$

The coefficients a_0, a_1 satisfy the equation:

$$\begin{bmatrix} u^\alpha a_\alpha \\ q^\alpha a_\alpha \end{bmatrix} = \begin{bmatrix} 1 & \frac{(u\cdot q)}{T} \\ \frac{(u\cdot q)}{T} & \frac{q^2}{T^2} \end{bmatrix} \begin{bmatrix} a_0 \\ a_1 \end{bmatrix}. \tag{3.103}$$

Since $u \cdot V = 0$, a^α can only be proportional to q^α hence, after inverting the 2x2 matrix, the projection operator reads

$$P^\alpha = \frac{q^2}{q^2 - (q\cdot u)^2} u^\alpha - \frac{q\cdot u}{q^2 - (q\cdot u)^2} q^\alpha. \tag{3.104}$$

Hence, using the projector P^α on a_α yields

$$\begin{aligned} a_1 = &\int \frac{d^3p_1}{(2\pi)^3 p_1^0}\frac{d^3p_2}{(2\pi)^3 p_2^0} n(p_1\cdot u - \mu_B/3) n(p_2\cdot u + \mu_B/3) \left[1 - n(p_1\cdot u - \mu_B/3)\right] \times \\ &\times \frac{q^2}{2}\sigma\delta^4(q - p_1 - p_2)\left[\frac{n_B T}{\varepsilon + P} - \frac{T}{3(p_1\cdot u)}\right]\frac{p_1^\alpha}{T}\left[\frac{q^2}{q^2 - (q\cdot u)^2}u_\alpha - \frac{q\cdot u}{q^2 - (q\cdot u)^2}q_\alpha\right] \\ &+ \int \frac{d^3p_1}{(2\pi)^3 p_1^0}\frac{d^3p_2}{(2\pi)^3 p_2^0} n(p_1\cdot u - \mu_B/3) n(p_2\cdot u + \mu_B/3) \left[1 - n(p_2\cdot u + \mu_B/3)\right] \times \\ &\times \frac{q^2}{2}\sigma\delta^4(q - p_1 - p_2)\left[\frac{n_B T}{\varepsilon + P} + \frac{T}{3(p_2\cdot u)}\right]\frac{p_2^\alpha}{T}\left[\frac{q^2}{q^2 - (q\cdot u)^2}u_\alpha - \frac{q\cdot u}{q^2 - (q\cdot u)^2}q_\alpha\right]. \end{aligned} \tag{3.105}$$

Performing all but one integral in the rest frame of the medium gives

$$\begin{aligned} a_1 = &\int_{E_-}^{E_+} dp_1^0 n(p_1^0 - \mu_B/3) n(q^0 - p_1^0 + \mu_B/3)\left[1 - n(p_1^0 - \mu_B/3)\right]\left[\frac{n_B T}{\varepsilon + P} - \frac{T}{3p_1^0}\right] \times \\ &\times \frac{q^2}{2}\sigma\frac{q^2}{|\mathbf{q}|^3}\left[\frac{q^0}{2} - p_1^0\right] \\ &+ \int_{E_-}^{E_+} dp_2^0 n(q^0 - p_2^0 - \mu_B/3) n(p_2^0 + \mu_B/3)\left[1 - n(p_2^0 + \mu_B/3)\right]\left[\frac{n_B T}{\varepsilon + P} + \frac{T}{3p_2^0}\right] \times \\ &\times \frac{q^2}{2}\sigma\frac{q^2}{|\mathbf{q}|^3}\left[\frac{q^0}{2} - p_2^0\right], \end{aligned} \tag{3.106}$$

where $E_\pm = \frac{q^0 \pm |\mathbf{q}|}{2}$.

3.4.5 Baryon diffusion correction to the vector meson self-energy

Using the same procedures as in section 3.4.2, the decomposition of the diffusive contribution to the vector meson self-energy is of the form:

$$\delta\Pi_{\kappa(V,a)} = \frac{A_a^\alpha V_\alpha}{T\hat{\kappa}}, \tag{3.107}$$

where $A_a^\alpha = A_{0,a}u^\alpha + A_{1,a}p_V^\alpha$, as in Eq. (3.102), and p_V^α satisfies $p_V^2 = m_V^2$. Applying the projector operator in Eq. (3.104), to determine $A_{1,a}$, yields

$$\begin{aligned} A_{1,a} = -4\pi \int \frac{d^3k}{(2\pi)^3\omega}\sqrt{s} f_{Va}^{\text{c.m.}}(s) n_a(k\cdot u - b_a\mu_B)\left[1 - n_a(k\cdot u - b_a\mu_B)\right] \times \\ \times \left[\frac{n_B T}{\varepsilon + P} - \frac{b_a T}{(k\cdot u)}\right]\left[\frac{p^2(k\cdot u)}{p^2 - (p\cdot u)^2} - \frac{(p\cdot u)(p\cdot k)}{p^2 - (p\cdot u)^2}\right]. \end{aligned} \tag{3.108}$$

The integrals in Eq. (3.108) are performed following the procedure in Section 3.4.2. Care needs to be taken when treating each of the contributing particles, π, N, and $\bar{N}$, as differents values of b_a are present. Letting,

$$A_{1,a} = A_{1,a}^{(n_B)}\frac{n_B T}{\varepsilon + P} + b_a A_{1,a}^{(b_a)}, \tag{3.109}$$

the final answer, after summing over all scattering partners, reads:

$$\sum_{a=\pi,N,\bar{n}} \delta\Pi_{\kappa(V,a)} = \sum_{a=\pi,N,\bar{n}} \left[A_{1,a}^{(n_B)}\frac{n_B T}{\varepsilon + P} + b_a A_{1,a}^{(b_a)}\right]\frac{p_a\cdot V}{T\hat{\kappa}}, \tag{3.110}$$

where the coefficients $A_{1,a}^{(n_B)}$ and $A_{1,a}^{(b_a)}$ are given by:

$$\begin{aligned} A_{1,a}^{(n_B)} &= -\frac{m_V^2}{|\mathbf{p}|^2}\frac{m_N}{\pi}\int_{m_a}^{\infty} d\omega' |\mathbf{k}'| f_{Va}^{\text{a's rest}}\left(\frac{m_V}{m_a}\omega'\right) \times \\ &\times \left\{\frac{1}{e^{\beta_0\omega_- - b_a\beta_0\mu_B} \pm 1} + \frac{1}{e^{\beta_0\omega_+ - b_a\beta_0\mu_B} \pm 1} \pm \frac{2T}{\omega_+ - \omega_-}\ln\left[\frac{1 \pm e^{\beta_0\omega_+ - b_a\beta_0\mu_B}}{1 \pm e^{\beta_0\omega_+ - b_a\beta_0\mu_B}}\right]\right\} \\ A_{1,a}^{(b_a)} &= -\frac{m_V^2}{|\mathbf{p}|^2}\frac{m_N}{\pi}\int_{m_a}^{\infty} d\omega' |\mathbf{k}'| f_{Va}^{\text{a's rest}}\left(\frac{m_V}{m_a}\omega'\right) \times \\ &\times \left\{\frac{2T}{\omega_+ - \omega_-}\left[\frac{1}{e^{\beta_0\omega_- - b_a\beta_0\mu_B} + 1} - \frac{1}{e^{\beta_0\omega_+ - b_a\beta_0\mu_B} + 1}\right]\right. \\ &- \left.\frac{\omega_+ + \omega_-}{\omega_+ - \omega_-}G(\omega_+/T; \omega_-/T; b_a\mu_B/T)\right\}, \end{aligned} \tag{3.111}$$

$\omega_\pm$ is defined in Eq. (3.56), while the upper (lower) signs refer to Fermions (Bosons), and the function G is given by

$$G(x; y; w) = \int_y^x dz \frac{1}{z}\frac{e^{w-z}}{(1 + e^{w-z})^2}. \tag{3.112}$$

The dilepton rates and the dissipative corrections explored within this thesis have now been derived. An exploration of the phenomenological implications these dissipative effects have on dilepton production now follows.

4

Viscous hydrodynamics & dilepton production

The two goals of this chapter are to explore the effects viscous hydrodynamics induce on dilepton production, and to study the interplay of various sources of dilepton emission on the overall dilepton yield and elliptic flow, created in a relativistic heavy-ion collision. Thus, the effects of a non-vanishing shear viscosity η, modeled though constant shear viscosity to entropy density ratio η/s, will first be investigated on the dilepton yield and anisotropic flow observables, to ascertain the possible features that are of theoretical and experimental importance. Then, the effects of higher order QGP rates will be considered, before including the cocktail dileptons, to assess their contributions to the overall elliptic flow of dileptons. The aim is to determine how all of these dilepton sources add up and affect the dilepton production that experimental data observes.

4.1 Influence of shear viscosity on thermal dileptons

The main results presented in this section were taken from [5], except for sections 4.4 and 4.5, which contain unpublished results.

To understand the effects of shear viscosity, dileptons were computed using both ideal and viscous hydrodynamics. All effects from bulk viscosity are left for future studies. To solve the viscous equations of motion given in Chapter 2, specific values for the viscous transport coefficients must be chosen. The equation of motion for the shear viscous tensor is

$$\Delta^{\mu}_{\alpha}\Delta^{\nu}_{\beta}u^{\sigma}\partial_{\sigma}\pi^{\alpha\beta} = -\frac{1}{\tau_{\pi}}\left(\pi^{\mu\nu} - 2\eta\sigma^{\mu\nu}\right) - \frac{4}{3}\pi^{\mu\nu}\theta, \tag{4.1}$$

where the following choice was used for $\tau_\pi = 5\frac{\eta}{\varepsilon+P}$, $\eta/s = 1/4\pi$, $\delta_{\pi\pi} = \frac{4}{3}\tau_\pi$, with all other transport coefficients being set to zero. η/s is a free-parameter chosen such as to fit the yield and elliptic flow of hadronic observables, whereas the coefficients 5 in τ_π and $\frac{4}{3}$ in $\delta_{\pi\pi}$ originate from solving the Boltzmann equation for a classical gas with constant interaction cross section in the ultra-relativistic limit, where masses of constituent particles play no role [67, 66].

The dynamics of relativistic heavy-ion collisions make it especially advantageous to work in so-called hyperbolic coordinates, such that the coordinate transformation is $x^\mu = (t, x, y, z) \to (\tau, x, y, \eta_s)$, with $\tau = \sqrt{t^2 - z^2}$ and $\eta_s = (1/2)\ln\left[(t+z)/(t-z)\right]$: the space-time rapidity. In addition, it is straightforward to show that $t = \tau\cosh\eta_s$, $z = \tau\sinh\eta_s$, and that $g_{\mu\nu} = \mathrm{diag}(1, -1, -1, -\tau^2)$. Throughout this thesis, the hydrodynamical equations of motion will be solved in hyperbolic coordinates.

The code which solves for the time evolution of the fluid equations is MUSIC [29], a 3+1D numerical hydrodynamics simulation which relies on the Kurganov-Tadmor algorithm [125]. For values of parameters required by the Kurganov-Tadmor algorithm to evolve the hydrodynamical equations describing media at $\sqrt{s_{NN}} = 200$ GeV produced at RHIC, see Table I of Ref. [29]. Given the current value of $\tau_0 = 0.4$ fm/c, a 10% reduction in the initial energy density ε_0 is required when solving viscous hydrodynamical equations in order to account for entropy buildup by the dissipative dynamics. The equation of state used was the chemically equilibrated version of Ref. [21]. Also, the hydrodynamic initial state here is free of fluctuations, i.e. the initial conditions are provided by the Optical Glauber model; fluctuations will be included in the next chapter, sections 5.1 and 5.2.

4.1.1 Thermal dilepton yield: the transverse momentum and invariant mass dependence

The yield of lepton pairs is obtained by integrating the production rates in Eq. (3.30) and Eq. (3.84), over the space-time history of the collision, using relativistic hydrodynamics to simulate the time- and space-dependent background fields. Purely QGP dileptons originate from region of the medium with temperature $T > 220$ MeV, while purely hadronic matter (HM) dileptons are coming from $T < 184$ MeV. In the region $184 < T < 220$ MeV, a linear interpolation between these two rates is used. Recall from the discussion at the beginning of Chapter 3, that the choice over which an interpolation between QGP and HM dilepton rates occurs was guided by the calculations of the QCD EoS in Ref. [102]. There, it was found that using partonic degrees of freedom, one can explain the QCD EoS for temperatures as low as 200-300 MeV. So, though the choice to interpolate between the QGP and the HM dilepton rates in the region $180 \lesssim T \lesssim 220$ MeV seems natural, the precise values $T < 184$ MeV for HM and $T > 220$ MeV for QGP are somewhat arbitrary, e.g. one could have easily designated the purely HM region to be $T < 175$ MeV, while the purely QGP region to be for $T > 230$ MeV.

It is instructive to compare the transverse momentum spectra associated with different values of the dilepton invariant mass. In order to highlight in turn the hadronic and QGP thermal contributions, two values chosen can be associated with the "low mass region" ($M = m_\rho$), and the "intermediate mass region" ($M = 1.5$ GeV), respectively. First, the effects of viscous corrections are considered only on the dileptons originating from the HM phase [see Eq. (3.93)]. In Fig. 4.1 (left panel), the

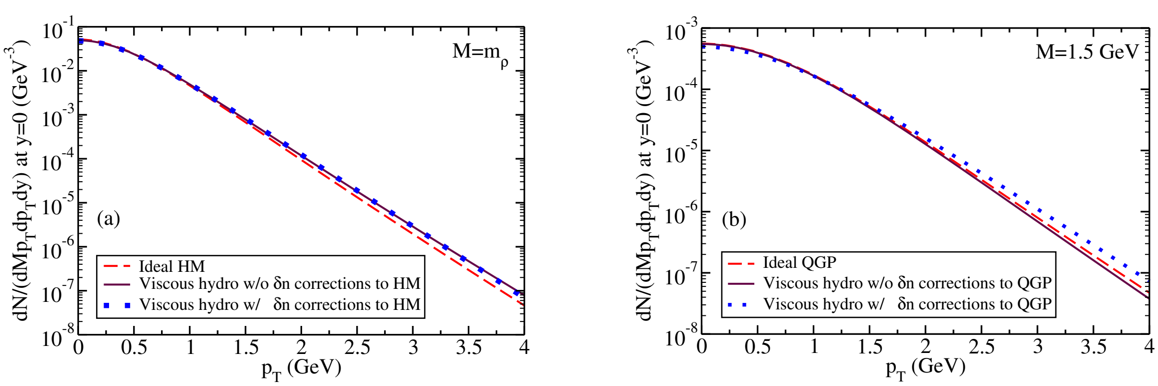

Figure 4.1: Left panel (a): Dilepton yield from the hadronic medium (HM) only, in the 0-10% centrality class and fixed invariant mass $M = m_\rho$. The contribution from: (i) ideal hydro evolution (dashed line), (ii) viscous hydro evolution alone (solid line), and (iii) viscous hydro evolution including viscous corrections to ideal dilepton rates are shown (square dots). Right panel (b): Dilepton yield from the QGP only, in the same centrality class, and for $M = 1.5$ GeV. The above figure is also available in Ref. [5].

dilepton yields as a function of p_T for the 0-10% centrality at a fixed invariant mass $M = m_\rho$ are plotted, considering in turn three cases: that of inviscid hydrodynamics, then allowing for viscous corrections to the bulk evolution but not to the rates, and then finally correcting both the rates and the bulk evolution. The viscous effects on the bulk evolution in the hadronic phase raise the yield slightly ($\sim 60\%$) at momenta from 3 to 4 GeV, as the viscous evolution slows down the temperature drop in the high-T portion of the hadronic phase [30, 126]. Also notice, on the scale of the plot in the left panel of Fig. 4.1, that viscous corrections to the hadronic emission rates have basically no effect over that of the viscous evolution. The physical reason explaining the irrelevance of δn corrections on the yield arises from the fact that dileptons from the hadronic phase are mostly emitted late ($\tau \gtrsim 4$ fm/c) at which time $\pi^{\mu\nu}$ is small (see the left panel of Fig. 4.2). Note that this explanation is somewhat qualitative as many cells with different temperatures contribute to the net dilepton yield. However, this statement is verified by a direct calculation, and viscous photon yields exhibit the same behavior [126].

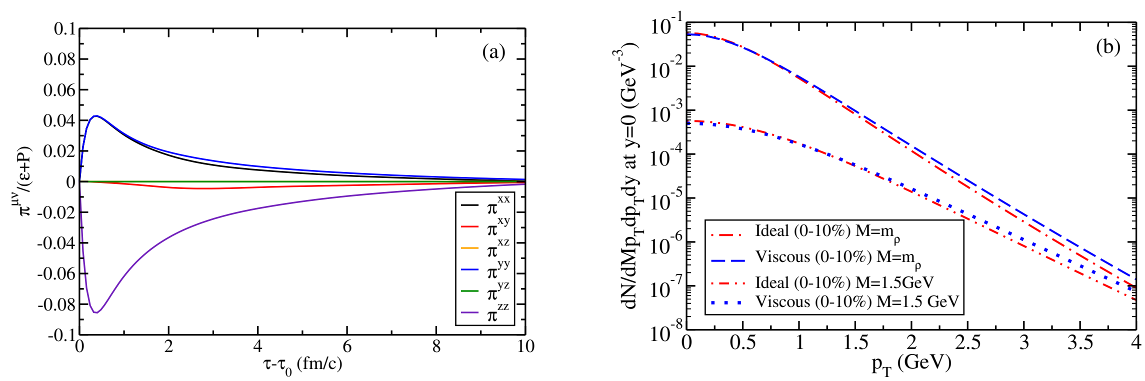

Figure 4.2: Left panel (a): Shear stress tensor in the local rest frame of the cell located at $x = y = 8/3$ fm $z = 0$ fm in the 0-10% centrality class. Right panel (b): Total thermal dilepton yield (HM+QGP) as a function of p_T and at two different invariant masses: $M = m_\rho$ and $M = 1.5$ GeV. The above figure is taken from Ref. [5].

Turning to dileptons from the QGP phase only, this statement receives further support from the dilepton transverse momentum spectrum for $M = 1.5$ GeV, shown on the right panel of Fig. 4.1. Correcting the bulk evolution only leads to a slight decrease of the yield at transverse momentum values of $p_T \sim 2 - 4$ GeV. This slight decrease is occurring because the initial temperature in the viscous case is lower than that in the inviscid case, owing to entropy generation[1]: recall that the entropy in the final state is directly related to the observed particle multiplicity. Unlike the case of the hadronic medium, the δn correction does influence the net dilepton yield as the emission occurs at early times when the temperature is high, which coincides with the proper time interval where the magnitude of the shear pressure tensor is maximal.

The right panel of Figure 4.2 displays the net thermal dilepton yield (including both HM and QGP contributions) as a function of transverse momentum in the 0 - 10% centrality class, for two values of invariant mass. For invariant masses in the low mass region, the higher momentum yield's sensitivity to the shear viscosity coefficient manifests itself almost exclusively through that of the bulk evolution. On the other hand, the thermal yield at higher invariant masses shows that the initial conditions (here, mainly T_i, the initial hydro temperature), the hydro evolution, and the viscous corrections to the distribution functions all have an effect. While the different ingredients invoked here leave a quantitative imprint on the dilepton transverse momentum spectrum that is still quantitatively modest, these findings do confirm the potential of lepton pairs as both a precise thermometer and viscometer.

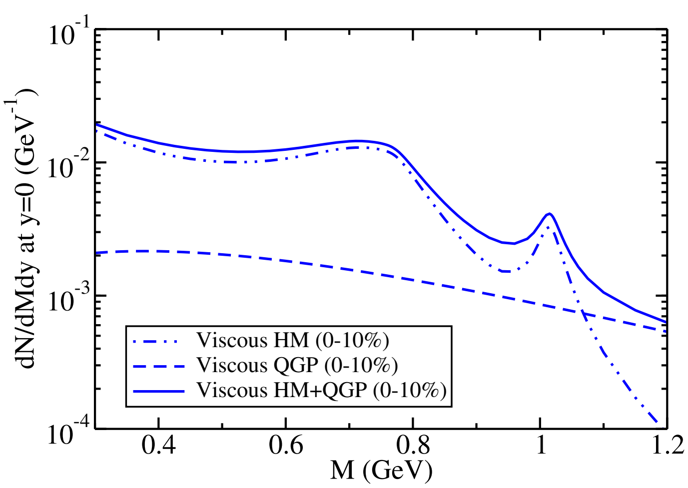

Figure 4.3: Dilepton yield from hadronic medium and QGP as a function of invariant mass, in the 0 - 10% centrality class. This result is also presented in Ref. [5].

[1]See, for example, Fig. 1 in Ref. [126].

The effect of viscous corrections to the dilepton invariant mass distribution is now investigated. It is straightforward to show that, owing to defining symmetry properties of the shear pressure tensor ($\Delta_{\mu\nu}\pi^{\mu\nu} = 0$), the viscous corrections to the QGP and HM dilepton rates as a function of the invariant mass M vanish: $d\,\delta R/dM = 0$. In fact, the proof follows the same steps as outlined in Section 2.3.2. Hence, the differences between the invariant mass profiles in the inviscid and viscous cases entirely stem from the different time-evolutions. For the conditions in this study, those appropriate for RHIC, the viscous evolution has an effect on the thermal dilepton spectrum that is essentially indistinguishable from that of the ideal hydrodynamic evolution: only the viscous case is plotted in Figure 4.3. So, though the invariant mass dilepton yield is a poor viscometer, the same statement doesn't hold for the asymmetry of the momentum spectrum, as quantified by the elliptic flow.

4.1.2 Thermal dilepton elliptic flow

Penetrating probes such as photons and dileptons are ideal to study viscosity, as they are influenced by the entire evolution of the medium [127, 128, 129]. Hadrons, on the other hand, will reflect properties that prevailed at the point of their last scattering.

The elliptic flow of thermal lepton pairs is quantified through v_2, a Fourier coefficient of the azimuthal angle expansion of the yield spectrum with respect to the event plane, whose physical origin and geometrical interpretation was discusses in Section 2.3.3. Neglecting fluctuations in the initial state, the flow coefficients are defined via:

$$\frac{dN}{dMp_Tdp_Td\phi dy} = \frac{1}{2\pi}\frac{dN}{dMp_Tdp_Tdy}\left\{1+\sum_{n=1}^{\infty}2v_n\cos\left[n\left(\phi-\psi_n\right)\right]\right\} \tag{4.2}$$

Note that since Optical Glauber initial conditions, derived in Section 2.2.4, are used here, the event plane angle ψ_n is set to zero.

Shear viscosity introduces friction between adjacent fluid layers, thus coupling faster moving fluid layers to slower moving ones, which ultimately isotropizes the angular velocity distribution of the medium and slows down its expansion. As is the case for hadrons, the elliptic flow (v_2) of dileptons as a function of invariant mass is modified by the presence of shear viscosity. Following a sequence similar to that of the previous section, we start by presenting our v_2 results as a function of p_T at fixed invariant masses in Fig. 4.4.

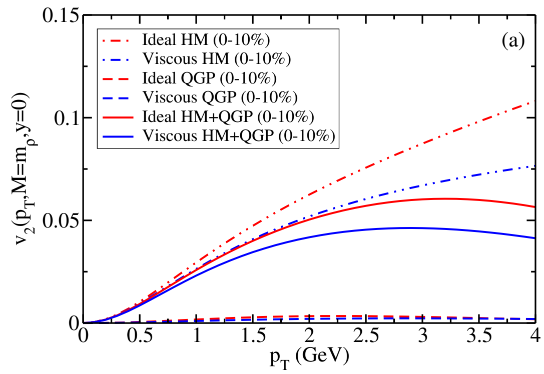

Figure 4.4: Dilepton v_2 from the hadronic medium and QGP as a function of p_T for two invariant masses. The panel on the left (a) is for $M = m_\rho$, whereas the one on the right (b) is for $M = 1.5$ GeV (note the scaling applied to the HM v_2). The calculations shown here are for the 0 -10% centrality class, which is also available in Ref. [5].

At all invariant masses, the effect of viscosity is to reduce v_2 of dileptons. This can be seen by comparing the red (ideal) and blue (viscous) curves in Fig. 4.4. Importantly, when several sources of dileptons contribute to the net dilepton yield, the final v_2 is a weighted average of the different elliptic flows, with the weight being the dilepton yield. This makes the interpretation of both panels of Fig. 4.4 clear: in the low mass region, where the HM thermal dileptons outshine those from the QGP, one observes the net v_2 to follow more closely that of the HM. At higher invariant masses ($M = 1.5$ GeV) where the QGP yield dominates that of the HM, the final thermal dilepton v_2 is close to that of the dileptons from the QGP, even though $v_2^{\rm HM} > v_2^{\rm QGP}$. Therefore, monitoring the thermal dileptons as a function of their invariant mass should help to map out the transition from a HM-dominated regime to that of a QGP. Together with a model for the time-evolution of the colliding system, such measurements could turn into a measurement of the effective temperature of the different phases. In addition, as is more clearly observed for the QGP dilepton distribution, the viscous corrections reduce the peak of v_2 by 45% and shifts it to higher momenta, mainly because of the momentum-dependence of δn [see Eq. (2.93)]. The results shown here consistently include the effects of viscosity, of using a medium-dependent vector spectral density, and of using a 3+1D hydrodynamics simulation.

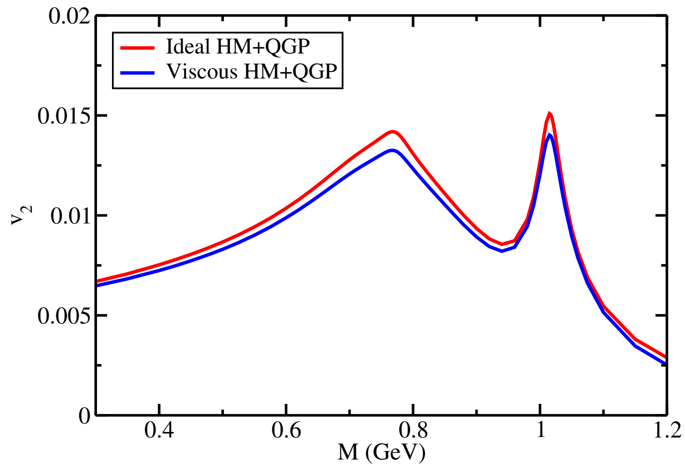

Figure 4.5: The thermal dilepton v_2 as a function of M for both ideal hydrodynamics (top curve) and viscous hydrodynamics (bottom curve), also figuring in Ref. [5].

The distribution of v_2 as a function of invariant mass is given in Fig. 4.5. There, one can clearly see that the peaks related to the $\rho - \omega$ complex and to the ϕ are present in the v_2 spectrum — also noticed in Ref. [127]. Unlike the invariant mass distribution of the yield, the v_2 distribution is actually sensitive to the presence of viscosity: it is decreased compared to its value in the inviscid case (see Fig. 4.5). One also notices that $\rho - \omega$ complex is made slightly broader by the viscous dynamics, owing to the different temperature and flow profiles.

The study of thermal dileptons is challenging experimentally, as competing sources have to be removed. In the intermediate mass region, the most important of these sources is charm/beauty hadrons[1], and their removal allows to expose direct QGP radiation. To that end, charmed and beauty hadrons require precise c- and b-quark tagging. However, the physics of heavy flavor dileptons is interesting in and of itself, as it opens a "clean" window to study heavy quark energy loss and gain mechanisms. Thus, the next section is precisely dedicated to heavy quarks, more specifically to

[1]One reaction producing dileptons that was not included here is $4\pi \to e^+e^-$. This channel was found to be sub-dominant at SPS energies [120], but will be considered in the future.

charmed quarks.

4.2 Heavy flavor hadrons and dilepton production

As mentioned in the Introduction, at intermediate and high invariant dilepton masses, there are two contributions to dileptons from the heavy flavor sector: (i) decays of open heavy flavor (where one of the quarks in the hadron is a charm or bottom quark), and decays of heavy vector meson bound states, i.e. charmonium or bottomonium (recall the discussion in section 1.4).

Before discussing the contribution of charm quarks to dilepton production, an overview of heavy flavor dilepton production is instructive, so that the physical mechanisms for dilepton production from heavy flavor are clear. This section is therefore subdivided into to three parts: (i) the first part gives an overview of the production mechanisms responsible for generating heavy flavor partons/hadrons — paying particular attention to the modifications the medium introduces on their subsequent evolution – before decaying the heavy flavor hadrons into dileptons; (ii) the second part concentrates on describing the particular model used to compute these medium-induced modifications on the evolution of charm/anticharm quarks, before hadronization and ultimate decay into dileptons; (iii) while the last part assesses the influence of open charm hadrons on the overall dilepton yield and elliptic flow. Note that the same evolution of the medium — described in the previous section – is used to compute the contribution of the open charm hadrons.

Let it be made clear at this point that no decays of heavy vector mesons will be discussed in this thesis, as those vector mesons contribute in the high invariant mass section, i.e. $M > 2.5$ GeV, and focus is given on explaining low ($M < 1.2$ GeV) and intermediate (from 1.2 GeV $< M <$ 2.5 GeV) mass dileptons. Furthermore, in the intermediate mass region, the dominant contribution to dilepton production comes from open charm hadrons [130]; open beauty hadrons only become important for $M > 2.5$ GeV (see Fig. 1.3) and hence they will also be neglected.

4.2.1 Overview of dilepton production from the heavy flavor sector

The original production of heavy flavor quarks is illustrated in Fig. 1.4 (a) and (b). What happens next to these quarks is in principle a complicated process, which is still not fully understood. Conceptually there are two limiting cases regarding the physics involved thereafter. On the one hand, once the charm or beauty quarks are produced, they travel through the medium, thus losing their energy, while their original trajectories are being deflected, before hadronizing. The other option is that the hadronization happens before the medium is created, and then it is the hadrons that travel through the medium. The most probable scenario is that a non-perturbative process in between these two extreme cases happens in experiment. If a perturbative calculation is to be performed, one typically assumes either the former or the latter scenario. A strongly coupled calculation can also be performed using gauge-gravity duality models.

Assuming that the interaction between the heavy quark and the QGP is perturbative, i.e. that the medium interacts with the quark before it hadronizes, the energy loss/gain (and angular deflection) of the heavy quark traveling through the medium is of the pQCD type. This topic has received much attention over the recent years [131, 132, 133, 134, 135, 136]. A review of several pQCD calculations compared to experimental data has recently been done in Ref. [137] (see also reference therein for a comparison of various models). Another option is to describe the interaction between the heavy quark and the medium through an effective model, e.g. via Langevin dynamics [5]. In this work, it is the Langevin dynamics approach that will be used to describe charm quarks' interaction with the medium (see sections 4.2.2 and 4.2.3). If the interaction between the heavy quark and the medium is substantial, gauge-gravity duality can be used to describe this interaction (see e.g. [138] for a recent calculation). The modeling of the interactions between the heavy quark and the medium described in this paragraph, is well suited to calculate the distribution of open heavy flavor hadrons. This type of approach doesn't describe heavy flavor vector mesons as it doesn't take into account the influence of the medium on the binding energy of the vector meson. Thus, to describe heavy flavor vector mesons, one proceeds by first hadronizing the heavy quarks/antiquark pair into these vector mesons, and then describes the interaction between the vector mesons and the surrounding medium via non-relativistic QCD. In that case, one is solving a Schrödinger-type equation for the wave function of the heavy hadron whose interaction with the medium is a potential taken from lattice QCD calculations (see e.g. [139] for details).

Once the heavy quark leaves the medium and hadronizes, the lepton pairs are produced by combining the lepton/antilepton pairs from the semi-leptonic decays of open charm and anticharm hadrons.

4.2.2 Dileptons from open charm decays: modeling medium interactions

Focus is now given to the modeling involved in the computation of dilepton production from open charm hadrons. A charm quark decays semi-leptonically into an electron with a branching fraction of approximately 10% [1]. This decay proceeds through the weak interaction [recall Fig. 1.4 (c)], unlike the case of thermal dileptons which are emitted via an electromagnetic reaction. Since the mass of a charm quark pair is much greater than the temperature reached in any model of the heavy-ion collisions at RHIC or the LHC, thermal production is negligible in comparison with the partonic annihilation in the initial collision [140]. The mass of a charm quark pair is also significantly larger than $\Lambda_{\rm QCD}$, and the production can be treated perturbatively. For proton-proton collisions, fixed-order next-to-leading-log (FONLL) calculations [141] fit the available experimental data well by including both next-to-leading order results at low momenta and terms proportional to $\alpha_s \log(p/m)$ and $\alpha_s^2(\log(p/m))^2$, and by treating the heavy quarks as effectively massless at large p_T. In heavy-ion collisions, the initial production of charm (and anti-charm) is affected by changes in the parton distribution functions: there can be - depending on the energy scale - shadowing/anti-shadowing of the parton distribution functions as well as isospin dependence of the heavy quark cross sections [142, 143]. The measured nuclear parton distribution functions can be evolved to different values of Q with the DGLAP equations [10]. Then, one needs to calculate the effect of the in-medium evolution of heavy quarks in heavy-ion collisions. The transport coefficients for heavy quarks have proven to be difficult to estimate reliably with Hard Thermal Loop effective theory [144]; however, for heavy quark momenta both less than and on the order of the heavy quark mass, the evolution of heavy quarks can be approximated to be diffusive, and relativistic Langevin equations describe their dynamics [136], allowing the heavy quark diffusion coefficient to be estimated phenomenologically. In the rest frame of the medium the Langevin equation reads

$$\frac{dp^i}{d\tau} = -\eta_D p^i + \xi^i(\tau) \tag{4.3}$$

where τ is the proper time, $\xi^i(\tau)$ is the thermal noise source with expectation value $\langle \xi^i(\tau)\xi^j(0)\rangle = \kappa\delta^{ij}\delta(\tau)$, $\kappa = 2M_c T\eta_D$ with M_c being the mass of the charm quark, T is the temperature, while η_D is the momentum drag coefficient.

PYTHIA8 [145] was used to generate events with heavy quarks. In addition, EKS98 [142, 143] was also used to determine the initial parton distribution functions in the nuclei. Then, using the same hydrodynamical description as was used to determine the thermal dilepton production, the heavy quarks are evolved using relativistic Langevin dynamics and the heavy quark spatial diffusion coefficient $D_c = \frac{3}{2\pi T}$ [140], which is related to κ via $\kappa = \frac{2T^2}{D_c}$. The heavy quarks then hadronize according to Peterson fragmentation [146] into D, $\bar{D}$, D^*, and Λ_c particles that then decay semi-leptonically. The quantitative results of this modeling are reported in the next section.

4.2.3 Including the dilepton contribution from charm decays

In order to make comparisons with experimental dilepton yield results for invariant masses up to — and including – the intermediate mass region, the contribution from semi-leptonic decays of charm to dileptons must be included. As discussed in the section 4.2.2, the dynamics of heavy quarks whose velocity $\gamma v \lesssim 1$ is approximated accurately with a relativistic Langevin equation for its momentum. We use MARTINI

[147, 140] as an event generator for charm quarks in heavy-ion collisions: the momenta of pairs of charm quarks are sampled using PYTHIA8 and the geometry in the transverse plane is sampled with the Glauber model, the Langevin equation is solved using the same calculations with MUSIC (including shear viscosity) that determined the thermal dilepton rates, and finally the species of charmed hadrons, and their decays, are sampled.

The total contribution to dN/dM is shown in Figure 4.6 (left panel), representing the comparison of all our results with preliminary data from the STAR collaboration [148] for the dilepton yields in gold-gold collisions at RHIC in the 0-10% centrality class. Note that the STAR acceptance requires the electron candidates to have $|\eta^e| < 1$ and $p_T^e > 0.2$ GeV, and dileptons to have $|y^{ee}| < 1$. Many ρ, ω, and ϕ mesons are produced in these collisions and decay into dileptons; the data from STAR includes thermal dileptons as well as dileptons from in the decays of the many hadrons produced in heavy-ion collisions. For this reason, we include the cocktail yield, as evaluated by the experimental collaboration: an extrapolation of hadron yields decaying to dilepton yields. The solid green line represents the sum of the thermal rates, the cocktail, and the contribution of charm without evolution in the medium, while the solid purple line represents the sum of the thermal rates and the cocktail with the charm contribution after evolving according to relativistic Langevin dynamics. The

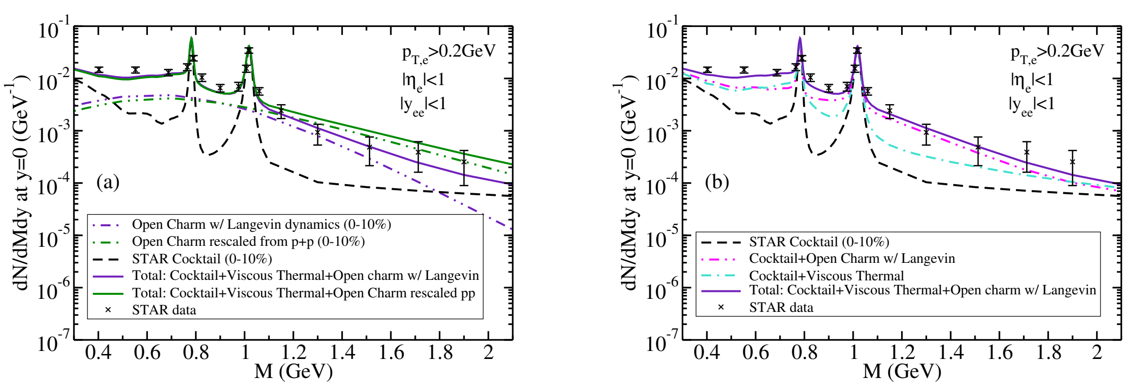

Figure 4.6: Left panel (a): Dilepton invariant mass yields compared with experimental data at 0-10% centrality: importance of Langevin dynamics. Right panel (b): Dilepton invariant mass yields compared with experimental data at 0-10% centrality: importance of thermal radiation. The experimental acceptance cuts are indicated on the figures.

energy exchange of charm quarks with the medium leads to a depletion in dN/dM at large M, and the charm contribution alone can differ by an order of magnitude at $M = 2.1$ GeV, depending on whether Langevin evolution is considered or not. The data has a slight preference for Langevin evolution, which is an encouraging result, but the size of the error precludes a stronger conclusion at this point. However, the inclusion — or not – of the possibility of charm energy variation will affect any determination of the cross sections using dilepton yield data[1]. At lower invariant masses, the STAR data seems compatible with this theoretical calculation, though the latter *is still below the data*[2]. However, it is clear that acceptance-corrected data will make a much more compelling case for model compatibility. Before such data is available, one can improve the comparison between the theoretical calculation and the current data by including higher order corrections to the Born QGP dilepton rate. This is done in section 4.4 (see in particular Fig. 4.11).

The right panel of Figure 4.6 investigates the importance of thermal radiation to describe the STAR data. In the low invariant mass region, the cocktail systematically underestimates the data and including charmed hadrons (with Langevin dynamics) is not enough to raise the calculation to the level of the measurements: the inclusion of thermal radiation is crucial. For intermediate dilepton invariant masses, the situation is less clear given STAR's current experimental uncertainties. However, the trend does suggest that thermal radiation from the QGP is present and must participate in the interpretation of the data.

The STAR collaboration also has preliminary measurements of minimum bias $v_2(M)$ of dileptons (albeit with still large error bars) over a large momentum range, and this also includes the dileptons produced by semi-leptonic decays of charmed mesons. The theoretical results for this observable are shown in Fig. 4.7, not including the contribution of the cocktail. A calculation including the cocktail will be presented in section 4.5. Including the charm contribution to v_2 has two important

[1]Indeed, the analysis of the dilepton spectrum provides an indirect measurement of the charm cross section.

[2]Note that Fig. 4.6 is plotted on a logarithmic scale.

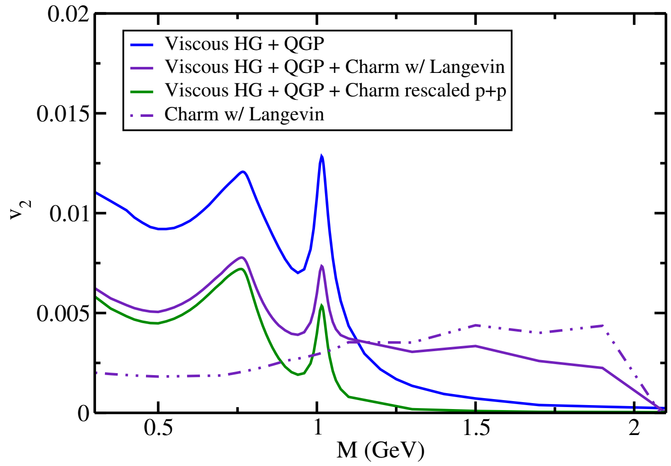

Figure 4.7: Dilepton invariant mass v_2 including thermal and charm contributions at 0-10% centrality.

effects: first, it reduces the v_2 in the 0 - 1 GeV invariant mass range by about a factor of two, and it increases the v_2 in the 1.5 - 2 GeV invariant mass range where the charm contribution dominates the dilepton yields. The flow of the charm contribution is smaller than the flow of the hadronic matter contribution and it is larger than the flow of the QGP contribution, but also bear in mind that the net elliptic flow is a weighted average of its individual components. Notably, the absolute magnitude of the final elliptic flow is small. But let it be made clear again: no efforts have been made here to search for conditions that will maximize this signal, such as going to a higher centrality class, including fluctuating initial states, etc. These will be explored in sections 5.1 and 5.2.

Before leaving this section, it is pertinent to recall that electromagnetic radiation samples the entire space-time including the early stages where the validity for the viscosity correction, linear in the viscous pressure tensor [see Eq. (3.72)], can be questioned. Part of this investigation was performed in Ref. [126], those results still hold and will not be repeated here. Suffice it to say that systematic corrections to the δn will be explored section 5.2 when a temperature dependent η/s in the QGP phase is considered.

4.3 The influence of shear viscosity on dileptons: a summary

In the previous section, a systematic study of viscosity effects on dilepton spectra in heavy-ion collisions was conducted. The effects of viscosity were studied (a) in the microscopic emission rates (b) in the macroscopic evolution, while the semileptonic contribution was modified owing to the presence of the medium. It was found that the largest effects of viscosity are seen in the part of the signal that is attributable to the QGP, as the shear pressure tensor ($\pi_{\mu\nu}$) is maximal in this phase. For essentially all conditions considered here, the effects of the viscous dynamics are numerically not large, but are non-negligible. Moreover and importantly, the viscous corrections are required to ensure theoretical consistency. As the shear viscosity to entropy ratio increases however, via a temperature dependent η/s in the QGP phase for example (see section 5.2), viscous effects will become more important.

For the purpose of comparing with recent experimental data, the calculations presented also include a Langevin evolution of charmed quark distributions in a viscous hydrodynamics background. The dilepton signal originating from open charm hadron decays was then added to that of thermal sources. These results compared well with dilepton invariant mass yield data on Au - Au collisions from the STAR collaboration at RHIC, suggesting that the data is consistent with viscous dynamics in the low mass region. The intermediate invariant mass region opens a possibility to measure the energy shift of heavy quarks that interact with the hot and dense evolving medium, and the results shown here also support this assertion. Furthermore, it should also be possible to access the QGP dilepton radiation in the intermediate mass region — from 1.2 GeV to 2.5 GeV – provided that precise experimental tagging of heavy flavor exists. In that case, it may be experimentally possible to remove the lepton pairs originating from open charm and beauty decays, thus exposing direct radiation from the QGP. A simultaneous analysis of yield and v_2 of the high-mass lepton pairs, coupled with a removal of non-photonic electrons produced in the semi-leptonic decays of open heavy flavor hadrons, would produce a clear picture of the early stages of the nuclear collision. This analysis could also be used to constrain the size of η/s, as will be discussed in the last section of this chapter.

To fully appreciate the amount of lepton pair production from the QGP, higher order corrections to the Born QGP dilepton rate need to be included, which is the topic of the next section.

4.4 Higher order corrections to the QGP dilepton rate

As mentioned in the Introduction, going beyond the Born dilepton rate implies performing calculations at $\mathcal{O}(\alpha_s \alpha_{EM})$. These calculations become rather involved in a thermalized medium, as the medium introduces coherence effects that spoil the vacuum power counting of perturbative calculations. So certain diagrams that in vacuum would contribute to higher order in the perturbative expansion, get parametrically promoted to a lower order in perturbative expansion, once a thermalized medium is present. The physical mechanisms modulating the thermal dilepton production in a medium, relative to the vacuum, are known as Landau damping and Debye screening. These mechanisms will be discussed in section 4.4.1, while section 4.4.2 is reserved for a more in-depth exploration of the Feynman diagrams that need be resummed, along with the results obtained using these higher order rates.

4.4.1 QGP dilepton production at $\mathcal{O}(\alpha_s \alpha_{EM})$ and beyond

For the sake of simplicity, assume for now that the 3-momentum of the virtual photon is $|\mathbf{q}| = 0$. When the invariant mass of the virtual photon is soft $M \sim g_s T$, and the typical momentum of the quark propagator [see Fig. 1.6 (b), (c), and (d)] is of order $|\mathbf{p}|^2 \sim g_s^2 T^2$, then the propagating quark will scatter multiple times with in-medium gluons whose typical momentum is of the order $|\mathbf{p}|^2 \sim T^2$. Since the frequency of scattering is proportional to the temperature, multiple scatterings will occur and they need to be resummed in order to determine the total effect on the quark propagator. Performing this sum changes the quark propagator, by making it acquire a thermal mass, i.e. $p^{-2} \to\sim (p^2 - m_D^2)^{-1}$, where the thermal quark mass is $m_D^2 = g_s^2 T^2/6$ [149]. This phenomenon, called Landau damping [150], will cause a reduction in the amount of virtual photons emitted relative to the same production mechanism happening in vacuum, where the propagator doesn't have a thermal mass.

The quark-photon vertex also acquires a thermal correction. Indeed, at finite temperature, the gluon field fluctuates constantly and these fluctuations act to screen the vacuum electromagnetic charge of the quark-photon vertex. This mechanism is called Debye screening [150] will reduce the virtual photon emission probability (for more details see section 4.4.2). Therefore both Landau damping and Debye screening reduce the soft ($M \sim g_s T$) virtual photon production rate depicted in Fig. 1.6 (b), (c), and (d) relative to the same diagrams in vacuum.

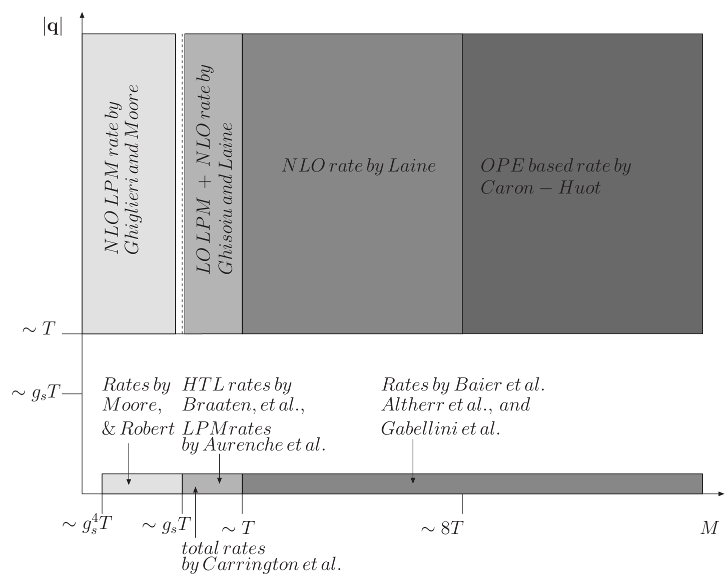

Figure 4.8: Regions of phase space where the dilepton rates have been computed.

The first calculation of the thermal dilepton rates at next-to-leading order (NLO), i.e. $\mathcal{O}(\alpha_s \alpha_{EM})$, was performed in Refs. [46, 47, 48]. They used the simplifying assumption $|\mathbf{q}| = 0$, while also assuming that the invariant mass is larger that the temperature of the medium $M \gtrsim T$ (see also Fig. 4.8). In that kinematic regime, Landau damping and Debye screening can be neglected. Refs. [46, 47, 48] found that the $\alpha_s = \frac{g_s^2}{4\pi}$ correction to the Born rate is small. Going below $M \sim T$, Ref. [149] found that the previously small α_s correction to the dilepton rate actually becomes of $\mathcal{O}(1)$, i.e. as important as the Born rate, when $M \sim g_s T$ (see Fig. 4.8). In that case, a resummation of an entire set of diagrams is required, known as the Hard Thermal Loop (HTL) resummation [103]. This resummation captures the physics of Landau damping affecting the propagation of quarks in the medium [i.e. the quark propagator between the photon and the gluon vertex in Fig. 1.6 (b), (c), and (d)] and in-medium Debye screening of the electromagnetic charge affecting the quark-photon vertex in Fig. 1.6 (b), (c), and (d) [103].

Still remaning in the $|\mathbf{q}| = 0$ limit, it is possible to go even lower in M, namely up to $M \sim g_s^4 T$ (see Fig. 4.8) by solving the linearized Boltzmann equation for quarks [151]. At such a low virtuality, one is sensitive to the electrical conductivity of the QGP which shows up as a finite-sized peak in the dilepton emission spectrum as $M \to 0$ for $|\mathbf{q}| = 0$. Indeed, in Ref. [151] the size of the electrical conductivity, i.e. the height of the peak, was determined parametrically to be $\sim \alpha_{EM} \frac{T}{g_s^4}$ with the actual numerical values quoted in that reference. Though theoretically enlightening, calculations at $|\mathbf{q}| = 0$ have a very limited usefulness for describing dilepton emission from a QGP formed in relativistic heavy-ion collisions. To address this shortcoming, progress has been made in computing the QGP dilepton rates for $|\mathbf{q}| \gtrsim T$. Ref. [6] computes the dilepton rates at NLO (i.e. $\mathcal{O}(\alpha_s \alpha_{EM})$), thus extending the rate of Refs. [46, 47, 48] for $|\mathbf{q}| \gtrsim T$ (see Fig. 4.8). The result of Ref. [149], which includes physics at $(M \gtrsim g_s T, |\mathbf{q}| = 0)$, was extended to $(M \gtrsim g_s T, |\mathbf{q}| \gtrsim T)$ (see Fig. 4.8) in Ref. [7]. The next section is devoted to describing, in some detail, the two calculations in Refs. [6, 7].

4.4.2 Exploring recent developments in QGP dilepton calculations

The calculation performed in Ref. [6], done in the limit $M \gtrsim T$ and $|\mathbf{q}| \gtrsim T$, was rendered possible owing to a recent development by Ref. [121]. Using the Operator Product Expansion (OPE), Ref. [121] computed the asymptotic behavior of spectral functions in the high energy limit, i.e $M \gg T$, $|\mathbf{q}| \gg T$, and $M > |\mathbf{q}|$. Ref. [6] has shown that the NLO dilepton rate converges to the OPE result for $M \gg 8T$ (see Fig. 4.8). To go lower in virtuality, namely to $M \gtrsim g_s T$, while remaining in the limit $|\mathbf{q}| \gtrsim T$, HTL resummations must be included.

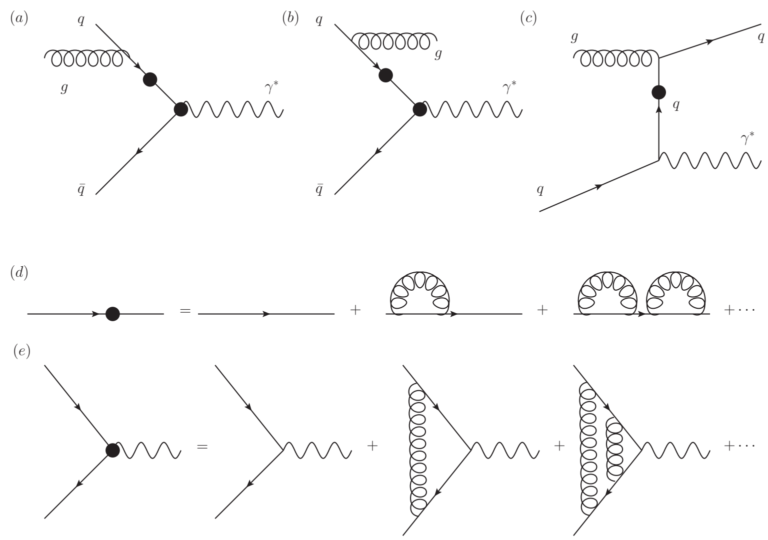

Figure 4.9: (a) Gluon absorption (b) Gluon emission (c) Compton scattering diagrams contributing to NLO dilepton production from the QGP. The HTL correction to quark propagator (d) and the photon vertex (e) are also shown. HTL corrections are required when the momentum of the quark propagator is small (i.e. $|\mathbf{p}|^2 \sim g_s^2 T^2$) or when the virtuality of the emitted photon is small $M^2 \sim g_s^2 T^2$ while the quark entering/leaving the vertex is soft ($|\mathbf{p}|^2 \sim g_s^2 T^2$).

The HTL corrected quark propagator and quark-photon vertex are presented in Fig. 4.9 (a), (b), and (c). The diagrams that need to be resummed to obtain the medium-modified quark propagator are presented in Fig. 4.9 (d), while those for photon vertex are illustrated in Fig. 4.9 (e). However, resumming these diagrams is not enough. The medium also has a significant number of gluons with momentum $|\mathbf{p}|^2 \sim g_s^2 T^2$ that can interact with hard on-shell quarks with energy of order $p^0 \sim T$. This interaction between soft gluons and hard quarks leads to an enhancement of virtual photon production in the region $M^2 \sim g_s^2 T^2$ known as the Landau-Pomeranchuk-Migdal (LPM) effect. One can understand the LPM effect as follows. Every time a hard quark acquires a soft gluon, its virtuality gets increased by $p^2 \sim g_s^2 T^2$. Because the virtuality is small, the resulting state can live for a long time allowing for multiple such interactions from the medium to be added coherently, as depicted in Fig. 4.10. So, since the involved gluons are soft, these diagrams should not be taken at face value, which would naively suggest that those diagrams contribute at higher order in the strong coupling. Indeed, these soft gluons parametrically enhance the scattering probability of these diagrams making them contribute to the leading order virtual photon/dilepton production. The subsequent decay of this long-lived quark state

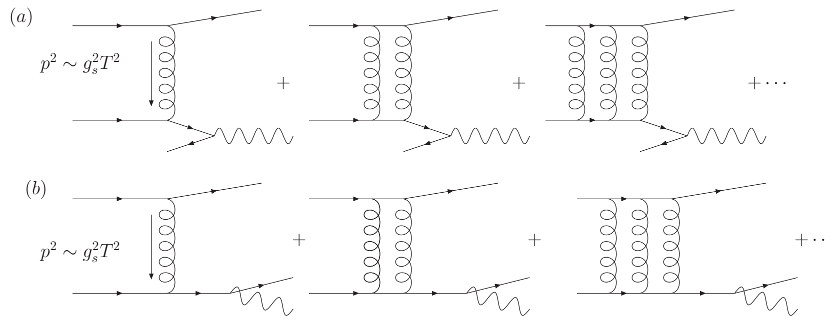

Figure 4.10: Diagrams contributing to the LPM effect: (a) LPM correction to $q\bar{q}$ annihilation diagram (b) LPM correction to the Compton scattering diagram.

gives rise to nearly on-shell virtual photons with $M \sim g_s T$, thus enhancing their yield in the low mass region. Since similar physical processes are present in both LPM resummation given in Fig. 4.10 and the HTL resummation in Fig. 4.9, the sum of these two effects will be referred to as the LPM effect from now on. In fact, the calculation in Ref. [7] was the first complete calculation of coherence effects from the LPM effect at leading order (LO) in the electromagnetic coupling constant (and $\mathcal{O}(1)$ in g_s) in the phase space region ($M \gtrsim g_s T$, $|\mathbf{q}| > T$).[1] The calculation in Ref. [7] has also successfully matched the LO LPM rate valid at low virtuality to the NLO dilepton rate valid at high M. This smooth connection was made possible using the prescription of Ref. [153] which describes how to avoid any kind of double counting of diagrams that contribute to both the LO LPM sector and the NLO dilepton rate. Indeed, diagrams that contribute to both the NLO dilepton rates at $M \gtrsim T$ and the LO LPM sector (for $M \gtrsim g_s T$) were removed in the NLO sector and solely included in as part of the LPM effect [7].

To truly appreciate the convergence of the NLO calculation of the thermal dilepton rate, the size of the dilepton rate from the QGP should be computed at higher order in the strong coupling constant, including its LPM effect. This has been done for

[1]The LPM effect was first computed for $M \gtrsim g_s T$ and $q^0 \gtrsim T$ in Ref. [152]. However, that calculation contains a slight error [153] and will therefore not be used here.

the LPM effect alone in Ref. [8], which goes up to $\mathcal{O}(g_s\alpha_s\alpha_{EM})$, and is valid in the low invariant mass region $M \lesssim g_sT$. For the calculation in Ref. [8] to be complete, the total dilepton rate should be calculated at next-to-next-to-leading order (NNLO). The NNLO dilepton rate calculation is very difficult and was not attempted yet at high M.

However, even though the full NNLO dilepton rate is not known, the biggest effect of the NNLO rates should come from the NLO LPM correction in the low invariant mass sector. Incidentally, this is the same region where dileptons from the hadronic medium are important. Of course, as the invariant mass increases, the effects of the higher order corrections should become small, and the NNLO dilepton rates are expected to be a small correction to the NLO rates at high M. So, to quantify the importance of the NNLO corrections to the dilepton yields in the low M region, especially compared to the hadronic yields, the NLO LPM correction was added on top of the NLO rates using either no weight (light blue curve in Fig. 4.11) or a decaying exponential $\exp[-(q^0 - |\mathbf{q}|)/T]$ weight (dark blue curve in Fig. 4.11). Note that when the exponential is applied to the the NLO LPM contribution, the total rate does converge to the NLO calculation of Ref. [6] at high invariant masses, i.e. the dark blue curve converges towards the light purple curve. The same ideal hydrodynamical

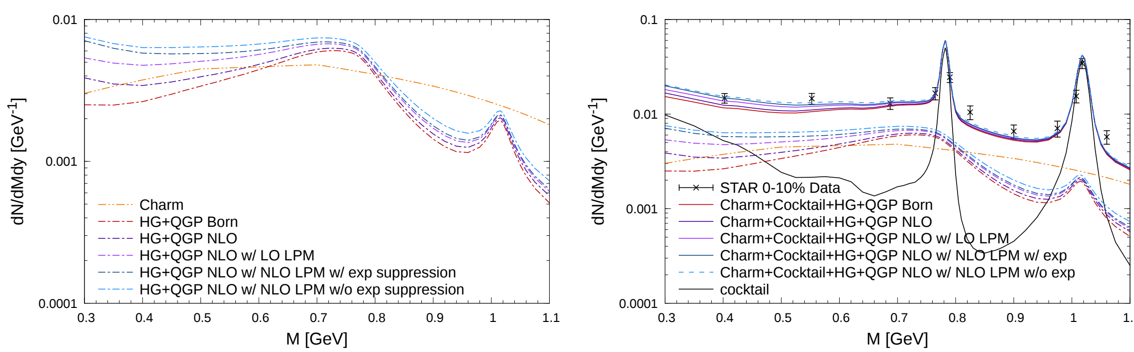

Figure 4.11: Both calculations are done using ideal hydrodynamics. Left panel: Thermal dilepton invariant mass yields including NLO QGP dilepton rate in the 0-10% centrality. Right panel: Dilepton invariant mass yield compared with experimental data at 0-10% centrality including NLO QGP dilepton rate and the STAR experimental cocktail. Note that the experimental data contains only the statistical uncertainties.

calculation as in section 4.1 was used here to compute the dilepton yield in Fig. 4.11, as the viscous correction to any dilepton rate beyond the LO Born rate has not been computed yet. However, recall that the *invariant mass yield* of dileptons is essentially unaffected by the presence of shear viscosity, hence this calculation of the *dilepton yield* is actually as good as the viscous one presented in Fig. 4.6. The left panel of Fig. 4.11 summarizes the effects of including the various higher order corrections to the QGP dilepton rates. Indeed, including higher order corrections to the QGP dilepton rates significantly increases their yield at low M ($M \lesssim 1.2$ GeV); the QGP yield is now competing with the HM one. One should nevertheless be careful not to draw any definitive conclusion from this result, since any phenomenological calculation has its caveats. Indeed,

- The amount of dileptons from the QGP vs HM depends on the initial/freeze-out conditions chosen for the hydrodynamical evolution, which do change if one is to include fluctuation in the initial conditions as we will see in sections 5.1 and 5.2.

- Also the temperature range ($184 < T < 220$ MeV) for the cross over phase, over which the QGP and the HM rates were linearly interpolated, was a *choice* (recall the discussion at the beginning of Chapter 3). Changing this choice will affect the results presented here.

The right panel of Fig. 4.11 shows a tangible improvement in the description of the dilepton yield owing to the higher order QGP rates.

The elliptic flow of thermal dileptons is presented in Fig. 4.12. The thermal $v_2(M)$ is significantly reduced when comparing higher order QGP dilepton emission to that from the LO Born approximation, due to the increase of the QGP yield. Indeed, the size of the $v_2(M)$ of QGP dileptons *alone* is not significantly affected by higher order rates[1], it is really the increase in the yield that drives the reduction in the thermal

[1] This is because the same ideal hydrodynamical simulation was used (along with the same interpolation prescription between HM and QGP dilepton sources). So, the same initial eccentricity $\epsilon_{2,2}^{c}$ is present, and will get converted to a similar momentum anisotropy, i.e. v_2, of dileptons (recall discussion in section 2.3.3).

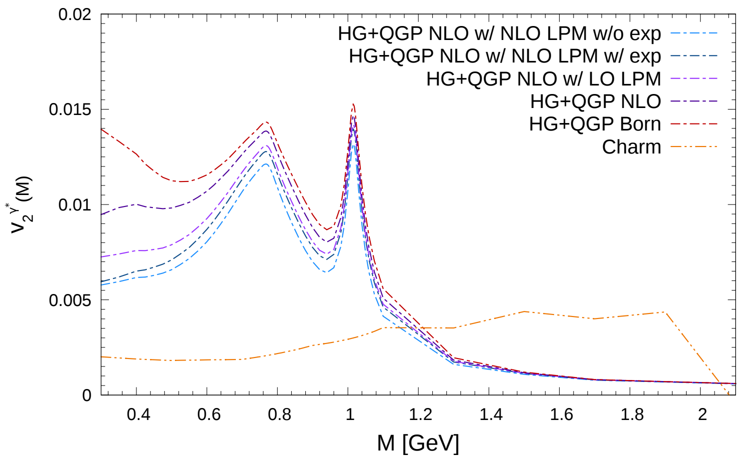

Figure 4.12: Thermal dilepton elliptic flow as a function of invariant mass including NLO QGP dilepton rate in the 0-10% centrality using ideal hydrodynamics.

$v_2(M)$. However, to better appreciate the effects of these higher order corrections to QGP rates on dilepton elliptic flow from a theoretical perspective, viscous corrections to these rates need to be included as they *will* affect the elliptic flow of dileptons. This will be done in the near future. As far as the experimental implications are concerned, the current calculation is missing the anisotropic flow of cocktail dileptons, i.e. late decays into dileptons of long-lived vector and pseudoscalar mesons, which is the subject of the next section.

Therefore, a high precision measurement of $v_2(M)$ in the low mass region, would shed some light at the physical processes at play, provided other competing sources (i.e. charm and cocktail) are removed.

4.5 Cocktail dileptons and the overall dilepton flow

As the cocktail plays a key role in describing both the total yield and v_2 of dileptons, the goal of this section is to explore the influence of the cocktail on the total $v_2(M)$ of dileptons. The main result of this section is to show that, though the cocktail is an important contribution to the observed $v_2(M)$, the thermal component is equally vital as any effect of the thermal contribution shows up in the total. The results presented in this section were obtained using the same ideal hydrodynamical evolution as in section 4.1.

The cocktail contribution to dilepton production can be calculated by decaying the final hadron spectra, obtained through the Cooper-Frye prescription and resonance decays, into dileptons. The main sources of dileptons contributing to the cocktail are decays of pseudoscalar mesons and vector mesons. The important decay channels of pseudoscalar mesons contributing to dilepton production are:

- $\pi^0 \to \gamma\gamma^* \to \gamma\ell^+\ell^-$
- $\eta \to \gamma\gamma^* \to \gamma\ell^+\ell^-$
- $\eta' \to \gamma\gamma^* \to \gamma\ell^+\ell^-$

while for vector mesons, there are two types of decays: direct decays into dileptons and 3-body decays, that is

- $\rho \to \gamma^* \to \ell^+\ell^-$
- $\omega \to \gamma^* \to \ell^+\ell^-$
- $\omega \to \pi^0\gamma^* \to \pi^0\ell^+\ell^-$
- $\phi \to \gamma^* \to \ell^+\ell^-$
- $\phi \to \eta\gamma^* \to \eta\ell^+\ell^-$

Direct decays of vector mesons produced at the Cooper-Frye freeze-out surface into dileptons can be obtained by slightly generalizing the Cooper-Frye formula. Starting from the Cooper-Frye prescription in Eq. (2.90):

$$\begin{aligned} N_V &= \int \frac{d^3p}{(2\pi)^3 p^0} \int d^3\Sigma_\mu p^\mu n_{V,0}\left[\frac{p^\mu}{T}u_\mu\right] \\ &= \int \frac{d^4p}{(2\pi)^4}(2\pi)2\delta(p^2-m^2)\Theta(p^0) \int d^3\Sigma_\mu p^\mu n_{V,0}\left[\frac{p^\mu}{T}u_\mu\right] \\ &= \int \frac{d^4p}{(2\pi)^3}2g_i\left[\frac{-\mathrm{Im}D_V^R}{\pi}\right] \int d^3\Sigma_\mu p^\mu n_{V,0}\left[\frac{p^\mu}{T}u_\mu\right] \end{aligned} \tag{4.4}$$

where the factor of $g_i = 3$ accounts for the spin degrees of freedom of vector mesons, $n_{V,0}$ is simply the Bose-Einstein distribution. The spectral distribution which in the original Cooper-Frye formula assumes that vector mesons are stable, i.e. $\delta(p^2 - m^2)\Theta(p^0)$, was replaced by the more accurate version which includes a vector meson width, i.e. $\frac{-\mathrm{Im}D_V^R}{\pi}$. To obtain the total number of dileptons, one needs to simply multiply Eq. (4.4) by the branching fraction of $V \to \ell^+\ell^-$. That is,

$$
\begin{aligned}
B_{V\to\ell^+\ell^-} &= \frac{M\Gamma_{V\to\ell^+\ell^-}}{M\Gamma_V} \\
&= \frac{\alpha^2}{3}\frac{m_V^4}{g_V^2/(4\pi)}\frac{1}{M^2}\left(1+\frac{2m_\ell^2}{M^2}\right)\left(1-\frac{4m_\ell^2}{M^2}\right)^{1/2}\frac{1}{-\mathrm{Im}\Pi_V^R}
\end{aligned}
\tag{4.5}
$$

where $M\Gamma_{V\to\ell^+\ell^-}$ was obtained using Eq. (3.34), while $M\Gamma_V = -\mathrm{Im}\Pi_V^R$. Combining Eq. (4.4) and Eq. (4.5) gives:

$$
\frac{dN_{V\to\ell^+\ell^-}}{d^4q} = \frac{\alpha^2}{\pi^3}\frac{m_V^4}{g_V^2}\frac{1}{M^2}\left(1+\frac{2m_\ell^2}{M^2}\right)\left(1-\frac{4m_\ell^2}{M^2}\right)^{1/2}\left|D_V^R\right|^2\int d^3\Sigma_\mu p^\mu n_{V,0}\left[\frac{p^\mu}{T}u_\mu\right]
\tag{4.6}
$$

where the square of the magnitude of the retarded propagator $\left|D_V^R\right|^2$, also called the form factor, is now present. This only accounts for the thermal production of vector mesons. There are also a lot of high mass resonances decaying into vector mesons. MUSIC takes those into account by decaying all high mass resonances into lower mass states including vector mesons, thus obtaining a "final" distribution $\frac{p^0 dN_V}{d^3p}$ which can then be combined with Eq. (4.5) to obtain the final dilepton spectrum from vector mesons. Given the rather large width of the ρ meson in the vacuum, and the fact that its width will significantly be modified in the medium, this particle is actually not included in the experimental cocktail presented in Figs. 4.6 and 4.11, since a reliable reconstruction of the ρ meson from experimental pion spectra is not done. Hence to be compatible with experimental designation convention, the term cocktail will explicitly exclude the contribution from the ρ. On the theoretical side however, the ρ contribution from both the Cooper-Frye surface and from the decay of heavier resonances is included, and therefore the cocktail plus ρ contribution will be used throughout this section.

The 3-body decays channels contributing to dilepton production are more complicated. However, if ones considers any 3-body decay as a 2-step 2-body decay process, the calculation becomes simpler. Take for example the decay of $\omega \to \pi^0\ell^+\ell^-$. One can obtain analytically the distribution of the virtual photon γ^* from the Cooper-Frye formula assuming $\omega \to \pi^0\gamma^*$. Indeed, in the rest frame of the ω meson, the distribution of virtual photons is obtained by [154]:

$$\begin{aligned}\frac{q^0 dN_{\gamma^*}}{d^3q} &= \int \frac{d^3p}{p^0}\frac{1}{4\pi|\mathbf{q}|}\delta(p^0 - q^0)\frac{p^0 dN_\omega}{d^3p} \\ &= \int \frac{d^3p}{p^0}\frac{q^0}{4\pi|\mathbf{q}|^2}\delta(|\mathbf{p}| - |\mathbf{q}|)\frac{p^0 dN_\omega}{d^3p} \end{aligned} \tag{4.7}$$

where, q^0 is the energy and $|\mathbf{q}|$ is the momentum of the virtual photon in the rest frame of the ω meson, while $\frac{p^0 dN_\omega}{d^3p}$ is the distribution of ω mesons, including resonance decay contributions, as obtained from MUSIC. Performing the integral in the rest frame of the virtual photon yields:

$$\frac{q^0 dN_{\gamma^*}}{d^3q} = \int d\Omega' \frac{m_\omega^2}{M^2}\frac{p'^0 dN_\omega}{d^3p'} \tag{4.8}$$

where ($'$) denotes quantities in the rest frame of the virtual photon and $d\Omega' = \sin\theta' d\theta' d\phi'$, the usual solid angle phase space. The phase space distribution of the branching fraction was derived in [155] and reads:

$$\begin{aligned}\frac{dB_{\omega\to\pi^0\gamma^*}}{dM^2} &= A\frac{1}{M^2}\left(1 + \frac{2m_\ell^2}{M^2}\right)\left(1 - \frac{4m_\ell^2}{M^2}\right)^{1/2} \times \\ &\times \left\{\left[1 + \frac{M^2}{m_\omega^2 - m_{\pi^0}^2}\right]^2 - \frac{4m_\omega^2 M^2}{\left(m_\omega^2 - m_{\pi^0}^2\right)^2}\right\}^{3/2} F_{\omega\to\pi^0\gamma^*}(M^2)\end{aligned} \tag{4.9}$$

where to determine $F_{\omega\to\pi^0\gamma^*}(M^2)$ one uses the Vector Meson Dominance model [see [155] for details]. Different authors have different definitions regarding the strength of the coupling between photons and vector mesons, and for this reason, A is not quoted in the formula above. However, there is a sum rule that can be used to determine A:

$$\int_{2m_\ell}^{m_\omega - m_{\pi^0} - 2m_\ell} d(M^2)\frac{dB_{\omega\to\pi^0\gamma^*}}{dM^2} = B_{\omega\to\pi^0\gamma^*} \tag{4.10}$$

where A is chosen such that the experimental branching fraction $B_{\omega\to\pi^0\gamma^*}$ is obtained. Using Eq. (4.9) it is easy to obtain the branching fraction of $\pi^0 \to \gamma\gamma^*$, $\eta \to \gamma\gamma^*$ and so on. Therefore, a direct calculation of the cocktail can be made.

It is now possible to discuss is the influence of the cocktail, including the ρ contribution, on the overall elliptic flow of dileptons. The elliptic flow of dileptons originating from the various sources is illustrated in Fig. 4.13. The thermal contribution includes the NLO QGP rate with NLO LPM correction suppressed by $\exp[-(q^0 - |\mathbf{q}|)/T]$. Other than the peaks in $v_2(M)$ corresponding to the dilepton radiation from vector mesons, the shape of the $v_2(M)$ distribution originates from threshold effects present in 3-body decays. Indeed, there is no contribution from η mesons for $M > m_\eta = 0.547$ GeV, while for $M > m_\omega - m_\pi$ there is no contribution from the $\omega \to \pi\gamma^*$ channel. In fact, the shoulder present for M between 0.5–0.65 GeV in Fig. 4.13 comes from the $\omega \to \pi\gamma^*$ channel. All other 3-body decay channels are subdominant and their contribution cannot directly be seen in Fig. 4.13. The most important point of Fig. 4.13

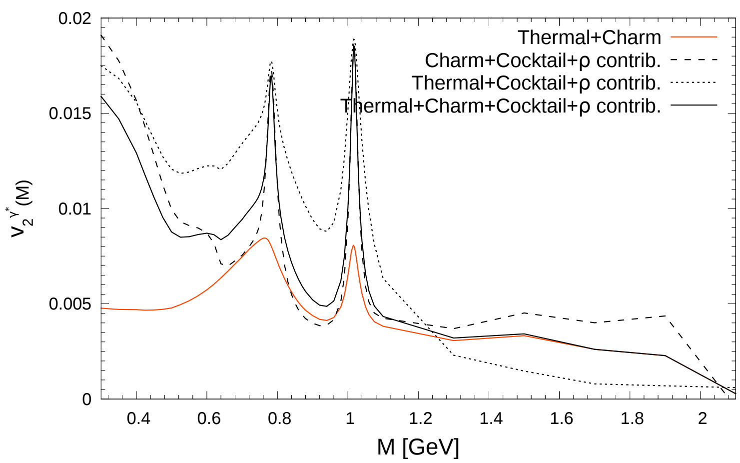

Figure 4.13: The various sources of dilepton v_2 are shown. An ideal hydrodynamical calculation was used in the 0-10% centrality class, as there is no viscous correction incorporated in the NLO QGP rate.

is to show that no combination of two contributions is responsible for the majority of the total v_2 signal. That is, the mechanisms that modify the thermal contribution, such as those discussed in the next two sections, namely 5.1 and 5.2, should have a visible effect on the total elliptic flow of thermal dileptons and hence may be observable in experiment provided sufficient amount of data is collected. A comparison with experimental data is not particularly revealing at this time, since the experimentally measured dilepton $v_2(M)$ from the STAR collaboration still has significant statistical and systematic uncertainties [156].

4.6 Summary and outlook

In this chapter, all main sources of dileptons in the small and intermediate invariant mass range ($M \lesssim 2.5$ GeV) have been considered. As far as thermal sources are concerned, a detailed analysis has revealed that dileptons are rather sensitive viscometers of strongly interacting media. However, to be able to constrain the size of the shear viscosity from data, more dilepton sources needed to be taken into account. To this end, the contribution of open charm hadrons was included, along with improved QGP dilepton rates and cocktail dileptons. All three sources must be present to describe the dN/dM yield measured in experiment. However, given the large experimental uncertainties in the measurement of dielectron elliptic flow [156], a firm conclusion regarding the importance of these three sources to the overall $v_2(M)$ cannot be made at this point.

A careful examination of the results presented points to a window where thermal dilepton radiation is essential to describe the overall dilepton production present in data; this namely happens in a window roughly between 0.6 and 0.75 GeV in invariant mass. In that region the HM dileptons still dominate, and there is hope to constrain the size of η/s from experimental measurements in the hadronic sector, provided the cocktail is removed. Removing the contribution from open heavy flavor and looking at the anisotropic flow of dileptons in the intermediate mass region, further allows to constrain η/s in the QGP sector, while also generating better constraints on in the hadronic sector as well.

5

Sensitivity to initial conditions & transport coefficients

Having explored the different sources of dilepton production in the previous chapter, the main goal of this chapter is to explore the sensitivity of thermal dileptons to the dissipative properties of strongly interacting media.

Other than shear viscosity, the relaxation time τ_π is the second most important transport coefficient governing the size of shear viscous pressure. This transport coefficient will be investigated first and, unlike hadronic observables which have a modest sensitivity to τ_π, dileptons will be more sensitive to τ_π. Thus dileptons can be used to constrain the size of τ_π, provided more precise experimental anisotropic flow data is available. A similar statement holds true regarding the initial conditions of the shear viscous pressure. Furthermore, it will be shown that thermal dilepton anisotropic flow is sensitive to a temperature-dependent η/s in the QGP phase, for temperatures accessible in gold-gold collisions at RHIC, thus breaking the degeneracy observed in the anisotropic flow of charged hadrons. Hence, given the upcoming detector upgrades to be installed within the STAR detector at RHIC, most notably the Muon Telescope Detector (MTD), it may be possible to constrain various properties of strongly interacting matter, as the expected precision of the dilepton (i.e. dimuon) data coming from the MTD is significant. A brief exploration of dilepton emission from the Beam Energy Scan (BES) program at RHIC will also be presented.

As a last note, the effects of τ_π, $\eta/s(T)$, and initial conditions of the shear pressure tensor, will be presented sequentially in sections 5.1 and 5.2. Indeed, these transport coefficients/initial conditions will be varied one at a time, while keeping all other transport coefficients and initial/freeze-out conditions the same, so that their effects on the evolution of the medium are clear. A new set of initial conditions, based on the Glauber model, will however be used for the Beam Energy Scan results presented in section 5.3.

5.1 Effects of τ_π and initial conditions on dilepton anisotropic flow

As the more sophisticated QGP rates presented in Section 4.4 are not yet in a form that can include viscous corrections, only the Born QGP rate will be used for the rest of the thesis.

5.1.1 Initial and freeze-out conditions

The hydrodynamical equations assume that at a given time τ_0, chosen to be 0.4 fm/c, a hot and dense state of nuclear matter is created at rest in hyperbolic coordinate system, which was defined in the previous section. The initial energy density profile is assumed to be factorized into a longitudinal part and a transverse part. The energy density in the transverse direction is given by the Monte-Carlo Glauber (MC Glauber) model, specified in Eqs. (2.86) and (2.79), while the longitudinal part is given by Eq. (2.82), with the final expression for the energy density given in Eq. (2.83). N_{part} and N_{bin} are the number of participants and binary collision of a given event. The number and coordinates of participants and binary collisions is calculated taking the measured total nucleon-nucleon inelastic cross section at $\sqrt{s_{NN}}$ =200 GeV, which is σ_{NN} = 42.1 mb. The overall normalization ε_0 = 6.16 GeV/fm and α = 0.25 for all simulations was chosen by fitting the pion spectra and the charged hadron v_2, and similarly the fluctuation scale in Eq. (2.86) is taken to be σ = 0.4 fm.[1] The behavior of the energy density in the longitudinal direction is given in Eq. (2.82)

[1]The effects of varying σ on thermal photon production were first studied by [33]. However, hadronic observables [157, 34] were also shown to be sensitive to σ. So, to reach a more definitive conclusion regarding the sensitivity of thermal photons to σ, the effects of this parameter should be studied on hadron and photon production at the same time, so that features mostly/solely affecting thermal photons can be identified.

where the following values were used: $\eta_{\rm flat} = 5.9$ and $\eta_\sigma = 0.4$. The fit for the default hydrodynamical simulation, namely for $\tau_\pi = \frac{5\eta}{\varepsilon+P}$ and $\pi^{\mu\nu}(\tau_0) = 0$, to pion spectra and charged hadron v_2 was done in Ref. [158].

In the MC Glauber model, the centrality class is selected by sampling events in a certain range of impact parameters. For the 20–40% class sample events were chosen with impact parameters, $b_{\rm imp}$, ranging from $b_{\rm imp} = 6.7$–9.48 fm. For each value of τ_π and $\pi^{\mu\nu}(\tau_0)$ explored in this study, 200 MC Glauber events were generated, and each event is evolved via hydrodynamics.

Finally, one still has to provide initial conditions for the 4-velocity, u^μ, and shear-stress tensor, $\pi^{\mu\nu}$. Here, the initial flow profile was taken to be zero, i.e., $u^\mu_0 = (1,0,0,0)$ in (τ, η_s) coordinates, while the initial shear-stress tensor is always assumed to be proportional to its corresponding Navier-Stokes value,

$$\pi^{\mu\nu}(\tau_0) = c \times 2\eta\sigma^{\mu\nu}$$

with c being varied between 0 and 1. The hydrodynamical equations are solved until all cells have crossed the freeze-out hypersurface chosen to coincide with a constant temperature hypersurface $T_{FO} = 145$ MeV. This freeze-out temperature was obtained by fitting the hydrodynamical calculations to reproduce the observed hadron yield and elliptic flow.

5.1.2 *Modeling the relaxation time for the shear viscous pressure*

The hydrodynamical equations of motion are exactly the same as in section 4.1, except that now the relaxation time τ_π will be varied. Also, the partial chemical equilibrium equation of state taken from Ref. [21] is being used, with chemical equilibration present $T > 0.16$ GeV, and a partial chemical equilibrium prescription, which assumes that particle ratios remain fixed, exiting for all $T \leq 0.16$ GeV [159, 160].

Transport coefficients are in general complicated functions of the temperature (and the baryon chemical potential, if the net baryon number density is non-zero) that, in principle, should be computed from the underlying microscopic theory. However, reliable calculations of the aforementioned transport coefficients in the strongly coupled regime are not yet possible. Hence effective values for the shear viscosity coefficient, proportional to the entropy density, is used:

$$\frac{\eta}{s} = \frac{1}{4\pi}.$$

Meanwhile, the relaxation time is assumed to be of the form,

$$\tau_\pi = b_\pi \frac{\eta}{\varepsilon + P}, \tag{5.1}$$

with b_π being varied from 5 to 20, with the default value set at $b_\pi = 5$. Recall from the discussion surrounding Eq. (2.52) that in order to preserve causality, the coefficient b_π is constrained to be $b_\pi \geq 4/[3\,(1 - c_s^2)]$, where c_s is the velocity of sound [68].

The fluid-dynamical equations are solved numerically using the MUSIC 2.0 simulation code, an updated version of the simulation code presented in Ref. [29, 161, 162]. This simulation code has recently been tested against semi-analytic solutions of Müller-Israel-Stewart theory, and was shown to provide accurate solutions of such type of equations [163]. The simulations performed henceforth use a time step of $\Delta\tau = 0.03$ fm and a grid spacing of $\Delta x = \Delta y = 1/6$ fm and $\Delta\eta = 1/5$. Such values are small enough to ensure that the continuum limit for the particular observables studied is achieved.

5.1.3 Effect of the shear relaxation time on thermal dileptons

The shear relaxation time dictates the time it takes for the shear stress tensor $\pi^{\mu\nu}$ to relax towards the Navier-Stokes (NS) value, $\pi^{\mu\nu}_{NS} = 2\eta\sigma^{\mu\nu}$, as imposed by Eq. (4.1). Since hadrons are produced predominantly during the later phase of the medium's evolution, the shear relaxation time is only expected to have an effect on them if τ_π is of the order of the entire lifetime of the medium. On the other hand, electromagnetic probes are produced throughout the evolution, and should show a larger sensitivity to the value of the relaxation time, with the parametrization of the relaxation time given by Eq. (5.1). The effect of different relaxation times is modeled through the parameter b_π, which here is chosen to have three possible values $b_\pi = 5, 10, 20$. The initialization of $\pi^{\mu\nu}$ is taken to be $\pi^{\mu\nu}(\tau_0) = 0$. The dimensionless ratio $\bar{\pi}^{\mu\nu} = \pi^{\mu\nu}(\tau)/(\varepsilon + P)$ for

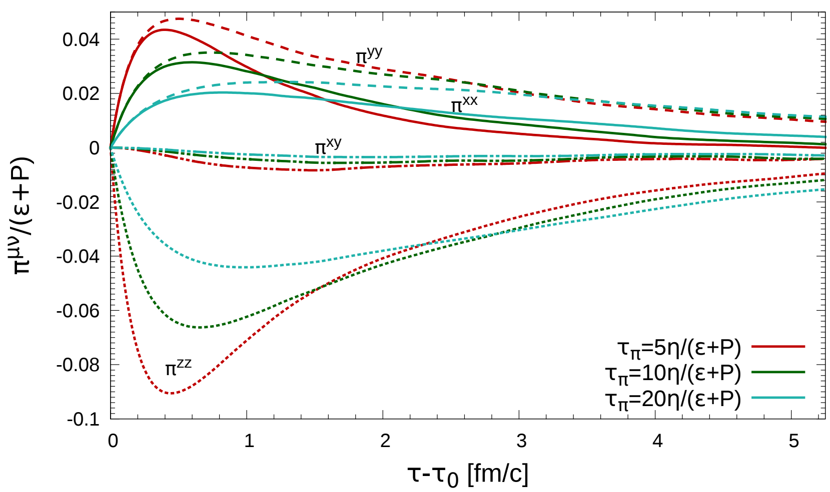

Figure 5.1: Event-averaged shear-stress tensor for $b_\pi = 5, 10, 20$ in the local rest frame of the fluid cell located at x=y=2.625 fm, z=0 fm. Results with $b_\pi = 5$ are in red, $b_\pi = 10$ in dark green and $b_\pi = 20$ in light green.

the three values of τ_π is shown in Fig. 5.1 for a given transverse position averaged over the 200 hydrodynamical events generated. Notice that $\bar{\pi}^{\mu\nu}$ builds up mostly at early times. This was first explained in Ref. [164]: the large pressure gradients in the longitudinal direction are reduced by the presence of a negative $\bar{\pi}^{zz}$. Furthermore, any non-vanishing $\bar{\pi}^{zz}$ component must be accompanied with a positive $\bar{\pi}^{xx}$ and $\bar{\pi}^{yy}$ components as $\bar{\pi}^{\mu\nu}$ is traceless in the rest frame of the fluid cell. Thus $\bar{\pi}^{\mu\nu}$ introduces a coupling between the longitudinal and transverse pressure gradients, and transfers part of the large pressure gradients present in the longitudinal direction onto the transverse plane [164]. Increasing τ_π postpones the build-up of $\bar{\pi}^{\mu\nu}(\tau)$ for a medium starting in perfect thermal equilibrium. This is manifested by a smaller build-up of $\bar{\pi}^{\mu\nu}(\tau)$ at early times, but also by the reduction of the decay rate of $\bar{\pi}^{\mu\nu}$ at late times. For this reason, $\bar{\pi}^{\mu\nu}(\tau)$ at late times is larger as τ_π increases.

Fig. 5.2 shows the pion transverse momentum spectra (a) and the elliptic flow of charged hadrons (b) for the three choices of relaxation time. The charged hadron v_2 displayed in Fig. 5.2 (b) corresponds to the root mean square value obtained from the 200 hydrodynamical events. Notice that changes in the relaxation time have little effect on pion transverse momentum spectrum and charge hadron v_2. This is

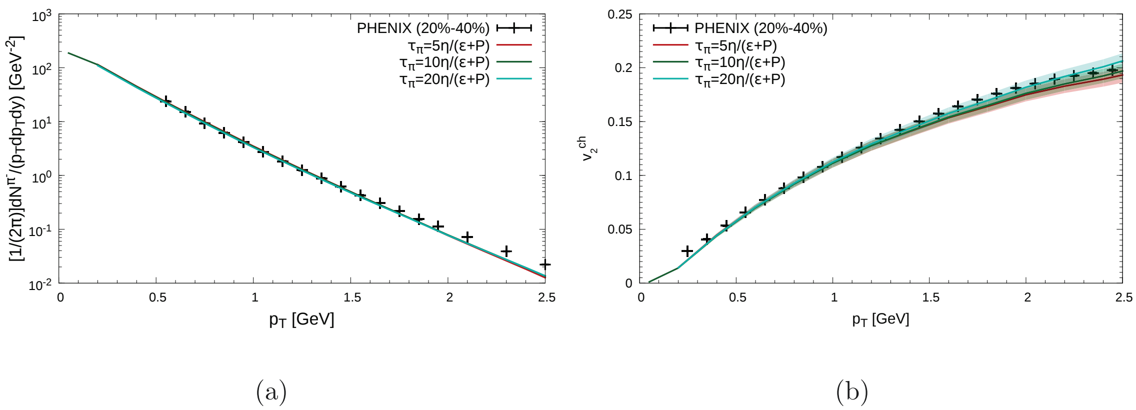

Figure 5.2: Pion transverse momentum spectra (a) and charged hadron differential elliptic flow (b) as a function of transverse momentum, for different values of shear relaxation time. The colored bands represent the statistical uncertainty associated with 200 hydrodynamical events.

consistent with the small differences seen in $\bar{\pi}^{\mu\nu}$ at late times in Fig. 5.1.

Since initial conditions come from the MC-Glauber model, a prescription for computing the anisotropic flow harmonics must be specified. The dilepton elliptic flow was computed using the scalar product method:

$$v_n^{\gamma^*} = \frac{\left\langle v_n^h v_n^{\gamma^*} \cos\left[n\left(\Psi_n^{\gamma^*} - \Psi_n^h\right)\right]\right\rangle_{\rm ev}}{\sqrt{\langle (v_n^h)^2 \rangle_{\rm ev}}} \tag{5.2}$$

where $\langle \ldots \rangle_{\rm ev}$ is an average over events. The v_n^s and Ψ_n^s in single event are given by

$$v_n^s e^{in\Psi_n^s} = \frac{\int dp_T dy d\phi p_T \left[p^0 \frac{d^3N^s}{d^3p}\right] e^{in\phi}}{\int dp_T dy d\phi p_T \left[p^0 \frac{d^3N^s}{d^3p}\right]} \tag{5.3}$$

where $p^0 d^3N^s/d^3p$ is the single-particle distribution of particle species s. The hadronic v_n^h and Ψ_n^h used in Eq. (5.2) are integrated over $-0.35 < \eta < 0.35$ and $0.035 < p_T <$ 3 GeV to simulate the large bin used experimentally by the PHENIX experiment at RHIC. Note that the hadron yield and elliptic flow is the same in both STAR and PHENIX experiments once their geometrical and efficiency limitations are taken into account. Thus either experiment can be used to fit the hydrodynamical parameters. The dilepton $v_n^{\gamma^*}$ and $\Psi_n^{\gamma^*}$ are evaluated at mid-rapidity however a more general single-particle distribution d^4N^s/d^4p is used in Eq. (5.3).

The differential elliptic flow of thermal dileptons $v_2(p_T)$ is presented in Fig. 5.3 (a), for a low invariant mass $M = m_\rho$ — where the p_T-integrated dilepton yield is

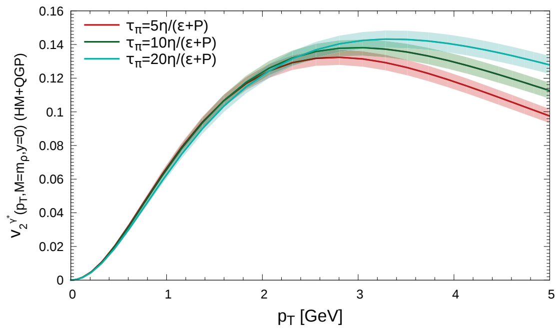

(a)

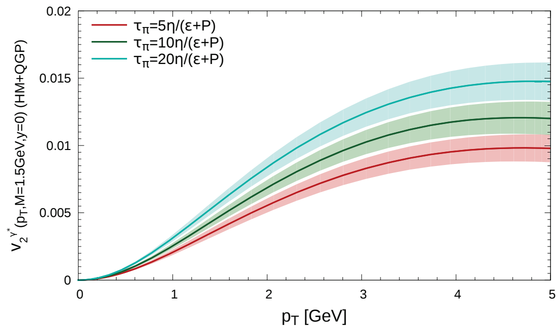

(b)

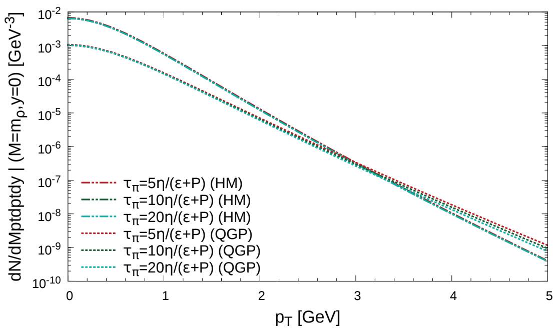

(c)

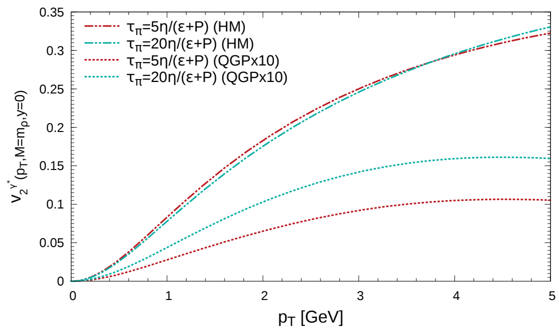

(d)

Figure 5.3: Differential elliptic flow of thermal dileptons for (a) $M = m_\rho$ and (b) $M = 1.5$ GeV as a function of transverse momentum, for different values of shear relaxation time. The HM and QGP contributions to the thermal p_T yield at $M = m_\rho$ is presented in (c) while (d) presents their contribution to the thermal $v_2(p_T)$. Error bands representing the statistical uncertainty associated with 200 hydrodynamical events were removed for visual clarity.

HM dominated. At low M, the $v_2(p_T)$ is affected by τ_π and increases it by more than 50% at large momenta ($p_T > 3$ GeV). This increase in the $v_2(p_T)$ at high p_T actually originates from the QGP contribution, as is clearly visible in the dilepton p_T yield depicted in Fig. 5.3 (c) and in the $v_2(p_T)$ of the individual dilepton sources shown in Fig. 5.3 (d). The elliptic flow of thermal dileptons emitted in the hadronic stage of the evolution is little affected by the relaxation time (at most 10%), while the elliptic flow originating from the QGP thermal dileptons displays a strong dependence on τ_π. Note that the elliptic flow of QGP dileptons in Fig. 5.3 (d) has been magnified by a factor of 10, so that the effects of τ_π can be clearly seen. Through not shown here, a similar behavior is observed with thermal photons [158]. The flow of intermediate mass dileptons in Fig. 5.3 (b), where QGP emission is the main source, has an increased sensitivity to τ_π, as expected. The effect of τ_π is not limited to $v_2(p_T)$, and is also affecting higher flow harmonics in a similar fashion, as can be seen in Fig. 5.4. Lastly, in Fig. 5.5 (a) and (b) elliptic flow of dileptons emitted from the QGP and HM is presented, respectively, this time as a function of the dilepton invariant mass.

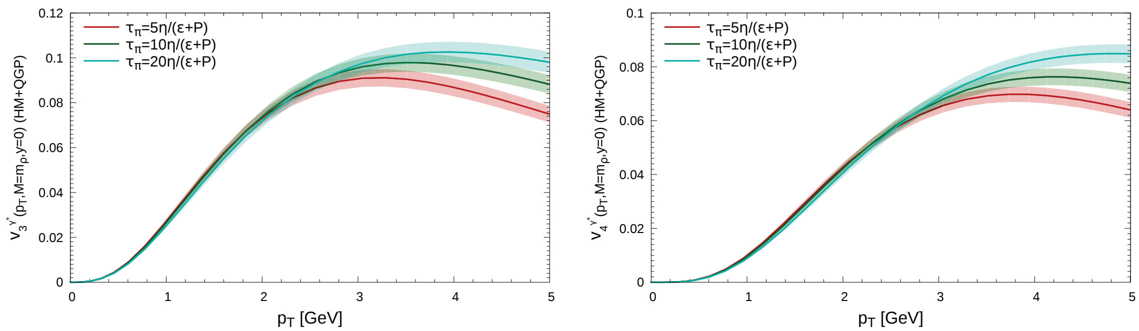

(a) (b)

Figure 5.4: Influence of τ_π on higher flow harmonics of thermal dileptons at $M = m_\rho$: (a) $v_3(p_T)$ (b) $v_4(p_T)$. The colored bands represent the statistical uncertainty associated with 200 hydrodynamical events.

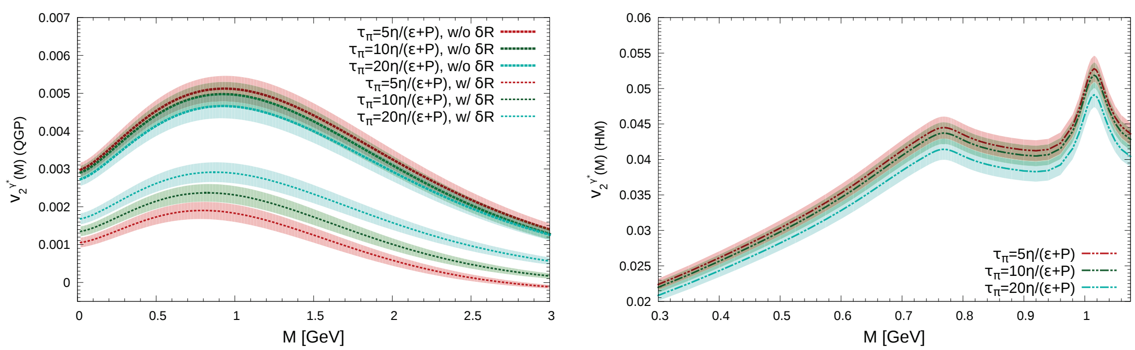

(a) (b)

Figure 5.5: Differential elliptic flow of dileptons emitted by the QGP (a) and emitted by the hadronic medium (b) as a function of the dilepton invariant mass, for different values of shear relaxation time. The effects of the viscous corrections to the QGP rate are presented in (a) whereas those of the HM rate are small, and hence only results using the rate including viscous corrections are presented. The colored bands represent the statistical uncertainty associated with 200 hydrodynamical events.

To understand the reason behind the opposite behavior of QGP and HM dileptons to τ_π one must look back at Fig. 5.1. At early times and for $\bar{\pi}^{\mu\nu}(\tau_0) = 0$, a system with large relaxation time takes longer to develop $\bar{\pi}^{\mu\nu}(\tau)$, i.e. it appears to be less viscous, since dissipative effects take longer to be developed. Thus, in the QGP phase the flow anisotropy develops faster with increasing τ_π. This is consistent with the smaller momentum anisotropy present in viscous hydrodynamics relative to ideal hydrodynamics. To fully understand the effects of τ_π on v_2 from the QGP, the contribution originating from the hydrodynamical evolution and that from the viscous δR corrections [see Eq. (3.84)] were separated. Indeed, the total QGP $v_2(M)$, i.e. the one with the viscous correction (δR) to the production rate, increases with τ_π (getting closer to the "ideal result"), while the importance of δR correction to the total QGP $v_2(M)$ decreases with larger τ_π. These two effects are supporting the assertion that the medium is less viscous early on. The reason why the QGP v_2 without the viscous δR correction decreases with τ_π, is coming from the fact that the presence of $\pi^{\mu\nu}$ will effectively increase the gradients $\partial^\mu u^\nu$. Indeed, without viscous corrections, one is lead to the incorrect interpretation that the medium develops anisotropic flow faster when viscosity is present relative to the inviscid case. This was in fact first shown for the case of viscous photon in Ref. [126]. Hence one must take into account the full $T^{\mu\nu}$ to get the correct interpretation, thus viscous δR corrections are crucial.

At later stages however, the system has had more time to develop dissipative effects, and in fact becomes more viscous, i.e. develops a larger $\bar{\pi}^{\mu\nu}$ [see Fig. 5.1], hence the flow develops slower as can be seen in Fig. 5.5 (b) giving $v_2(M)$ of HM dileptons. This is in agreement with Fig. 5.3 (a) [see also HM results in 5.3 (d)] at low p_T and low M. Not shown here is the role played by δR corrections in the HM sector, but from the discussion in section 4.1 and the actual calculation without δR corrections in the hadronic sector, it is found that δR corrections play a small role in the overall size of $v_2(M)$ from the HM. Thus, larger values of τ_π, which generate a more viscous system at late times, actually lead to smaller a elliptic flow coefficient; a 10% effect[1].

Fig. 5.6 displays the total (QGP+HM) thermal dilepton elliptic flow as a function

[1]The reduction in $v_2(p_T)$ is also seen in hadronic photon v_2 at low p_T, thus confirming the dilepton result [158].

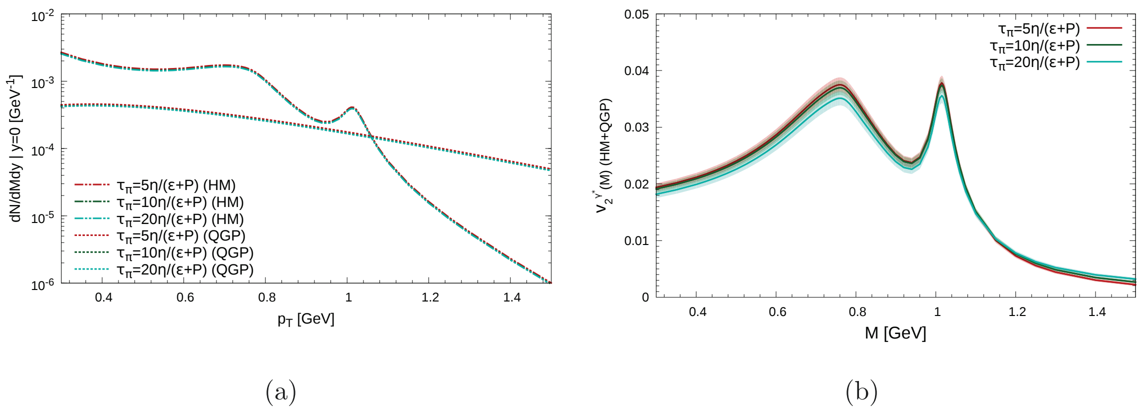

Figure 5.6: Elliptic flow of dileptons as a function of the dilepton invariant mass, for different values of shear relaxation time. The colored bands represent the statistical uncertainty associated with 200 hydrodynamical events.

of invariant mass, for all three values of the shear relaxation time. At small invariant masses, $M < 1.1$ GeV, the HM dileptons are dominant and one sees that the elliptic flow is reduced as the relaxation time increases. On the other hand, for larger invariant masses, $M > 1.1$ GeV, the QGP contribution starts to dominate and the dependence on the relaxation time is inverted. One should note that the invariant mass over which this behavior switches (here, $M \approx 1.1$ GeV) is not universal and depends on other parameters, such as the freeze-out temperature and the initialization time. If one starts the simulation earlier, more QGP thermal dileptons can be emitted, while if one decreases the freeze-out temperature, more hadronic dileptons are emitted. In fact, because of the initial and freeze-out conditions chosen, the net effect of τ_π on the total thermal $v_2(M)$ is not large; there being incomplete cancellations between the behavior in the QGP and HM sectors. So, one should always take into account the initial and freeze-out conditions when interpreting results of thermal dilepton (and photon) emissions in heavy-ion collision simulations.

5.1.4 Effect of different initial shear-stress tensors

The Navier-Stokes limit of $\pi^{\mu\nu}$, which is rescaled by a constant c, is used as an ansatz for the initial shear-stress tensor:

$$\pi^{\mu\nu}(\tau_0) = c \times 2\eta\sigma^{\mu\nu},$$

where $\sigma^{\mu\nu} = \Delta^{\mu\nu}_{\alpha\beta}\partial^\alpha u^\beta$ as in Eq. (4.1). Three different values of $c = 0, \frac{1}{2}, 1$ are explored. The case $c = 1$ corresponds to the Navier-Stokes limit. The relaxation time

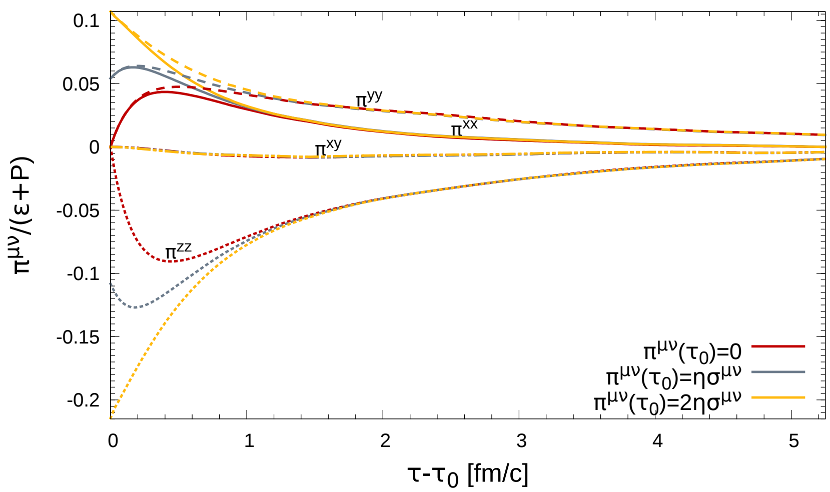

Figure 5.7: Shear-stress tensor for $c = 0, 1/2, 1$ in the local rest frame of the fluid cell located at x=y=2.625 fm, z=0 fm, averaged over all events. Results with $c = 0$ are displayed in red, $c = 1/2$ in gray, and $c = 1$ in yellow.

is kept at its default value $\tau_\pi = 5\eta/(\varepsilon + P)$ for this whole section. As was shown in the previous section, the choice of τ_π is important since it determines the timescale for $\pi^{\mu\nu}$ to converge to the Navier-Stokes limit from the chosen initial conditions. To quantify this effect, Fig. 5.7 shows the time dependence of various components of $\bar{\pi}^{\mu\nu}(\tau) = \frac{\pi^{\mu\nu}}{(\varepsilon+P)}$, in the rest frame of the fluid, for the three different choices of initial conditions. Notice that differences in $\bar{\pi}^{\mu\nu}$ at early times are washed out within about 1.5 fm/c, which is about a quarter of the medium's lifetime (see Fig. 5.7). This implies that hadrons should be largely insensitive to such changes in the initial $\pi^{\mu\nu}$, although dileptons (and photons) produced early enough stages of the collision should be affected by different initial conditions. Thus, the spectra and v_2 of hadrons (Fig. 5.8) — showing a very weak dependence on the initial $\pi^{\mu\nu}$ – comes as no surprise, as this was already anticipated from Fig. 5.7. The dilepton spectra and $v_2(p_T)$ at $M = m_\rho$ are shown on Figs. 5.9 (a) and (b) respectively. The effect of the initial $\pi^{\mu\nu}$ on the dilepton p_T-spectra is not large, similar to that seen on hadrons. The effect on $v_2(p_T)$ is also small, but shows more features: a small increase at low p_T

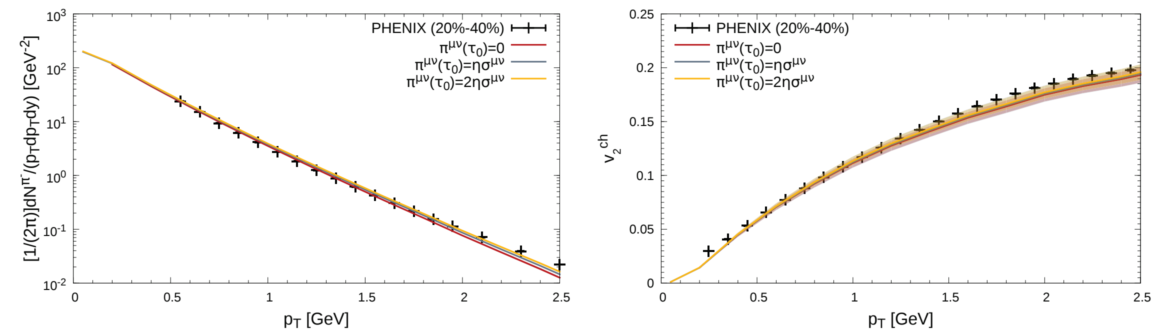

(a) (b)

Figure 5.8: Pion transverse momentum spectra (a) and charged hadron differential elliptic flow (b) as a function of transverse momentum, for different values of the initial shear-stress tensor. The colored bands represent the statistical uncertainty associated with 200 hydrodynamical events.

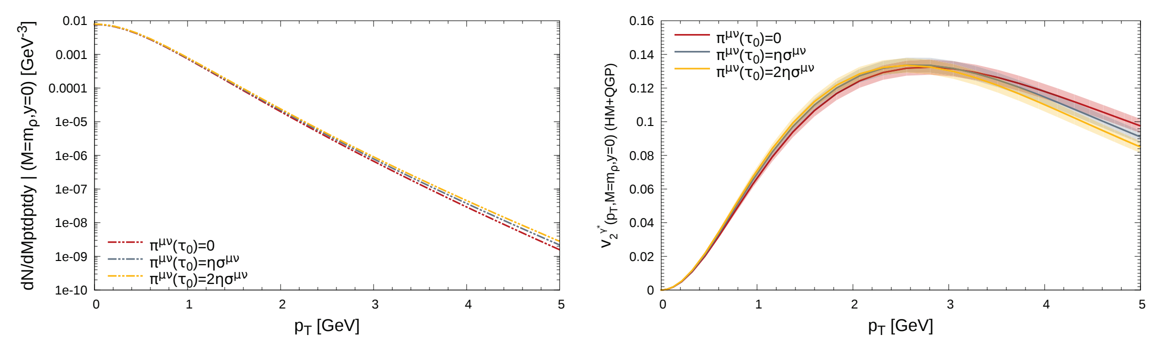

(a) (b)

Figure 5.9: Transverse momentum spectra (a) and elliptic flow of thermal dileptons (b) as a function of transverse momentum at $M = m_\rho$, for different values of initial $\pi^{\mu\nu}$. The colored bands represent the statistical uncertainty associated with 200 hydrodynamical events.

but the reverse behavior that higher p_T. To better understand the origin of these features, Fig. 5.10 shows the v_2 without and with the effect of δR to the production rate, which isolates the effects of the hydrodynamical feedback of the initial $\pi^{\mu\nu}$ on the temperature and flow profiles from changes due to $\pi^{\mu\nu}$ on the production rate. Indeed, the effect of the initial $\pi^{\mu\nu}$ on the hydrodynamical evolution is not small, and alone produces a significant increase of the $v_2(p_T)$. The change of behavior seen at high p_T is thus solely due to the effect of the viscous correction δR to the production rate. It is more apparent at high p_T because the viscous correction to the rate is larger in that region. Furthermore, higher flow harmonics as a function of p_T are are

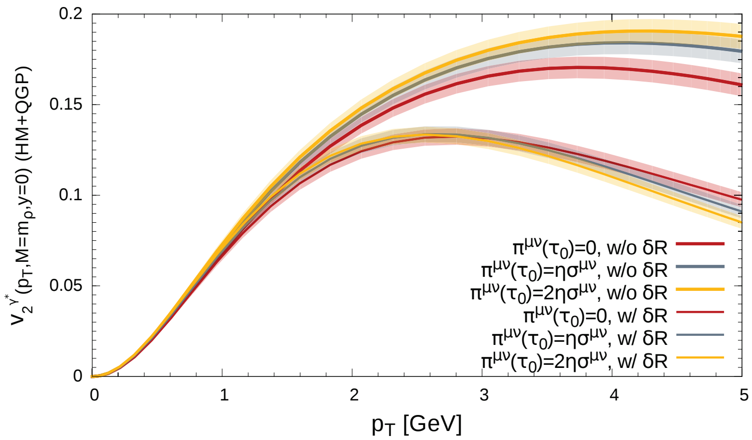

Figure 5.10: Thermal dilepton elliptic flow with and without viscous corrections (δR) to the emission rates. The colored bands represent the statistical uncertainty associated with 200 hydrodynamical events.

affected in very similar way to v_2. Hence, focus will immediately be shifted on the invariant mass distribution.

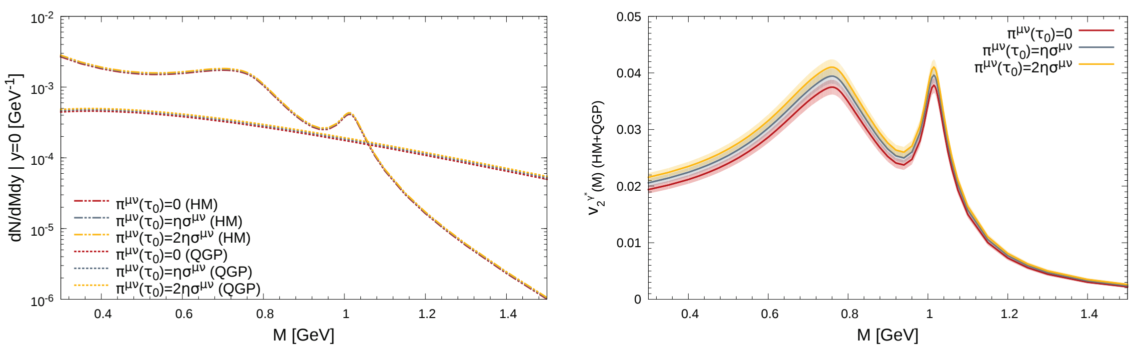

(a) (b)

Figure 5.11: Elliptic flow of dileptons as a function of the dilepton invariant mass, for different values of shear relaxation time. The colored bands represent the statistical uncertainty associated with 200 hydrodynamical events.

The invariant mass yield of thermal dileptons doesn't depend on any viscous corrections[1] and hence it is only sensitive to the entropy generation that a non-zero $\pi^{\mu\nu}(\tau_0)$ injects into the system, which is small as can be seen in Fig. 5.11 (a). Also,

[1]After performing a tensor decomposition on δR, and integrating over the 3-momentum $\mathbf{q}$, the only tensor that can be constructed is proportional to $u_\mu u_\nu$ which vanishes when contracted with $\bar{\pi}^{\mu\nu}$. Hence the invariant mass distribution of dilepton yield must be independent of δR.

since the invariant mass yield is unaffected by δR, $v_2(M)$ from both thermal sources behaves in a more monotonic fashion as $\pi^{\mu\nu}(\tau_0)$ increases [see Fig. 5.11 (b)].

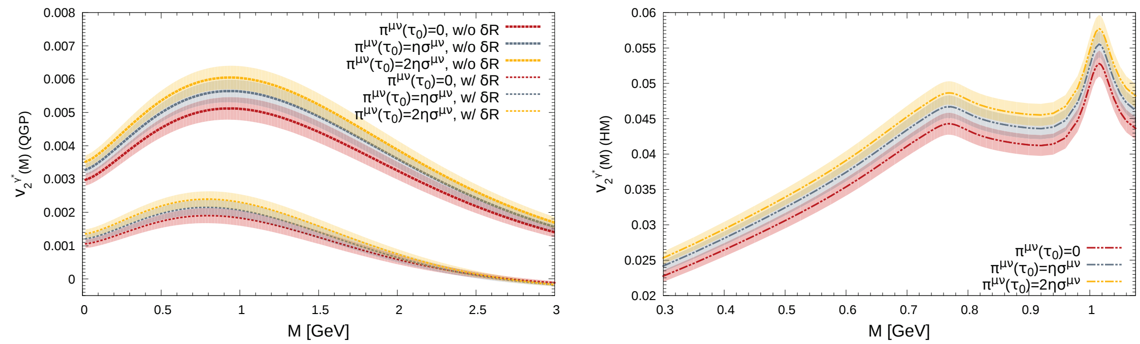

(a) (b)

Figure 5.12: Differential elliptic flow of dileptons emitted by the QGP (a) and emitted by the hadronic medium (HM) (b) as a function of the dilepton invariant mass, for different values of initial shear stress tensor. As was done in the previous section, only the QGP dileptons are calculated with and without viscous corrections δR to the rate, while the HM dileptons are calculated with viscous δR corrections to the rate. The colored bands represent the statistical uncertainty associated with 200 hydrodynamical events.

Similarly to $v_2(p_T)$ without δR, $v_2(M)$ for the QGP in Fig. 5.12 (a) increases with $\pi^{\mu\nu}(\tau_0)$, while the viscous corrections are mostly reducing the v_2. The shape of the $v_2(M)$ changes somewhat at higher M as $\pi^{\mu\nu}(\tau_0)$ increases owing to δR effects in the numerator of v_2, however those viscous corrections are not inverting the order of the $v_2(M)$ curves, unlike for $v_2(p_T)$, and are giving a definite trend as far as the behavior of the elliptic flow with increasing $\pi^{\mu\nu}$. The dilepton HM sector behaves monotonically as a function of M as $\pi^{\mu\nu}(\tau_0)$ increases, as shown in Fig. 5.12 (b), receiving an increase of at most $\sim 10\%$ by the time $\pi^{\mu\nu}(\tau_0) = 2\eta\sigma^{\mu\nu}$. Again, though the effect is small, it is the increasing trend that is important. In fact, a simpler Optical Glauber calculation was performed with $\pi^{\mu\nu}(\tau_0) = 4\eta\sigma^{\mu\nu}$ [165], which shows that the dilepton elliptic flow is still increasing while the hadronic $v_2(p_T)$ remains largely insensitive to $\pi^{\mu\nu}(\tau_0)$. Hence, $v_2(M)$ of QGP and HM are directly exposing the modifications of the hydrodynamical evolution.

The reason for the increase in v_2 with $\pi^{\mu\nu}(\tau_0)$ is coming from the large pressure gradients in the longitudinal direction, which are more significantly reduced via a non-zero $\pi^{zz}(\tau_0)$, and thus are more efficiently transferred onto the transverse plane.

This coupling of the longitudinal and transverse pressure gradients causes an increase in the $v_2(M)$ of QGP dileptons. The elliptic flow of HM dileptons is also increased owing to the fact that a cross-over phase transition allows for HM dileptons to be emitted from early times before $\pi^{\mu\nu}$ has relaxed to the Navier-Stokes value. Thus $v_2(M)$ of HM dileptons is also increased.

5.1.5 *Summary regarding the effects of τ_π and $\pi^{\mu\nu}(\tau_0)$*

In summary, the shear relaxation time has a significant effect dilepton $v_2(p_T)$ and higher flow harmonics, with larger values of relaxation time leading to an increase of anisotropic flow. The same statement holds true for thermal photons [158], while charged hadrons' $v_2(p_T)$ is largely insensitive to variations in τ_π chosen here. Thus electromagnetic (EM) probes may be used in the future to probe or even constrain the size of the relaxation time of QCD matter. In addition EM radiation is sensitive to the initial conditions, that is the initial shear stress tensor $\pi^{\mu\nu}(\tau_0)$: elliptic flow of thermal dileptons as a function of invariant mass is increased as one raises $\pi^{\mu\nu}(\tau_0)$. Charged hadrons on the other hand are poorly affected by $\pi^{\mu\nu}(\tau_0)$.

The planned improvements to the STAR detector will allow for precise heavy flavor tracking, which can be used to not only study the effects of the medium on open heavy flavor propagation, but also to remove their signal from the measured dilepton flow in the intermediate mass region. Performing this subtractions in experimental dilepton data opens a window to directly measure the transport coefficients of QGP, and possibly constrain τ_π and $\pi^{\mu\nu}(\tau_0)$.

The final point to be made here is that the traditional procedure to fix the free parameters involved in the fluid description of heavy-ion collisions using just hadronic observables is not sufficient. Indeed, different sets of parameters leading to almost the same value of hadronic observables, impose different values of dilepton elliptic flow. In this sense, a more constraining way to describe the medium would be to simultaneously use dilepton (and photon) radiation along with hadronic emissions to obtain a global fit varying all hydrodynamical free parameters at the same time.

5.2 Sensitivity to a temperature-dependent shear viscosity of the QGP

Throughout this section, the initial shear-stress tensor was set to vanish, while all the other initial and freeze-out conditions are the same as those outlined in the previous section. As far as transport coefficients are concerned, the default value for $\tau_\pi = 5\eta/(\varepsilon + P)$ was used throughout, and $\eta/s(T)$ is the only parameter that will be varied.

5.2.1 *Temperature-dependent shear viscosity*

Since reliable calculations of the shear viscosity in the strongly coupled regime are not yet possible[1], one is phenomenologically motivated to assume some analytic form of the temperature dependence for the shear viscosity-to-entropy density ratio. The two simplest forms are a linear and a quadratic dependence of η/s:

$$\begin{aligned} \frac{\eta}{s}(T) &= m\left(\frac{T}{T_{tr}} - 1\right) + \frac{1}{4\pi}, \\ \frac{\eta}{s}(T) &= a\left(\frac{T}{T_{tr}} - 1\right)^2 + \frac{1}{4\pi} \end{aligned} \tag{5.4}$$

where $T_{tr} = 0.18$ GeV, while $m = 0.5516, 0.2427$ and $a = 0.4513, 0.1986$ are selected such that $\frac{\eta}{s} = 0.755$ at $T = 0.4$ GeV, and half that value, respectively. Fig. 5.13 illustrates all the various forms of temperature dependence used in this calculation. The parametrization chosen here is inspired by Ref. [31].

5.2.2 *Anisotropic (viscous) correction to dilepton production rates: Generalizing the Israel-Stewart (I-S) ansatz*

In order to have consistent calculation of dilepton production when a viscous hydrodynamical simulation is used, dilepton emission rates need to take into account deviations from local thermodynamic equilibrium in both the hadronic and QGP sector. However, when shear viscosity is large in the QGP sector, which can occur with

[1]At present, there is only one calculation of the shear viscosity coefficient in the strong coupling regime, using lattice techniques, and that study done using a pure SU(3) gauge theory [166].

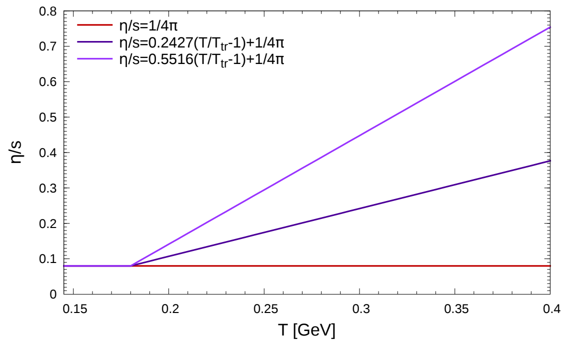

(a)

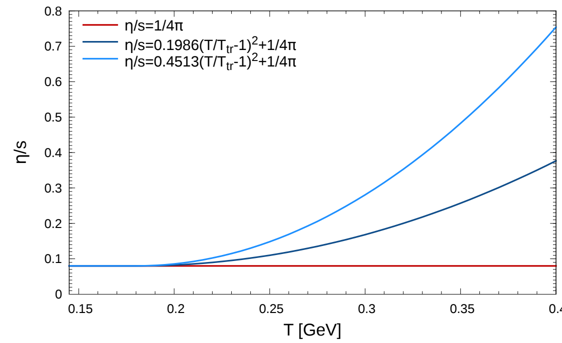

(b)

Figure 5.13: Linear (a) and quadratic (b) temperature dependence of $\frac{\eta}{s}$.

a temperature dependent $\frac{\eta}{s}$, the dilepton rates become more sensitive to the form of the viscous correction $\delta n_{\mathbf{k}}$ to the thermal single-quark momentum distribution. The correction $\delta n_{\mathbf{k}}$ can be modified to meet the additional requirement imposed by a temperature dependent $\frac{\eta}{s}$. Thus, a generalized version of the quark distribution function $n_{\mathbf{k}}$ is used:

$$n_{\mathbf{k}} = \left[\exp\left(y_{\mathbf{k}}\right) + 1\right]^{-1} \tag{5.5}$$

where $y_{\mathbf{k}} = y(k^\nu, u^\nu; T, \mu)$. Assuming $y_{\mathbf{k}} = y_{0,\mathbf{k}} + \delta y_{\mathbf{k}}$, where $y_{0,\mathbf{k}} = (u^\nu k_\nu - \mu)/T$ and $\delta y_{\mathbf{k}} \ll y_{0,\mathbf{k}}$, one can expand Eq. (5.5) to leading order in $\delta y_{\mathbf{k}}$, yielding

$$\begin{aligned} n_{\mathbf{k}} &= n_{0,\mathbf{k}} + \delta n_{\mathbf{k}} \\ \delta n_{\mathbf{k}} &= n_{0,\mathbf{k}} \left[1 - n_{0,\mathbf{k}}\right] \delta y_{\mathbf{k}} \end{aligned} \tag{5.6}$$

where $n_{0,\mathbf{k}} = \left[\exp\left(y_{0,\mathbf{k}}\right) + 1\right]^{-1}$ is the Fermi-Dirac distribution. Expanding out $\delta y_{\mathbf{k}}$ gives

$$\delta y_{\mathbf{k}} = \mathcal{G}_{\mathbf{k}} \frac{\pi^{\mu\nu} k_\mu k_\nu}{\left[2T^2(\varepsilon + P)\right]}, \tag{5.7}$$

where $\mathcal{G}_{\mathbf{k}}$ was first introduced in Eq. (2.92). To determine $\mathcal{G}_{\mathbf{k}}$ a microscopic theory must be used. Assuming that that theory is the Boltzmann equation describing a massless gas of particles with constant interaction cross section, $\mathcal{G}_{\mathbf{k}}$ is computed to be (see Appendix B for details)

$$\mathcal{G}_{\mathbf{k}}^{\mathrm{low/high}} = \begin{cases} \frac{5.12}{0.1+x}\left[a_1 + a_2 x + a_3 x^2 + a_4 x^3\right] & \forall x < x_0 \\ \frac{161.8484462}{(0.1+x)^4}\left[b_1 + b_2 x + b_3 x^2 + b_4 x^3\right] & \forall x > x_0 \end{cases} \tag{5.8}$$

where $x = \frac{k\cdot u}{T}$, $\mathcal{G}_{\mathbf{k}}^{\mathrm{low}}$ valid for $x < x_0$, while $\mathcal{G}_{\mathbf{k}}^{\mathrm{high}}$ is well behaved for $x > x_0$, where x_0=11.2. The coefficients a_i and b_i are given in Table 5.1.

Table 5.1: The parameters a_i and b_i used in $\mathcal{G}_{\mathbf{k}}^{\mathrm{low/high}}$.

i	1	2	3	4
a_i	0.40460300	0.15593117	-0.00740483	0.0001693308
b_i	-0.25870870	0.47053682	-0.24183275	0.065467807

The two regions are matched via

$$\mathcal{G}_{\mathbf{k}} = \left[\frac{1-\tanh(2x-2x_0)}{2}\right]\mathcal{G}_{\mathbf{k}}^{\mathrm{low}} + \left[\frac{1+\tanh(2x-2x_0)}{2}\right]\mathcal{G}_{\mathbf{k}}^{\mathrm{high}}. \tag{5.9}$$

Given the functional form of $\delta y_{\mathbf{k}}$ is compatible with the derivation of the viscous correction δR to the dilepton rate in Chapter 3, the same procedure can be used to compute the new viscous correction to the rate. Using the projection operator of Eq. (3.82), the viscous correction to the dilepton rate from the QGP is:

$$\begin{aligned} \frac{d^4\delta R}{d^4q} &= \frac{q^\alpha q^\beta \pi_{\alpha\beta}}{2T^2(\epsilon+P)} b_2(q^0/T, |\mathbf{q}|/T) \qquad (5.10)\\ \frac{d^4\delta R}{d^4q} &= \frac{q^\alpha q^\beta \pi_{\alpha\beta}}{2T^2(\epsilon+P)}\left[C_q \frac{q^2}{2}\frac{\sigma}{(2\pi)^5}\frac{1}{|\mathbf{q}|^5}\int_{E_-}^{E_+} dE_{\mathbf{k}} n_{0,\mathbf{k}}[1-n_{0,\mathbf{k}}] n_0(q\cdot u - k\cdot u) D'\right] \end{aligned}$$

where $E_\pm = \frac{q^0 \pm |\mathbf{q}|}{2}$, n_0 is also the Fermi-Dirac distribution which a slightly different argument than $n_{0,\mathbf{k}}$, while

$$D' = \left[(3q_0^2 - |\mathbf{q}|^2)E_{\mathbf{k}}^2 - 3q^0 E_{\mathbf{k}} q^2 + \frac{3}{4}q^4\right]\mathcal{G}_{\mathbf{k}}, \tag{5.11}$$

and $C_q \approx 0.99$. The complete QGP rate can therefore be expressed as $\frac{d^4R}{d^4q} = \frac{d^4R_0}{d^4q} + \frac{d^4\delta R}{d^4q}$, where the first and second terms are found in Eq. (3.70) and Eq. (5.10), respectively.

It is difficult to compare the viscous correction δR directly to the isotropic rate R_0, which from now on will be called the ideal rate, given that the viscous correction depends on the size of $\pi^{\mu\nu}$ at a space-time point. What can be done, however, is to compare the envelope of the viscous correction, namely the function b_2, to the ideal rate. Therefore it is instructive to study the ratio

$$A(q^0/T, |\mathbf{q}|/T) = \frac{b_2(q^0/T, |\mathbf{q}|/T)}{\frac{d^4R_0}{d^4q}}, \tag{5.12}$$

and see how it changes going from I-S viscous correction to the one in Eq. (5.10). The ratio A has a very weak dependence on $|\mathbf{q}|/T$, hence evaluating $|\mathbf{q}|/T = 0$ is sufficient. Fig. 5.14 shows that the ratio A of the I-S viscous correction is bounded between 1/3

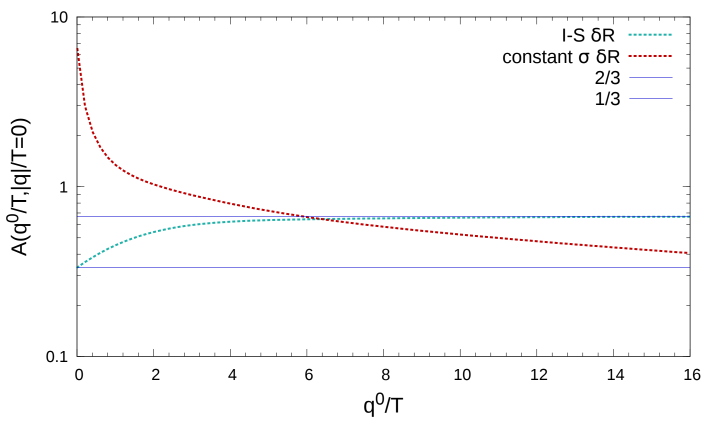

Figure 5.14: Relative size of the envelope of the viscous correction relative to the (ideal) isotropic rate.

and 2/3. Since $\frac{q^\alpha q^\beta \pi_{\alpha\beta}}{2T^2(\epsilon+P)}$ is well behaved in the vanishing q^μ limit, the lower bound on A is not a source of concern. Thus using only the upper bound, the I-S correction to the QGP dilepton rate becomes ill-behaved when $\frac{q^\alpha q^\beta \pi_{\alpha\beta}}{2T^2(\epsilon+P)} > 3/2$. In that respect, the new viscous correction is better behaved at large q^0/T as $A \sim (q^0/T)^{-1}$, and is furthermore is finite at $q^0/T = 0$. Such a suppression at large q^0/T will definitely help δR to remain as small as possible (relative to R_0) when a large $\pi^{\mu\nu}$ is present due to a $\frac{\eta}{s}(T)$.

In the Hadronic Medium (HM), the viscous corrections to the dilepton rates are accounted for through a modification of the vector meson self-energy. Since the modification to the self-energy $\delta\Pi$ [see Eq. (3.85)], originating from the I-S viscous correction to the thermal distribution, is a very steeply falling function of $(M, \mathbf{q})$ [5], there is no need to devise a different viscous correction.

5.2.3 *Linear* $\frac{\eta}{s}(T)$

The goal of this section is to investigate the sensitivity of thermal dileptons to the size of $\frac{\eta}{s}(T)$'s slope. Since the effects a temperature dependent $\frac{\eta}{s}$ induces on the evolution of the medium are rather complex, keeping identical initial conditions, regardless of any entropy production that $\frac{\eta}{s}(T)$ introduces, is important. Furthermore, since the amount of entropy generation is smaller than the effects $\frac{\eta}{s}(T)$ instigates on the anisotropic evolution of the system, compensating for entropy production by changing in initial/freeze-out conditions is not mandatory.

To quantify the amount of entropy and radial flow generated via a linearly dependent $\frac{\eta}{s}(T)$, the yield of thermal dileptons as a function of M and the yield of pions as a function of p_T is plotted in Fig. 5.15. Note that the differential yield of pions is also sensitive to δn effects. The invariant mass thermal dilepton yield is increased

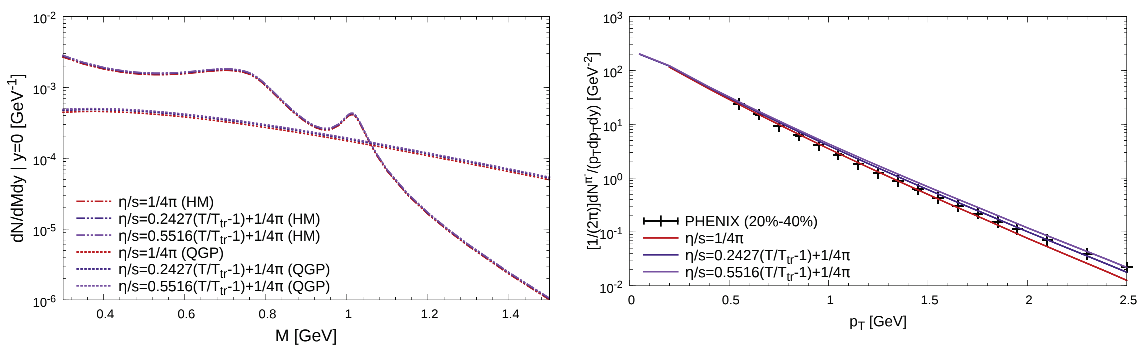

(a) (b)

Figure 5.15: Yield of thermal dileptons (a) and pions (b) for various values of $\frac{\eta}{s}(T)$.

by 5% in the HM region while the QGP region receives an increase of 10%, when comparing the red and light purple curves in Fig. 5.15 (a). Since M is a Lorentz invariant quantity, the increase in the invariant mass yield is a measure of the entropy production of a dissipative system. The somewhat larger increase in the pion yield at

$p_T \gtrsim 1$ GeV [see Fig. 5.15 (b)] is explained by a combination of a greater radial flow and larger δn effects, while entropy production and radial flow explains the increase in the yield at $p_T \lesssim 1$ GeV. However, this larger radial flow is not affecting the elliptic flow of charged hadrons at RHIC energies as can be seen in Fig. 5.16 (a), and was first noticed in Ref. [31].

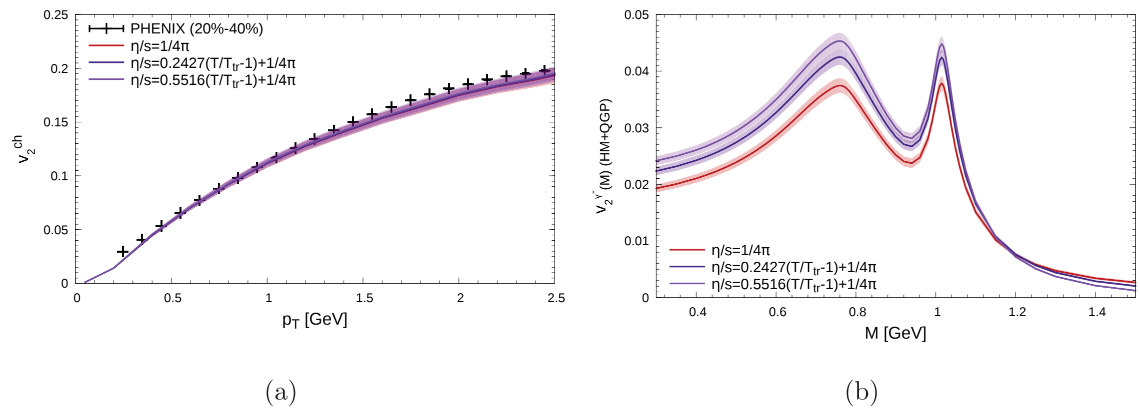

Figure 5.16: Elliptic flow of charged hadrons (a) and thermal dileptons (b) with different slopes of $\frac{\eta}{s}(T)$. The colored bands represent the error bands associated with the 200 events used in this study.

On the other hand, a linearly dependent $\frac{\eta}{s}(T)$ changes the flow of thermal dileptons quite substantially [see Fig. 5.16 (b)]. Even though the temperature dependence is present solely in the QGP phase, a different evolution of the fluid will occur in the HM and QGP sectors. It is therefore instructive to look at the HM and QGP contributions individually to understand mechanisms responsible for the modified evolution in both sectors of the fluid. The elliptic flow of the QGP in Fig. 5.17 (a) without viscous corrections δR, is increased with $\frac{\eta}{s}(T)$, owing to the fact that (i) $\pi^{\mu\nu}$ at early times increases the velocity gradients of the fluid and (ii) R_0 solely couples to fluid velocity u^μ and temperature T and hence is directly sensitive to increase in velocity gradients. On the other hand, δR couples to $\pi^{\mu\nu}$ in addition to u^μ and T, and is responsible for decreasing the elliptic flow as shown in section 4.1. This is also confirmed in Fig. 5.18 (a), where ideal $T^{\mu\nu}$ refers to the momentum anisotropy $\langle T^{xx} - T^{yy}\rangle / \langle T^{xx} + T^{yy}\rangle$ computed using only $T^{\mu\nu}_{(0)}$ of a viscous evolution, while the full $T^{\mu\nu}$ curves also include $\pi^{\mu\nu}$ contribution. The momentum anisotropy of the QGP

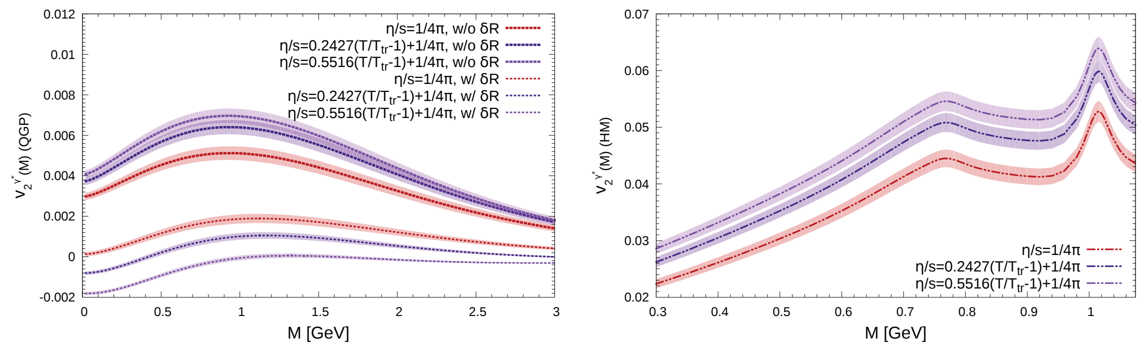

(a) (b)

Figure 5.17: Elliptic flow of QGP (a) and HM (b) dileptons with different slopes of $\frac{\eta}{s}(T)$. The colored bands represent the statistical uncertainty associated with 200 hydrodynamical events.

was obtained after integrating over all fluid cells in the QGP phase and averaging over 200 hydro events. A similar averaging was done in the HM phase.

The reason why the QGP $v_2(M)$ goes negative comes from the fact that the event plane angle, along which particles are preferentially emitted, for QGP dileptons and charged hadrons is misaligned. Indeed, if $\pi/2 < n(\Psi_n^{\gamma^*} - \Psi_n^h) < 3\pi/2$, any flow harmonic will automatically become negative. This misalignment between the angles $\Psi_n^{\gamma^*}$ and Ψ_n^h is evident in Fig. 5.18 [see curves labeled full $T^{\mu\nu}$ in (a) and (b)] and is responsible for driving the $v_2(M)$ of QGP dileptons to become negative.[1] Indeed, Fig. 5.18 (a) shows that the development of anisotropy is slower in the cases where $\frac{\eta}{s}(T)$, causing large differences between $\Psi_n^{\gamma^*}$ and Ψ_n^h which are driving v_2 to negative values. Physically, a medium with a large viscosity at large temperatures is keeping the original geometrical anisotropy, of the part of the medium that is mostly in the QGP phase, in a more prolate configuration for the first 1.5 fm/c of evolution; clearly seen in Fig. 5.18 (a) using the full $T^{\mu\nu}$. During the same 1.5 fm/c of evolution, the rest of the medium, which is mostly in the HM sector, evolves as expected given that it has $\frac{\eta}{s} = \frac{1}{4\pi}$. Furthermore, the medium with $\frac{\eta}{s}(T)$ has more entropy production at early times that the one with $\frac{\eta}{s} = \frac{1}{4\pi}$. Taking these two effects into account, one can conclude that a medium with $\frac{\eta}{s}(T)$ in the QGP phase will cool slower at early times

[1]Note that the misalignment is caused by δR.

than the one with $\frac{\eta}{s} = \frac{1}{4\pi}$, as can be seen in Fig. 5.19 (a).

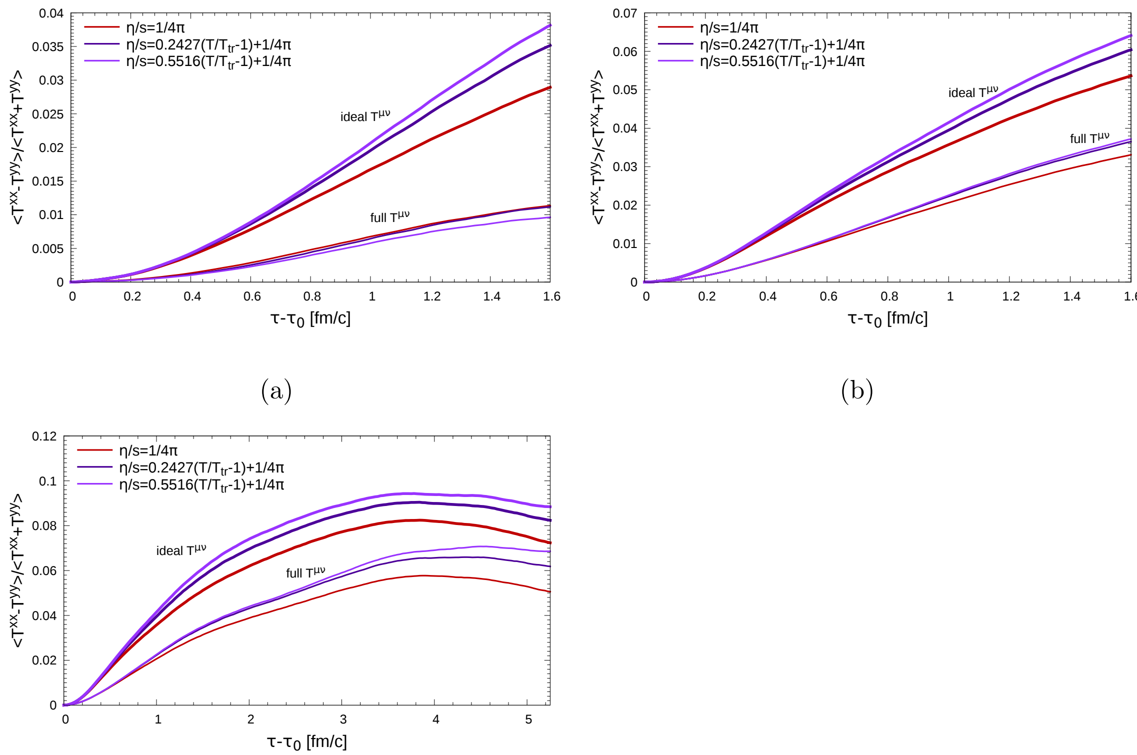

(a) (b)

(c)

Figure 5.18: Momentum anisotropy of the fluid. The QGP phase is in (a), the HM sector at early times is in (b), while (c) shows the HM anisotropy evolution for a larger time span. The meaning of ideal/full $T^{\mu\nu}$ is explained in the text.

However, such a situation cannot be maintained indefinitely, since hotter media (with $\frac{\eta}{s}(T)$) will exert more pressure than the one with $\frac{\eta}{s} = \frac{1}{4\pi}$. So, as soon as the viscosity is low enough for the anisotropic pressure gradients to start developing anisotropic flow, which happens between 1.5 – 2.5 fm/c in our calculation [see Fig. 5.19 (b)], the fluids with $\frac{\eta}{s}(T)$ will start cooling faster than the one with $\frac{\eta}{s} = \frac{1}{4\pi}$ and ultimately will freeze-out sooner [see Fig. 5.19 (c)]. This late anisotropic push of the media with $\frac{\eta}{s}(T)$ results in a higher $v_2(M)$ of HM dileptons as can be seen in Fig. 5.17 (b). Note that the flow harmonics of HM dileptons are little affected by viscous corrections in our model, hence it is sufficient to show the full results that include the δR correction. Thus both the HM and QGP dileptons track the momentum anisotropy rather closely, as shown in Fig. 5.18.

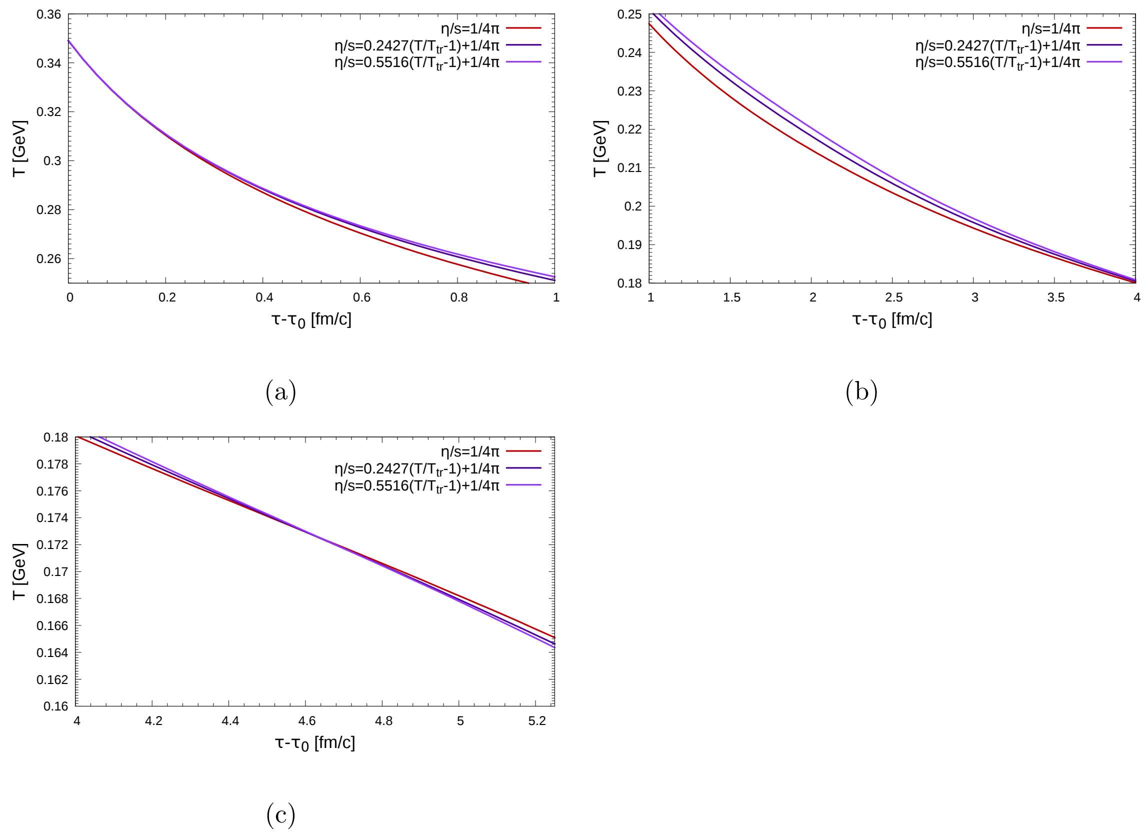

Figure 5.19: Temperature of the cell (x,y,z)=(0,0,0) during the first fm of evolution (a) and at later stages (b) (c). This temperature was obtained after averaging over 200 hydro events.

As a confirmation that HM dileptons are experiencing a greater push at late stages of the evolution, Fig. 5.20 plots the temperature profile in the transverse plane at late time. The medium with a $\frac{\eta}{s}(T)$ produces a more oblate shape than $\frac{\eta}{s} = \frac{1}{4\pi}$, see Fig. 5.20 (a) and (b), respectively. Of course, in both cases, the initial conditions were the same.

For charged hadron v_2 to be consistent with this picture, the shape of the freeze-out surface boundary should not vary significantly between $\frac{\eta}{s}(T)$ and $\frac{\eta}{s} = \frac{1}{4\pi}$, as is seen Fig. 5.21. Hence the wavefront responsible for increasing the $v_2(M)$ of HM dileptons didn't have enough time to propagate to the freeze-out surface and leave a significant imprint there. Thus, the $v_2(p_T)$ of charged hadrons is unaffected by an $\eta/s(T)$ in the QGP phase.

Since the transverse momentum dependence of the elliptic and triangular flow

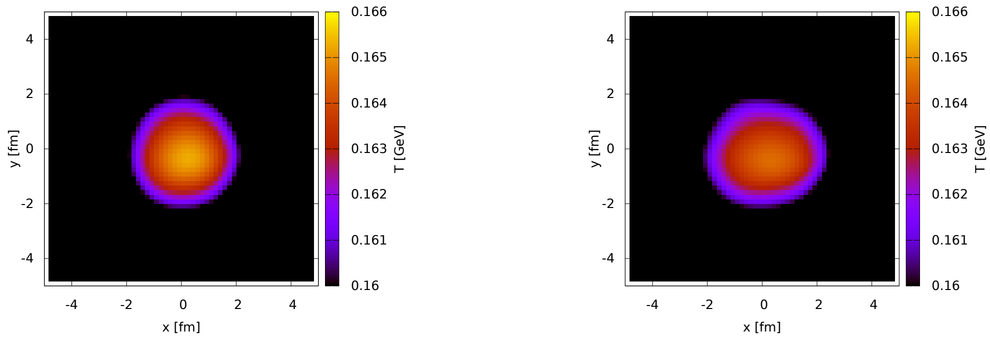

(a) (b)

Figure 5.20: Temperature in the transverse plane at $z = 0$ at $(\tau - \tau_0) = 5.25$ fm/c for $\frac{\eta}{s} = \frac{1}{4\pi}$ (a) and $\frac{\eta}{s} = 0.4513\left(\frac{T}{T_{tr}} - 1\right) + \frac{1}{4\pi}$ (b). This temperature was obtained after averaging over 200 hydro events.

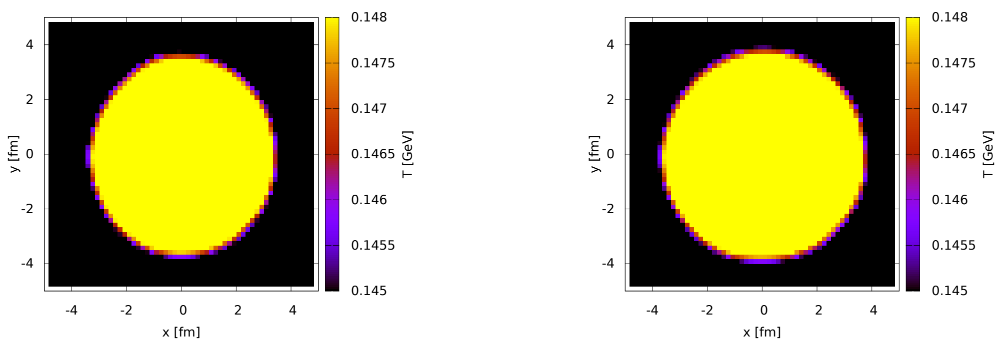

(a) (b)

Figure 5.21: Temperature in the transverse plane at $z = 0$ at $(\tau - \tau_0) = 5.25$ fm/c for $\frac{\eta}{s} = \frac{1}{4\pi}$ (a) and $\frac{\eta}{s} = 0.4513\left(\frac{T}{T_{tr}} - 1\right) + \frac{1}{4\pi}$ (b) near the freeze-out surface boundary. This temperature was obtained after averaging over 200 hydro events.

is rather sizable (see Fig. 5.22), these flow harmonics bear promise to potentially constrain, in experimental data, the slope of $\frac{\eta}{s}(T)$. To maximize this effect, the invariant mass M was chosen (recall the discussion in section 4.6) in a region where the thermal radiation dominates over all other sources (see the red curves in Fig. 4.11) . Given the difference in the evolution of flow harmonics — especially $v_2(p_T \gtrsim 2$ GeV) and $v_3(p_T \gtrsim 3$ GeV), it may be possible to experimentally constrain the slope of $\frac{\eta}{s}(T)$.

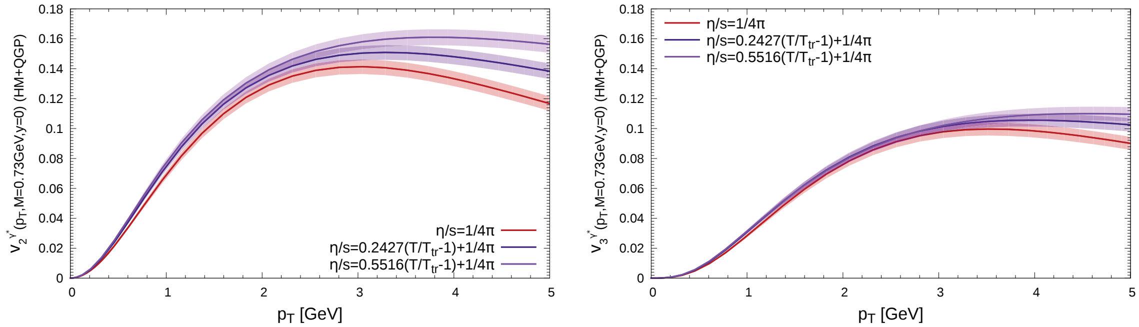

(a) (b)

Figure 5.22: Elliptic (a) and triangular (b) flow of thermal dileptons for a linearly dependent $\frac{\eta}{s}(T)$.

5.2.4 Quadratic $\frac{\eta}{s}(T)$

Full attention is now turned towards the second derivative of $\frac{\eta}{s}(T)$. The initial and freeze-out conditions are unchanged. The amount of entropy production for

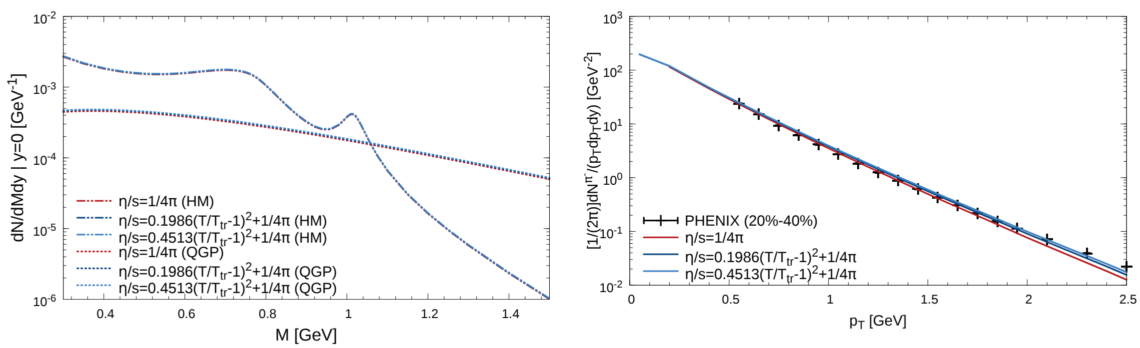

(a) (b)

Figure 5.23: Yield of thermal dileptons (a) and pions (b) for various values of $\frac{\eta}{s}(T)$.

a quadratic $\frac{\eta}{s}(T)$ is about 2% in the HM and 6% in the QGP region, as extracted from comparing the red and light blue lines in Fig. 5.23 (a), while the amount of radial flow has been reduced by a factor of $\sim$2 compared to the linear $\frac{\eta}{s}(T)$ [see Fig. 5.23 (b)]. As before, the charged hadron elliptic flow is not affected by $\frac{\eta}{s}$, while the elliptic flow of thermal dileptons is [see Fig. 5.24].

As the invariant mass distribution of thermal dilepton v_2 for a quadratic $\frac{\eta}{s}(T)$ is similar to a linear $\frac{\eta}{s}(T)$, attention is given to whether the transverse momentum

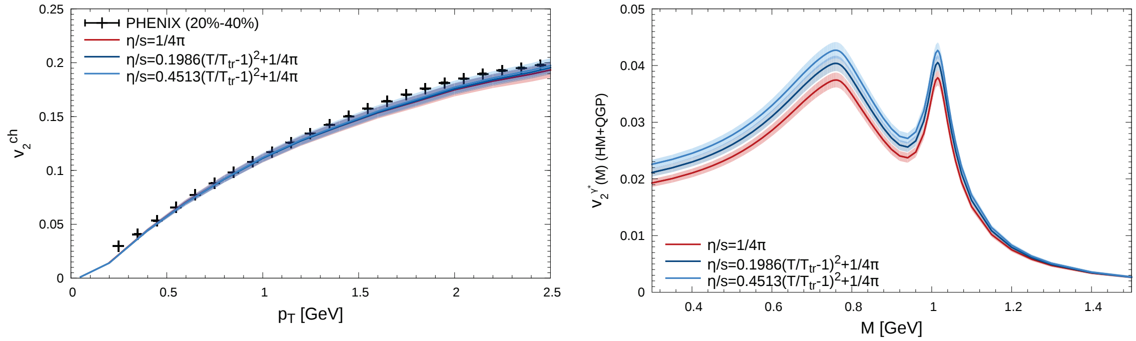

(a) (b)

Figure 5.24: Elliptic flow of charged hadrons (a) and thermal dileptons (b) with different slopes of $\frac{\eta}{s}(T)$. The colored bands represent the statistical uncertainty associated with 200 hydrodynamical events.

distribution is sensitive to whether $\frac{\eta}{s}(T)$ is linear or quadratic.

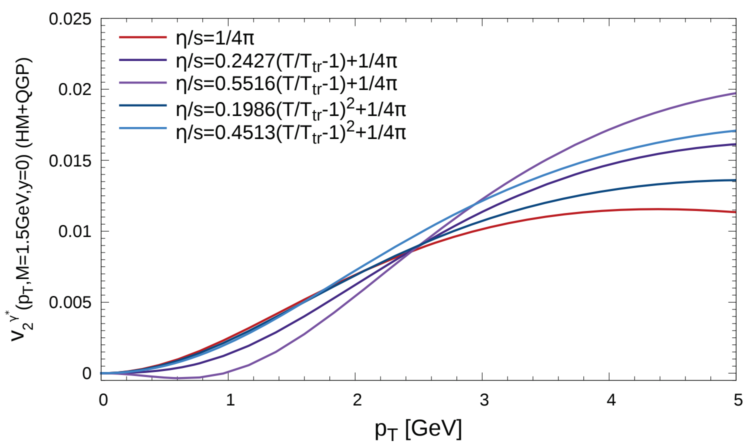

Figure 5.25: A comparison of v_2 of thermal dileptons using linear and quadratic $\frac{\eta}{s}(T)$ at low invariant mass.

Indeed, at high invariant masses, Fig. 5.25 shows that $v_2(p_T)$ can clearly distinguish between the two function chosen for $\frac{\eta}{s}(T)$, though the signal is small.

At low invariant masses, higher flow harmonics do show a moderate difference going from linear to quadratic $\frac{\eta}{s}(T)$ at $p_T \gtrsim 3$ GeV [see Fig. 5.26], which cannot be accounted for via changes in the slope for example. Unfortunately, experimentally distinguishing between the various forms of $\frac{\eta}{s}(T)$ will be challenging at RHIC given the sensitivity required, be it in the overall magnitude of the signal or in the relative

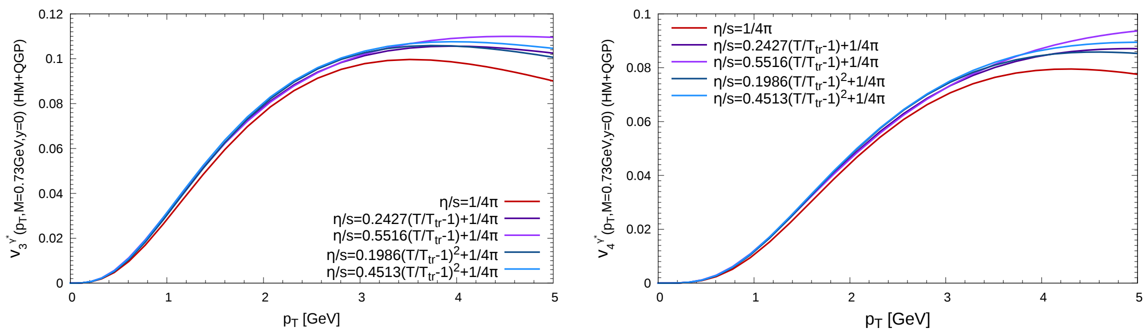

Figure 5.26: A comparison of v_3 (a) and v_4 (b) of thermal dileptons using linear and quadratic $\frac{\eta}{s}(T)$ at low invariant mass.

difference between signals.

5.2.5 *Summary regarding the effects of $\eta/s(T)$*

In summary, as was first pointed out by Ref. [31], hadronic elliptic flow is poorly sensitive to any temperature dependence of $\frac{\eta}{s}$ in the QGP sector at top RHIC energy. Furthermore, the the size of the second derivative of $\frac{\eta}{s}$ doesn't change that finding.

As far as dileptons are concerned, though a difference in the slope or the size of the second derivative did influence the magnitude of dilepton flow harmonics in an experimentally quantifiable way, distinguishing between a linear and a quadratic temperature dependence is difficult in the low invariant mass sector. Indeed, it is only when comparing v_3 and v_4 at high transverse momenta, at a fixed low invariant mass, that one starts noticing a moderate difference in the signal between a linear and a quadratic temperature dependence. At intermediate invariant masses, while the difference between a linear and a quadratic $\frac{\eta}{s}(T)$ is greater, the overall magnitude of the signal is significantly smaller. Given the differential nature of this measurement, extracting the signal with enough statistics is experimentally challenging at high invariant masses or from $v_{n>2}$ flow harmonics at low M.

Therefore at RHIC energies, future v_2 measurements may distinguish between variations in the size of $\frac{\eta}{s}(T)$ in the QGP phase using, for example the upcoming Muon Telescope Detector at STAR. Distinguishing between a linear and a quadratic

$\frac{\eta}{s}(T)$ is probably outside the capabilities of RHIC. Thus, computing dilepton flow at LHC energies might potentially have the power to distinguish between a linear and quadratic $\frac{\eta}{s}(T)$. Such a study is currently in progress.

5.3 Dileptons from the Beam Energy Scan at RHIC

Theoretically, studying the medium within the context of the beam energy scan (BES) has only become feasible in recent years. Indeed, recent developments in ℓQCD calculations using Taylor expansion in the net baryon chemical potential, has allowed to extract the QCD pressure $P(T, \mu_B)$ [17, 18], thus enabling hydrodynamical studies to be conducted once the ℓQCD EoS is matched to the hadron resonance gas model at finite μ_B. There is a large ongoing effort in the nuclear physics community to describe the medium generated in gold-gold collisions from the BES using hydrodynamics. Given this context, the goal of this section is to study *trends* observed within dilepton yield and anisotropic flow coming from the presence of net baryon number density (and its diffusion) within a hydrodynamical evolution. Thus, as was the case in the rest of the thesis, this is an exploratory study of the influence the net baryon chemical potential and baryon diffusion have on dilepton production, with a more quantitative study being planned in the near future once the hydrodynamical description of the medium is perfected.

5.3.1 *Initial conditions at finite net baryon number density and the hydrodynamical equations of motion*

Since the BES program at RHIC is designed to study the properties of strongly interacting media in an environment that has non-zero net baryon density, the initial condition used in hydrodynamical simulations needs to specify a distribution for the net baryon density n_B. Note that the initial energy density is distributed according to the average distribution obtained from 1000 MC-Glauber events. The averaging is done such that the elliptic flow contained within these 1000 events is preserved, by rotating, event-by-event, the energy density profiles such that the event plane angles

Ψ_2 are aligned[1]. The normalized net baryon density profile is given by:

$$g_B = N\left\{\Theta(|\eta_s|-\eta_{s,0})\exp\left[-\frac{(|\eta_s|-\eta_{s,0})^2}{2\Delta\eta_{s,1}^2}\right]\right.$$
$$\left.+\left[1-\Theta(|\eta_s|-\eta_{s,0})\right]\left[A+(1-A)\exp\left[-\frac{(|\eta_s|-\eta_{s,0})^2}{2\Delta\eta_{s,2}^2}\right]\right]\right\}, \tag{5.13}$$

where η_s is the usual space-time rapidity and

$$N = \frac{1}{\sqrt{2\pi}\Delta\eta_{s,1} + (1-A)\sqrt{2\pi}\Delta\eta_{s,2} + 2A\eta_{s,0}} \tag{5.14}$$

is chosen such that $\int d\eta_s g_B = 1$. The free parameters $\eta_{s,0}, A, \Delta\eta_{s,1}, \Delta\eta_{s,2}$ vary as a function of the collision energy begin studied (see Table 5.2). These parameters are chosen such that the net proton rapidity distribution dN/dy, observed at various collision energies probed by the BES at RHIC, is reproduced. A plot of g_B is given

Table 5.2: The parameters of the spatial η_s profile for various beam energies.

	$\eta_{s,0}$	A	$\Delta\eta_{s,1}$	$\Delta\eta_{s,2}$
$\sqrt{s_{NN}}$=7.7 GeV	2.09	0.8	0.7	1
$\sqrt{s_{NN}}$=19.6 GeV	3.03	0.5	0.7	1
$\sqrt{s_{NN}}$=64.2 GeV	4.2	0.3	0.7	1
$\sqrt{s_{NN}}$=200 GeV	5.36	0.3	0.7	1

in Fig. 5.27, where the free parameter A governs the size of g_s at $\eta_s = 0$.

In the transverse plane, the net baryon density profile has the same shape as the energy density, while its normalization is tuned such that the number of participants N_{part} obtained from the Glauber model is reproduced for a particular beam energy and centrality class. We focus on the 0-80% centrality class.

Specific values for the viscous transport coefficients must be chosen in order to solve the viscous equations of motion [see Chapter 2]. The equation of motion for net baryon number diffusion is:

$$\tau_V \Delta^\mu_\nu \frac{dV^\nu}{d\tau} + V^\mu = \kappa\nabla^\mu\alpha_0 - \delta_{VV}V^\mu\theta - \lambda_{VV}\sigma^{\mu\nu}V_\nu. \tag{5.15}$$

[1] $\Psi_2 = \frac{1}{2}\arctan\left[\frac{\epsilon^s_{2,2}}{\epsilon^c_{2,2}}\right]$ where $\epsilon^{c,s}_{2,2}$ are defined in section 2.3.3.

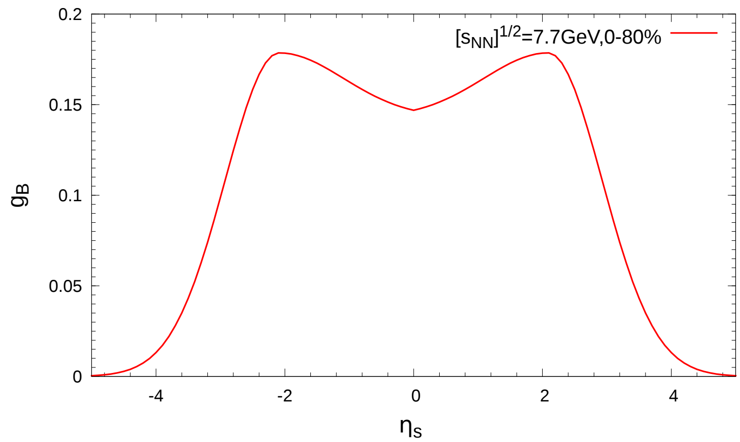

Figure 5.27: The normalized net baryon number density spatial rapidity (η_s) profile for 0-80% centrality in gold-gold collisions at $\sqrt{s_{NN}}$ =7.7 GeV.

where $\alpha_0 = \frac{\mu_B}{T}$, while the term λ_{VV} can be derived from microscopic theory [67, 66], but is not present in Eq. (2.47). The transport coefficients are given by $\tau_V = \frac{0.2}{T}$, $\kappa = 0.2\frac{n_B}{\mu_B}$, $\delta_{VV} = \tau_V$, $\lambda_{VV} = \frac{3}{5}\tau_V$. The choice for transport coefficients $\delta_{VV} = \tau_V$ and $\lambda_{VV} = \frac{3}{5}\tau_V$, comes from solving the Boltzmann equation for an ideal gas of massless relativistic particles with constant cross section [67, 66]. τ_V and κ come from the AdS/CFT calculation in Ref. [167]. Lastly, the initial condition for the net baryon number diffusion is $V^\mu = 0$. As far as the relaxation equation for the shear viscous pressure is concerned, the equation of motion is still the same as in Eq. (4.1) and so are the transport coefficients except instead of $\eta/s = 1/4\pi$ being a constant it is $\eta T/(\varepsilon + P) = 0.08$. The initial conditions $\pi^{\mu\nu} = 0$ still hold while the initialization (or thermalization) time is $\tau_0 = 0.6$ fm/c. The freeze-out energy density of 0.1 GeV/fm^3 was chosen instead of a freeze-out temperature as it provided a better fit to hadronic observables. The equation of state was provided by [168].

5.3.2 *Dilepton yield and elliptic flow from the BES*

The effects of net baryon number density and its diffusion are now explored. The new features that net baryon number density/diffusion induce on the evolution of the medium are most prominent at the lowest beam energy $\sqrt{s_{NN}} = 7.7$ GeV as depicted in Fig. 5.28.

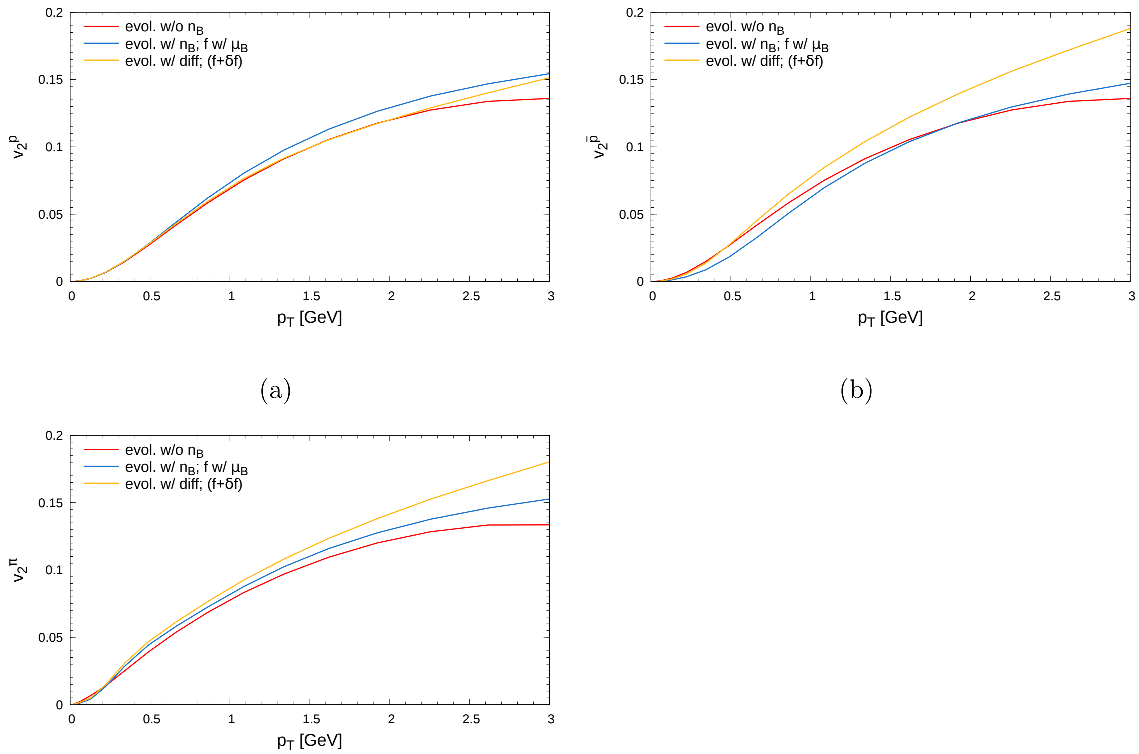

(a) (b) (c)

Figure 5.28: A comparison of the influence of net baryon number and its diffusion on the v_2 of pions (a), protons (b), and antiprotons (c) for 0-80% centrality class and $\sqrt{s_{NN}} = 7.7$ GeV collision energy.

The yield of thermal dileptons is also sensitive to a net baryon chemical potential μ_B. To fully quantify the various effects net baryon density and its diffusion introduce into dilepton production, it is instructive to turn off both μ_B in the dilepton rates and also turn off baryon diffusion. That way one can compare the difference in the evolution owing to the pressure being solely dependent on energy density versus both energy density and μ_B.

For the same energy density, as the net baryon chemical potential μ_B introduces a new degree of freedom, the temperature of the fluid must be lowered throughout its evolution as depicted in Fig. 5.29 (a). Thus for a medium for which the pressure depends on both the energy density and μ_B, the dilepton yield is reduced [see Fig. 5.29 (b)] owing to the fact that the temperature profile of the medium is reduced.

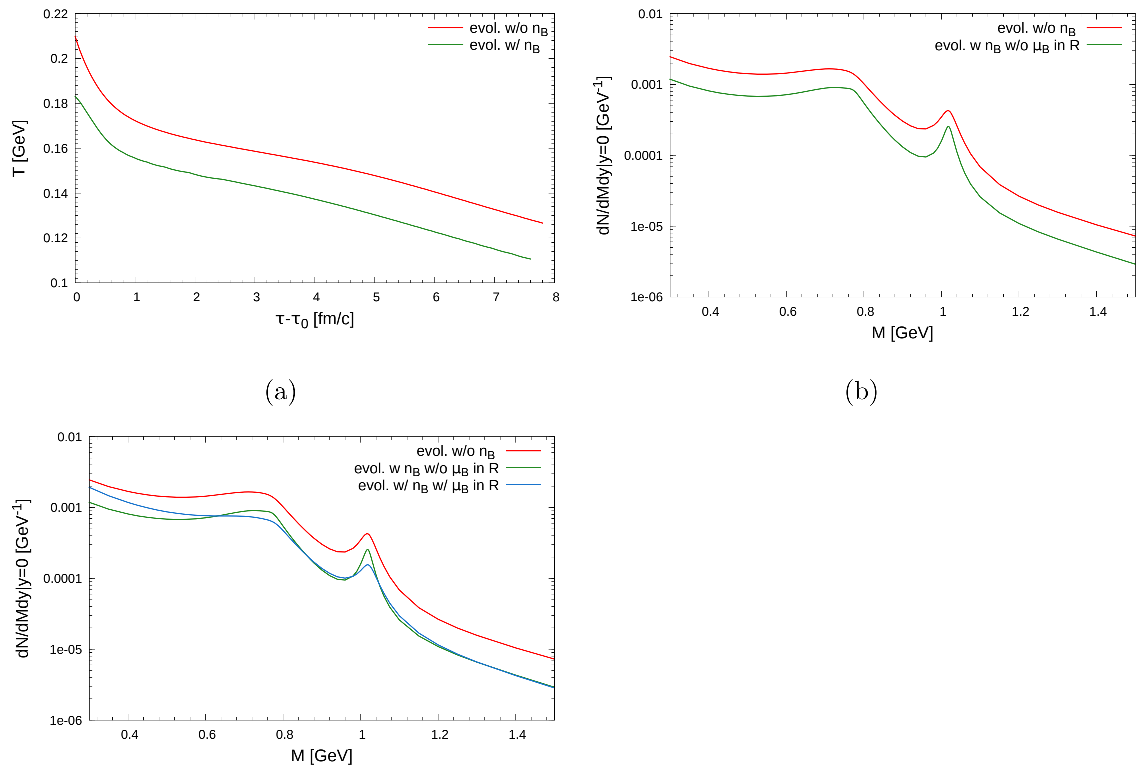

(c)

Figure 5.29: Temperature profile of the central cell (x=y=η_s=0) as a function of time τ since the beginning of the hydrodynamical evolution (a) and it influence on the dilepton yield without μ_B (b) and with μ_B (c), for 0-80% centrality class and $\sqrt{s_{NN}} = 7.7$ GeV collision energies.

Once the chemical potential is introduced in the dilepton rates (using the the same medium evolution as for $\mu_B = 0$), it has the expected effect of broadening the width of vector mesons in the medium [see Fig. 5.29 (c)], which enhances dilepton production away from the vector meson mass poles while reducing it at the poles, due to the Lorentzian shape of the distribution $-\mathrm{Im}\left[D_V^R\right]$.

The effects of net baryon diffusion on dilepton yield are shown in Fig. 5.30. The invariant mass dilepton yield isn't significantly affected by the presence of net baryon number diffusion, since the latter doesn't significantly increase μ_B, given the current assumption of the baryon diffusion constant κ. Furthermore, this value of κ doesn't generate a lot of entropy and hence the $dN/dMdy$ of thermal dileptons isn't affected.

On the other hand, the p_T differential dilepton yield and elliptic flow are affected

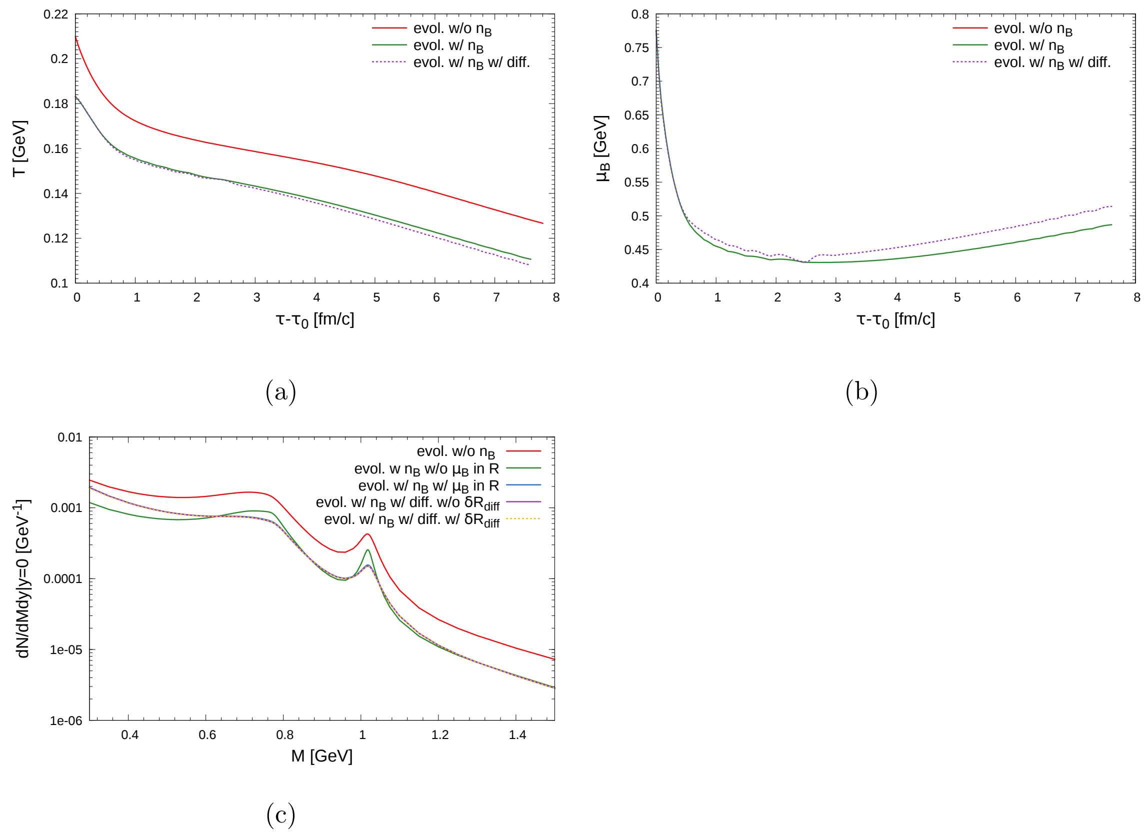

Figure 5.30: Temperature (a) and chemical potential μ_B (b) profile of the central cell (x=y=η_s=0) as a function of time τ including baryon diffusion effects in the hydrodynamical evolution of the medium. (c) Dilepton yield including baryon diffusion. There results again assume a 0-80% centrality and $\sqrt{s_{NN}} = 7.7$ GeV collision energy.

by the presence of both the net baryon chemical potential μ_B and baryon diffusion [see Fig. 5.31]. Indeed, a reduction in the dilepton yield at high p_T, mostly caused by a reduction in HM dilepton yield [see Fig. 5.31 (b)], shifts the balance between HM and QGP contributions to dilepton v_2, giving more weight to the QGP dileptons radiation with increasing p_T, thus reducing the overall thermal $v_2(p_T)$, as QGP dileptons do not have a significant elliptic flow. One can understand the reason behind the increase of μ_B in the central regions with the aid of Eq. (5.15) and Fig. 5.32. Notice that in Eq. (5.15), the diffusion of rate of V^μ is not governed by the spatial gradient of n_B, as is the case for heat diffusion, but is instead governed by the spatial gradient (in the fluid rest frame) of its (thermodynamical) conjugate variable μ_B. Looking at Fig. 5.32 (a) one notices that the largest spatial gradients, at the edge of the simulated

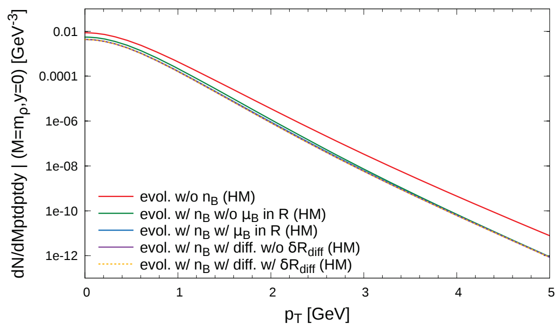

(a)

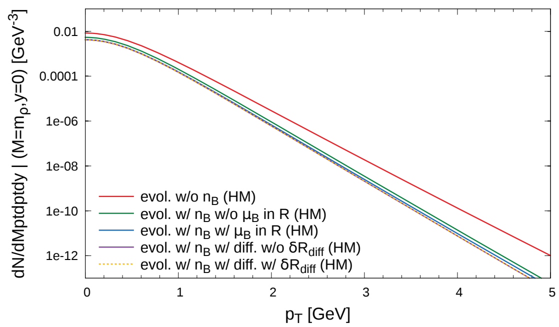

(b)

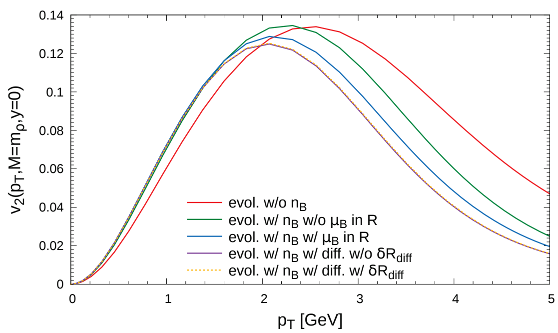

(c)

Figure 5.31: Dilepton total (HM+QGP) yield (a), HM yield (b) and total elliptic flow (c) as a function of p_T at $M = m_\rho$, for $\sqrt{s_{NN}} = 7.7$ GeV collision energy and 0-80% centrality.

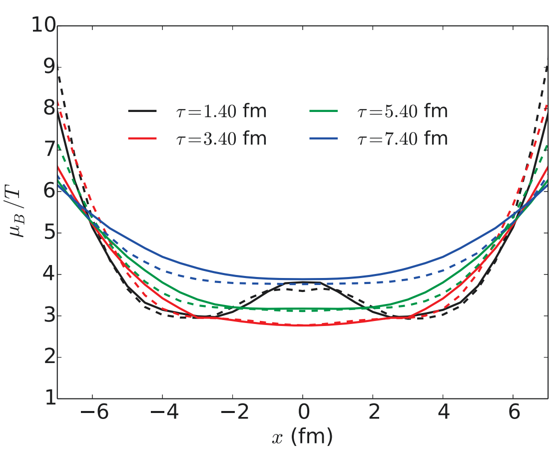

(a)

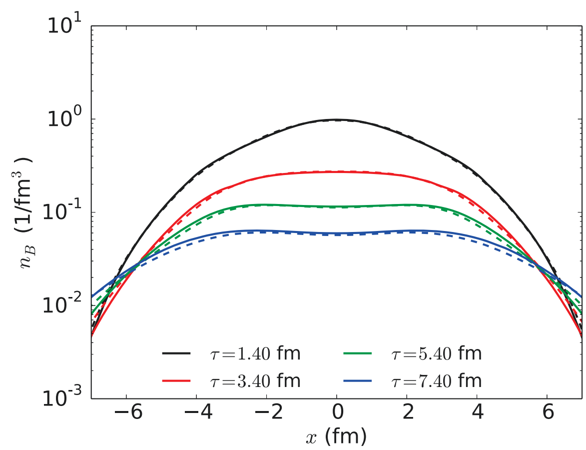

(b)

Figure 5.32: Evolution of μ_B/T (a) and n_B (b) for a hydrodynamical simulation without net baryon number diffusion (dashed line) and with net baryon number diffusion (solid lines) for the slice at $y = \eta_s = 0$ and for $\sqrt{s_{NN}} = 7.7$ GeV collision energy and 0-80% centrality.

region along the x-axis, point inwards towards $x = 0$. Therefore as time goes on, in a medium with baryon diffusion [solid lines in Fig. 5.32 (a)] there should be a build-up of μ_B/T towards the center $x = 0$ while there is a depletion at the edges, both driven by the $\nabla^\mu \left[\frac{\mu_B}{T}\right]$. Such a buildup is comparatively slower in the case where $V^\mu = 0$. As far as the net baryon number density n_B is concerned, net baryon number diffusion V^μ also causes a build-up in n_B (solid curves) relative to no diffusion (dashed curves), see Fig. 5.32 (b).

So though the preliminary dilepton results are promising, more studies need to me made (e.g. exploring higher values of κ) to fully understand the effects of net baryon number conductivities on dilepton production. In particular, it is important to determine whether the diffusive correction in the dilepton yield can play a more significant role, than it currently does, which would help in constraining κ using experimental data. In sum, the $v_2(p_T)$ of thermal dileptons in Fig. 5.31 (c) can be used to constrain the size of the baryon diffusion coefficient κ. This transport coefficient is currently poorly known and any sensitivity shown by dileptons (or hadrons) will shed more light regarding how its size affects flow coefficients.

Of course, at lower beam energies, one can legitimately ask the question: " how much of the medium is described by hydrodynamics; and for how long?" This is still an open question that is currently being investigated. Furthermore, after the hydrodynamical evolution ceases to be valid, the hydrodynamical degrees of freedom need to be converted to hadronic degrees of freedom, to be evolved further via hadronic transport models. Fortunately, this is something that has been studied in the past, see e.g. [169] for a recent development in this direction. However, less attention was given to describing electromagnetic radiation from a hadronic transport model, and from that perspective, the dilepton calculation presented here is state-of-the-art.

5.4 Summary and outlook

This chapter has shown that thermal dileptons can be used to constrain the size of two transport coefficients governing the size of the shear viscous pressure: τ_π and

$\frac{\eta}{s}(T)$. Moreover, dilepton's sensitivity to the initial conditions of $\pi^{\mu\nu}$ may give some information regarding the size of shear stresses in early time dynamics of strongly interacting media, when more precise data on dilepton flow coefficients are available from the STAR experiment at RHIC. Charged hadrons on the other hand are poorly sensitive to τ_π, $\frac{\eta}{s}(T)$, and the initial conditions $\pi^{\mu\nu}$ explored within this study.

Furthermore, dileptons have demonstrated sensitivity to the net baryon chemical potential μ_B and net baryon conductivity κ. In particular, using the sensitivity of dilepton $v_2(p_T)$ on upcoming dilepton flow data, one can constrain the size of κ. Given that hadronic flow observables are also sensitive to κ, it may be possible to pin-down the "effective" value (i.e. integrated over the entire evolution of the fluid) of this transport coefficient using simultaneously the hadrons and dileptons. Also, the BES program at RHIC, along with other low energy collisions planned at FAIR, open the possibility to study all transport coefficients presented in this thesis *at finite T and μ_B*. Thus dileptons play a pivotal role in learning more about transport coefficients and initial conditions of strongly interacting matter.

Except for bulk viscosity, which is currently being studied, all other tools are now in place, and as soon as new dilepton flow data from RHIC and dilepton yield data from the LHC become available, the project of constraining the transport coefficients of strongly interacting media, using hadrons and dileptons, can begin in earnest.

6

Conclusion

Though rarely produced, electromagnetic probes constitute the only source of thermal radiation that is emitted throughout the entire evolution of the hot and dense medium produced in heavy ion collisions. Hence, they are the only ones capable of providing direct information about the different stages of the evolution. In particular, using the invariant mass distribution of thermal dileptons radiation, it is possible to distinguish between early QGP dilepton emission from late emission coming mostly from the HM; QGP radiation plays an important role once NLO corrections to QGP rates are applied. This capacity to distinguish between late and early emission was used to extract as much information regarding the QCD medium as possible.

Semi-leptonic decays of open charm hadrons were used to learn about the strongly interacting medium, where energy loss/gain and angular deflection played an important role in describing the data. Indeed, experimental data seem to prefer a medium-modified invariant mass yield coming from decays of open charm hadrons, where interactions with the medium have depleted dilepton production at higher invariant masses, while enhancing it at lower invariant masses. Through the same interaction with the medium, open charm hadrons acquired an elliptic flow. As soon as the precision of the experimental dilepton flow data at RHIC improves, or data from the LHC becomes available, a more quantitative assertion will be made.

The most important result however lies in the sensitivity of thermal dileptons to the initial conditions of the medium and its transport coefficients. Indeed, the anisotropic flow coefficients of dileptons are affected by the initial conditions of the shear stress tensor $\pi^{\mu\nu}(\tau_0)$ and its relaxation time τ_π, as well as the size of the shear viscosity coefficient, particularly when a temperature dependent shear viscosity to entropy density ratio (η/s) is used in the QGP phase. This sensitivity to $\frac{\eta}{s}(T)$ in the QGP phase opens the possibility to study the size of η/s around the transition temperature between the QGP and the HM phases of the medium. The elliptic flow of charged hadrons is essentially insensitive to these transport coefficients and to the shear initial conditions. In the case where there is no temperature dependence for η/s, both dileptons and hadrons are sensitive to the size of this transport coefficient. Hence, dileptons and hadronic observables should be used together to pin down the transport properties of strongly interacting media. Doing this with hadronic observables (i.e. p_T-spectra and flow harmonics) alone is insufficient. Furthermore, with the improvement of detection of heavy flavor hadrons, it may become possible to remove their contribution from the dilepton spectrum at intermediate invariant masses, exposing direct QGP radiation. This would be a "golden" window to directly assess for properties of strongly interacting partonic medium created in heavy-ion collisions. All tools being now in place to study the shear viscosity using dileptons, new experimental flow data from RHIC (or the LHC) are eagerly awaited.

One aspect of viscous hydrodynamics on dilepton production that has not been explored yet is the effects of bulk viscous pressure on dileptons. This is one of the first aspects that will be explored more thoroughly in the near future as the effects of bulk viscosity (ζ) on hadron production are important. For instance in the case of ultra-central collisions, bulk viscosity can reduce the v_2 of charged hadrons while leaving v_3 essentially unaffected [170]. Investigating the effects of bulk viscous pressure on dilepton production is certainly of interest, especially if one is to change the temperature dependence of ζ. To do that of course, deformation induced by the bulk viscous pressure on the thermal (i.e. Bose-Einstein/Fermi-Dirac) distribution profiles needs to be taken into account on both the hadronic and the partonic sector.

The Beam Energy Scan program at RHIC also allows to inspect the effects of net baryon chemical potential and net baryon diffusion on electromagnetic and hadronic probes. The first step in that direction was given in section 5.3, however a lot more work is required. For instance, it would be interesting to compare the influence of various models of baryon conductivity κ, baryon diffusion relaxation time τ_V, and the initial conditions of the baryon diffusion vector V^μ on the evolution of the medium. Another avenue that has not been explored is the manner in which shear and bulk viscosity are affected by the net baryon chemical potential μ_B. To that end, dilepton data from both RHIC and FAIR are needed, especially in the intermediate mass region. At lower beam energies, the production of open heavy flavor is reduced (owing to the lack of beam energy required to generate an important amount of charm/bottom quarks), and hence access to thermal QGP radiation is easier [120, 171]. Hence, pinning down the transport coefficients of the QGP may be easier at lower beam energies; an exciting avenue indeed. Lastly, to be able to fully appreciate the effects of various hydrodynamical transport coefficients, one needs to supplement the hydrodynamical simulation with a hadronic transport model. Indeed as beam energies are being lowered, the medium spends a decreasing amount of time in the space-time region where the Knudsen numbers are small enough such that the assumptions for a hydrodynamical behavior of the fluid are valid. Hence supplementing a hydrodynamical dilepton calculation with dilepton production from a hadronic transport model should also be considered, to obtain a realistic simulation of dileptons from the hadronic medium.

In sum, the exploration of dilepton radiation from dissipative media produced in heavy-ion collisions is only just beginning, with lots of exciting new avenues to explore.

A

The asymptotic behavior of the forward scattering amplitude

The full t-channel representation of the scattering amplitude (i.e. the scattering amplitude at fixed t), is

$$f(s,t) = 16\pi \sum_{l=0}^{\infty} (2l+1) f_l(t) P_l(z_t), \tag{A.1}$$

similar to the s-channel presentation in Eq. (2.54), where $z_t = 1 + \frac{2s}{t-4m^2}$, l is the total angular momentum of the system as it is assumed that the scattering particles are identical and have zero spin. In a relativistic theory of the scattering amplitude, two scattering amplitudes $f^{\pm}(l,t)$ are typically introduced such that

$$f^{\pm}(l,t) = \begin{cases} f_l(t) & l \text{ even} \\ f_l(t) & l \text{ odd} \end{cases} \tag{A.2}$$

Hence, the t-channel representation of the partial-wave expansion in Eq. (A.1) takes the form

$$f(s,t) = f^{+}(s,t) + f^{-}(s,t) \quad \text{where} \tag{A.3}$$

$$f^{\pm}(s,t) = 8\pi \sum_{l=0}^{\infty} (2l+1) f_l(t) \left(P_l(z_t) \pm P_l(-z_t)\right) \tag{A.4}$$

where the identity $P_l(-z_t) = (-1)^l P_l(z_t)$ was used. $f^{+}(s,t)$ receives contributions only when l is even, and $f^{-}(s,t)$ only from odd l. So, in $f^{+}(s,t)$ one substitutes $f_l(t)$ by $f_l^{+}(t)$, and similarly for $f^{-}(s,t)$. One can use Cauchy's theorem to rewrite the partial-wave series in an integral form. To do that, assume that $f^{\pm}(l,t)$ is an analytic function of l throughout the right-hand half of the l-plane with no essential singularities and only isolated singularities. This is a fundamental assumption upon which the applicability of the above expansion rests. Although not proven in general, this expansion is found to be true order-by-order in a perturbative series of relativistic quantum field theory. Furthermore, it seems to agree well with experiment. If there are only isolated singularities, one can continue past them, and rewrite the partial wave series as:

$$f^{\pm}(s,t) = 8\pi i \int_C dl(2l+1) f^{\pm}(l,t) \frac{P_l(-z_t) \pm P_l(z_t)}{\sin(\pi l)} \tag{A.5}$$

where C surrounds the real axis from 0 to ∞ and the only singularities are the poles coming from $1/\sin(\pi l)$ in Fig. A.1. The sum of residues of $1/\sin(\pi l)$ of the poles at $l = 0, 1, 2, \cdots$ gives the original series for $f^{\pm}(s,t)$. At this point one deforms

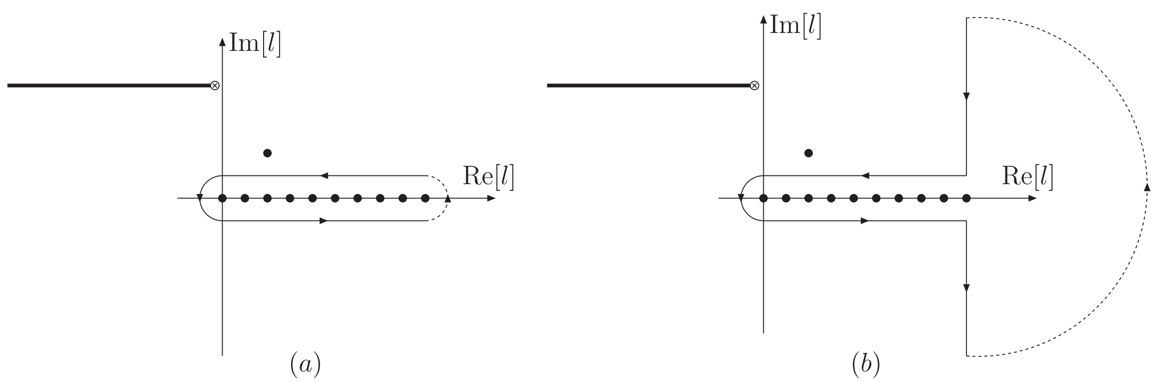

Figure A.1: (a) The integration contour C used in the Sommerfeld-Watson transform where the included poles along real l-axis come from $\frac{1}{\sin(\pi l)}$. Also, the illustration includes a possible pole and branch cut that comes from $f^{\pm}(l,t)$. (b) A deformed version of the contour C. The dashed curve is a semicircle of infinite radius whose center is located far along the real l-axis.

the contour assuming that $f^{\pm}(l,t)$ are analytic for values of l such that Re[l] are sufficiently large [see Fig. A.1 (b)]. As one brings the origin of the semicircle closer to Re[l] $= 0$, care needs to be taken as there are isolated singularity of $f^{\pm}(l,t)$. [1] Only one is depicted in Fig. A.2 for simplicity. Getting very close to the pole, requires to deform the contour as shown in the Fig. A.2 in order to be able to move it to the left of the pole of $f^{\pm}(l,t)$. The resulting contour is shown in the right panel of Fig. A.2. Integrating along this contour further imposes to integrate around the pole and

[1] In principle, it may also have a branch point but that case will not be of concern.

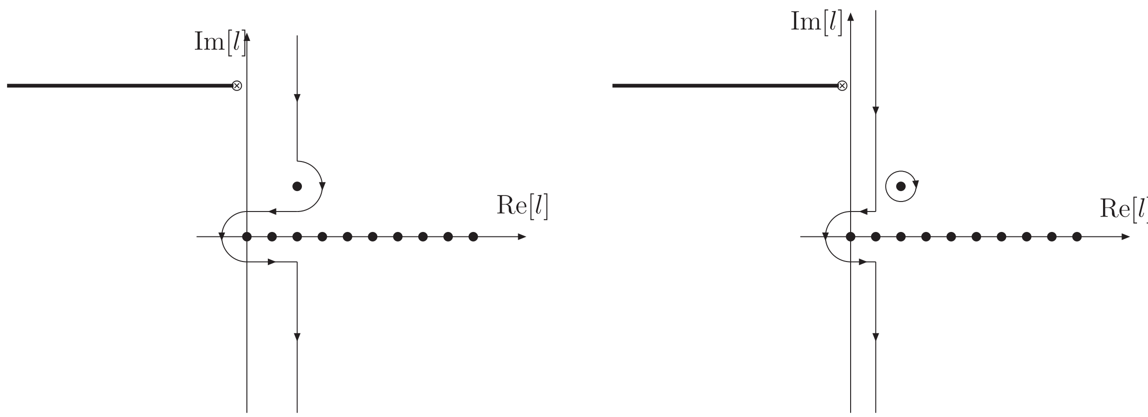

Figure A.2: Result of moving the contour in Fig.A.1 past a pole of $f^{\pm}(l,t)$.

therefore pick up its residue, giving:

$$f^{\pm}(s,t) = -16\pi^2 \sum_i \frac{(2\alpha_i^{\pm}(t)+1)r_i^{\pm}(t)}{\sin(\pi\alpha_i^{\pm}(t))}\left(P_{\alpha_i^{\pm}(t)}(-z_t) \pm P_{\alpha_i^{\pm}(t)}(z_t)\right) + 8\pi i \int_{-\frac{1}{2}-i\infty}^{-\frac{1}{2}+i\infty} dl(2l+1)f^{\pm}(l,t)\frac{P_l(-z_t) \pm P_l(z_t)}{\sin(\pi l)} \tag{A.6}$$

where $\alpha_i^{\pm}(t)$ are the positions of the poles in the complex l-plane including the ones along the positive real l-axis, while $r_i^{\pm}(t)$ are their residues. The integral along $\mathrm{Re}[l] = -\frac{1}{2}$ is called the "background integral". Since it is possible to make the background integral arbitrarily small [117, 172], it can in fact be neglected. Hence the FSA looks like,

$$f^{\pm}(s,t) = -16\pi^2 \sum_i \frac{(2\alpha_i^{\pm}(t)+1)r_i^{\pm}(t)}{\sin(\pi\alpha_i^{\pm}(t))}\left(P_{\alpha_i^{\pm}(t)}(-z_t) \pm P_{\alpha_i^{\pm}(t)}(z_t)\right) \tag{A.7}$$

Rewriting Eq.(A.7), using the relation of the form $P_\alpha(z) = \exp(-i\pi\alpha)P_\alpha(-z) - \frac{2}{\pi}\sin(\pi\alpha)Q_\alpha(-z)$ [173], with Q_α being the Legendre function of the second kind, results in

$$f^{\pm}(s,t) = -16\pi^2 \sum_i \frac{(2\alpha_i^{\pm}(t)+1)r_i^{\pm}(t)}{\sin(\pi\alpha_i^{\pm}(t))} \times \times \left(P_{\alpha_i^{\pm}(t)}(-z_t) \pm \exp(-i\pi\alpha)P_{\alpha_i^{\pm}(t)}(-z_t) \mp \frac{2}{\pi}\sin(\pi\alpha)Q_\alpha(-z_t)\right) \tag{A.8}$$

Using the asymptotic expansion of $Q_\alpha(z)$, this expression can be simplified further. Indeed

$$\lim_{z\to\infty}[Q_\alpha(z)] \sim \sqrt{\pi}\frac{\Gamma(\alpha+1)}{\Gamma(\alpha+\frac{3}{2})}(2z)^{-\alpha-1} \tag{A.9}$$

Dropping this term in the series as it is asymptotically insignificant [1], one obtains

$$f^{\pm}(s,t) \sim \sum_i \frac{(2\alpha_i^{\pm}(t)+1)r_i^{\pm}(t)}{\sin(\pi\alpha_i^{\pm}(t))}\left(1 \pm \exp(-i\pi\alpha_i^{\pm}(t))\right) P_{\alpha_i^{\pm}(t)}(-z_t) \tag{A.10}$$

Using the asymptotic behavior of Legendre functions of the first kind $P_\alpha(z)$, it is possible to simplify this series further

$$\lim_{z\to\infty}[P_\alpha(z)] \sim \begin{cases} \frac{1}{\sqrt{\pi}}\frac{\Gamma(\alpha+\frac{1}{2})}{\Gamma(\alpha+1)}(2z)^{\alpha} & \mathrm{Re}[\alpha] \geq -\frac{1}{2} \\ \frac{1}{\sqrt{\pi}}\frac{\Gamma(-\alpha-\frac{1}{2})}{\Gamma(-\alpha)}(2z)^{-\alpha-1} & \mathrm{Re}[\alpha] \leq -\frac{1}{2} \end{cases} \tag{A.11}$$

along with the fact that for fixed t, $z_t \sim s$. Finally

$$f^{\pm}(s,t) \sim \sum_i \frac{(2\alpha_i^{\pm}(t)+1)r_i^{\pm}(t)}{\sin(\pi\alpha_i^{\pm}(t))}\left(1 \pm \exp(-i\pi\alpha_i^{\pm}(t))\right) s^{\alpha_i} \tag{A.12}$$

where we have absorbed the gamma functions by redefining the residue $r_i^{\pm}(t)$. This curve represents the high energy (i.e. high s and fixed t) behavior of $f^{\pm}(s,t)$. Now it is easy to understand how the form of the high energy FSA in Eq. (3.58) comes about and where the second term in the low energy FSA in Eq. (3.57) comes from.

[1] Recall that large z_t implies large s at fixed t due to $z_t = 1 + \frac{2s}{t-4m^2}$.

B

Systematic corrections to $\delta n_{\mathbf{k}}$

The discussion presented here follows Ref. [69]. In order to derive the $\delta n_{\mathbf{k}}$ used in Eq. (5.8), the starting point is the generalized version of the quark distribution function $n_{\mathbf{k}}$

$$n_{\mathbf{k}} = \left[\exp\left(y_{\mathbf{k}}\right) + 1\right]^{-1} \tag{B.1}$$

where $y_{\mathbf{k}} = y(k^{\nu}, u^{\nu}; T)$ and setting all chemical potentials to zero. Assuming $y_{\mathbf{k}} = y_{0,\mathbf{k}} + \delta y_{\mathbf{k}}$, where $y_{0,\mathbf{k}} = (u^{\nu} k_{\nu} - \mu)/T$ and $\delta y \ll y_{0,\mathbf{k}}$, one can expand Eq. (B.1) in powers of $\delta y_{\mathbf{k}}$ obtaining to first order

$$\begin{aligned} n_{\mathbf{k}} &= n_{0,\mathbf{k}} + \delta n_{\mathbf{k}} \\ \delta n_{\mathbf{k}} &= n_{0,\mathbf{k}} \left[1 - n_{0,\mathbf{k}}\right] \delta y_{\mathbf{k}} \end{aligned} \tag{B.2}$$

where $n_{0,\mathbf{k}} = \left[\exp\left(y_{0,\mathbf{k}}\right) + 1\right]^{-1}$. The $\delta y_{\mathbf{k}}$ is parametrized as

$$\delta y_{\mathbf{k}} = \mathscr{G}_{\mathbf{k}} \phi_{\mathbf{k}} \tag{B.3}$$

where $\phi_{\mathbf{k}}$ is be computed after performing an irreducible tensor decomposition and $\mathscr{G}_{\mathbf{k}}$ is an arbitrary function of $k^{\mu} u_{\mu}$. Indeed, one can decompose $\phi_{\mathbf{k}}$ as

$$\phi_{\mathbf{k}} = \lambda_{\mathbf{k}}^{(0)} + \sum_{\ell=1}^{\infty} \lambda_{\mathbf{k}}^{\langle \mu_1 \cdots \mu_\ell \rangle} k_{\langle \mu_1} \ldots k_{\mu_\ell \rangle} \tag{B.4}$$

where $\lambda_{\mathbf{k}}^{\langle \mu_1 \cdots \mu_\ell \rangle} = \Delta^{\mu_1 \cdots \mu_\ell}_{\nu_1 \cdots \mu_{\ell'}} \lambda_{\mathbf{k}}^{\nu_1 \cdots \nu_{\ell'}}$ with $\Delta^{\mu_1 \cdots \mu_\ell}_{\nu_1 \cdots \mu_{\ell'}}$ being defined in Ref. [64, 69]. For $\ell = 1$ and $\ell = 2$, the irreducible tensor $\Delta^{\mu_1 \cdots \mu_\ell}_{\nu_1 \cdots \mu_{\ell'}}$ simplifies to Δ^{μ}_{ν}, and $\Delta^{\mu\nu}_{\alpha\beta}$, respectively. These two tensors were defined in section 2.1. The tensors $\lambda_{\mathbf{k}}^{\langle \mu_1 \cdots \mu_\ell \rangle}$, being expanded in terms of the mutually orthogonal irreducible tensors $k_{\langle \mu_1} \ldots k_{\mu_\ell \rangle}$, can be further factorized into a linear combination of an orthonormal set of functions $P^{(\ell)}_{n,\mathbf{k}}$, that explicitly depend on $E_{\mathbf{k}} = u^{\nu}k_{\nu}$, and a set of rank-$\ell$ tensor coefficient $c_n^{\langle\mu_1\cdots\mu_\ell\rangle}$ as

$$\lambda_{\mathbf{k}}^{\langle\mu_1\cdots\mu_\ell\rangle} = \sum_{n=0}^{N_\ell} c_n^{\langle\mu_1\cdots\mu_\ell\rangle} P^{(\ell)}_{n,\mathbf{k}}. \tag{B.5}$$

So, the expansion basis of the tensorial structure of $\phi_{\mathbf{k}}$ are $k_{\langle\mu_1}\ldots k_{\mu_\ell\rangle}$, which, analogous to spherical harmonics, contain the angular dependence of $\phi_{\mathbf{k}}$. The expansion coefficients are $c_n^{\langle\mu_1\cdots\mu_\ell\rangle}$. The irreducible tensors $k_{\langle\mu_1}\ldots k_{\mu_\ell\rangle}$ satisfy the orthogonality condition

$$\int dK n_{\mathbf{k}} k_{\langle\mu_1}\ldots k_{\mu_\ell\rangle} k^{\langle\mu_1}\ldots k^{\mu_{\ell'}\rangle} = \frac{\ell!(2\ell+1)\delta_{\ell\ell'}}{(2\ell+1)!!}\int dK(\Delta^{\alpha\beta}k_\alpha k_\beta)^\ell n_{\mathbf{k}} \tag{B.6}$$

where

$$\int dK \equiv \int \frac{d^4k}{(2\pi)^4}\delta\left(k^\nu k_\nu - m^2\right)\theta\left(k^0\right). \tag{B.7}$$

On the other hand, $\phi_{\mathbf{k}}$'s radial dependence is expanded using the orthonormal basis functions $P^{(\ell)}_{n,\mathbf{k}}$, which can be written as

$$P^{(\ell)}_{n,\mathbf{k}} = \sum_{r=0}^{n} a^{(\ell)}_{n,r}E^r_{\mathbf{k}}. \tag{B.8}$$

The orthonormal basis functions $P^{(\ell)}_{n,\mathbf{k}}$ satisfy

$$\int dK P^{(\ell)}_{n,\mathbf{k}}P^{(\ell)}_{m,\mathbf{k}}\omega^{(\ell)} = \delta_{mn} \tag{B.9}$$

where

$$\omega^{(\ell)} = \frac{(-1)^\ell}{(2\ell+1)!!}\frac{(\Delta^{\alpha\beta}k_\alpha k_\beta)^\ell(1-n_{0,\mathbf{k}})n_{0,\mathbf{k}}\mathscr{G}_{\mathbf{k}}}{\int dK(-\Delta^{\alpha\beta}k_\alpha k_\beta)^\ell n_{0,\mathbf{k}}(1-n_{0,\mathbf{k}})\mathscr{G}_{\mathbf{k}}} \tag{B.10}$$

and has the property $\int dK\omega^{(\ell)} = 1$. Being only interested in computing $\delta y_{\mathbf{k}}$ for shear viscosity, the only term needed is $\ell = 2$. Thus $\delta y_{\mathbf{k}}$ can be expressed as

$$\delta y_{\mathbf{k}} = \mathscr{G}_{\mathbf{k}}\sum_{n=0}^{N_2} P^{(2)}_{n,\mathbf{k}}c_n^{\langle\mu\nu\rangle}k_{\langle\mu}k_{\nu\rangle}. \tag{B.11}$$

where, using the orthogonality condition of the irreducible tensors,

$$c_n^{\langle\mu\nu\rangle} = \frac{1}{2!}\frac{\int dK\mathscr{G}_{\mathbf{k}}P^{(2)}_{n,\mathbf{k}}k^{\langle\mu}k^{\nu\rangle}\delta n_{\mathbf{k}}}{\int dK(-\Delta^{\alpha\beta}k_\alpha k_\beta)^2 n_{0,\mathbf{k}}(1-n_{0,\mathbf{k}})\mathscr{G}_{\mathbf{k}}}. \tag{B.12}$$

It is convenient to re-express $\delta y_{\mathbf{k}}$ in terms of irreducible moments of $\delta n_{\mathbf{k}}$,

$$\rho_n^{\mu\nu} = \int dK E_{\mathbf{k}}^n k^{\langle\mu} k^{\nu\rangle} \delta n_{\mathbf{k}} \tag{B.13}$$

such that

$$\delta n_{\mathbf{k}} = n_{0,\mathbf{k}}(1 - n_{0,\mathbf{k}}) \mathscr{G}_{\mathbf{k}} \sum_{n=0}^{N_2} \mathcal{H}_{n,\mathbf{k}}^{(2)} \rho_n^{\mu\nu} k_{\langle\mu} k_{\nu\rangle} \tag{B.14}$$

where

$$\mathcal{H}_{n,\mathbf{k}}^{(2)} = \frac{1}{2!} \frac{\sum_{m=n}^{N_2} a_{mn}^{(2)} P_{m,\mathbf{k}}^{(2)} \mathscr{G}_{\mathbf{k}}}{\int dK (-\Delta^{\alpha\beta} k_\alpha k_\beta)^2 n_{0,\mathbf{k}}(1 - n_{0,\mathbf{k}}) \mathscr{G}_{\mathbf{k}}} \tag{B.15}$$

At this point we have expressed $\delta n_{\mathbf{k}}$ in terms of its moments $\rho_n^{\mu\nu}$. However, only the lowest of these moments, $\rho_0^{\mu\nu} = \pi^{\mu\nu}$, are described within hydrodynamics. In order to apply this formula to describe the momentum distribution of particles within a fluid, it is still necessary to approximate the remaining moments in terms of the fluid dynamical degrees of freedom. In the hydrodynamical limit, one can assume that all moments $\rho_n^{\mu\nu}$ have sufficiently approached their asymptotic values such that they have relaxed to their Navier-Stokes values. That is,

$$\rho_n^{\mu\nu} \approx 2\eta_n \sigma^{\mu\nu}. \tag{B.16}$$

With this approximation it becomes possible to express all moments $\rho_n^{\mu\nu}$ in terms of $\pi^{\mu\nu}$, in the following way:

$$\rho_n^{\mu\nu} \approx \frac{\eta_n}{\eta} \pi^{\mu\nu}, \tag{B.17}$$

where we have used the Navier-Stokes limit for $\pi^{\mu\nu}$, namely $\pi^{\mu\nu} = 2\eta\sigma^{\mu\nu}$. Here, η_n is a set of transport coefficients which contain the microscopic information of the system. In fact, η_0 is nothing but the usual shear viscosity coefficient η already discussed in this thesis. The remaining transport coefficients are less known, but can be calculated within the framework of the Boltzmann equation (or Kinetic Theory). For the purposes of this thesis, an estimate of these transport coefficients was derived in Ref. [67] within the Boltzmann equation, assuming the colliding quarks are massless and that their $2 \to 2$ scattering cross section is constant. Note that this approximation is not valid in the hadronic sector, where all colliding particles are massive. The final expression for $\delta n_{\mathbf{k}}$ then becomes:

$$\delta n_{\mathbf{k}} = n_{0,\mathbf{k}}(1 - n_{0,\mathbf{k}})\mathscr{G}_{\mathbf{k}} \left[\sum_{n=0}^{N_2} H^{(2)}_{n,\mathbf{k}} \frac{\eta_n}{\eta}\right] \frac{\pi^{\mu\nu}}{2(\varepsilon + P)} \frac{k_\mu}{T} \frac{k_\nu}{T}, \tag{B.18}$$

where $\mathcal{G}_{\mathbf{k}} = \mathscr{G}_{\mathbf{k}} \left[\sum_{n=0}^{N_2} H^{(2)}_{n,\mathbf{k}} \frac{\eta_n}{\eta}\right]$, and the temperature dependence was introduced by replacing all instances of k^μ with $\frac{k^\mu}{T}$ in the above derivation. Keeping terms up to $N_2 = 3$, to improve convergence of the series for $\delta n_{\mathbf{k}}$, the form $\mathscr{G}_{\mathbf{k}} = \frac{1}{0.1+x}$, with $x = \frac{k \cdot u}{T}$, was chosen in the low x region, while choosing $\mathscr{G}_{\mathbf{k}} = \frac{1}{(0.1+x)^4}$ in the high x region. Collecting powers of x after expanding out the series $\sum_{n=0}^{N_2} H^{(2)}_{n,\mathbf{k}} \frac{\eta_n}{\eta}$, one can derive Eq. (5.8). Furthermore, the $\delta n_{\mathbf{k}}$ in Eq. (5.8) has converged, since going to higher order $N_2 = 4$ doesn't significantly change the coefficients the power series of x. Note that the coefficients in Eq. (5.8) were computed assuming that all chemical potentials are set to zero. If that is not the case, which happens when baryon diffusion is considered for example, then the coefficients depend on the chemical potential. Lastly note that setting $\mathscr{G}_{\mathbf{k}} = 1$, and letting $N_2 = 0$, recovers the original I-S viscous correction.

Going beyond the simple physical system used to systematically expand $\delta n_{\mathbf{k}}$ above is difficult.

- Indeed, using perturbative QCD (pQCD) to derive $\delta n_{\mathbf{k}}$ would not be suitable. For one, the shear viscosity η_0 obtained through pQCD would be very large [174] (and possibly leading to very large η_n). Implementing such a large η_0 in a hydrodynamical simulation would not only prevent any fit to experimental data, but would in fact violate the small Knudsen number assumption of dissipative hydrodynamics.

- If one is to apply the above procedure to the hadronic sector, not only is the mass of hadrons participating in a particular interaction needed, but also the scattering cross section (or matrix element) associated with that particular interaction. So, every single hadron would have its own $\delta n_{\mathbf{k}}$. Given that a multitude of hadronic interaction cross sections are simply not know experimentally (and are poorly constrained theoretically), there is very little incentive to systematically expand $\delta n_{\mathbf{k}}$ in the hadronic sector; especially since $\frac{\eta}{s} = \frac{1}{4\pi}$ in the hadronic sector for all the calculations presented in this thesis.

Bibliography

[1] Particle Data Group, K. Olive *et al.*, Chin.Phys. **C38**, 090001 (2014).

[2] https://inspirehep.net/record/1247972/files/pd.png.

[3] http://www.phenix.bnl.gov/WWW/plots/show_plot.php?editkey=p1146.

[4] M. Luzum, J. Phys. **G38**, 124026 (2011), [arXiv:nucl-th/1107.0592].

[5] G. Vujanovic *et al.*, Phys.Rev. **C89**, 034904 (2014), [arXiv:nucl-th/1312.0676].

[6] M. Laine, JHEP **1311**, 120 (2013), [arXiv:hep-ph/1310.0164].

[7] I. Ghisoiu and M. Laine, JHEP **1410**, 83 (2014), [arXiv:hep-ph/1407.7955].

[8] J. Ghiglieri and G. D. Moore, JHEP **1412**, 029 (2014), [arXiv:hep-ph/1410.4203].

[9] L. Landsberg, Sov.Phys.Usp. **28**, 435 (1985).

[10] M. E. Peskin and D. V. Schroeder, *An Introduction to quantum field theory* Reading, USA, Addison-Wesley (1995).

[11] K. Wilson and J. B. Kogut, Phys.Rept. **12**, 75 (1974).

[12] B. R. Martin and G. Shaw, *Particle Physics*, Chichester, UK, Wiley (1997).

[13] O. Philipsen, Prog. Part. Nucl. Phys. **70**, 55 (2013), [arXiv:hep-lat/1207.5999].

[14] STAR Collaboration, L. Kumar, Nucl. Phys. **A904-905**, 256c (2013), [arXiv:nucl-ex/1211.1350].

[15] CBM, J. Heuser and V. Friese, Nucl. Phys. **A931**, 1136 (2014).

[16] V. Freise, Strangeness in Quark Matter, July 6–11, 2015, Dubna, Russia (https://indico-new.jinr.ru/contributionDisplay.py?contribId=60&confId=34).

[17] S. Borsanyi *et al.*, JHEP **1201**, 138 (2012), [arXiv:hep-lat/1112.4416].

[18] HotQCD, A. Bazavov *et al.*, Phys.Rev. **D86**, 034509 (2012), [arXiv:hep-lat/1203.0784].

[19] R. Dashen, S.-k. Ma, and H. J. Bernstein, Phys. Rev. **187**, 345 (1969).

[20] R. Venugopalan and M. Prakash, Nucl.Phys. **A546**, 718 (1992).

[21] P. Huovinen and P. Petreczky, Nucl.Phys. **A837**, 26 (2010), [arXiv:hep-ph/0912.2541].

[22] W. Weinhold, B. Friman, and W. Norenberg, Phys.Lett. **B433**, 236 (1998), [arXiv:nucl-th/9710014].

[23] W. Weinhold, B. Friman, and W. Noerenberg, Acta Phys.Polon. **B27**, 3249 (1996).

[24] W. Weinhold, B. Friman, and W. Noerenberg, Darmstadt GSI - GSI-Nachr.-95-08 (95,rec.Sep.) 6-10 (1995).

[25] W. Weinhold, *Thermodynamik mit Resonanzzustnden*, PhD Thesis, TU Darmstadt (1998).

[26] P. de Forcrand, PoS **LAT2009**, 010 (2009), [arXiv:hep-lat/1005.0539].

[27] D. Sexty, Phys. Lett. **B729**, 108 (2014), [arXiv:hep-lat/1307.7748].

[28] D. Sexty, Nucl. Phys. **A931**, 856 (2014), [arXiv:hep-lat/1408.6767].

[29] B. Schenke, S. Jeon, and C. Gale, Phys.Rev. **C82**, 014903 (2010), [arXiv:hep-ph/1004.1408].

[30] H. Song and U. W. Heinz, Phys.Rev. **C77**, 064901 (2008), [arXiv:nucl-th/0712.3715].

[31] H. Niemi, G. S. Denicol, P. Huovinen, E. Molnar, and D. H. Rischke, Phys.Rev.Lett. **106**, 212302 (2011).

[32] M. Luzum and P. Romatschke, Phys.Rev. **C78**, 034915 (2008), [arXiv:nucl-th/0804.4015].

[33] R. Chatterjee, H. Holopainen, I. Helenius, T. Renk, and K. J. Eskola, Phys.Rev. **C88**, 034901 (2013), [arXiv:hep-ph/1305.6443].

[34] H. Petersen, C. Coleman-Smith, S. A. Bass, and R. Wolpert, J. Phys. **G38**, 045102 (2011), [arXiv:nucl-th/1012.4629].

[35] J. M. Maldacena, Int.J.Theor.Phys. **38**, 1113 (1999), [arXiv:hep-th/9711200].

[36] M. P. Heller, R. A. Janik, and P. Witaszczyk, Phys.Rev.Lett. **108**, 201602 (2012), [arXiv:hep-th/1103.3452].

[37] J. Casalderrey-Solana, M. P. Heller, D. Mateos, and W. van der Schee, Phys.Rev.Lett. **111**, 181601 (2013), [arXiv:hep-th/1305.4919].

[38] A. Kurkela and G. D. Moore, JHEP **1112**, 044 (2011), [arXiv:hep-ph/1107.5050].

[39] A. Kurkela and Y. Zhu, (2015), [arXiv:hep-ph/1506.06647].

[40] T. Epelbaum and F. Gelis, Phys.Rev. **D88**, 085015 (2013), [arXiv:hep-ph/1307.1765].

[41] T. Epelbaum and F. Gelis, Phys.Rev.Lett. **111**, 232301 (2013), [arXiv:hep-ph/1307.2214].

[42] H. Niemi and G. Denicol, (2014), [arXiv:nucl-th/1404.7327].

[43] A. G. Kosovichev, **832**, 3 (2011), [arXiv:astro-ph.SR/1103.1707].

[44] R. C. Hwa and K. Kajantie, Phys. Rev. **D32**, 1109 (1985).

[45] K. Kajantie, J. I. Kapusta, L. D. McLerran, and A. Mekjian, Phys. Rev. **D34**, 2746 (1986).

[46] R. Baier, B. Pire, and D. Schiff, Phys.Rev. **D38**, 2814 (1988).

[47] T. Altherr and P. Aurenche, Z.Phys. **C45**, 99 (1989).

[48] Y. Gabellini, T. Grandou, and D. Poizat, Annals Phys. **202**, 436 (1990).

[49] R. Rapp and J. Wambach, Adv.Nucl.Phys. **25**, 1 (2000), [arXiv:hep-ph/9909229].

[50] C. Gale, S. Jeon, and B. Schenke, Int. J. Mod. Phys. **A28**, 1340011 (2013), [arXiv:nucl-th/1301.5893].

[51] J. I. Kapusta, B. Muller, and M. Stephanov, Phys. Rev. **C85**, 054906 (2012), [arXiv:nucl-th/1112.6405].

[52] K. Murase and T. Hirano, (2013), [arXiv:nucl-th/1304.3243].

[53] L. D. Landau and E. M. Lifshitz, Fluid Mechanics Second Edition: Volume 6 (Course of Theoretical Physics), Butterworth-Heinemann (1987).

[54] I. Muller, Z.Phys. **198**, 329 (1967).

[55] W. Israel, Annals of Physics **100**, 310 (1976).

[56] J. M. Stewart, Proceedings of the Royal Society of London A: Mathematical, Physical and Engineering Sciences **357**, 59 (1977).

[57] W. Israel and J. Stewart, Annals Phys. **118**, 341 (1979).

[58] A. Muronga, Phys.Rev. **C69**, 034903 (2004), [arXiv:nucl-th/0309055].

[59] U. W. Heinz, H. Song, and A. K. Chaudhuri, Phys.Rev. **C73**, 034904 (2006), [arXiv:nucl-th/0510014].

[60] P. Romatschke, Int.J.Mod.Phys. **E19**, 1 (2010), [arXiv:hep-ph/0902.3663].

[61] C. Eckart, Phys. Rev. **58**, 919 (1940).

[62] J. Bjorken, Phys.Rev. **D27**, 140 (1983).

[63] H1, ZEUS, F. Aaron *et al.*, JHEP **1001**, 109 (2010), [arXiv:hep-ex/0911.0884].

[64] S. R. de Groot, W. A. van Leeuwen, and C. G. van Weert, *Relativistic Kinetic Theory: Principles and Applications* (North-Holland; Elsevier, Amsterdam; New York, 1980).

[65] G. S. Denicol, T. Kodama, T. Koide, and P. Mota, J. Phys. **G35**, 115102 (2008), [arXiv:hep-ph/0807.3120].

[66] G. Denicol, *Microscopic foundations of relativistic dissipative fluid dynamics*, Dr., Johann Wolfgang Goethe-Universitt Frankfurt am Main, 2012, http://d-nb.info/1027082807; Johann Wolfgang Goethe-Universitt Frankfurt am Main, Diss., 2012.

[67] G. S. Denicol, H. Niemi, E. Molnar, and D. H. Rischke, Phys. Rev. **D85**, 114047 (2012), [arXiv:nucl-th/1202.4551], [Erratum: Phys. Rev.D91,no.3,039902(2015)].

[68] S. Pu, T. Koide, and D. H. Rischke, Phys.Rev. **D81**, 114039 (2010), [arXiv:hep-ph/0907.3906].

[69] G. Denicol, J.Phys. **G41**, 124004 (2014).

[70] O. Kaczmarek and A. Francis, J.Phys. **G38**, 124178 (2011), [arXiv:hep-lat/1109.4054].

[71] M. L. Miller, K. Reygers, S. J. Sanders, and P. Steinberg, Ann.Rev.Nucl.Part.Sci. **57**, 205 (2007), [arXiv:nucl-ex/0701025].

[72] H.-J. Drescher, A. Dumitru, A. Hayashigaki, and Y. Nara, Phys. Rev. **C74**, 044905 (2006), [arXiv:nucl-th/0605012].

[73] H.-J. Drescher and Y. Nara, Phys. Rev. **C76**, 041903 (2007), [arXiv:nucl-th/0707.0249].

[74] D. Kharzeev and M. Nardi, Phys. Lett. **B507**, 121 (2001), [arXiv:nucl-th/0012025].

[75] D. Kharzeev and E. Levin, Phys. Lett. **B523**, 79 (2001), [arXiv:nucl-th/0108006].

[76] H. Niemi, K. J. Eskola, and R. Paatelainen, (2015), [arXiv:hep-ph/1505.02677].

[77] K. Werner, B. Guiot, I. Karpenko, and T. Pierog, Phys. Rev. **C89**, 064903 (2014), [arXiv:nucl-th/1312.1233].

[78] B. Schenke, P. Tribedy, and R. Venugopalan, Phys. Rev. Lett. **108**, 252301 (2012), [arXiv:nucl-th/1202.6646].

[79] B. Schenke, P. Tribedy, and R. Venugopalan, Phys. Rev. **C86**, 034908 (2012), [arXiv:hep-ph/1206.6805].

[80] J. Bartels, K. J. Golec-Biernat, and H. Kowalski, Phys. Rev. **D66**, 014001 (2002), [arXiv:hep-ph/0203258].

[81] H. Kowalski and D. Teaney, Phys. Rev. **D68**, 114005 (2003), [arXiv:hep-ph/0304189].

[82] A. Kovner, L. D. McLerran, and H. Weigert, Phys. Rev. **D52**, 3809 (1995), [arXiv:hep-ph/9505320].

[83] A. Kovner, L. D. McLerran, and H. Weigert, Phys. Rev. **D52**, 6231 (1995), [arXiv:hep-ph/9502289].

[84] Y. V. Kovchegov and D. H. Rischke, Phys. Rev. **C56**, 1084 (1997), [arXiv:hep-ph/9704201].

[85] A. Krasnitz and R. Venugopalan, Nucl. Phys. **B557**, 237 (1999), [arXiv:hep-ph/9809433].

[86] A. Krasnitz and R. Venugopalan, Phys. Rev. Lett. **84**, 4309 (2000), [arXiv:hep-ph/9909203].

[87] A. Krasnitz and R. Venugopalan, Phys. Rev. Lett. **86**, 1717 (2001), [arXiv:hep-ph/0007108].

[88] T. Lappi, Phys. Rev. **C67**, 054903 (2003), [arXiv:hep-ph/0303076].

[89] H. Kowalski, L. Motyka, and G. Watt, Phys. Rev. **D74**, 074016 (2006), [arXiv:hep-ph/0606272].

[90] H. Kowalski, T. Lappi, and R. Venugopalan, Phys. Rev. Lett. **100**, 022303 (2008), [arXiv:hep-ph/0705.3047].

[91] C. Gale, S. Jeon, B. Schenke, P. Tribedy, and R. Venugopalan, Phys. Rev. Lett. **110**, 012302 (2013), [arXiv:nucl-th/1209.6330].

[92] B. Schenke, S. Jeon, and C. Gale, Phys. Lett. **B702**, 59 (2011), [arXiv:hep-ph/1102.0575].

[93] J. J. Sakurai, *Modern Quantum Mechanics*, New York, USA, Addison-Wesley (1994).

[94] W. Florkowski, *Phenomenology of Ultra-Relativistic Heavy-Ion Collisions*, Singapore ; Hackensack, NJ : World Scientific (2010).

[95] R. D. Woods and D. S. Saxon, Phys.Rev. **95**, 577 (1954).

[96] T. Hirano and Y. Nara, Phys.Rev. **C79**, 064904 (2009), [arXiv:nucl-th/0904.4080].

[97] K. J. Eskola, H. Niemi, and P. V. Ruuskanen, Phys. Rev. **C77**, 044907 (2008), [arXiv:hep-ph/0710.4476].

[98] H. Holopainen and P. Huovinen, J. Phys. Conf. Ser. **509**, 012114 (2014), [arXiv:nucl-th/1310.0347].

[99] F. Cooper and G. Frye, Phys.Rev. **D10**, 186 (1974).

[100] D. Teaney and L. Yan, Phys.Rev. **C83**, 064904 (2011), [arXiv:nucl-th/1010.1876].

[101] F. G. Gardim, F. Grassi, M. Luzum, and J.-Y. Ollitrault, Phys.Rev. **C85**, 024908 (2012), [arXiv:nucl-th/1111.6538].

[102] J. O. Andersen, N. Haque, M. G. Mustafa, M. Strickland, and N. Su, (2014), [arXiv:hep-ph/1411.1253].

[103] R. D. Pisarski, Nucl.Phys. **B309**, 476 (1988).

[104] J. Kapusta and C. Gale, *Finite-temperature field theory: Principles and applications* (Cambridge University Press, 2006).

[105] M. Bellac, *Thermal Field Theory,*Cambridge Monographs on Mathematical Physics (Cambridge University Press, 2000).

[106] C. Gale and J. I. Kapusta, Nucl.Phys. **B357**, 65 (1991).

[107] G. Gounaris and J. Sakurai, Phys.Rev.Lett. **21**, 244 (1968).

[108] V. Eletsky, M. Belkacem, P. Ellis, and J. I. Kapusta, Phys.Rev. **C64**, 035202 (2001), [arXiv:nucl-th/0104029].

[109] C. Gale, D. Seibert, and J. I. Kapusta, Phys.Rev. **D56**, 508 (1997), [arXiv:hep-ph/9702269].

[110] O. Linnyk, W. Cassing, J. Manninen, E. L. Bratkovskaya, and C. M. Ko, Phys. Rev. **C85**, 024910 (2012), [arXiv:nucl-th/1111.2975].

[111] B. L. Ioffe, V. A. Khoze, and L. N. Lipatov, *Hard processes, vol. 1: phenomenology, quark parton model*, Amsterdam, Netherlands, North-Holland (1984).

[112] G. Vujanovic, J. Ruppert, and C. Gale, Phys.Rev. **C80**, 044907 (2009), [arXiv:nucl-th/0907.5385].

[113] K. L. Haglin and C. Gale, Nucl.Phys. **B421**, 613 (1994), [arXiv:nucl-th/9401003].

[114] J. Durso, Phys.Lett. **B184**, 348 (1987).

[115] S. Jeon and P. J. Ellis, Phys.Rev. **D58**, 045013 (1998), [arXiv:hep-ph/9802246].

[116] H. Harari, Phys. Rev. Lett. **20**, 1395 (1968).

[117] P. D. B. Collins, *An Introduction to Regge Theory and High-Energy Physics*, Cambridge, UK, University Press (1977).

[118] A. Donnachie and P. V. Landshoff, Phys. Lett. B **296**, 227 (1992), [arXiv:hep-ph/9209205].

[119] A. T. Martell and P. J. Ellis, Phys. Rev. C **69**, 065206 (2004), [arXiv:nucl-th/0404057].

[120] J. Ruppert, C. Gale, T. Renk, P. Lichard, and J. I. Kapusta, Phys.Rev.Lett. **100**, 162301 (2008), [arXiv:hep-ph/0706.1934].

[121] S. Caron-Huot, Phys. Rev. **D79**, 125009 (2009), [arXiv:hep-ph/0903.3958].

[122] C. Shen, J.-F. Paquet, U. Heinz, and C. Gale, Phys. Rev. **C91**, 014908 (2015), [arXiv:nucl-th/1410.3404].

[123] K. Dusling and S. Lin, Nucl.Phys. **A809**, 246 (2008), [arXiv:nucl-th/0803.1262].

[124] D. Teaney, Phys.Rev. **C68**, 034913 (2003), [arXiv:nucl-th/0301099].

[125] A. Kurganov and E. Tadmor, Journal of Computational Physics **160**, 241 (2000).

[126] M. Dion *et al.*, Phys. Rev. C **84**, 064901 (2011).

[127] R. Chatterjee, D. K. Srivastava, U. Heinz, and C. Gale, Phys. Rev. C **75**, 054909 (2007).

[128] J. Deng, Q. Wang, N. Xu, and P. Zhuang, Phys.Lett. **B701**, 581 (2011), [arXiv:nucl-th/1009.3091].

[129] P. Mohanty *et al.*, Phys.Rev. **C85**, 031903 (2012), [arXiv:nucl-th/1111.2159].

[130] A. Shor, Phys. Lett. **B233**, 231 (1989), [Erratum: Phys. Lett.B252,722(1990)].

[131] E. V. Shuryak, Phys.Rev. **C55**, 961 (1997), nucl-th/9605011.

[132] H. van Hees, V. Greco, and R. Rapp, Phys.Rev. **C73**, 034913 (2006), [arXiv:nucl-th/0508055].

[133] S. Caron-Huot and G. D. Moore, Phys. Rev. Lett. **100**, 052301 (2008).

[134] P. Gossiaux, J. Aichelin, and T. Gousset, Prog.Theor.Phys.Suppl. **193**, 110 (2012), [arXiv:hep-ph/1201.4038].

[135] M. Younus, C. E. Coleman-Smith, S. A. Bass, and D. K. Srivastava, (2013), [arXiv:nucl-th/1309.1276].

[136] G. D. Moore and D. Teaney, Phys.Rev. **C71**, 064904 (2005), [arXiv:hep-ph/0412346].

[137] JET Collaboration, K. M. Burke *et al.*, Phys.Rev. **C90**, 014909 (2014), [arXiv:nucl-th/1312.5003].

[138] W. Horowitz, Nucl.Phys. **A931**, 541 (2014).

[139] A. Mocsy, P. Petreczky, and M. Strickland, Int.J.Mod.Phys. **A28**, 1340012 (2013), [arXiv:hep-ph/1302.2180].

[140] C. Young, B. Schenke, S. Jeon, and C. Gale, Phys.Rev. **C86**, 034905 (2012), [arXiv:nucl-th/1111.0647].

[141] M. Cacciari, M. Greco, and P. Nason, JHEP **9805**, 007 (1998), [arXiv:hep-ph/9803400].

[142] K. J. Eskola, V. J. Kolhinen, and C. A. Salgado, Eur.Phys.J. **C9**, 61 (1999), [arXiv:hep-ph/9807297].

[143] K. J. Eskola, V. J. Kolhinen, and P. V. Ruuskanen, Nucl.Phys. **B535**, 351 (1998), [arXiv:hep-ph/9802350].

[144] S. Caron-Huot and G. D. Moore, JHEP **0802**, 081 (2008), [arXiv:hep-ph/0801.2173].

[145] T. Sjostrand, S. Mrenna, and P. Z. Skands, Comput. Phys. Commun. **178**, 852 (2008), [arXiv:hep-ph/0710.3820].

[146] C. Peterson, D. Schlatter, I. Schmitt, and P. M. Zerwas, Phys. Rev. D **27**, 105 (1983).

[147] B. Schenke, C. Gale, and S. Jeon, Phys.Rev. **C80**, 054913 (2009), [arXiv:hep-ph/0909.2037].

[148] STAR Collaboration, L. Ruan, Nucl. Phys. **A910-911**, 171 (2013), [arXiv:nucl-ex/1207.7043].

[149] E. Braaten, R. D. Pisarski, and T.-C. Yuan, Phys.Rev.Lett. **64**, 2242 (1990).

[150] M. H. Thoma, (2000), [arXiv:hep-ph/0010164].

[151] G. D. Moore and J.-M. Robert, (2006), [arXiv:hep-ph/0607172].

[152] P. Aurenche, F. Gelis, G. D. Moore, and H. Zaraket, JHEP **12**, 006 (2002), [arXiv:hep-ph/0211036].

[153] M. E. Carrington, A. Gynther, and P. Aurenche, Phys. Rev. **D77**, 045035 (2008), [arXiv:hep-ph/0711.3943].

[154] J. I. Kapusta, Phys.Rev. **C16**, 1493 (1977).

[155] L. Landsberg, Phys.Rept. **128**, 301 (1985).

[156] STAR Collaboration, L. Adamczyk *et al.*, Phys.Rev. **C90**, 064904 (2014), [arXiv:nucl-ex/1402.1791].

[157] H. Holopainen, H. Niemi, and K. J. Eskola, Phys. Rev. **C83**, 034901 (2011), [arXiv:hep-ph/1007.0368].

[158] J.-F. Paquet, Private Communication .

[159] H. Bebie, P. Gerber, J. Goity, and H. Leutwyler, Nucl.Phys. **B378**, 95 (1992).

[160] T. Hirano and K. Tsuda, Phys.Rev. **C66**, 054905 (2002), [arXiv:nucl-th/0205043].

[161] B. Schenke, S. Jeon, and C. Gale, Phys.Rev.Lett. **106**, 042301 (2011), [arXiv:hep-ph/1009.3244].

[162] B. Schenke, S. Jeon, and C. Gale, Phys.Rev. **C85**, 024901 (2012), [arXiv:hep-ph/1109.6289].

[163] H. Marrochio *et al.*, (2013), [arXiv:nucl-th/1307.6130].

[164] P. Romatschke and U. Romatschke, Phys.Rev.Lett. **99**, 172301 (2007).

[165] G. Vujanovic *et al.*, Nucl.Phys. **A932**, 230 (2014), [arXiv:hep-ph/1404.3714].

[166] A. Nakamura and S. Sakai, Phys.Rev.Lett. **94**, 072305 (2005), [arXiv:hep-lat/0406009].

[167] M. Natsuume and T. Okamura, Phys.Rev. **D77**, 066014 (2008), [arXiv:hep-th/0712.2916].

[168] A. Monnai, Private Communication .

[169] S. Ryu *et al.*, (2015), [arXiv:nucl-th/1502.01675].

[170] J.-B. Rose *et al.*, Nucl. Phys. **A931**, 926 (2014).

[171] R. Rapp, J. Wambach, and H. van Hees, Landolt-Bornstein **23**, 134 (2010), [arXiv:hep-ph/0901.3289].

[172] S. Donnachie, H. G. Dosch, O. Nachtmann, and P. Landshoff, *Pomeron physics and QCD*, Camb. Monogr. Part. Phys. Nucl. Phys. Cosmol. (2002).

[173] I. S. Gradsteyn and I. M. Ryzhik, *Table of integrals, series and products*, London, UK, Academic Press (1963).

[174] P. B. Arnold, G. D. Moore, and L. G. Yaffe, JHEP **05**, 051 (2003), [arXiv:hep-ph/0302165].